UNIVERSITY OF CALIFORNIA SAN DIEGO

Colloidal Syntheses and Redox Chemistries of Tunable Plasmonic Copper Phosphide Nanocrystals

A Dissertation submitted in partial satisfaction of the requirements
for the degree Doctor of Philosophy

in

Chemistry

by

Alexander Gregory Rachkov

Committee in charge:

Professor Alina M. Schimpf, Chair
Professor Joshua S. Figueroa
Professor Jesse V. Jokerst
Professor Andrew C. Kummel
Professor Michael J. Sailor

2023

The Dissertation of Alexander Gregory Rachkov is approved, and it is acceptable in quality and form for publication on microfilm and electronically.

University of California San Diego

2023

DEDICATION

In loving memory of Атанас Рашков

TABLE OF CONTENTS

LIST OF FIGURES

LIST OF TABLES

LIST OF SCHEMA

LIST OF ABBREVIATIONS

bv	By volume
CAN	Cerium(IV) ammonium nitrate
$Cu_{3-x}P$	Copper phosphide
EDS	Energy dispersive X-ray spectroscopy
Equiv	Equivalents (molar)
ε_x	Extinction coefficient at x nm (or eV) in units of M^{-1} cm^{-1}
h	Hours
ICP–MS	Inductively coupled plasma mass spectrometry
Li	Lithium metal
LSPR	Localized surface plasmon resonance
MAS ssNMR	Magic-angle spinning solid-state nuclear magnetic resonance
MeCN	Acetonitrile
MeOH	Methanol
min	Minutes
ml	Milliliter
MS	Mass spectrometry
NMR	Nuclear magnetic resonance
OAm	Oleylamine
OTf	Trifluoromethanesulfonate (also triflate)
$P(NEt_2)_3$	Phosphorus triamide, hexaethyl- (also tris(diethylamino)phosphine)
pXRD	Powder X-ray diffraction
s	Seconds

STEM	Scanning transmission electron microscopy
TBA	Tetrabutylammonium
TEM	Transmission electron microscopy
THF	Tetrahydrofuran
TOA	Tri-n-octylamine
TOP	Tri-n-octylphosphine

ACKNOWLEDGEMENTS

The following personal acknowledgements are thematically grouped and ordered. The level of detail for any given acknowledgement is not a reliable indicator of my gratitude towards the pertinent person(s); words are woefully inadequate for expressing the depth of my appreciation, in any case.

I can say that my work for this dissertation, and the research projects detailed within, could not have been undertaken in the absence of the contributions and support from my advisor, Prof. Alina Schimpf. I am grateful that Alina has, from the moment I joined her research lab, afforded me the opportunity to dictate, to a substantial degree, the direction of my research endeavors. I have grown as an independent thinker under Alina's mentorship. Effective written and visual science communication is one of the many valuable skills which I have improved upon by working with Alina.

I want to recognize current and former Schimpf lab members whom I have had the pleasure of interacting with these past (almost) six years: Liana Alves, Haeun Chang, Dr. Linfeng Chen, Michel Chen, Dr. Jessica Geisenhoff, Alea Ha, Olivia Hawkins, Dion Jiao, Dr. Hankyeol Jung, Carl Lemmon, Natacha Oget, Haley Palm, Billy Pistel, Khin San, Daniela Sung, Ashley Tamura, Bruce Thompson, Dr. Michael Turo, and Hang Yin. Each of them has played a big part in the cultivation of a warm and inviting lab atmosphere filled with jokes and laughter, as well as uplifting commiserations during tough times. I am especially thankful to Michael and Jessica for helping me get started working in the lab and for offering invaluable daily assistance with and feedback on experimental design and ideas during my first year as a graduate student. I also am grateful to have mentored Dion, an undergraduate researcher, during her time in the Schimpf lab. Dion faced the unique challenges and uncertainties of scientific

research with a commendably upbeat attitude and an open mind, a perspective which I strive to maintain as best as I can.

I benefitted from collaborations and external guidance while carrying out the work of this dissertation. I am thankful to Prof. Joshua Figueroa for sharing his expertise with me and Alina during discussions on the bonding and reactivity of aminophosphines. I would also like to thank the other committee members, Prof. Jesse Jokerst, Prof. Andrew Kummel, and Prof. Michael Sailor, for asking insightful questions about my work. Adam Grippo, a graduate student in the Figueroa lab, graciously took the time to test alternative synthetic routes to aminophosphine precursors, an endeavor which was outside my area of expertise. I am appreciative that Prof. Gregory Holland was willing to collaborate by hosting the magic-angle spinning solid-state NMR experiments of this dissertation and lending his expertise for the interpretation of the results. Dr. Kevin Chalek, a postdoctoral researcher in the Holland lab, greatly assisted with sample preparation and data processing and was the one who actually ran and troubleshot the NMR experiments. Finally, I was very lucky to be able to learn from Dr. Milan Gembicky, who proved to be an invaluable resource for anything related to crystallography. Milan taught me most of my practical knowledge of X-ray diffraction and directly assisted me with the collection of single-crystal X-ray diffraction data and the corresponding structure determination. It always brightened my day when I could have a spontaneous mid-day espresso with Milan and swap stories about our outdoor, nature-seeking excursions to the American Southwest.

Several undergraduate professors and/or mentors at the University of Washington played critical roles in shaping my academic trajectory and encouraging me on my path to graduate school. It was in the lab of Prof. Brian Kraemer that I got my first exposure to academic

research. I am very grateful that he took a chance on me as a completely inexperienced first-year undergraduate student. It was under Brian's patient mentorship that I started building up many of the research skills which I now possess. The class taught by Prof. James Mayer was my first exposure to inorganic and materials chemistry and he played no small role in inspiring me to pivot and change my major to chemistry. I must also thank Prof. Daniel Gamelin, my second undergraduate research advisor. Daniel's scientific creativity and deep knowledge of various subfields were amazing to experience during group meetings. Daniel's unique combination of intellectual rigor, curiosity, and kindness were, and still are, an inspiration for me. I am additionally grateful to have worked alongside my then-graduate-student-mentors Dr. José Araujo and Dr. Michael De Siena, who have taught me most of what I know about colloidal synthesis and nanocrystal characterization.

There is no person who better understands the personal struggles which I endured during my time as a graduate student than my dear friend, Dr. Christian Seitz. Christian has always lent an ear and been an empathic listener who is ready and willing to propose helpful solutions, share alternative perspectives, or give otherwise comforting words. Christian's dependable companionship and our adventures together have made my time living in San Diego far more enjoyable and memorable. The early Blonde Bar outings, Anza-Borrego camping trips, Thanksgiving road trips, and tennis practice sessions have all been a blast, and it's far from over!

I have been fortunate enough to make many great friends since moving to San Diego for graduate school. As a result of befriending Dr. Madison Edwards, I participated in my first trail half-marathon, got the idea to pick up mountain biking as one of my now-favorite hobbies, got inspired to pursue a career in education, and, most importantly, improved myself to become

a more broad-minded and considerate individual. The original Benhurst Ave housemates Edo, Tjeerd, Victor and Davide were a constant and welcome presence during the more isolating times of the pandemic. Our soccer scrimmages at the park and backyard barbecues gave some semblance of normality to troubling and stressful times. The other friends that I have made during my time living in San Diego are fantastic and my interactions with them have served as very much welcome, and necessary, reminders during my graduate studies that there is a big, wide world outside of academia.

The last group of people that I want to thank did not directly affect my graduate studies, my academic trajectory, or my immediate life in San Diego. Even still, I would surely be lost in this life if not for my "Sacred" family and my closest childhood friends. Any efforts to put my appreciation into words sound abjectly underwhelming to me. So, I'll just say instead: "Хайде наздраве!" (to the former) and "I'm coming home at last!" (to the latter).

Chapter 2, in full, is a reprint of the material as it appears in "Colloidal Synthesis of Tunable Copper Phosphide Nanocrystals" *Chem. Mater.* **2021**, 33, 1394. The dissertation author was the primary author of this paper and gratefully acknowledges the contributions of coauthor Alina M. Schimpf. TEM imaging was performed at the National Center for Microscopy and Imaging Research at UC San Diego. ESI-TOF mass spectrometry was performed at the Molecular Mass Spectrometry Facility at University of California, San Diego. Powder X-ray diffraction measurements were performed at the UC San Diego Crystallography Facility.

Chapter 3, in part, is currently being prepared for imminent submission for publication of the material. The dissertation author was the primary author of this paper and gratefully acknowledges the contributions of coauthors Kevin R. Chalek, Mingjie Xu, Gregory P.

Holland, and Alina M. Schimpf. This research was primarily supported by the National Science Foundation through the UC San Diego Materials Research Science and Engineering Center (DMR-2011924). TEM imaging was performed at the National Center for Microscopy and Imaging Research at UC San Diego. Powder X-ray diffraction measurements were performed at the UC San Diego Crystallography Facility with the welcome technical guidance of Dr. Milan Gembicky. STEM–EDS imaging and mapping were performed at the Irvine Materials Research Institute. The authors thank Haeun Chang for assistance with ICP–MS data collection, which was performed at the Environmental and Complex Analysis Laboratory at UC San Diego.

Chapter 4 is comprised of unpublished work which may eventually be published in some form in the more distant future. The dissertation author was the primary author of this chapter and gratefully acknowledges the contributions of advisor Alina M. Schimpf. This research was primarily supported by the National Science Foundation through the UC San Diego Materials Research Science and Engineering Center (DMR-2011924). TEM imaging was performed at the National Center for Microscopy and Imaging Research at UC San Diego. Single-crystal and powder X-ray diffraction measurements were performed at the UC San Diego Crystallography Facility with the welcome technical guidance of Dr. Milan Gembicky.

VITA

2017 Bachelor of Science in Chemistry, University of Washington

2019 Master of Science in Chemistry, University of California San Diego

2023 Doctor of Philosophy in Chemistry, University of California San Diego

PUBLICATIONS

Rachkov, A. G., Chalek, K. R., Xu, M., Holland, G. P., and Schimpf, A. M. "Redox Chemistries and Plasmonic Tunability of Vacancy-Doped Copper Phosphide Nanocrystals" *In preparation*

Rachkov, A. G. and Schimpf, A. M. "Colloidal Synthesis of Tunable Copper Phosphide Nanocrystals" *Chem. Mater.* **2021**, *33*, 1394.

De Siena, M. C., ***Rachkov, A. G.,*** Fainblat, R., James, D., Creutz, S. E., Stoll, S. L., and Gamelin, D. R. "Using Redox Titrations to Probe the Role of Trivalent Impurity Ions in the Ferromagnetism of Colloidal EuS Nanocrystals" *Chem. Mater.* **2020**, *32*, 8633.

ABSTRACT OF THE DISSERTATION

Colloidal Syntheses and Redox Chemistries of Tunable Plasmonic Copper Phosphide Nanocrystals

by

Alexander Gregory Rachkov

Doctor of Philosophy in Chemistry

University of California San Diego, 2023

Professor Alina M. Schimpf, Chair

Colloidal copper phosphide ($Cu_{3-x}P$) nanocrystals are attractive electronic materials due to their ability to support excess delocalized holes, with both synthesis and dynamic redox modulation allowing tuning of localized surface plasmon resonance (LSPR) absorption in the near-IR. This dissertation presents developments in the colloidal syntheses and post-synthetic redox chemistries of high-quality $Cu_{3-x}P$ nanoplatelets with the attainment of tunable nanocrystallite lateral sizes, LSPR energies, compositions, and optoelectronic properties. A one-pot, colloidal synthesis of $Cu_{3-x}P$ nanoplatelets with copper halide salt and aminophosphine

in the presence of oleylamine is presented in Chapter 2. The reactivity of an *in situ* copper-phosphorus precursor is modulated by varying precursor composition and coordinating solvent ratio to tune nanocrystal lateral size. Oleylamine-to-aminophosphine molar ratio is found to alter particle nucleation activity and access atom-efficient size tuning. By modulating precursor reactivity, the syntheses presented in Chapter 2 are used to access nanocrystals with lateral sizes of 6.1–23 nm and LSPR energies of 709–861 meV. The low polydispersity, size- and LSPR-tunability and colloidal stability make aminophosphine-synthesized $Cu_{3-x}P$ nanocrystals promising candidates for investigations into factors governing their LSPR energy, around which the findings of the subsequent chapter are based. Three copper-coupled redox chemistries are presented in Chapter 3 which allow post-synthetic modulation of the delocalized hole concentrations and corresponding LSPR absorption in colloidal $Cu_{3-x}P$ nanocrystals. Changes in the structural, optical, and compositional properties are evaluated by powder X-ray diffraction, electronic absorption spectroscopy, ^{31}P magic-angle spinning solid-state nuclear magnetic resonance spectroscopy and elemental analysis. The redox chemistries are shown to access nanocrystals with LSPR energies of 660–890 meV, a larger range than has been possible through synthetic tuning. The largest structural and LSPR modulation is achieved through the use of a divalent metal halide and trioctylphosphine, with the smallest reported unit-cell volume (295.2 $Å^3$) and most downfield ^{31}P chemical shift (+346 ppm) reported for $P6_3cm$ $Cu_{3-x}P$. In Chapter 4, the platform for systematic mechanistic investigations developed in Chapter 2 is extended to use copper phosphide as a model system for the study of aminopnictine precursor chemistry and the elucidation of metal pnictide nanocrystal formation mechanisms. Preliminary findings are presented for the investigation of the synthetic roles of copper salt counteranion and aminophosphine amide identity.

CHAPTER 1. Introduction

1.1 Introduction to Colloidal Synthesis

An overarching goal for the development of novel materials is their eventual integration into devices through the targeted utilization of their unique electronic, magnetic, and optical properties. A promising strategy for the development of new materials with unexplored properties, which may be of long-term significance for application-based research and development, is the nanoscaling of familiar bulk solid-state systems. Colloidal synthesis is a particularly promising approach for the attainment of high-quality nanosized solid-state systems and is utilized for the studies of nanoscale copper phosphide presented in this dissertation.

Inorganic colloidal nanocrystals are attractive systems that have been a central focus of materials chemistry research for over two decades. A seminal study which set the stage for the development of these nanomaterials is a report on colloidal cadmium chalcogenides (CdE; E = S, Se, Te) from Bawendi and coworkers. Low-polydispersity nanocrystal ensembles were attained by inducing a homogenous nucleation event in which organometallic reagents were pyrolyzed by injection into a hot long-chain coordinating solvent.[1] The LaMer nucleation model was invoked to explain this result and describes a monomer concentration threshold for self-nucleation below which only diffusion-limited growth occurs.[2] After the temporally discrete nucleation event associated with the injection in the Bawendi synthesis, slow growth and annealing occur with no further formation of new nuclei. This phase involves growth by monomer diffusion and a process known as Ostwald ripening, involving the dissolution of smaller particles with higher solubility to grow larger particles and minimize surface energy of the ensemble.[3-4] The coordination of long-chain ligands to the nanocrystal surface creates an organic–inorganic interface[5] (illustrated in

Figure 1.1), which prevents uncontrolled growth through stabilization and passivation of the surface. The versatility of this bottom-up 'hot injection' method was demonstrated by the preparation of monodisperse CdSe crystallites ranging from 12 to 115 Å in diameter through variation of temperature and growth time.[1]

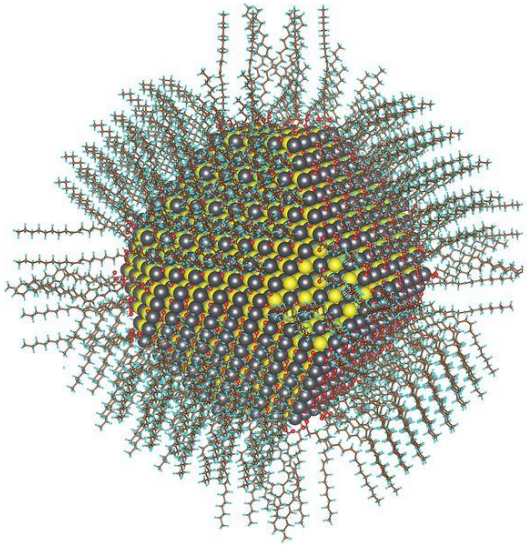

Figure 1. 1. Calculated structure of a 5-nm-diameter lead sulfide nanocrystallite with surface passivation by long-chain carboxylate and hydroxyl anion. Reprinted with permission from reference 6.

The utilization of the organic–inorganic interface formed by long-chain ligand coordination to kinetically control colloidal crystallite growth has been successfully generalized beyond cadmium chalcogenides. This synthetic strategy has enabled the development of unary metal,[7-8] other metal chalcogenide (e.g. II-VI and I-III-VI semiconductors)[9-10] and metal oxide[11] colloidal nanocrystals. In these reports, monodisperse, size tunable, and high-quality colloidal crystallites are synthesized through empirical optimization of reaction parameters such as temperature, temporality of precursor decomposition, the amount and composition of coordinating ligand, and the identity and concentration of precursor. These experimental factors can be leveraged to attain tunability of material properties such as nanocrystal size and shape and crystal

phase (Scheme 1.1), although the reaction variables are often interdependent and complexly related to one another. A limited set of examples includes: i) use of coordinating solvent and the influence on precursor conversion to access a metastable phase of tungsten diselenide while simultaneously tuning particle size[12] and ii) rational control of crystallite anisotropy through selective adhesion of coordinating ligand to particular crystal facets to inhibit growth.[5, 13-14] The high degree of synthetic control over morphology and size without deleteriously affecting ensemble dispersity, as well as inexpensive fabrication and solution processability are the primary benefits of colloidal nanocrystals for use as functional materials.

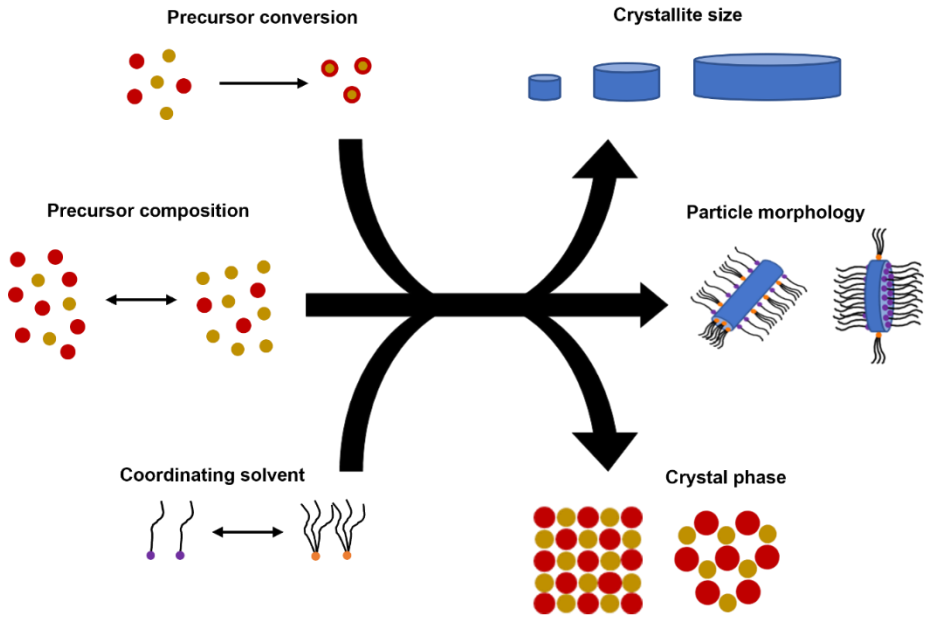

Scheme 1. 1. Tunability of material properties, such as crystallite size, particle morphology, and crystal phase, which is attainable in colloidal synthesis through an interplay of experimental factors, including coordinating solvent and precursor composition and conversion.

The largely empirical development of high-quality colloidal syntheses for colloidal unary metals, metal chalcogenides and metal oxides have enabled research studies on their emergent nanoscale physical properties. The following examples only represent a small portion of the wide body of literature on physical property studies of colloidal nanocrystals. They are presented

nonetheless in order to showcase the importance of developing rational solution-phase synthetic routes to tunable and well-defined nanocrystals for the purpose of targeting specific material properties. Monodisperse and quantum-confined visible light-emitting nanocrystals, also known as 'quantum dots', are being explored for display applications as tunable high-color-purity phosphors.[15] Solution-phase chemical and photochemical injection of charge carriers have been demonstrated to allow tunability of optical and electronic properties.[16-17] Heterogeneous photoredox catalysis has been made possible through surface functionalization of semiconducting nanocrystals.[18] This dissertation represents a contribution to the expansion of the synthetic and mechanistic framework for metal phosphide nanocrystal formation, a necessary precondition for analogous characterizations and physical property studies.

Atom-efficient size control of colloidal nanocrystals represents a significant synthetic advancement over the empirical improvements which have been predominant in the literature for the past thirty years. A seminal example is the exquisite, atom-efficient synthetic control of lead sulfide nanocrystal size (Figure 1.2) which was demonstrated by Hendricks and coworkers upon varying substituted thiourea precursor identity.[19] The synthetic advancement of nanoscale metal phosphides, characterized by their high metal–metalloid and metalloid–metalloid covalency and kinetically persistent molecular intermediates,[20] stands to particularly benefit from building similar rational and predictive design principles derived from mechanistic elucidation, rather than "blindly" relying on empirical trial-and-error optimization.

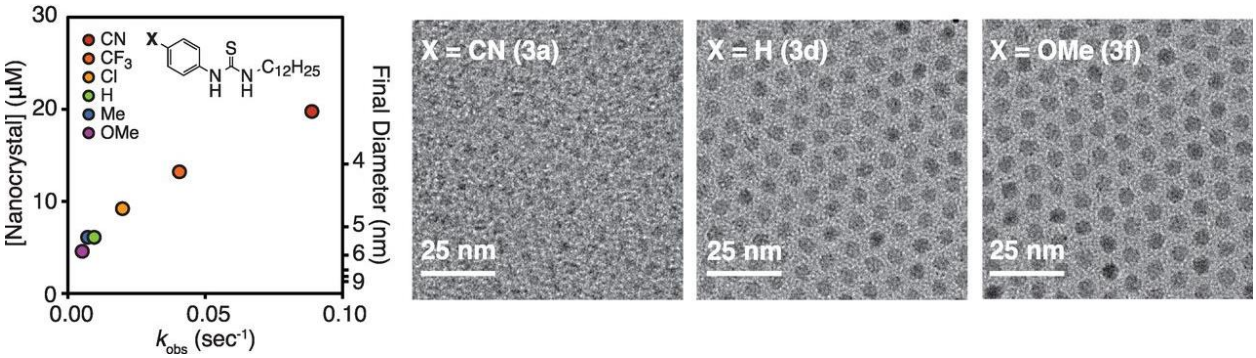

Figure 1. 2. Tunability of substituted thiourea precursor conversion reactivity for exquisite control over nucleation activity and final nanoparticle size in an atom-efficient manner. Reprinted with permission from reference 19.

1.2 Introduction to Nanoscale Metal Phosphides and Aminophosphine Precursors

Bulk metal phosphides have been used for numerous commercial applications as semiconductors,[21] magnetic refrigerants,[22] and catalysts.[23] Nanoscale metal phosphides, by contrast, are a comparatively exotic class of materials with a dearth of reliable synthetic methodology.[24] The absence of conceptual mechanistic frameworks for these nanomaterials' syntheses has considerably limited the possibilities for physical property studies. A brief historical account of the nanoscaling efforts for metal phosphides is instructive and contextualizes the contribution of this dissertation to the field of metal phosphide colloidal synthesis.

It is important to make the clear distinction that the findings of this dissertation do not represent an early report of metal phosphide colloidal synthesis. Indium phosphide, in particular, has been a target in materials chemistry research as far back as 1960, with one of the very first reported binary semiconductor syntheses reacting phosphine gas with trimethylindium.[25] Much of the subsequent research during the 20th century on solution routes to nanoscale materials was driven by interest in the development of tunable band gap semiconductors.[24] It is for this reason that indium phosphide continued to feature as an important model system during the surfactant-

supported synthetic breakthrough studies of the 1990s, such as the seminal reports from Mićić and coworkers.[26-27]

Metal–phosphine single-source precursors[28-30] were extensively prepared and used in colloidal synthesis during the 1990s, with an investigational emphasis on understanding molecular reaction pathways for precise synthetic control. Decomposition routes, such as silylphosphine methanolysis, were identified in these pioneering works by Buhro and coworkers.[31-32] Several drawbacks, however, have limited the efficacy of colloidal synthesis using silylphosphine-based single-source precursors, including i) high precursor toxicity, ii) competitive non-productive decomposition pathways, and iii) too-unstable preformed bonds of the single-source precursors. Thus, while silylphosphine-based single-source precursors have proved useful for gleaning insights into reaction intermediates and mechanisms, their expensiveness and scalability issues led to the subsequent consideration of alternative phosphorus precursors.

Over the past twenty-five years, a wide variety of other molecular phosphorus precursors have been investigated for use in colloidal metal phosphide syntheses. These include, but are not limited to, trioctylphosphine (TOP), other "PH_3-forming" species (e.g., sodium hypophosphite), and elemental phosphorus (Figure 1.3).[24] TOP, in particular, merits deeper consideration on account of its diametric opposition to silylphosphine precursors. TOP is a prototypical surfactant in colloidal synthesis and has also been exploited in silylphosphine-based syntheses to solubilize metal precursors and stabilize the resulting metal phosphide colloids.[33-35] TOP was first demonstrated in 2004 as a phosphorus source for colloidal synthesis in two separate publications on iron phosphide nanocrystals.[36-37] Since then, TOP and other alkyl- and aryl-phosphines have become the most predominant class of phosphorus precursors for the colloidal synthesis of metal phosphides due to their versatility and easy-to-handle nature (Figure 1.3).[24] TOP is inexpensive

and scalable, which are important considerations for overcoming the "silylphosphine problem." Unfortunately, TOP is also quite unreactive, typically used in large excess, and difficult to use in systematic mechanistic studies.[24] TOP only decomposes at high temperatures, above which unary metal intermediates tend to form, and, therefore, metal phosphide syntheses using TOP are incredibly complex and typically involve solid-state-mediated reactivity pathways.[38] While use of TOP has led to improvements in synthetic outcomes for metal phosphide nanocrystal syntheses, the developments have been empirical, with arbitrary synthesis design guidelines that are highly dependent on exquisite temperature control and, most typically, time-controlled reagent additions.[24]

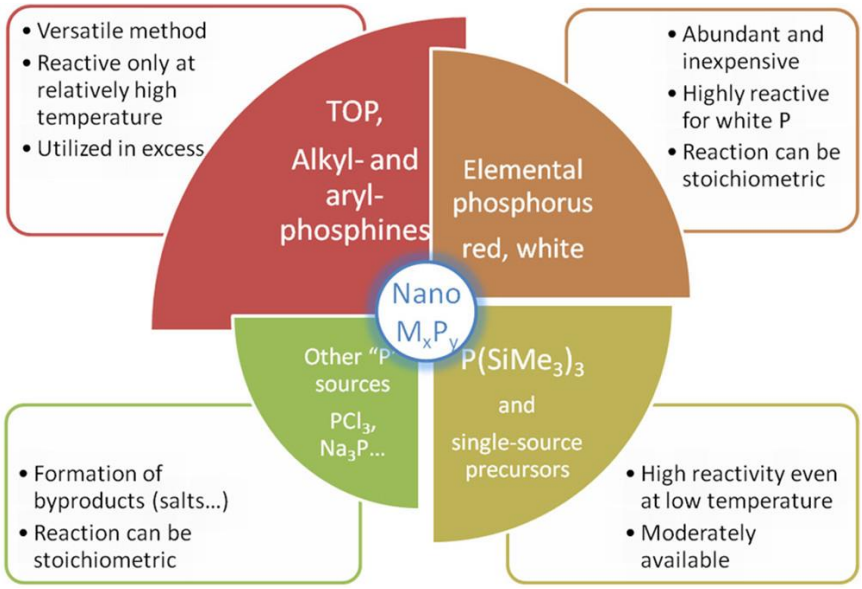

Figure 1. 3. Overview of the molecular phosphorus precursors used in the syntheses of metal phosphide nanoparticles, with slice size proportional to prevalence of the precursors in the literature. Reprinted with permission from reference 24.

Tris(dialkylamino)phosphine precursors have quite recently emerged as easy-to-handle substitutes in the colloidal synthesis of InP nanocrystals.[39-44] Their use was thereafter extended to the syntheses of Zn-, Ni-, Co- and Cd-based (but not Cu-based) metal phosphide nanocrystals.[45]

Aminophosphines are particularly promising up-and-coming precursors because of their versatility, as indicated by their successful use with both other metals and other pnictides[46-50], as well as their intermediate reactivity between those of alkylphosphines and silylphosphines. Aminophosphine precursors are utilized in this dissertation to achieve tunable, low-polydispersity syntheses of colloidal copper phosphide nanocrystals, with the grand, big-picture aim of providing a medium for fresh investigations on understanding molecular reaction pathways, such as those which characterized the earliest synthetic efforts in metal phosphide colloidal synthesis during the 1990s. Precise nanocrystal size control and nanoscale self-assembly remain important yet elusive targets for metal phosphide nanomaterial development and aminophosphines might just hold the key for their attainment.

As of the writing of this dissertation, the colloidal syntheses of copper phosphide presented herein are the only examples in the literature where an aminopnictine precursor is used to access substantial reactivity and size tunability, while maintaining low ensemble polydispersity, in the absence of external metal precursors (e.g., use of Zn^{2+} in InP synthesis[39-42]) or reducing agents[48], the presence of which would complicate mechanistic analysis. Thus, colloidal copper phosphide nanocrystals synthesized with easy-to-handle trisaminophosphine are appraised and verified as a simple, promising model system for the rational development of general solution-phase synthetic principles for the attainment of well-defined nanocrystalline metal phosphides with tailored properties. It is anticipated that the insights derived from the colloidal syntheses of copper phosphides in this dissertation and future work will more broadly inform the development of improved synthetic methodologies for other metal pnictides due to similarities in pnictogen precursor chemistry (such as with trisaminoarsines[46-48, 50] or pnictogen chlorides[49]).

1.3 Introduction to Electronic Doping and Copper Phosphide

Colloidal nanocrystals which support excess delocalized charge-carriers and host tunable carrier densities are burgeoning electronic nanomaterials.[16, 51-55] Modulation of charge-carrier concentration, most typically demonstrated in metal oxide semiconducting nanocrystal systems, is often achieved via post-synthetic redox or photo-redox manipulations,[16, 54, 56-58] or through defect incorporation and activation during synthesis[54, 59-66] (Scheme 1.2). These material transformations access interesting photophysical properties, including tunable localized surface plasmon resonances (LSPRs) in the mid- or near-IR.[54, 58-71] Nanocrystals for which LSPR absorption is derived from delocalized holes carriers[66, 72] are less common than those exhibiting *n*-type electronic doping as demonstrated with Scheme 1.2. Copper chalcogenides are the most widely studied[61, 65, 67-68, 70, 73-78] *p*-type doped nanomaterials with delocalized holes arising to compensate intrinsic copper vacancies. The LSPR absorption in the near-IR for these degenerately p-typed doped copper chalcogenide nanomaterials has been exploited for a number of applications, including plasmon-enhanced chemical conversion of chemisorbed species[79] and surface-enhanced Raman scattering sensing of nonpolar analytes[80] (Figure 1.4), which are inaccessible to the traditional noble metal LSPR-exhibiting nanomaterials (Ag, Au) due to their incompatible surface chemistry.

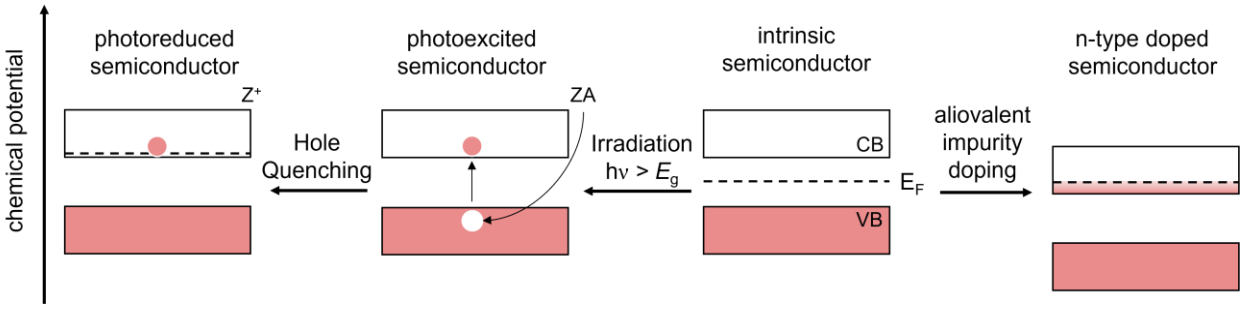

Scheme 1. 2. Strategies for introducing and modulating excess delocalized electron carriers in an intrinsic semiconductor nanocrystal, $M_n^{x+}E_m^{y-}$. On the right, the *n*-type aliovalent ion acts as shallow donor and its $(x+1)^+$ charge compensates for excess electrons (a similar diagram with the reverse situation applies for *p*-type doping). On the left, a photoexcited electron-hole pair is reduced by hole quenching agent ZA, with the resulting Z^+ ion acting as charge compensation for the leftover electron.

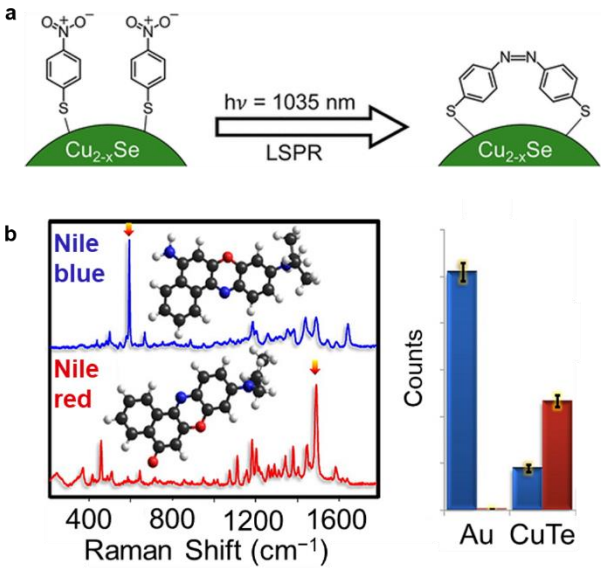

Figure 1. 4. Surface-chemistry-dependent LSPR applications unique to copper chalcogenide nanocrystals: **(a)** plasmon-driven chemical transformation and **(b)** sensing using surface-enhanced Raman scattering. Reprinted with permission from references 79 and 80.

The strong dependence of nanoplasmonic application efficacy on surface chemistry illustrates the value of expanding the arsenal of available LSPR-exhibiting nanomaterials. Copper phosphide is an excellent candidate system for use in colloidal nanoplasmonics on account of its potential for distinct surface chemistry as a metal phosphide and also its unique phase stability

which contrasts the with cascade of phase changes that accompany copper chalcogenide nanomaterials upon redox tuning.[81] The crystal structure of $Cu_{3-x}P$, the sole metal-rich binary copper phosphide and only polymorph relevant for this dissertation, was reported by Olofsson in the 1970s (space group $P6_3cm$).[82] Non-stiochiometry arises from copper vacancies within a phase homogeneity range of $0.17<x<0.33$, according to recent theoretical calculations.[83] This composition range corresponds to 1–2 Cu vacancies per $P6_3cm$ unit cell (Figure 1.5a). The first vacancy is predicted[83] to be present at all Cu chemical potentials within the homogeneity range of $P6_3cm$ $Cu_{3-x}P$, whereas the second vacancy is only favorable under Cu-poor chemical potentials (Figure 1.5b). The ability of the $Cu_{3-x}P$ structure to tolerate a wide composition range has been experimentally validated by elemental analysis[82, 84] and solid-state ^{31}P NMR spectroscopy.[85-86]

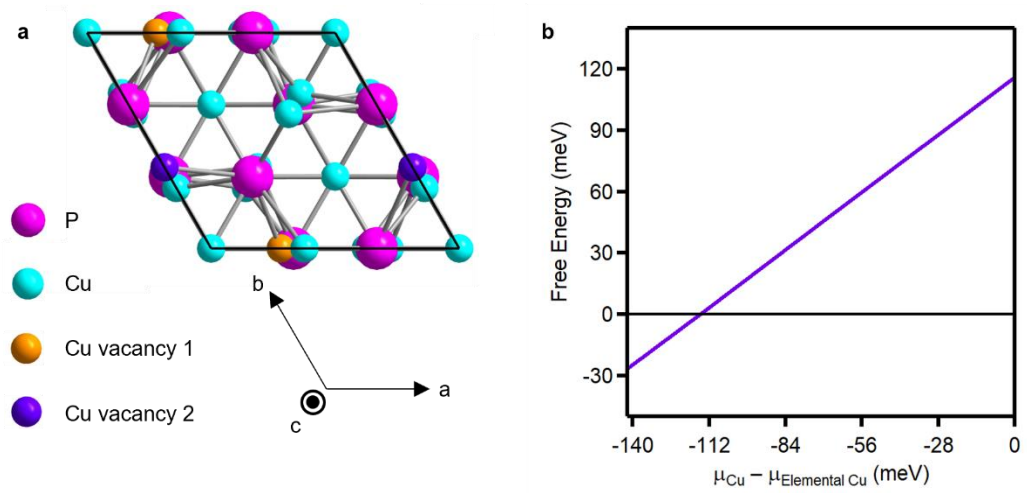

Figure 1. 5. $Cu_{3-x}P$ (space group $P6_3cm$) and its intrinsic Cu vacancies: **(a)** (001) view of primitive unit cell structure with indicated Cu vacancy positions and **(b)** formation free energies of vacancy 2 as a function of Cu chemical potential, μ_{Cu}. Adapted with permission from reference 83.

1.4 Characterizations and Experimental Scope of the Dissertation

This dissertation presents advances made in the colloidal syntheses and post-synthetic redox chemistries of $Cu_{3-x}P$ nanoplatelets with the attainment of tunable nanocrystallite lateral sizes, LSPR energies, compositions, and optoelectronic properties.

In Chapter 2, a new one-pot, colloidal synthesis of $Cu_{3-x}P$ nanoplatelets with copper halide salt and aminophosphine in the presence of oleylamine is presented. The reactivity of an *in situ* copper-phosphorus precursor, identified by mass spectrometry (MS) and further characterized by nuclear magnetic resonance (NMR) spectroscopy, can be modulated by varying precursor composition and coordinating solvent ratio to tune nanocrystal lateral size. Powder X-ray diffraction confirms single-crystallinity and phase purity of the resulting $Cu_{3-x}P$ nanoparticles. Transmission electron microscopy (TEM) is used to assess the size polydispersities of the resulting ensembles. Lateral sizes statistically analyzed from TEM images are used together with Cu atom synthesis yields from elemental analysis to estimate relative nucleation activity, with higher nucleation activity leading to more particles and smaller lateral sizes when normalizing for synthesis yield (Scheme 1.3). Relative nucleation activities for different conditions are experimentally compared as yield divided by the square of lateral dimension, with the assumption of constant platelet height perpendicular to the basal plane. A key finding is that oleylamine-to-aminophosphine molar ratio alone, among the reaction conditions investigated, alters relative nucleation activity and accesses atom-efficient size tuning. Additionally, an empirical relation relating growth reactivity, as semi-qualitatively approximated as color change duration, and the corresponding $Cu_{3-x}P$ LSPR energy, as measured by electronic absorption spectroscopy, is discovered.

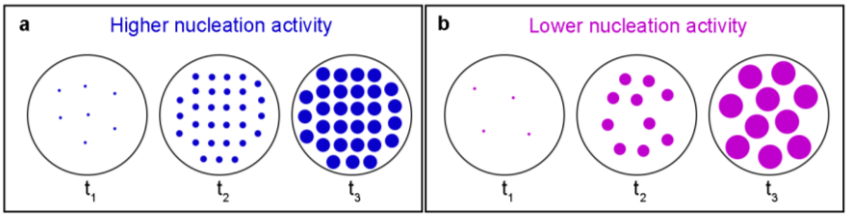

Scheme 1. 3. The evolution of a nanocrystal ensemble during synthesis for two hypothetical cases: **(a)** higher nucleation activity and **(b)** lower nucleation activity. The time t_1 denotes a time while nucleation of new nanocrystals is still occurring, time t_2 denotes the end of the timeframe of new nanocrystal nucleation, and time t_3 denotes the end of a synthesis once nanocrystal growth has ceased.

In Chapter 3, three copper-coupled redox chemistries are presented which allow post-synthetic modulation of $Cu_{3-x}P$ nanocrystal near-IR LSPR energies and delocalized hole carrier concentrations. Concerted structural, optical, and compositional post-redox characterizations of $Cu_{3-x}P$ nanocrystals by powder X-ray diffraction, electronic absorption spectroscopy, ^{31}P magic-angle spinning solid-state nuclear magnetic resonance spectroscopy, and elemental analysis allow the interrogation of a previously unknown oxidation chemistry, which uses both divalent metal halide and trioctylphosphine. Two copper-coupled redox chemistries, with Cu^+-ion and iodine, from previous studies with copper chalcogenide nanomaterials are used for post-synthetic modulation of $Cu_{3-x}P$ nanocrystals for the first time and the results are used as benchmarks for comparison to the new oxidation chemistry.

In Chapter 4, the colloidal synthesis strategies of Chapter 2 are extended to use copper phosphide as a model system for study of aminopnictine precursor chemistry and elucidation of the mechanisms of metal pnictide nanocrystal formation. Preliminary findings are presented for the investigation of the mechanistic roles of metal salt counteranion and aminophosphine amide identity. The characterization techniques used are identical to those of Chapter 2.

1.5 References

1. Murray, C. B.; J., N. D.; G., B. M. Synthesis and Characterization of Nearly Monodisperse CdE (E = Sulfur, Selenium, Tellurium) Semiconductor Nanocrystallites. *J. Am. Chem. Soc.* **1993,** *115*, 8706.

2. LaMer, V. K.; Dinegar, R. H. Theory, Production and Mechanism of Formation of Monodispersed Hydrosols. *J. Am. Chem. Soc.* **1950,** *72*, 4847.

3. Ostwald, W. On the Supposed Isomerism of Red and Yellow Mercury Oxide and the Surface Tension of Solid Substances. *Z. Phys. Chem.* **1900,** *34*, 495.

4. Talapin, D. V.; Rogach, A. L.; Haase, M.; Weller, H. Evolution of an Ensemble of Nanoparticles in a Colloidal Solution: Theoretical Study. *J. Phys. Chem. B* **2001,** *105*, 12278.

5. Yin, Y.; Alivisatos, A. P. Colloidal Nanocrystal Synthesis and the Organic–Inorganic Interface. *Nature* **2005,** *437*, 664.

6. Zherebetskyy, D.; Scheele, M.; Zhang, Y.; Bronstein, N.; Thompson, C.; Britt, D.; Salmeron, M.; Alivisatos, P.; Wang, L.-W. Hydroxylation of the Surface of PbS Nanocrystals Passivated with Oleic Acid. *Science* **2014,** *344*, 1380.

7. Brust, M.; Walker, M.; Bethell, D.; Schiffrin, D. J.; Whyman, R. Synthesis of Thiol-Derivatised Gold Nanoparticles in a Two-Phase Liquid–Liquid System. *J. Chem. Soc., Chem. Commun.* **1994**, 801.

8. Puntes, V. F.; Krishnan, K. M.; Alivisatos, A. P. Colloidal Nanocrystal Shape and Size Control: The Case of Cobalt. *Science* **2001,** *291*, 2115.

9. Hines, M. A.; Guyot-Sionnest, P. Bright UV-Blue Luminescent Colloidal ZnSe Nanocrystals. *J. Phys. Chem. B* **1998,** *102*, 3655.

10. Zhong, H.; Zhou, Y.; Ye, M.; He, Y.; Ye, J.; He, C.; Yang, C.; Li, Y. Controlled Synthesis and Optical Properties of Colloidal Ternary Chalcogenide $CuInS_2$ Nanocrystals. *Chem. Mater.* **2008,** *20*, 6434.

11. Liu, Q.; Lu, W.; Ma, A.; Tang, J.; Lin, J.; Fang, J. Study of Quasi-Monodisperse In_2O_3 Nanocrystals: Synthesis and Optical Determination. *J. Am. Chem. Soc.* **2005,** *127*, 5276.

12. Geisenhoff, J. Q.; Tamura, A. K.; Schimpf, A. M. Using Ligands to Control Reactivity, Size and Phase in the Colloidal Synthesis of WSe_2 Nanocrystals. *Chem. Commun.* **2019,** *55*, 8856.

13. Puzder, A.; Williamson, A. J.; Zaitseva, N.; Galli, G.; Manna, L.; Alivisatos, A. P. The Effect of Organic Ligand Binding on the Growth of CdSe Nanoparticles Probed by Ab Initio Calculations. *Nano Lett.* **2004,** *4*, 2361.

14. Manna, L.; Wang; Cingolani, R.; Alivisatos, A. P. First-Principles Modeling of Unpassivated and Surfactant-Passivated Bulk Facets of Wurtzite CdSe: A Model System for Studying the Anisotropic Growth of CdSe Nanocrystals. *J. Phys. Chem. B* **2005,** *109*, 6183.

15. Choi, M. K.; Yang, J.; Hyeon, T.; Kim, D.-H. Flexible Quantum Dot Light-Emitting Diodes for Next-Generation Displays. *npj Flexible Electronics* **2018,** *2*, 1.

16. Shim, M.; Guyot-Sionnest, P. n-Type Colloidal Semiconductor Nanocrystals. *Nature* **2000,** *407*, 981.

17. Rinehart, J. D.; Schimpf, A. M.; Weaver, A. L.; Cohn, A. W.; Gamelin, D. R. Photochemical Electronic Doping of Colloidal CdSe Nanocrystals. *J. Am. Chem. Soc.* **2013,** *135*, 18782.

18. Weiss, E. A. Designing the Surfaces of Semiconductor Quantum Dots for Colloidal Photocatalysis. *ACS Energy Lett.* **2017,** *2*, 1005.

19. Hendricks, M. P.; Campos, M. P.; Cleveland, G. T.; Jen-La Plante, I.; Owen, J. S. A Tunable Library of Substituted Thiourea Precursors to Metal Sulfide Nanocrystals. *Science* **2015,** *348*, 1226.

20. Cossairt, B. M. Shining Light on Indium Phosphide Quantum Dots: Understanding the Interplay among Precursor Conversion, Nucleation, and Growth. *Chem. Mater.* **2016,** *28*, 7181.

21. Krames, M. R.; Ochiai-Holcomb, M.; Höfler, G. E.; Carter-Coman, C.; Chen, E. I.; Tan, I. H.; Grillot, P.; Gardner, N. F.; Chui, H. C.; Huang, J. W.; Stockman, S. A.; Kish, F. A.; Craford, M. G.; Tan, T. S.; Kocot, C. P.; Hueschen, M.; Posselt, J.; Loh, B.; Sasser, G.; Collins, D. High-Power Truncated-Inverted-Pyramid $(Al_xGa_{1-x})_{0.5}In_{0.5}P$/GaP Light-Emitting Diodes Exhibiting >50% External Quantum Efficiency. *Appl. Phys. Lett.* **1999,** *75*, 2365.

22. Tegus, O.; Brück, E.; Buschow, K. H. J.; de Boer, F. R. Transition-Metal-Based Magnetic Refrigerants for Room-Temperature Applications. *Nature* **2002,** *415*, 150.

23. Landau, M. V.; Herskowitz, M.; Hoffman, T.; Fuks, D.; Liverts, E.; Vingurt, D.; Froumin, N. Ultradeep Hydrodesulfurization and Adsorptive Desulfurization of Diesel Fuel on Metal-Rich Nickel Phosphides. *Ind. Eng. Chem. Res.* **2009,** *48*, 5239.

24. Carenco, S.; Portehault, D.; Boissière, C.; Mézailles, N.; Sanchez, C. Nanoscaled Metal Borides and Phosphides: Recent Developments and Perspectives. *Chem. Rev.* **2013,** *113*, 7981.

25. Didchenko, R.; Alix, J. E.; Toeniskoetter, R. H. Reactions of Phosphine with Trimethylindium. *Journal of Inorganic and Nuclear Chemistry* **1960,** *14*, 35.

26. Mićić, O. I.; Curtis, C. J.; Jones, K. M.; Sprague, J. R.; Nozik, A. J. Synthesis and Characterization of InP Quantum Dots. *J. Phys. Chem.* **1994,** *98*, 4966.

27. Mićić, O. I.; Nozik, A. J. Synthesis and Characterization of Binary and Ternary III–V Quantum Dots. *J. Lumin.* **1996,** *70*, 95.

28. Goel, S. C.; Chiang, M. Y.; Buhro, W. E. Synthesis of Homoleptic Silylphosphido Complexes $(M[P(SiMe_3)_2][\mu\text{-}P(SiMe_3)_2])_2$, where M = Zinc and Dadmium, and Their Use in Metalloorganic Routes to Cd_3P_2 and $MGeP_2$. *J. Am. Chem. Soc.* **1990,** *112*, 5636.

29. Goel, S. C.; Chiang, M. Y.; Rauscher, D. J.; Buhro, W. E. Comparing the Properties of Homologous Phosphido and Amido Complexes: Synthesis and Characterization of the Disilylphosphido Complexes $\{M[P(SiMe_3)_2]_2\}_2$ where M = Zinc, Cadmium, Mercury, Tin, Lead and Manganese. *J. Am. Chem. Soc.* **1993,** *115*, 160.

30. Matchett, M. A.; Viano, A. M.; Adolphi, N. L.; Stoddard, R. D.; Buhro, W. E.; Conradi, M. S.; Gibbons, P. C. Sol-Gel-Like Route to Crystalline Cadmium Phosphide Nanoclusters. *Chem. Mater.* **1992,** *4*, 508.

31. Buhro, W. E. Metallo-Organic Routes to Phosphide Semiconductors. *Polyhedron* **1994,** *13*, 1131.

32. Goel, S. C.; Buhro, W. E.; Adolphi, N. L.; Conradi, M. S. Low-Temperature Organometallic Synthesis of Crystalline and Glassy Ternary Semiconductors $MII MIVP_2$ where MII Zn and Cd, and MIV Ge and Sn. *J. Organomet. Chem.* **1993,** *449*, 9.

33. Talapin, D. V.; Rogach, A. L.; Mekis, I.; Haubold, S.; Kornowski, A.; Haase, M.; Weller, H. Synthesis and Surface Modification of Amino-Stabilized CdSe, CdTe and InP Nanocrystals. *Colloids Surf., A* **2002,** *202*, 145.

34. Kim, M. R.; Chung, J. H.; Lee, M.; Lee, S.; Jang, D.-J. Fabrication, Spectroscopy, and Dynamics of Highly Luminescent Core–Shell InP@ZnSe Quantum Dots. *J. Colloid Interface Sci.* **2010,** *350*, 5.

35. Ryu, E.; Kim, S.; Jang, E.; Jun, S.; Jang, H.; Kim, B.; Kim, S.-W. Step-Wise Synthesis of InP/ZnS Core−Shell Quantum Dots and the Role of Zinc Acetate. *Chem. Mater.* **2009,** *21*, 573.

36. Park, J.; Koo, B.; Hwang, Y.; Bae, C.; An, K.; Park, J.-G.; Park, H. M.; Hyeon, T. Novel Synthesis of Magnetic Fe_2P Nanorods from Thermal Decomposition of Continuously Delivered Precursors using a Syringe Pump. *Angew. Chem. Int. Ed.* **2004,** *43*, 2282.

37. Qian, C.; Kim, F.; Ma, L.; Tsui, F.; Yang, P.; Liu, J. Solution-Phase Synthesis of Single-Crystalline Iron Phosphide Nanorods/Nanowires. *J. Am. Chem. Soc.* **2004,** *126*, 1195.

38. Henkes, A. E.; Schaak, R. E. Trioctylphosphine: A General Phosphorus Source for the Low-Temperature Conversion of Metals into Metal Phosphides. *Chem. Mater.* **2007,** *19*, 4234.

39. Song, W.-S.; Lee, H.-S.; Lee, J. C.; Jang, D. S.; Choi, Y.; Choi, M.; Yang, H. Amine-Derived Synthetic Approach to Color-Tunable InP/ZnS Quantum Dots with High Fluorescent Qualities. *J. Nanopart. Res.* **2013,** *15*, 1750.

40. Tessier, M. D.; Dupont, D.; De Nolf, K.; De Roo, J.; Hens, Z. Economic and Size-Tunable Synthesis of InP/ZnE (E = S, Se) Colloidal Quantum Dots. *Chem. Mater.* **2015,** *27*, 4893.

41. Tessier, M. D.; De Nolf, K.; Dupont, D.; Sinnaeve, D.; De Roo, J.; Z, H. Aminophosphines: A Double Role in the Synthesis of Colloidal Indium Phosphide Quantum Dots. *J. Am. Chem. Soc.* **2016,** *138*, 5923.

42. Buffard, A.; Dreyffuss, S.; Nadal, B.; Heuclin, H.; Xu, X.; Patriarche, G.; Mézailles, N.; Dubertret, B. Mechanistic Insight and Optimization of InP Nanocrystals Synthesized with Aminophosphines. *Chem. Mater.* **2016,** *28*, 5925.

43. Laufersky, G.; Bradley, S.; Frécaut, E.; Lein, M.; Nann, T. Unraveling Aminophosphine Redox Mechanisms for Glovebox-Free InP Quantum Dot Syntheses. *Nanoscale* **2018,** *10*, 8752.

44. McMurtry, B. M.; Qian, K.; Teglasi, J. K.; Swarnakar, A. K.; De Roo, J.; Owen, J. S. Continuous Nucleation and Size Dependent Growth Kinetics of Indium Phosphide Nanocrystals. *Chem. Mater*. **2020,** *32*, 4358.

45. Mundy, M. E.; Ung, D.; Lai, N. L.; Jahrman, E. P.; Seidler, G. T.; Cossairt, B. M. Aminophosphines as Versatile Precursors for the Synthesis of Metal Phosphide Nanocrystals. *Chem. Mater.* **2018,** *30*, 5373.

46. Grigel, V.; Dupont, D.; De Nolf, K.; Hens, Z.; Tessier, M. D. InAs Colloidal Quantum Dots Synthesis via Aminopnictogen Precursor Chemistry. *J. Am. Chem. Soc.* **2016,** *138*, 13485.

47. Srivastava, V.; Janke, E. M.; Diroll, B. T.; Schaller, R. D.; Talapin, D. V. Facile, Economic and Size-Tunable Synthesis of Metal Arsenide Nanocrystals. *Chem. Mater.* **2016,** *28*, 6797.

48. Srivastava, V.; Dunietz, E.; Kamysbayev, V.; Anderson, J. S.; Talapin, D. V. Monodisperse InAs Quantum Dots from Aminoarsine Precursors: Understanding the Role of Reducing Agent. *Chem. Mater.* **2018,** *30*, 3623.

49. Zhao, T.; Oh, N.; Jishkariani, D.; Zhang, M.; Wang, H.; Li, N.; Lee, J. D.; Zeng, C.; Muduli, M.; Choi, H.-J.; Su, D.; Murray, C. B.; Kagan, C. R. General Synthetic Route to High-Quality Colloidal III–V Semiconductor Quantum Dots Based on Pnictogen Chlorides. *J. Am. Chem. Soc.* **2019,** *141*, 15145.

50. Ginterseder, M.; Franke, D.; Perkinson, C. F.; Wang, L.; Hansen, E. C.; Bawendi, M. G. Scalable Synthesis of InAs Quantum Dots Mediated through Indium Redox Chemistry. *J. Am. Chem. Soc.* **2020,** *142*, 4088.

51. Vanmaekelbergh, D.; Liljeroth, P. Electron-Conducting Quantum Dot Solids: Novel Materials Based on Colloidal Semiconductor Nanocrystals. *Chem. Soc. Rev.* **2005,** *34*, 299.

52. Chikan, V. Challenges and Prospects of Electronic Doping of Colloidal Quantum Dots: Case Study of CdSe. *J. Phys. Chem. Lett.* **2011,** *2*, 2783.

53. Faucheaux, J. A.; Stanton, A. L. D.; Jain, P. K. Plasmon Resonances of Semiconductor Nanocrystals: Physical Principles and New Opportunities. *J. Phys. Chem. Lett.* **2014,** *5*, 976.

54. Schimpf, A. M.; Knowles, K. E.; Carroll, G. M.; Gamelin, D. R. Electronic Doping and Redox-Potential Tuning in Colloidal Semiconductor Nanocrystals. *Acc. Chem. Res.* **2015,** *48*, 1929.

55. Lhuillier, E.; Guyot-Sionnest, P. Recent Progresses in Mid Infrared Nanocrystal Optoelectronics. *IEEE J. Sel. Top. Quantum Electron.* **2017,** *23*.

56. Haase, M.; Weller, H.; Henglein, A. Photochemistry and Radiation-Chemistry of Colloidal Semiconductors. 23. Electron Storage on ZnO Particles and Size Quantization. *J. Phys. Chem.* **1988,** *92*, 482.

57. Liu, W. K.; Whitaker, K. M.; Smith, A. L.; Kittilstved, K. R.; Robinson, B. H.; Gamelin, D. R. Room-Temperature Electron Spin Dynamics in Free-Standing ZnO Quantum Dots. *Phys. Rev. Lett.* **2007,** *98*, 186804.

58. Palomaki, P. K. B.; Miller, E. M.; Neale, N. R. Control of Plasmonic and Interband Transitions in Colloidal Indium Nitride Nanocrystals. *J. Am. Chem. Soc.* **2013,** *135*, 14142.

59. Nutz, T.; zum Felde, U.; Haase, M. Wet-Chemical Synthesis of Doped Nanoparticles: Blue-Colored Colloids of n-Doped SnO_2 : Sb. *J. Chem. Phys.* **1999,** *110*, 12142.

60. Kanehara, M.; Koike, H.; Yoshinaga, T.; Teranishi, T. Indium Tin Oxide Nanoparticles with Compositionally Tunable Surface Plasmon Resonance Frequencies in the Near-IR Region. *J. Am. Chem. Soc.* **2009,** *131*, 17736.

61. Zhao, Y.; Pan, H.; Lou, Y.; Qiu, X.; Zhu, J.; Burda, C. Plasmonic $Cu_{2-x}S$ Nanocrystals: Optical and Structural Properties of Copper-Deficient Copper(I) Sulfides. *J. Am. Chem. Soc.* **2009,** *131*, 4253.

62. Buonsanti, R.; Llordes, A.; Aloni, S.; Helms, B. A.; Milliron, D. J. Tunable Infrared Absorption and Visible Transparency of Colloidal Aluminum-Doped Zinc Oxide Nanocrystals. *Nano Lett.* **2011,** *11*, 4706.

63. Rowe, D. J.; Jeong, J. S.; Mkhoyan, K. A.; Kortshagen, U. R. Phosphorus-Doped Silicon Nanocrystals Exhibiting Mid-Infrared Localized Surface Plasmon Resonance. *Nano Lett.* **2013,** *13*, 1317.

64. Fang, H. B.; Hegde, M.; Yin, P. H.; Radovanovic, P. V. Tuning Plasmon Resonance of In_2O_3 Nanocrystals throughout the Mid-Infrared Region by Competition between Electron Activation and Trapping. *Chem. Mater.* **2017,** *29*, 4970.

65. Marbella, L. E.; Gan, X. Y.; Kaseman, D. C.; Millstone, J. E. Correlating Carrier Density and Emergent Plasmonic Features in $Cu_{2-x}Se$ Nanoparticles. *Nano Lett.* **2017,** *17*, 2414.

66. Limpens, R.; Pach, G. F.; Mulder, D. W.; Neale, N. R. Size-Dependent Asymmetric Auger Interactions in Plasma-Produced n- and p-Type-Doped Silicon Nanocrystals. *J. Phys. Chem. C* **2019,** *123*, 5782.

67. Dorfs, D.; Härtling, T.; Miszta, K.; Bigall, N. C.; Kim, M. R.; Genovese, A.; Falqui, A.; Povia, M.; Manna, L. Reversible Tunability of the Near-Infrared Valence Band Plasmon Resonance in $Cu_{2-x}Se$ Nanocrystals. *J. Am. Chem. Soc.* **2011,** *133*, 11175.

68. Kriegel, I.; Jiang, C.; Rodríguez-Fernández, J.; Schaller, R. D.; Talapin, D. V.; da Como, E.; Feldmann, J. Tuning the Excitonic and Plasmonic Properties of Copper Chalcogenide Nanocrystals. *J. Am. Chem. Soc.* **2012,** *134*, 1583.

69. Niezgoda, J. S.; Harrison, M. A.; McBride, J. R.; Rosenthal, S. J. Novel Synthesis of Chalcopyrite $Cu_xIn_yS_2$ Quantum Dots with Tunable Localized Surface Plasmon Resonances. *Chem. Mater.* **2012,** *24*, 3294.

70. Xie, Y.; Riedinger, A.; Prato, M.; Casu, A.; Genovese, A.; Guardia, P.; Sottini, S.; Sangregorio, C.; Miszta, K.; Ghosh, S.; Pellegrino, T.; Manna, L. Copper Sulfide Nanocrystals with Tunable Composition by Reduction of Covellite Nanocrystals with Cu^+ Ions. *J. Am. Chem. Soc.* **2013,** *135*, 17630.

71. Schimpf, A. M.; Thakkar, N.; Gunthardt, C. E.; Masiello, D. J.; Gamelin, D. R. Charge-Tunable Quantum Plasmons in Colloidal Semiconductor Nanocrystals. *ACS Nano* **2014,** *8*, 1065.

72. Urso, C.; Barawi, M.; Gaspari, R.; Sirigu, G.; Kriegel, I.; Zavelani-Rossi, M.; Scotognella, F.; Manca, M.; Prato, M.; De Trizio, L.; Manna, L. Colloidal Synthesis of Bipolar Off-Stoichiometric Gallium Iron Oxide Spinel-Type Nanocrystals with Near-IR Plasmon Resonance. *J. Am. Chem. Soc.* **2017,** *139*, 1198.

73. Luther, J. M.; Jain, P. K.; Ewers, T.; Alivisatos, A. P. Localized Surface Plasmon Resonances Arising from Free Carriers in Doped Quantum Dots. *Nat. Mater.* **2011,** *10*, 361.

74. Hsu, S.-W.; On, K.; Tao, A. R. Localized Surface Plasmon Resonances of Anisotropic Semiconductor Nanocrystals. *J. Am. Chem. Soc.* **2011,** *133*, 19072.

75. Hsu, S.-W.; Bryks, W.; Tao, A. R. Effects of Carrier Density and Shape on the Localized Surface Plasmon Resonances of $Cu_{2-x}S$ Nanodisks. *Chem. Mater.* **2012,** *24*, 3765.

76. Kriegel, I.; Rodriguez-Fernandez, J.; Wisnet, A.; Zhang, H.; Waurisch, C.; Eychmuller, A.; Dubavik, A.; Govorov, A. O.; Feldmann, J. Shedding Light on Vacancy-Doped Copper Chalcogenides: Shape-Controlled Synthesis, Optical Properties, and Modeling of Copper Telluride Nanocrystals with Near-Infrared Plasmon Resonances. *ACS Nano* **2013,** *7*, 4367.

77. Hartstein, K. H.; Brozek, C. K.; Hinterding, S. O. M.; Gamelin, D. R. Copper-Coupled Electron Transfer in Colloidal Plasmonic Copper-Sulfide Nanocrystals Probed by in Situ Spectroelectrochemistry. *J. Am. Chem. Soc.* **2018,** *140*, 3434.

78. Gan, X. Y.; Crawford, S. E.; Eikey, E. A.; Sen, R.; Killinger, J. R.; Millstone, J. E. Optoelectronic Impacts of Particle Size in Water-Dispersible Plasmonic Copper Selenide Nanoparticles. *J. Phys. Chem. C* **2020,** *124*, 4747.

79. Gan, X. Y.; Keller, E. L.; Warkentin, C. L.; Crawford, S. E.; Frontiera, R. R.; Millstone, J. E. Plasmon-Enhanced Chemical Conversion Using Copper Selenide Nanoparticles. *Nano Lett.* **2019,** *19*, 2384.

80. Della Valle, G.; Scotognella, F.; Kandada, A. R. S.; Zavelani-Rossi, M.; Li, H.; Conforti, M.; Longhi, S.; Manna, L.; Lanzani, G.; Tassone, F. Ultrafast Optical Mapping of Nonlinear Plasmon Dynamics in $Cu_{2-x}Se$ Nanoparticles. *J. Phys. Chem. Lett.* **2013,** *4*, 3337.

81. Riha, S. C.; Johnson, D. C.; Prieto, A. L. Cu_2Se Nanoparticles with Tunable Electronic Properties Due to a Controlled Solid-State Phase Transition Driven by Copper Oxidation and Cationic Conduction. *J. Am. Chem. Soc.* **2011,** *133*, 1383.

82. Olofsson, O. The Crystal Structure of Cu_3P. *Acta Chem. Scand.* **1972,** *26*, 2777.

83. De Trizio, L.; Gaspari, R.; Bertoni, G.; Kriegel, I.; Moretti, L.; Scotognella, F.; Maserati, L.; Zhang, Y.; Messina, G. C.; Prato, M.; Marras, S.; Cavalli, A.; Manna, L. $Cu_{3-x}P$ Nanocrystals as a Material Platform for Near-Infrared Plasmonics and Cation Exchange Reactions. *Chem. Mater.* **2015,** *27*, 1120.

84. Schlenger, H.; Jacobs, H.; Juza, R. Ternäre Phasen des Lithiums mit Kupfer und Phosphor. *Z. Anorg. Allg. Chem.* **1971,** *385*, 177.

85. Furo, I.; Bakonyi, I.; Tompa, K.; Zsoldos, E.; Heinmaa, I.; Alla, M.; Lippmaa, E. ^{31}P Nuclear Magnetic Resonance Knight Shift and Linewidth in Ni_3P and Cu_3P: A Magic-Angle Spinning Study. *J. Phys. Condens. Matter* **1990,** *2*, 4217.

86. Wolff, A.; Pallmann, J.; Boucher, R.; Weiz, A.; Brunner, E.; Doert, T.; Ruck, M. Resource-Efficient High-Yield Ionothermal Synthesis of Microcrystalline $Cu_{3-x}P$. *Inorg. Chem.* **2016,** *55*, 8844.

CHAPTER 2. Colloidal Synthesis of Tunable Copper Phosphide Nanocrystals

2.1 Abstract

Colloidal copper phosphide ($Cu_{3-x}P$) nanocrystals are attractive materials due to their ability to support excess delocalized holes, leading to localized surface plasmon resonance (LSPR) absorption in the near-IR. We present a one-pot, colloidal synthesis of $Cu_{3-x}P$ nanoplatelets from copper halide salts and tris(diethylamino)phosphine ($P(NEt_2)_3$) in the presence of oleylamine (OAm) and trioctylamine. Mass spectrometry and nuclear magnetic resonance spectroscopy reveal that the formation of $Cu_{3-x}P$ is accompanied by an aminophosphonium byproduct, suggesting that $Cu_{3-x}P$ synthesis proceeds through a mechanism similar to other metal phosphide nanocrystals. The in-situ copper−phosphorus precursor is identified by mass spectrometry, providing insight into the pre-nucleation chemistry that not been possible in other aminophosphine-based metal phosphide syntheses. The final nanocrystal ensemble can be tuned by varying the precursor ratios (OAm/$P(NEt_2)_3$ or $P(NEt_2)_3$/CuCl), copper halide (CuCl vs CuBr) or temperature, maintaining low polydispersity over a wide parameter space. By modulating the reactivity, the syntheses presented herein can be used to access nanocrystals with lateral sizes of 6.1–23 nm with LSPR energies of 709–861 meV. Overall, this synthesis presents a platform for systematic mechanistic investigations of the chemical processes underlying $Cu_{3-x}P$ nanocrystal formation. The low polydispersity, size- and LSPR-tunability and colloidal stability make these nanocrystals promising candidates for further investigations into factors governing the LSPR energy in $Cu_{3-x}P$ nanomaterials.

2.2 Introduction

Colloidal semiconductor nanocrystals capable of supporting excess delocalized charge-carriers are an important class of emerging electronic materials[1-6] due to the potential for hosting

tunable carrier densities. Carrier concentrations can often be modulated via defect incorporation and activation during synthesis,[5, 7-14] or via post-synthetic redox or photo-redox manipulations.[1, 5, 15-17] These techniques allow access to tunable photophysical properties in semiconductor nanocrystals, including localized surface plasmon resonances (LSPRs) in the mid- or near-IR.[5, 7-14, 17-22] Nanocrystals in which the LSPR absorption is derived from delocalized holes[14, 23] are relatively uncommon, with copper chalcogenides (CuE or $Cu_{2-x}E$; E = S, Se, Te) being the most widely studied.[9, 13, 18-19, 21, 24-29] In these materials, delocalized holes arise to compensate copper vacancies, resulting in degenerately doped semiconductors with LSPR absorption in the near-IR that has been exploited for surface-enhanced Raman scattering,[30] plasmon-enhanced chemical conversion[31] and ultrafast optical switching.[30, 32] It was recently demonstrated that copper vacancies in copper phosphide ($Cu_{3-x}P$) nanocrystals also generate excess delocalized holes and near-IR LSPR absorption.[33-34] In contrast to the copper chalcogenides, which often undergo phase transformations with dynamic redox tuning,[35] $Cu_{3-x}P$ exists as the sole copper-rich phase. This phase-stability and potential for distinct surface chemistry make $Cu_{3-x}P$ a unique system for colloidal semiconductor nanoplasmonics. Here, we present a colloidal synthesis of high-quality $Cu_{3-x}P$ with tunable size and LSPR absorption.

The crystal structure of $Cu_{3-x}P$ (space group $P6_3cm$) was first reported by Olofsson in 1972.[36] According to recent theoretical calculations, the non-stoichiometry of the structure arises from copper vacancies within a phase homogeneity range of $0.17 < x < 0.33$.[33] The ability of the $Cu_{3-x}P$ structure to host a wide composition range has been experimental validated by elemental analysis[36-37] and solid-state ^{31}P nuclear magnetic resonance (NMR) spectroscopy.[38-39] The tolerance of the $Cu_{3-x}P$ phase to cation migration without major structural reorganization has been exploited in its demonstration as a candidate anode material for lithium ion batteries[40-41] and in its

use as a template in cation exchange to InP nanocrystals.[33, 42] In recent years, the nanoscaling of $Cu_{3-x}P$ has enabled its use in applications including catalysis,[43-44] supercapacitors,[45] photodetection,[46] chemodynamic therapy[47] and as a precursor to ternary copper chalcophosphate materials used in photovoltaics.[48-49]

The synthesis of low-polydispersity, colloidally stable and size-tunable $Cu_{3-x}P$ nanocrystals would enable plasmonic studies with minimal contribution from extrinsic effects. Early syntheses of $Cu_{3-x}P$ nanomaterials used solvothermal methods, which featured no control over domain-size or morphology.[50-52] $Cu_{3-x}P$ nanocrystals were first synthesized colloidally via phosphidation of Cu(0) nanocrystals,[53] but size-tunability or optimization of the size-distributions were not explored. Subsequent colloidal syntheses have been reported with direct nucleation of $Cu_{3-x}P$ using a variety of phosphorus precursors, including trioctylphosphine,[54] phosphine,[55] tris(trimethylsilyl)phosphine[56] and triphenyl phosphite.[57] These direct syntheses, however, have not demonstrated tunability in the final nanocrystal size without the use of toxic, highly reactive or expensive reagents. Tris(dialkylamino)phosphine precursors have emerged as easy-to-handle substitutes in the colloidal synthesis of InP nanocrystals,[58-63] and have recently been extended to Zn-, Ni-, Co- and Cd-based metal phosphide nanocrystals.[64] The versatility of using tris(dialkylamino)pnictines in colloidal synthesis has also been demonstrated for other metal pnictide nanocrystals.[65-69]

The success with tris(dialkylamino)phosphines in the synthesis of other metal phosphide nanocrystals[58-62, 64] and the binding affinity of phosphine ligands for copper(I) halides[70] suggest that aminophosphines can offer a promising route to high-quality $Cu_{3-x}P$ nanocrystals. Here, we develop a synthesis of colloidally stable $Cu_{3-x}P$ nanocrystals from copper halides (CuX; $X^- = Cl^-$, Br^-) and tris(diethylamino)phosphine ($P(NEt_2)_3$) in the presence of oleylamine (OAm) and

trioctylamine (TOA). This synthesis is optimal using a simple, one-pot heatup method, where relevant pre-nucleation species can be identified via mass spectrometry (MS) and NMR spectroscopy. Notably, a $P(NEt_2)_3$-coordinated Cu(I) species is observed by MS, providing insight into the chemistry of in-situ precursor formation. Observation of an aminophosphonium byproduct suggests that the mechanism of $Cu_{3-x}P$ formation is similar to that observed for other metal phosphide nanocrystals.[60-61, 64] Three synthetic parameters, OAm/P, P/Cu and temperature are explored as handles for tuning the nanocrystal size and LSPR absorption, and are found to greatly impact the nanocrystal nucleation and/or growth. This synthesis provides a platform for mechanistic investigations and post-synthetic evaluations of factors controlling the LSPR absorption in $Cu_{3-x}P$ nanocrystals.

2.3 Results and Analysis

$Cu_{3-x}P$ nanocrystals (Figures 2.1a–c) were synthesized by the reaction of $P(NEt_2)_3$ with copper(I) chloride (CuCl) in the presence of OAm and TOA. Similar to other metal phosphides synthesized using aminophosphine precursors,[58-64] $Cu_{3-x}P$ nanocrystals were first synthesized using a hot-injection method. Specifically, a 0.100 M CuCl solution in OAm and TOA (OAm/TOA/Cu = 24.0/4.8/1.0) was degassed at 125 °C for 3 h and heated 215 °C under Ar, at which point $P(NEt_2)_3$ (3.0 equiv P/Cu) was rapidly injected. This injection-temperature was chosen to avoid Cu(0) nucleation (observed for T > 220 °C) prior to $P(NEt_2)_3$ injection. Vaporization of $HNEt_2$ could be seen immediately upon injection, indicative of transamination. Simultaneously, the solution changed color from yellow to brown, indicative of $Cu_{3-x}P$ nanocrystal formation. After a brief drop in temperature, the reaction temperature was increased to T_{max} = 277 °C (Figure 2.1d). Transmission electron microscopy (TEM) imaging of the resulting nanocrystals (Figure 2.1a) reveals an ensemble of nanoplatelets with lateral dimension of 12 ± 2 nm (Figure 2.1e). The $P6_3cm$

phase of $Cu_{3-x}P$ was verified by powder X-ray diffraction (Figure 2.1f) and the absorption spectrum (Figure S2.1) contains a LSPR feature characteristic of $Cu_{3-x}P$.[33, 55-56]

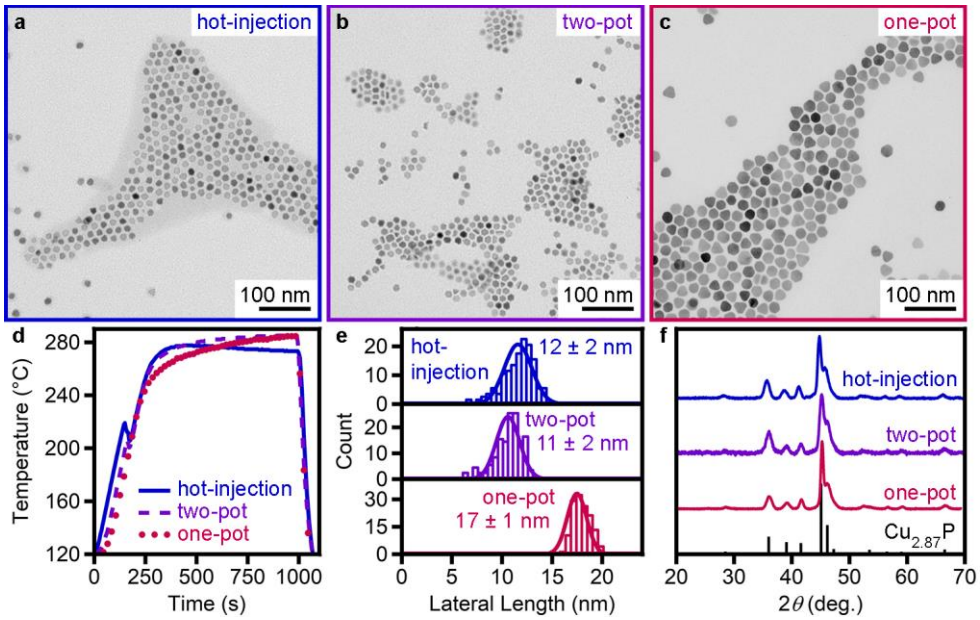

Figure 2. 1. Comparison of $Cu_{3-x}P$ nanocrystal syntheses with [Cu] = 0.100 M, OAm/P/Cu = 24.0/3.0/1.0 and $T_f \approx 280$ °C. TEM images of nanocrystals synthesized using (a) hot-injection (injection of $P(NEt_2)_3$ at $T_{inj} = 215$ °C), (b) two-pot (injection of pre-transaminated phosphine at $T_{inj} = 215$ °C) and (c) one-pot heatup methods. (d) Temperature profiles, (e) statistical analyses ($n = 150$) of lateral platelet dimension and (f) powder X-ray diffraction patterns (compared to that simulated for $P6_3cm$ $Cu_{2.87}P$, ref. 36) for the three methods.

It was recently shown that tuning the transamination kinetics of aminophosphines derived from N,N'-disubstituted ethylenediamines can alter the rate of InP nanocrystal formation.[63] The identification of transamination as a rate-limiting step of precursor conversion suggests that the decoupling transamination from nanocrystal formation may substantively alter nucleation and growth dynamics. To achieve transamination prior to nanocrystal nucleation, a "two-pot" method was used in which two separate solutions of (i) CuCl in OAm and TOA and (ii) 4.0/1.0 OAm/$P(NEt_2)_3$ were each degassed at 125 °C for 3 h. The OAm/$P(NEt_2)_3$ solution was then rapidly injected of the into the Cu/OAm/TOA solution at 215 °C and the combined mixture was heated to

T_f = 285 °C (Figure 2.1d). Similar to the hot-injection reaction, a color change from yellow to brown was observed immediately after the injection, indicative of $Cu_{3-x}P$ nanocrystal formation. This combined mixture contained the same Cu concentration ([Cu] = 0.100 M) and molar ratios (OAm/P/Cu = 24.0/3.0/1.0) as that of the hot-injection synthesis and followed a similar temperature profile (Figure 2.1d). TEM imaging of the resulting nanocrystals (Figure 2.1b) reveals an ensemble of nanoplatelets similar to that of the hot-injection synthesis, with lateral dimension of 11 ± 2 nm (Figure 2.1e). Powder X-ray diffraction (Figure 2.1f) and absorption spectroscopy (Figure S2.1) again confirm the presence of $Cu_{3-x}P$.

Even with use of vacuum to drive off diethylamine, it is possible that the transamination of 4.0/1.0 OAm/$P(NEt_2)_3$ may not proceed to completion.[60-61] In a two-pot synthesis with [Cu] = 0.100 M and OAm/P/Cu = 24.0/3.0/1.0, the volume of the OAm/$P(NEt_2)_3$ solution is already 40 % of the total post-injection volume, making higher OAm/$P(NEt_2)_3$ ratios infeasible from a reaction-design standpoint. Instead, a one-pot heatup method was used in which all reagents were combined, and transamination was performed in the presence of CuCl before heating the mixture to initiate nanocrystal formation. Specifically, a solution of CuCl, $P(NEt_2)_3$, OAm and TOA ([Cu] = 0.100 M, OAm/P/Cu = 24.0/3.0/1.0) was first degassed at 125 °C for 3 h to ensure complete transamination and subsequently heated to a final temperature of T_f = 285 °C (Figure 2.1d). At 220 °C, the solution began to darken from pale yellow to brown, indicating the start of nucleation. The solution continued to darken for 60 s, after which the solution appeared black and no further color-change could be detected by eye. TEM imaging of the resulting nanocrystals (Figure 2.1c) shows a low-polydispersity ensemble of nanoplatelets with a lateral dimension of 17 ± 1 nm, substantially larger than the two-pot or hot-injection methods (Figure 2.1e). Powder X-ray diffraction (Figure 2.1f) and absorption spectroscopy (Figure S2.1) again confirm the presence of $Cu_{3-x}P$. Given the

high-quality product and relative ease of the one-pot syntheses, this reaction type was used for the remainder of our synthetic investigations.

The ^{31}P-NMR spectra of the reaction supernatants each reveal a peak at 30 ppm (Figure S2.2), indicative of a tetra(alkylamino)phosphonium byproduct. Analogous aminophosphonium cations have been observed as the byproduct of disproportionation in aminophosphine-syntheses of InP, Cd_3P_2 and Zn_3P_2 nanocrystals.[60-61, 64] This observation suggests that, like these other metal phosphides, $Cu_{3-x}P$ nanocrystal formation occurs via transamination of $P(NEt_2)_3$ to form $P(NHC_{18}H_{35})_3$, which can further react to form Cu–P bonds and $[P(NHC_{18}H_{35})_4]^+$. To confirm the role of OAm in transamination, the synthesis was performed using TOA as the sole solvent (Figure S2.3), removing the possibility of transamination. This synthesis yielded an insoluble solid matrix with inhomogeneous reactivity evidenced by the formation of small, agglomerated particles (Figure S2.3a) and a metallic film plated on the inside of the reaction flask (Figure S2.3b). Although powder X-ray diffraction confirms the presence of $Cu_{3-x}P$ nanocrystals (Figure S2.3c), the ^{31}P NMR spectrum of the supernatant (Figure S2.3d) suggests a different reaction pathway is followed in the absence of primary amines.

To better understand the nanocrystal formation, the one-pot heatup method was first monitored as a function of time. Four aliquots were withdrawn from 45 s to 9 min after the start of nucleation (Figure 2.2a, Table S2.1). TEM imaging of the aliquots and the final product (Figures 2.2b−f) reveals that, throughout the reaction, the $Cu_{3-x}P$ nanoplatelets are characterized by low-polydispersity and monomodal size distributions. The ensemble lateral platelet dimension increases from 5.6 ± 0.8 nm in aliquot 1 to an asymptotic limit of 20 ± 2 nm in aliquot 4 and in the final product (Figure 2.2g). The powder X-ray diffraction patterns of the nanocrystals from aliquots 2–4 and the final product (Figure S2.4) each show a single-phase product consistent with

$P6_3cm$ $Cu_{3-x}P$. Nanocrystals collected from aliquot 1 had no detectable diffraction pattern, likely due to small size and low crystallinity at early times in the reaction. Absorption spectroscopy of the nanocrystal ensembles reveals a $Cu_{3-x}P$ LSPR feature for each aliquot, with a red-shift in the peak energy from 810 meV to 720 meV over the course of the reaction (Figure S2.5).

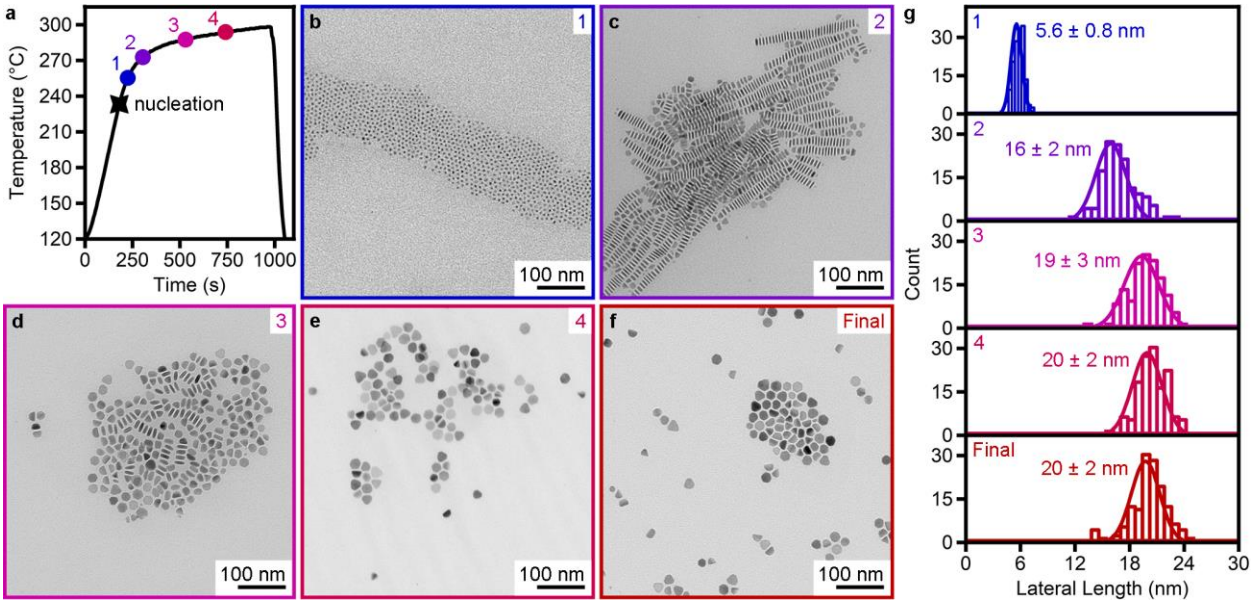

Figure 2. 2. (a) Temperature profile for a one-pot synthesis of $Cu_{3-x}P$ nanocrystals ([Cu] = 0.100 M, OAm/P/Cu = 24.0/3.0/1.0, T_f = 300 °C) with aliquot withdrawal indicated by colored circles. TEM images of aliquots taken **(b)** 45 s (1), **(c)** 125 s (2), **(d)** 350 s (3) and **(e)** 560 s (4) after the start of nucleation and of **(f)** the final product. **(g)** Statistical analyses (n = 150) of lateral platelet dimension of (top to bottom) aliquots 1, 2, 3, 4 and the final product.

To investigate the chemical species involved in the formation of $Cu_{3-x}P$ nanocrystals, the reaction progress was monitored by MS. An aliquot withdrawn prior to heating from 125 °C allowed for the identification of both Cu- and P-precursors in the pre-nucleation solution (Figure S2.6i). First, the peak at m/z = 831 is assigned to the fully transaminated aminophosphine, $P(NHC_{18}H_{35})_3$. Analogous species have been observed as the P-precursor in the synthesis of InP from aminophosphines.[60-61] Second, the peak at m/z = 1857 is assigned to $Cu_2Cl_2P_2(NHC_{18}H_{35})_6$ (**1a,** Scheme 2.1), a halide-bridged, aminophosphine-ligated, dinuclear Cu(I) complex. Similar

$Cu_2X_2L_2$ (X = Cl, Br, I; L = aminophosphine) motifs have been previously observed from the reaction of aminophosphines or aminophosphonites with copper halides.[70-73] Mass spectra of the post-nucleation aliquots and of the final product (Figure S2.6ii–iv) also contain a peak at *m*/*z* = 1096, which is assigned to $[P(NHC_{18}H_{35})_4]^+$, consistent with ^{31}P-NMR measurements (Figure S2.2). Additional mass spectral analysis is presented in the supplementary information (Section S2.1).

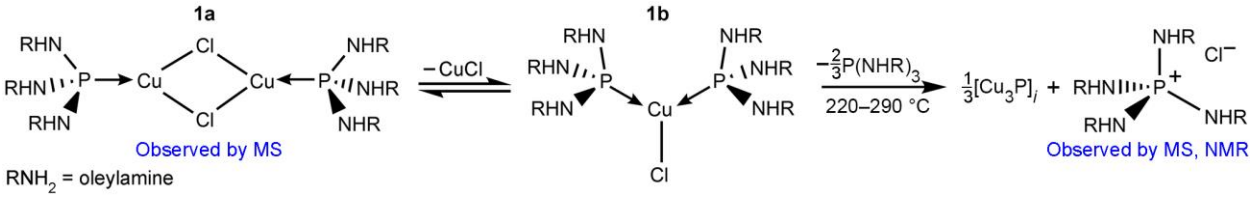

Scheme 2. 1. Formation of Cu_3P and an aminophosphonium cation from aminophosphine-ligated CuCl

The presence of $Cu_2Cl_2P_2(NHC_{18}H_{35})_6$ during the reaction was further monitored by ^{31}P-NMR spectroscopy (Figure S2.7). Prior to nucleation (Figure S2.7i), a broad peak is observed around 80 ppm, which is expected to contain $Cu_2Cl_2P_2(NHC_{18}H_{35})_6$. This peak is present following nucleation (Figure S2.7ii) but disappears by the time the reaction is complete (Figure S2.7iii). When transaminated aminophosphine, $P(NHC_{18}H_{35})_3$, is stirred overnight with CuCl at room temperature an upfield shift and broadening relative to the free $P(NHC_{18}H_{35})_3$ (Figure S2.7iv–v) is observed, corroborating the assignment of this peak as aminophosphine-ligated Cu. A similar upfield shift is observed when $P(NEt_2)_3$ is stirred with CuCl at 125 °C (Figure S2.8). These observations are consistent with an upfield shift in aminophosphine-coordinated CuCl complexes relative to free aminophosphine due to π-backbonding.[73] Additionally, the dinuclear species (**1a**) observed by MS is expected to exist in equilibrium with the mononuclear species, $CuClP_2(NHC_{18}H_{35})_6$ (**1b**, Scheme 2.1), when >2 equiv $P(NHC_{18}H_{35})_3$/Cu are present.[72] We thus

assign this broad peak around 80 ppm to aminophosphine-ligated CuCl complexes, likely including both $Cu_2Cl_2P_2(NHC_{18}H_{35})_6$ and $CuClP_2(NHC_{18}H_{35})_6$. The MS and NMR observations are consistent with Cu–P bond-formation following a pathway similar to those previously proposed for In–P bond-formation under comparable conditions (Scheme 2.1).[60-61]

It has been demonstrated that tris-primary-amine-substituted-phosphines, $P(NHR)_3$, exist in equilibrium with the diphosphine, $[P(NHR)_2]_2NR$.[74] It is expected that condensation of the monophosphine to the diphosphine is suppressed in the presence of excess free primary amine. Indeed, diphosphines $[P(NHC_{18}H_{35})_2]_2NC_{18}H_{35}$ and $P_2(NHC_{18}H_{35})_2(NC_{18}H_{35})_2$ have been observed when $P(NMe_2)_3$ is transaminated with 6 equiv OAm[61] and we observe $[P(NHC_{18}H_{35})_2]_2NC_{18}H_{35}$ when $P(NEt_2)_3$ is transaminated with 7.6 equiv OAm (Figure S2.7iv). Changes in the size and size-dispersion of colloidal InP nanocrystals have previously been has attributed to changes to the equilibrium of these species.[61] Similar diphosphines have been shown to bind low-valent metals,[75] including Cu(I).[71] A diphosphine peak is not observed in the presence of Cu, likely due to quadrupolar-relaxation and chemical-exchange-induced broadening upon coordination to Cu (Figures S2.7 and S2.8). To test whether changing the aminophosphine speciation yields tunability of $Cu_{3-x}P$ nanocrystals, a series of syntheses with varying OAm/P molar ratios was investigated (Figure 2.3). All syntheses were performed with [Cu] = 0.100 M, P/Cu = 3.0 and similar temperature profiles ($T_f \approx 280$ °C, Figure S2.9). The quantity of TOA was varied to maintain constant [Cu] across the series (Table S2.2). The lowest OAm/P molar (3.5) was chosen with consideration of the minimum stoichiometric ratio (3) needed for complete transamination. The highest OAm/P molar ratio (10.1) corresponds to OAm being the only solvent present in the synthesis. In all cases, once the solution began to darken (~220 °C), the duration of the color-change lasted 50–60 s (Table S2.2), after which the solution became black and no further

change could be detected by eye. TEM imaging (Figures 2.3a–c) of $Cu_{3-x}P$ nanocrystals synthesized in this series reveals an increase in nanocrystal size with increasing OAm/P (Figure 2.3d, Table S2.2), although monomodal ensembles are only obtained at OAm/P ≥ 5. When OAm/P = 3.5, a smaller subpopulation of nanocrystals is observed, likely due to a second nucleation event. Elemental analysis shows that low (3.5) and high (10.1) OAm/P ratios result in comparable yields (82 ± 3 and 85 ± 2 %, respectively, based on Cu; Table S2.3). Absorption spectroscopy reveals that the ensemble LSPR absorption blue-shifts with increasing OAm/P (Figure 2.3e, Table S2.2). Powder X-ray diffraction confirms that all syntheses yield $P6_3cm$ $Cu_{3-x}P$ (Figure 2.3f).

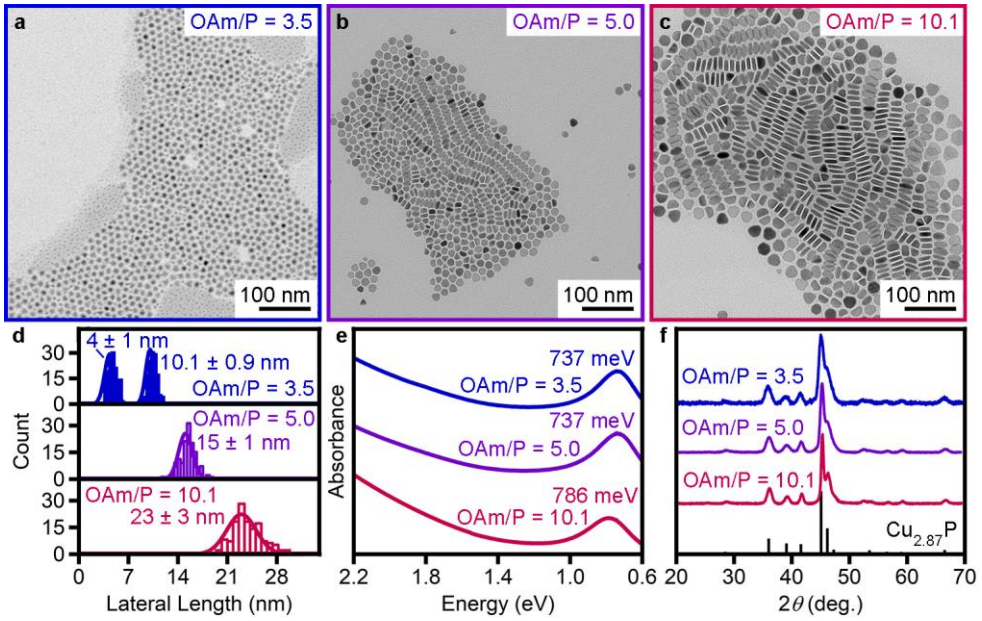

Figure 2. 3. TEM images of $Cu_{3-x}P$ nanocrystals synthesized with [Cu] = 0.100 M, P/Cu = 3.0, T_f ≈ 280 °C and OAm/P molar ratios of **(a)** 3.5, **(b)** 5.0, and **(c)** 10.1. **(d)** Statistical analyses (n = 150) of lateral platelet dimension, **(e)** absorption spectra and **(f)** powder X-ray diffraction patterns (compared to that simulated for $P6_3cm$ $Cu_{2.87}P$, ref. 36) for the three syntheses.

The idealized chemical equation describing the formation of Cu_3P (Equation 2.1, neglecting the non-stoichiometry of the lattice) requires a P/Cu molar ratio of 4/3.

$$3CuCl + 4P(NHC_{18}H_{35})_3 \rightarrow Cu_3P + 3[P(NHC_{18}H_{35})_4]Cl \quad (2.1)$$

As mentioned previously, the dinuclear $Cu_2Cl_2P_2(NHC_{18}H_{35})_6$ species (**1a**) observed by MS is likely in equilibrium with a mononuclear $CuCl(P(NHC_{18}H_{35})_3)_2$ species (**1b**), with the latter favored in higher aminophosphine excess. To test whether changes to the degree of aminophosphine excess, and the consequential shift in equilibrium of $P(NHC_{18}H_{35})_3$-coordinated Cu species, yields tunability of $Cu_{3-x}P$ nanocrystals, a series of syntheses with varying P/Cu molar ratios was investigated. All syntheses were performed with [Cu] = 0.100 M, OAm/P = 8.0 and similar temperature profiles ($T_f \approx 280$ °C, Figure S2.10). The quantities of OAm and TOA were varied to maintain constant OAm/P and [Cu] across the series (Table S2.4). The lowest P/Cu molar ratio (1.4) was chosen to be above that required by Equation 2.1 (1.33). The highest P/Cu molar ratio (3.8) corresponds to OAm being the only solvent. TEM imaging of the resulting nanocrystals (Figures 2.4a–c) shows increasing nanocrystal sizes and lower polydispersity with increasing P/Cu molar ratios (Figure 2.4d, Table S2.4). Absorption spectroscopy reveals that the ensemble LSPR absorption red-shifts with increasing P/Cu molar ratio (Figure 2.3e, Table S2.4). Powder X-ray diffraction confirms that all syntheses yield $P6_3cm$ $Cu_{3-x}P$ (Figure 2.4f).

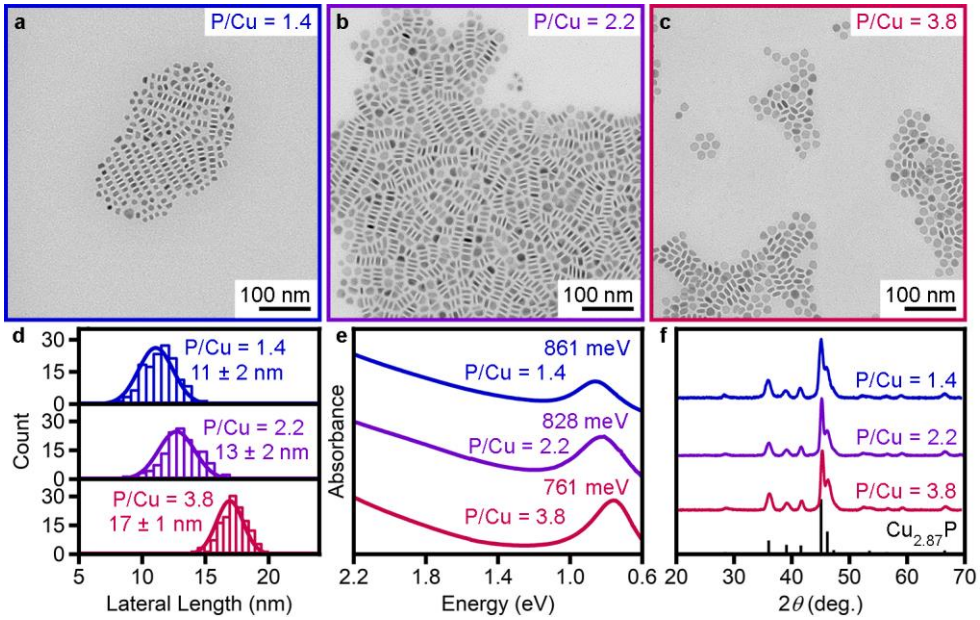

Figure 2. 4. TEM images for syntheses with [Cu] = 0.100 M, OAm/P = 8.0, T_f = 280 °C and P/Cu molar ratios of **(a)** 1.4, **(b)** 2.2 and **(c)** 3.8. **(d)** Statistical analyses (n = 150) of lateral platelet dimension, **(e)** absorption spectra and **(f)** powder X-ray diffraction patterns (compared to that simulated for $P6_3cm$ $Cu_{2.87}P$, ref. 36) for the three syntheses.

There is a discrete difference in the size of nanocrystals (Table S2.4) synthesized with P/Cu ≥ 3.0 (17 nm) and those synthesized with P/Cu ≤ 2.2 (11–13 nm). It is worth noting that the syntheses displayed a similar division in reactivity, as evidenced by the duration of the color-change following nucleation (Table S2.4). Specifically, when nanocrystals were synthesized with P/Cu ≥ 3.0, the solution rapidly turned from pale yellow to brown to black within 50−60 s, after which no further color-change was visible by eye. For reactions with P/Cu ≤ 2.2, this color-change took twice as long (100–120 s), suggesting slower nanocrystal nucleation/growth. Elemental analysis reveals that the synthesis with low (1.4) P/Cu ratio results in a yield of only 54 ± 2 % (based on Cu, Table S2.3), consistent with decreased P/Cu leading to lower reactivity.

It should be noted that the synthetic series presented in Figures 2.3 and 2.4 required varying the amount of TOA to maintain constant [Cu] and constant P/Cu or constant OAm/P ratios, respectively. TOA is expected to be a weakly coordinating ligand, which is outcompeted by OAm

due to larger steric bulk and lower ligand-surface-packing. To test the validity of the assumption that changing the relative quantity of TOA is a minor perturbation on the synthetic outcome, a control synthesis was conducted in which TOA was replaced with octadecane. The octadecane reaction (OAm/P/Cu = 10.6/1.4/1.0, comparable to the synthesis for nanocrystals presented in Figure 2.4a) yielded nanocrystals with an ensemble lateral dimension of 14 ± 3 nm (Figure S2.11), comparable to that of the analogous TOA-reaction (11 ± 2 nm; Figures 2.4a,d). In these reactions, the volume of the cosolvent (TOA or octadecane) was ~65 % of the total volume. Although TOA may have a small impact on the ensemble size and size distribution as a weakly coordinating solvent, variations in its relative quantity do not account for the observed reactivity trends of this study.

In a previous aminophosphine-based InP mechanistic study, a surface-attachment-limited kinetic regime resulted in the observation that low temperatures yielded smaller, low-polydispersity ensembles as a result of continuous nucleation and size-focusing growth.[63] To probe the effect of decreased temperature on the reactivity of $Cu_{3-x}P$ nanocrystal formation, a one-pot synthesis was conducted in which the temperature was held near that required for nucleation (~220 °C, Figure S2.12a). All other conditions were analogous to those used to synthesize the nanocrystals presented in Figure 2.1c ([Cu] = 0.100 M and OAm/P/Cu = 24.0/3.0/1.0). When the reaction temperature was kept at 210–220 °C, reactivity was substantially hindered, evidenced by a protracted duration of the color-change following nucleation (Table S2.4). This decreased reactivity yields $Cu_{3-x}P$ nanocrystals (Figure 2.5a) with an ensemble lateral dimension of 6.1 ± 0.8 nm (Figure S2.12b). Powder X-ray diffraction of the nanocrystals collected from the lower-temperature synthesis shows increased Scherrer broadening (Figure 2.5b), consistent with the

smaller size. Electronic absorption spectroscopy of the nanocrystal suspension (Figure S2.12c) reveals that the LSPR energy is blue-shifted with decreased reaction temperature (Table S2.5).

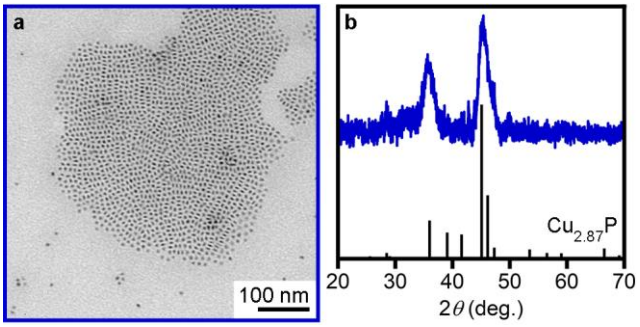

Figure 2. 5. **(a)** TEM image and **(b)** powder X-ray diffraction pattern (compared to that simulated for P6$_3$*cm* $Cu_{2.87}P$, ref. 36) of $Cu_{3-x}P$ nanocrystals synthesized with T_f = 220 °C. All other conditions were identical to those used in the one-pot synthesis presented in Figure 2.1 (([Cu] = 0.100 M, OAm/P/Cu = 24.0/3.0/1.0).

Under identical chemical conditions, the average lateral dimension of the $Cu_{3-x}P$ nanocrystals synthesized at T_f = 220 °C is ~3 times smaller than those synthesized at T_f = 285 °C (Table S2.5). If the yield and average nanoplatelet height were comparable, the lateral size-difference would suggest that using T_f = 220 °C leads to a factor of 9 greater nucleation activity. Although there is precedent of increased nucleation activity at lower temperatures in aminophosphine-based syntheses of InP, the largest increase in ensemble particle-count observed with a reduction in reaction-temperature was 3-fold.[63] To determine the extent to which size-reduction at low temperature can be attributed to lower chemical yield, a two-part synthesis with the same chemical conditions ([Cu] = 0.100 M, OAm/P/Cu = 24.0/3.0/1.0) was conducted (Figure S2.13). In the first part, the reaction temperature was held at $T \approx 225$ °C for 18 min (Figure S2.13a) to emulate the temperature profile of the low-temperature synthesis. In the second part, following the withdrawal of an aliquot, the reaction mixture was heated to T_f = 276 °C to drive the reaction to completion (Figure S2.13a). TEM imaging (Figure S2.13b) reveals a final $Cu_{3-x}P$ nanocrystal ensemble with an average lateral dimension of 22 ± 2 nm (Figure S2.13c), slightly larger than that

of the previous high-temperature synthesis (17 ± 1 nm, Figure 2.1c). These results suggest that, under these conditions, lower synthesis temperatures yield smaller nanocrystal sizes due to incomplete reactivity and low yield, rather than increased nucleation. Indeed, quantitative comparison between the absorption spectra of the aliquot and final product indicates a ~15× greater yield after the temperature is raised to T_f = 275 °C (Figure S2.13d). Similar results were seen when comparing temperature profiles for near-stoichiometric conditions ([Cu] = 0.100 M, OAm/P/Cu = 4.9/1.4/1.0; Figure S2.14).

Finally, we note that smaller nanocrystals were obtained when CuBr was used in place of CuCl (Figure S2.15, Table S2.5), consistent with previously reported metal-halide size-tuning.[59, 64] This smaller size is accompanied by a decreased yield of 51 ± 2 % (based on Cu, Table S2.3).

2.4 Discussion

The data presented in this study reveal both important similarities and differences between this and other metal phosphide nanocrystal syntheses that use tris(dialkylamino)phosphine precursors. The $Cu_{3-x}P$ syntheses are shown to first undergo transamination of the aminophosphine with a long-chain primary amine, followed by reactivity of the aminophosphine-coordinated metal to yield an aminophosphonium byproduct (Figures S2.2, S2.6–8).[60-61, 64] These observations suggest that Cu–P bond-formation follows a pathway similar to those previously proposed for In–P bond-formation under comparable conditions.[60-61] Specifically, the formation of InP has been proposed to occur via (1) an acid–base reaction between excess free amine and the aminophosphine-ligated In-precursor, followed by (2) a redox disproportionation to create In–P bonds with an aminophosphonium byproduct.[61] Although this pathway has not been directly confirmed, an analogous pathway for Cu–P bond-formation (Scheme 2.2) is presented for

discussion purposes. Similar pathways can be drawn for both the mono- and dinuclear species; the mononuclear pathway is shown for simplicity.

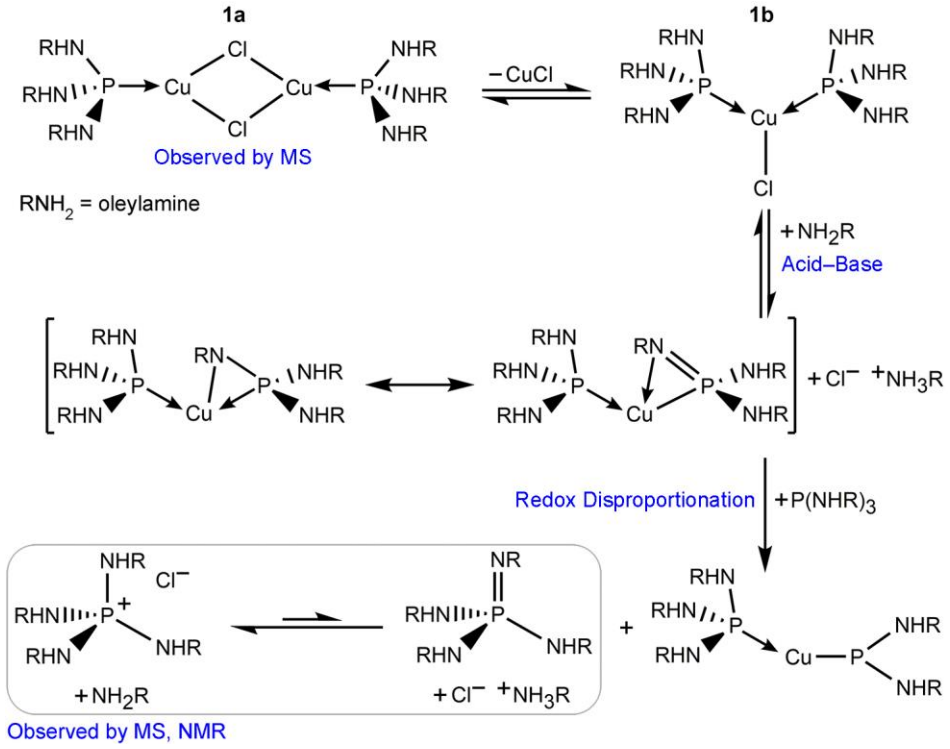

Scheme 2. 2. Pathway for Cu–P bond-formation based on that previously proposed for In–P.

Several key parameters investigated in previous aminophosphine-based InP syntheses are shown to influence the reactivity of $Cu_{3-x}P$ nanocrystal formation in this study. Increasing OAm/P molar ratios were found to correlate with larger nanocrystal sizes (Figure 2.3, Table S2.2), consistent with a previous InP report.[61] Smaller $Cu_{3-x}P$ nanocrystals were obtained when CuBr was used in place of CuCl (Figure S2.15, Table S2.5), consistent with the halide-induced size-tuning reported with Cd_3P_2 and InP nanocrystals.[59, 64] The decreased yield when using CuBr (Table S2.3) suggests that this decreased size is due to adsorption of Br^- on the nanocrystal surface, hindering heterogeneous reactivity.[59]

Influence of the amount of aminophosphine. We observe that increasing the $P(NEt_2)_3$/Cu ratio yields larger nanocrystal sizes (Figure 2.4, Table S2.3). This is in contrast to the synthesis of InP nanocrystals, where the opposite trend is observed.[61] This difference is likely due to differences in the chemistries of the $InCl_3$ and CuCl precursors. In addition to different starting coordination ($Cu_2Cl_2P_2(NHC_{18}H_{35})_6$ vs $InCl_3(NH_2C_{18}H_{35})_3$), the two metals likely differ in the stoichiometry required for redox disproportionation, which is expected to be the rate-limiting step.[61] In the pathway proposed for In–P bond formation[61] and in our analogous pathway (Scheme 2.2), redox disproportionation requires at least one free and one metal-bound equivalent of transaminated aminophosphine, $P(NHC_{18}H_{35})_3$. In the case of In, the P/In ratio required by the idealized chemical equation (P/In = 4) allows this condition to be met because $P(NHC_{18}H_{35})_3$ does not out-compete OAm for coordination to $InCl_3$.[61] In the case of Cu, however, a ratio of $P(NHC_{18}H_{35})_3/Cu \geq 3$ is needed in order to allow at least one free $P(NHC_{18}H_{35})_3$ in addition to the two bound to CuCl in the mononuclear $CuClP_2(NHC_{18}H_{35})_6$ species (**1b**), which is favored for $P(NHC_{18}H_{35})_3/Cu > 2$. The coordination of Cu thus enforces a need for P/Cu ≥ 3 for efficient redox disproportionation, which is greater than that required by the idealized chemical equation (P/Cu = 1.33, Equation 2.1). The plateau in the size-trend for P/Cu ≥ 3 (Table S2.4) supports this interpretation.

The above rationale suggests that increased $P(NEt_2)_3$ should lead to increased reactivity for Cu–P bond formation. Indeed, elemental analysis reveals a lower yield for P/Cu = 1.4 compared to reactions using P/Cu = 3.0 (Table S2.3). We thus conclude that the decrease in size with decreasing P/Cu is a result of incomplete reactivity (*i.e.*, incomplete consumption of the precursors) and does not represent atom-efficient size-tuning. As reactions with lower P/Cu have comparable nucleation activity (Table S2.3), this incomplete reactivity is likely due to the

suppression of heterogeneous reactivity (growth), similar to that observed for lower growth-temperatures. Additionally, reactions with P/Cu < 3.0 have a noticeably longer duration of the color-change following nucleation (Table S2.4), qualitatively supporting decreased reactivity with lower P/Cu ratio and suggesting that this protracted color-change corresponds to hindered heterogeneous reactivity. This decrease in heterogeneous reactivity may be due to a shift in the equilibrium toward the dinuclear $Cu_2Cl_2P_2(NHC_{18}H_{35})_6$ species (**1a**), yielding lower quantities of unbound $P(NHC_{18}H_{35})_3$. Additionally, **1a** is expected to be less reactive than **1b** due to its increased steric bulk and less-labile bridging halide. Thus, although Equation 1 requires only P/Cu = 1.33, full reactivity may necessitate larger P/Cu ratios, making it difficult to achieve atom-efficient size-tuning via this parameter.

It is worth noting that the strategy for varying the P/metal ratio employed in the previous study involved use of a fixed OAm/TOA ratio and a variable OAm/P ratio.[61] Here, on the other hand, we have fixed the OAm/P ratio and allowed the OAm/TOA ratio to vary when changing P/Cu molar ratio. This synthetic design choice was made to maintain a significant excess (>7 equiv to Cu) of free OAm (excluding that depleted by transamination) for all syntheses in the variable P/Cu series.

Influence of the amount of primary amine. Elemental analysis of the syntheses with the lowest and highest OAm/P molar ratios (OAm/P = 3.5 and 10.1, respectively) reveals no significant difference in the chemical yields of these two reactions. This result suggests that the smaller nanocrystal sizes at lower OAm/P (Table S2.2) are not due to incomplete reactivity. Additionally, there is no notable difference in the duration of the color-change following nucleation with varying OAm/P ratio (Table S2.2), qualitatively supporting similar heterogeneous reactivity across this series. Together, these observations suggest that the observed size-trend

(Table S2.2) can be attributed to decreasing nucleation activity with increasing OAm/P. Indeed, calculations converting the yield to number of particles reveal that the synthesis with OAm/P = 3.5 yields 5–30 times more particles than the synthesis with OAm/P = 10.1 (Table S2.3). To further support the claim that $Cu_{3-x}P$ nucleation activity is decreased with increasing OAm/P, a synthesis was performed using a large excess of oleylamine. Specifically, when OAm/P/Cu = 30.4/1.4/1.0 is used, nucleation of Cu(0) is observed (Figure S2.16). The trend of greater lower OAm/P yielding smaller nanocrystals is thus consistent with classical nucleation theory,[76-78] in which lower nucleation activity yields a smaller number of particles, ultimately producing larger particles in the final product.

A potential explanation for higher OAm/P leading to decreased $Cu_{3-x}P$ nucleation is that coordination of CuCl by OAm is competitive with $P(NHC_{18}H_{35})_3$ at the elevated temperatures used in nanocrystal syntheses. Even at room temperature, NMR measurements suggest that some CuCl-bound $P(NEt_2)_3$ can be replaced by OAm (Figure S2.17). When OAm (30 equiv/Cu) is added to $P(NEt_2)_3$-coordinated CuCl, a downfield shift of the ^{31}P-resonance toward free $P(NEt_2)_3$ is observed (Figure S2.17a). This OAm/$P(NEt_2)_3$/CuCl mixture also shows a downfield shift and broadening of the OAm α-carbon ^1H-resonance relative to free OAm (Figure S2.17b). It should be noted that OAm/P ratios near the stoichiometric quantity for transamination (OAm/P = 3.0) drive the equilibrium of tris-primary-amine-substituted-phosphines toward the diphosphine species $[P(NHC_{18}H_{35})_2]_2NC_{18}H_{35}$ and $P_2(NHC_{18}H_{35})_2(NC_{18}H_{35})_2$, due to a low quantity of free OAm.[61, 74] Although the diphosphines are said to be less-reactive than the monophosphine in the synthesis of InP,[61] they are still expected to coordinate CuCl,[71] and can likely participate in Cu–P formation. The observation of increased nucleation with lower OAm/P molar ratio suggests that

the accompanying shift in equilibrium to the diphosphine form does not lead to significantly decreased $Cu_{3-x}P$ nucleation.

It is important to note that monomodal ensembles were only obtained with molar ratios of OAm/P ≥ 5. OAm/P = 3.5 yields an additional, smaller-size population of nanocrystals (Figure 2.3a,d), likely from a second burst of nucleation. Additional nucleation events have been shown to be promoted with increased precursor reactivity within a kinetically controlled reactivity regime,[79] which serves as further support that low OAm/P molar ratios promote increased nucleation.

Influence of temperature. Lowering the reaction temperature was found to yield smaller nanocrystal sizes (Figure 2.5, Table S2.5). The ensembles resulting from syntheses conducted at $T \approx 220$ °C, were found to be characterized by low-polydispersity (Figures S2.12a and S2.14e), even with substantially hindered reactivity and protracted $Cu_{3-x}P$ nanocrystal formation. The temperature-dependent size-difference, however, is largely the result of a decreased yield, which is in contrast with the increased nucleation activity arising from surface-attachment-limited kinetics observed in aminophosphine-based syntheses of InP nanocrystals.[63] This difference may be due to the higher nucleation-temperature threshold for $Cu_{3-x}P$ nanocrystals (~210 °C), as the increased InP nucleation activity only occurred at lower temperatures ($T < 200$ °C) not accessible in our $Cu_{3-x}P$ nanocrystal syntheses. The higher temperatures needed to induce $Cu_{3-x}P$ nanocrystal formation could potentially be explained by the differences in halogen-coordination-number and Lewis acidity of the metal halide precursors, CuCl and $InCl_3$, or even the different compositions and coordination environments of the resultant materials, $Cu_{3-x}P$ and InP. Importantly, the insensitivity of the final $Cu_{3-x}P$ nanocrystal ensemble size and dispersion to the reaction temperature used during nucleation and early growth suggests that the relevant synthetic

intermediates for $Cu_{3-x}P$ nanocrystal formation are likely generated during the 125 °C degassing step.

Dependence of LSPR energy on the synthetic parameters. There is no clear correlation between nanocrystal lateral dimension and LSPR energy (Figure 2.6a), suggesting that vacancy concentration, rather than size, is determining the LSPR energy. Inspection of the $Cu_{3-x}P$ LSPR absorption throughout the synthesis reveals a red-shift with nanocrystal growth (Figure S2.5). Additionally, when varying OAm/P, P/Cu, and temperature, conditions that correspond to higher reactivity (higher P/Cu, lower OAm/P and higher temperature) lead to lower-energy LSPRs (Figure 2.6b). These trends may be due to a healing of lattice Cu vacancies via post-growth annealing. Interestingly, when the temperature is first held near the nucleation threshold (T ~ 225 °C) for 18 min before ramping to higher temperature (T_f = 276 °C), the LSPR does not further red-shift (Figure S2.13). This two-step synthesis yields a final ensemble with LSPR absorption at 855 meV, whereas rapid heating to T_f = 285 °C (Figure 2.1d) yielded nanocrystals with an LSPR energy of 770 meV (Figure S2.1). This difference suggests that temperature and/or rate of reactivity during early growth may bias the concentration of Cu vacancies to be more Cu-rich with higher reactivity. This effect is complementary to the post-growth healing of Cu vacancies; both lead to an apparent red-shift of the LSPR with increasing reactivity.

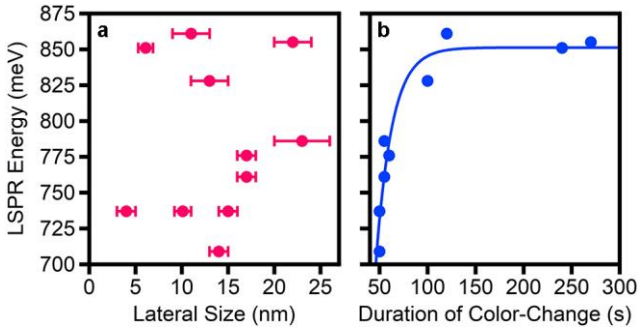

Figure 2. 6. Dependence of the LSPR energy on **(a)** nanocrystal lateral size and **(b)** duration of the color-change (used as a proxy for reactivity). The solid line is a guide to the eye.

Lower polydispersity with a one-pot synthesis. The two-pot synthesis, with addition of $P(NHC_{18}H_{35})_3$ to OAm-coordinated CuCl at $T_{inj} > T_{nucleation}$, yields an ensemble size distribution which is statistically the same as the $P(NEt_2)_3$ hot-injection synthesis (Figure 2.1e). On the other hand, the one-pot approach yields an ensemble with a statistically significant size-difference and lower polydispersity. The three syntheses with different pre-nucleation treatment were carefully controlled for chemical composition and post-nucleation reaction temperature (Figure 2.1d). The principal difference between the two-pot/hot-injection and one-pot reactions is the aminophosphine diffusion and OAm ligand-displacement, which must occur alongside redox disproportionation and nanocrystal formation in the former.

The one-pot synthesis has the lowest ensemble polydispersity, likely due to completion of transamination and attainment of equilibrium Cu–aminophosphine complexation (Scheme 2.2) prior to the initiation of nucleation. This speciation induces spatial and temporal uniformity in the subsequent aminophosphine redox disproportionation which drives nanocrystal formation. An extrapolation of the one-pot methodology to InP nanocrystals is unlikely to match the success observed with $Cu_{3-x}P$ nanocrystals in this study due to differences in thermodynamic favorability of L-type phosphine coordination of copper metal centers at low temperature. In situ P–Cu connectivity was observed by detection of a $Cu_2Cl_2P_2(NHC_{18}H_{35})_6$ species (Figures S2.6–8), consistent with precedented reactivity of copper halide salts.[70-73] Conversely, DFT calculations from a previous InP study have suggested that primary amine outcompetes aminophosphine for coordination of $InCl_3$ by $\Delta G = 4.8$ kcal/mol.[61]

Composition-dependent speciation of CuCl and Cu(0) formation. It is worth noting that another halide-bridged dinuclear binding motif has been proposed as an intermediate in the synthesis of Cu(0) nanocrystals from CuBr, OAm and trioctylphosphine (TOP) with OAm/P/Cu =

35/2/1.[80] In that study, $\{CuBr(TOP)_2\}_2$ undergoes redox disproportionation to form Cu(0) nuclei and Cu^{2+}. Importantly, the electronic structure of **1a** can be rationalized as having more P–Cu π-backbonding character and thus less electron density on the Cu_2X_2 core than $\{CuBr(TOP)_2\}_2$. We only observed Cu(0) nucleation in one-pot reactions with sufficiently high OAm excess (OAm/P/Cu = 30.4/1.4/1.0). The formation of Cu(0) outcompeting the nucleation of $Cu_{3-x}P$ under these conditions is evidenced by a change in color of the reaction from pale yellow to red (Figure S2.16a). Absorption spectroscopy confirms the presence of a Cu(0) LSPR feature and absence of a $Cu_{3-x}P$ LSPR feature (Figure S2.16b) in an aliquot withdrawn from the reaction mixture just after the color-change is observed. The analogous Cu(0) formation is not observed with reduced primary amine excess at OAm/P/Cu = 11.2/1.4/1.0 (Figure 2.4a), indicating that large primary-amine excesses reduce the reactivity of $Cu_{3-x}P$ nanocrystal formation. Another experimental condition which favors Cu(0) formation is the use of short degas times (<1 h), which suggests that ensuring complete metal halide solvation through the use of longer dissolution waiting times[68] may be important in disfavoring unary metal nucleation. These results indicate that, although **1a** may be capable of undergoing a disproportionation to Cu^0 and Cu^{2+}, such reactivity is suppressed by the combined use of a 3 h degassing step and appropriate reaction compositions.

2.5 Summary and Conclusions

We have developed a one-pot synthesis of size-tunable, phase-pure $Cu_{3-x}P$ nanocrystals with low polydispersity using tris(dialkylamino)phosphines, primary amines and copper halides. Similar to other metal phosphides, this reaction requires transamination of the aminophosphine with the primary amine to form $P(NHR)_3$, which coordinates to the metal precursor and further reacts to form the metal phosphide and an aminophosphonium byproduct. Unlike other metal phosphides, $Cu_{3-x}P$ nanocrystal formation is optimized with a one-pot heatup method, likely due

to formation of relevant Cu–P intermediates prior to nanocrystal nucleation. We demonstrate that the nucleation and growth reactivity can be tuned by varying the OAm/P or P/Cu molar ratios or the temperature, although thus far only variations in OAm/P have resulted in tuning the $Cu_{3-x}P$ nanocrystal properties without loss of yield. Similarly, these reactivity parameters can be used to tune the LSPR absorbance of the $Cu_{3-x}P$ nanocrystal ensemble. These results present the synthetic groundwork for obtaining atom-efficient size-tuning of high-quality $Cu_{3-x}P$ colloidal nanocrystals with tailored LSPR absorption.

2.6 Experimental Methods

2.6.1 Chemicals

Chemical manufacturers and purities are given in Table S2.4. Toluene, tetrahydrofuran (THF), and acetonitrile (MeCN) were obtained from a solvent purification system, transferred to a nitrogen-filled glovebox and stored over molecular sieves (3 Å) for two days before use. CuCl, CuBr, and d^6-benzene were opened, handled, and stored in a nitrogen-filled glovebox. OAm, TOA, $P(NEt_2)_3$, and octadecane were degassed upon receipt and stored in a nitrogen-filled glovebox over molecular sieves (4 Å) for two days before use. The ^{31}P-NMR spectrum of degassed $P(NEt_2)_3$ contained a peak at ~19 ppm (consistent with that observed for aminophosphine oxides) in addition to the primary resonance (118 ppm, Figure S2.17).[81]

2.6.2 Synthesis

Reaction temperatures were controlled through use of a 25-ml heating mantle connected to a contact voltage regulator (Volteq, $TDGC_2$ – 500VA). For all reactions, the temperature was measured using a thermocouple probe with the tip submerged in 3 mm of silicone oil and sheathed in a glass cover. The temperature output was stored digitally with an Omega data logger (OM-EL-USB-TC series) at five second intervals. The raw temperature was adjusted to a corrected

temperature with a temperature-dependent empirical quadratic function which was generated by calibration against an external mercury thermometer.

Heating profiles. In heat-up syntheses, a desired heating profile was achieved through a stepwise, two-voltage scheme. For the reaction with $T_f \approx 280$ °C (Figures 2.1, 2.3 and 2.4), a starting voltage of 105 V was used to set the initial ramp-rate ($dT/dt \approx 35$ °C/min). When the reaction began to darken (~220 °C), the voltage was lowered to 69 V to set the asymptotic temperature for the remaining 13 min of the reaction. For the reaction with $T_f \approx 220$ °C (Figure 2.5), a starting voltage of 105 V was used to expedite heating of the reaction. The voltage was decreased to 57 V when the reaction reached a temperature of 180 °C. The result was a protracted nucleation across the reaction temperature range of 210–220 °C.

One-pot synthesis of $Cu_{3-x}P$ nanocrystals with TOA as a cosolvent. Unless otherwise specified, the following method was used throughout this study. This synthetic method was adapted for other ratios of OAm/P/Cu by varying the quantity of TOA cosolvent such that a Cu concentration of 0.100 M and reaction volume of 5.00 ml was maintained.

In a typical synthesis with OAm/P/Cu = 24.0/3/1, a 25-ml round-bottom flask was loaded with CuCl (49.5 mg, 0.500 mmol), $P(NEt_2)_3$ (371 mg, 1.50 mmol), OAm (3.21 g, 3.95 ml, 12.0 mmol), and TOA cosolvent (851 mg, 1.05 ml). The mixture was stirred and degassed under vacuum at ~125 °C for 3 h, after which the pressure over the flask was equal to the equilibrium closed vacuum-line pressure due to removal of $HNEt_2$ that was generated by transamination of $P(NEt_2)_3$. The resulting pale, straw-colored solution was placed under argon and heated as outlined in the Heating Methods section. Following the reaction, the solution was transferred to a nitrogen-filled glovebox. The nanocrystals were precipitated with 16 ml toluene/THF/MeCN (1/4/3) and collected via centrifugation at 4000 rpm for 3 min. The resulting supernatant was saved for analysis

by ^{31}P NMR spectroscopy and ESI–MS. The nanocrystals were washed once more with 4 ml toluene/THF/MeCN (1/1/2) and resuspended in 2 ml toluene for further analysis.

One-pot synthesis of $Cu_{3-x}P$ nanocrystals with octadecane as a cosolvent. The reaction was conducted in the manner of the one-pot/TOA method with OAm/P/Cu = 10.6/1.4/1, replacing TOA (2.63 g, 3.25 ml) with an equal volume of octadecane (2.54 g, 3.25 ml), such that [Cu] = 0.100 M is maintained.

One-pot synthesis of $Cu_{3-x}P$ nanocrystals with CuBr as Cu source. For size comparison (Figure S15), the reaction was conducted in the manner of the one-pot/TOA method with OAm/P/Cu = 24.0/3.0/1.0, replacing CuCl (49.5 mg, 0.500 mmol) with an equimolar quantity of CuBr (71.7 mg, 0.500 mmol). For ESI–MS (Figure S2.6), the reaction was conducted in the absence of TOA with OAm/P/Cu = 30.4/4.0/1.0 using the same quantity of CuBr (71.7 mg, 0.500 mmol).

Two-pot synthesis of $Cu_{3-x}P$ nanocrystals with injection of transaminated $P(NEt_2)_3$. The principal difference from the one-pot/TOA method was the separation of transaminated $P(NEt_2)_3$ and CuX ($X^- = Cl^-$, Br^-) at reaction temperatures below 220 °C. In a 25-ml round-bottom flask, $P(NEt_2)_3$ (371 mg, 1.50 mmol) was mixed with OAm (1.60 g, 1.97 ml). In a separate 25-ml round-bottom flask, CuCl (49.5 mg, 0.500 mmol) was mixed with OAm (1.60 g, 1.97 ml) and TOA cosolvent (851 mg, 1.05 ml). The mixtures in both flasks were stirred and degassed under vacuum at 125 °C for 3 h. The transaminated $P(NEt_2)_3$ solution was held at 125 °C while the Cu solution was heated to 215 °C (~35 °C/min). At this point, the transaminated $P(NEt_2)_3$ solution was rapidly injected into the Cu solution. After 45 s the mixture blackened, at which point the voltage was lowered to 69 V to achieve the terminal temperature of ~280 °C. The subsequent treatment was identical to the one-pot/TOA method.

Synthesis of $Cu_{3-x}P$ nanocrystals by hot-injection of $P(NEt_2)_3$. In a 25-ml round-bottom flask, CuCl (49.5 mg, 0.500 mmol), OAm (3.21 g, 3.95 ml), and TOA were degassed under vacuum at 125 °C for 3 h. The solution was heated to 215 °C (~ 35 °C/min), at which point room-temperature $P(NEt_2)_3$ (0.41 ml, 1.5 mmol, stored) was rapidly injected. After ~1 min, the voltage was lowered to 69 V to achieve a terminal temperature of ~280 °C

Synthesis of InP nanocrystals by injection of $P(NEt_2)_3$. The methods of previous InP syntheses utilizing $P(NEt_2)_3$ injection[59-60] were adapted to be consistent with the method used herein. The reaction was conducted analogous to the hot-injection synthesis of $Cu_{3-x}P$ using OAm/P/In = 30.4/4.0/1.0. A solution of $InCl_3$ (111 mg, 0.500 mmol) and OAm (4.07 g, 5.00 ml) were degassed under vacuum at 125 °C for 3 h. The solution was heated to 225 °C (~ 35 °C/min), at which point room-temperature $P(NEt_2)_3$ (0.55 ml, 2.0 mmol, stored) was rapidly injected. After ~1 min the voltage was lowered to 69 V to achieve a terminal temperature of ~280 °C.

2.6.3 Evaluation of OAm–$P(NEt_2)_3$ ligand-exchange

CuCl (49.5 mg, 0.500 mmol), $P(NEt_2)_3$ (173 mg, 0.699 mmol, 192 µl), and TOA (249 mg, 0.704 mmol, 308 µl) were added to a 10-ml round-bottom flask. The mixture was stirred and degassed under vacuum at 125 °C for 30 min, followed by additional heating at 125 °C under Ar for 150 min. At elevated temperatures the solution appears homogeneous, but solids form upon cooling to room-temperature. In a nitrogen-filled glovebox, the mixture was heated to 70 °C to resolubilize the solids and ensure sample homogeneity. From the reaction solution 50 µl was transferred each to two separate vials. To one vial TOA (200 mg, 0.565 mmol) and THF (1.500 ml) were added to prepare the "0 equiv OAm" sample (Figure S2.17i, TOA/OAm/P/Cu = 24/0/1.4/1). To the other vial, OAm (200. mg, 0.748 mmol) and THF (1.500 ml) were added to prepare the '30 equiv OAm' sample (TOA/OAm/P/Cu = 1.4/30/1.4/1, Figure S2.17ii). Finally, a

control sample was prepared by mixing $P(NEt_2)_3$ (31.5 mg, 0.127 mmol), OAm (195 mg, 0.729 mmol), and THF (1.500 ml). The three solutions were left to sit for seven days to ensure complete diffusion and chemical equilibrium prior to NMR measurements. Each mixture (350 μl) was transferred to a screw-cap NMR tube (Wilmad-Labglass) and diluted with 300 μl benzene-d_6.

2.6.4 Characterization

Transmission electron microscopy (TEM). Sample grid preparation for TEM involved the drop-casting of nanocrystal suspensions in toluene onto a 100-mesh copper grid coated with Formvar and carbon (Electron Microscopy Sciences). Nanoplatelet lateral dimensions were determined via statistical analysis of TEM images collected on a FEI Spirit operating at 120 keV. Particles were analyzed with mitigated orientation bias by taking lateral dimension of the platelet to be the longest line that could be drawn along the particle's two-dimensional projection. The size distributions were derived from the analysis of 150 particles with the use of $13(\sqrt{150}+1)$ constant-width bins spanning the ensemble range. For samples containing bimodal distributions, 150 particles from each subset were analyzed.

Electronic absorption spectroscopy. In a nitrogen-filled glovebox 10 μl concentrated sample and 800 μl toluene were added to a quartz screw-cap cuvette (2-mm path-length). For quantitative measurements, 960 μl toluene/THF/MeCN (1/3/2) was added to 300 μl sample and the mixture was centrifuged at 4000 rpm for 3 min. The resulting pellet was dissolved in 120 μl toluene to create the "concentrated sample." Spectra were collected using a Cary 500 spectrometer in transmission mode. The LSPR energies were estimated by local fitting of the absorbance peak to a Gaussian function.

Powder X-ray diffraction. Samples were prepared by drying a pellet produced from washing the nanocrystals. This pellet was pulverized, and the resulting powder was used to fill a

well plate. The powder patterns were collected at ambient temperature in Bragg-Brentano geometry on a Bruker D8 Advance diffractometer at 40kV, 40 mA for Cu K_α (λ = 1.5418 Å), with a scan speed of 4.0 sec/step and a 2θ step size of 0.03°. The aliquots from the time-dependence study were measured on drop cast films with 6.0 sec/step because of low sample quantity. For comparison, the powder diffraction pattern of $Cu_{2.87}P$ was simulated from single-crystal data[36] using VESTA.[82]

$^{31}P\{^1H\}$ NMR spectroscopy. In a typical preparation, 100 µl supernatant and 600 µl toluene/benzene-d_6 (1/2) were added to a screw-cap NMR tube (Wilmad-Labglass). ^{31}P NMR spectra were collected on a JEOL ECA 500 MHz spectrometer with ^1H decoupling (1024 scans, relaxation delay = 0.5 s) and processed in Mestrenova using 5-Hz apodization. Chemical shifts were externally referenced to 85 % H_3PO_4 (δ = 0 ppm).

^1H NMR spectroscopy. In a typical preparation, 350 µl diluted sample in THF and 300 µl benzene-d_6 were transferred to a screw-cap NMR tube (Wilmad-Labglass). ^1H NMR spectra were collected on a JEOL ECA 500 MHz spectrometer (256 scans, relaxation delay = 1 s) and processed in Mestrenova using 0.25-Hz apodization. Chemical shifts were internally referenced to the α-carbon protons of THF in benzene-d_6 (δ = 3.57 ppm).[83]

Electrospray ionization mass spectrometry (ESI–MS). Typical sample preparation involved the dilution of 5 µl supernatant with 95 µl THF and 900 µl MeCN. Mass spectra were collected on a Thermo LCQ DECA Ion Trap with ESI ion source. Prior to measurement, the ESI source was flushed with MeCN to minimize aminophosphine methanolysis. The following parameters were used: source voltage = 5 kV, sheath gas flow = 80 units, auxiliary gas flow = 20 units, capillary temperature = 250 °C, and infusion flow rate = 50 µl/min.

Inductively coupled plasma mass spectrometry (ICP–MS). Prior to elemental analysis, nanocrystals were washed two additional times with 1.5 ml toluene/MeCN (1/2) to remove any residual precursors. The dried nanocrystal pellets were digested overnight in 85% HNO_3 (Optima grade, Sigma Aldrich) and filtered with a 0.22 μm PVDF syringe filter. Samples were analyzed using a Thermo iCAP RQ ICP–MS.

2.7 Appendix: Supplementary Information

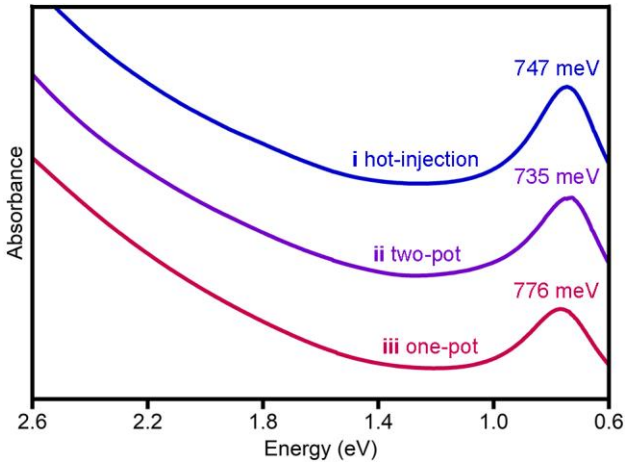

Figure S2. 1. Absorption spectra of $Cu_{3-x}P$ nanocrystals synthesized with [Cu] = 0.100 M, OAm/P/Cu = 24.0/3.0/1.0 and $T_f \approx 280$ °C using three different methods (Figure 2.1): (i) "hot-injection" (injection of $P(NEt_2)_3$ at $T_{inj} = 215$ °C), (ii) "two-pot" (injection of pre-transaminated phosphine at $T_{inj} = 215$ °C) and (iii) "one-pot" heat-up.

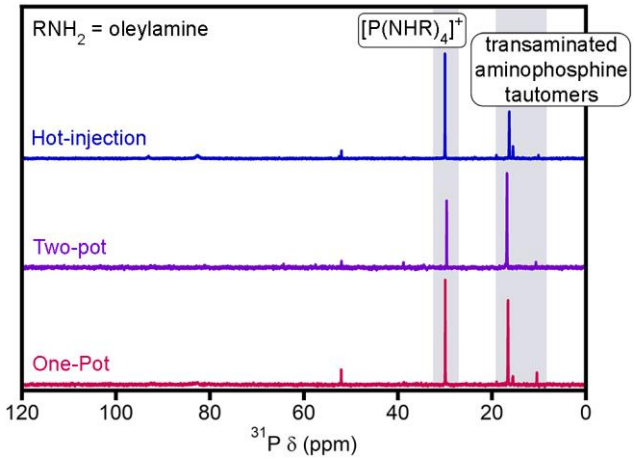

Figure S2. 2. ^{31}P-NMR spectra of post-reaction supernatants for $Cu_{3-x}P$ nanocrystals synthesized with [Cu] = 0.100 M, OAm/P/Cu = 24.0/3.0/1.0 and $T_f \approx 280$ °C using three different methods (Figure 2.1): (i) "hot-injection" (injection of $P(NEt_2)_3$ at $T_{inj} = 215$ °C), (ii) "two-pot" (injection of pre-transaminated phosphine at $T_{inj} = 215$ °C) and (iii) "one-pot" heat-up. The "transaminated aminophosphine tautomers" region may also contain small amounts of aminophosphine oxide, which is present in the starting material, $P(NEt_2)_3$ (Figure S2.18).

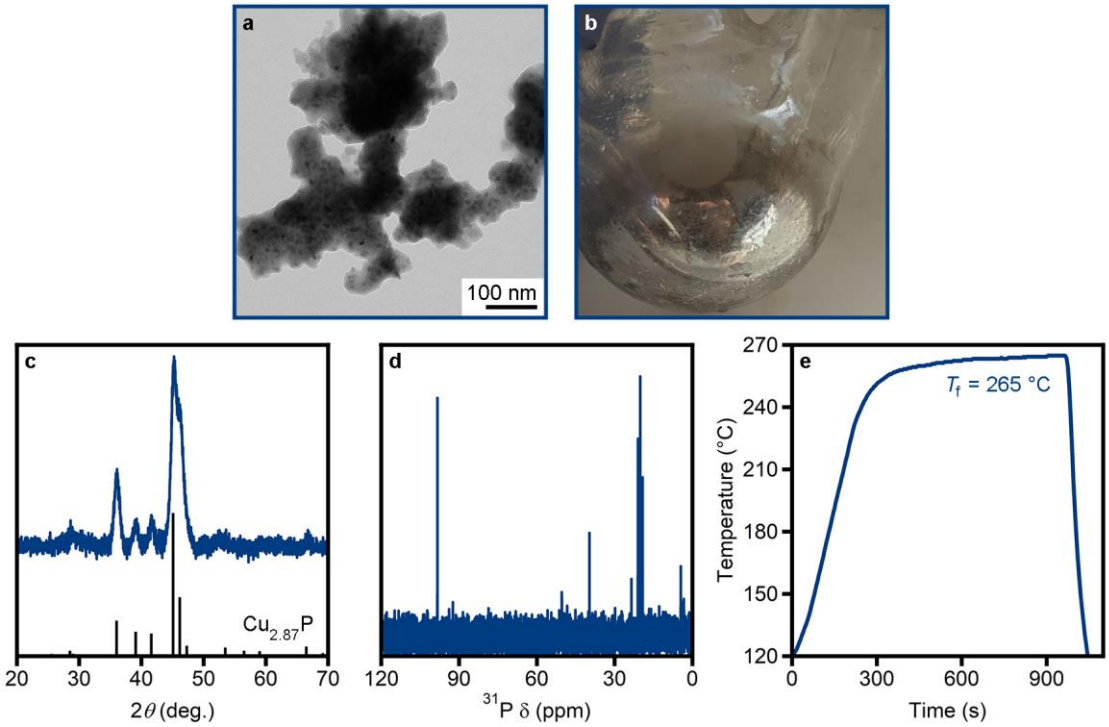

Figure S2. 3. $Cu_{3-x}P$ nanocrystal synthesis using $P(NEt_2)_3$ and TOA with no primary amine ([Cu] = 0.100 M, TOA/P/Cu = 22.8/3.0/1.0, T_f = 265 °C). **(a)** TEM image of nanocrystal product. **(b)** Photograph of metallic film formed on the reaction flask. **(c)** Powder X-ray diffraction pattern of the nanocrystal product compared to that simulated for $P6_3cm$ $Cu_{2.87}P$ (ref. 36). **(d)** The ^{31}P-NMR spectrum of the reaction supernatant does not show typical byproducts (Figure S2.2). **(e)** Temperature profile of the reaction.

Table S2. 1. Time and temperature of aliquots taken during a one-pot synthesis of $Cu_{3-x}P$ nanocrystals with [Cu] = 0.100 M, OAm/P/Cu = 24.0/3.0/1.0 and T_f = 300 °C (Figure 2.2).

Aliquot	Time following start of nucleation (s)	Temperature (°C)
1	45	255
2	125	273
3	350	287
4	560	292

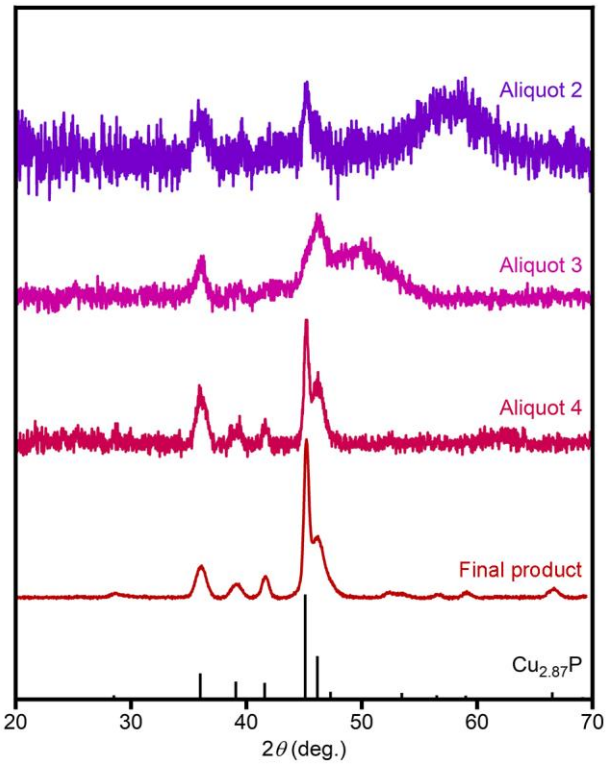

Figure S2. 4. Powder X-ray diffraction patterns of the aliquots and final product collected from a one-pot synthesis of $Cu_{3-x}P$ nanocrystals ([Cu] = 0.100 M, OAm/P/Cu = 24.0/3.0/1.0, T_f = 300 °C; Figure 2.2). The simulated pattern for $P6_3cm$ $Cu_{2.87}P$ (ref. 36) is shown for comparison. Aliquots were collected 45 s (aliquot 1, no diffraction observed), 125 s (aliquot 2), 350 s (aliquot 3) and 560 s (aliquot 4) after the reaction began to change color ("nucleation").

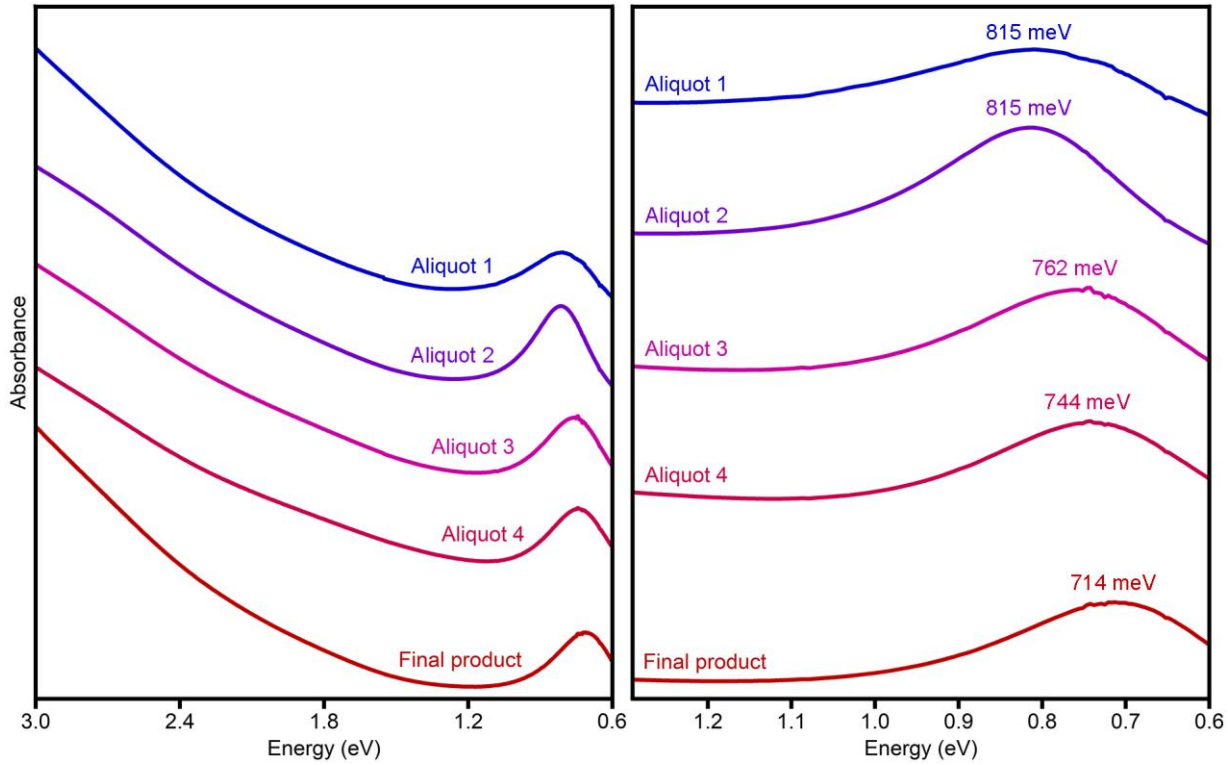

Figure S2. 5. (a) Absorption spectra of the aliquots and final product collected from a one-pot synthesis of $Cu_{3-x}P$ nanocrystals ([Cu] = 0.100 M, OAm/P/Cu = 24.0/3.0/1.0, T_f = 300 °C; Figure 2.2). **(b)** Magnification of the NIR spectral region. Aliquots were collected 45 s (aliquot 1), 125 s (aliquot 2), 350 s (aliquot 3) and 560 s (aliquot 4) after the reaction began to change color ("nucleation"). The ensemble LSPR red-shifts over the course of the reaction.

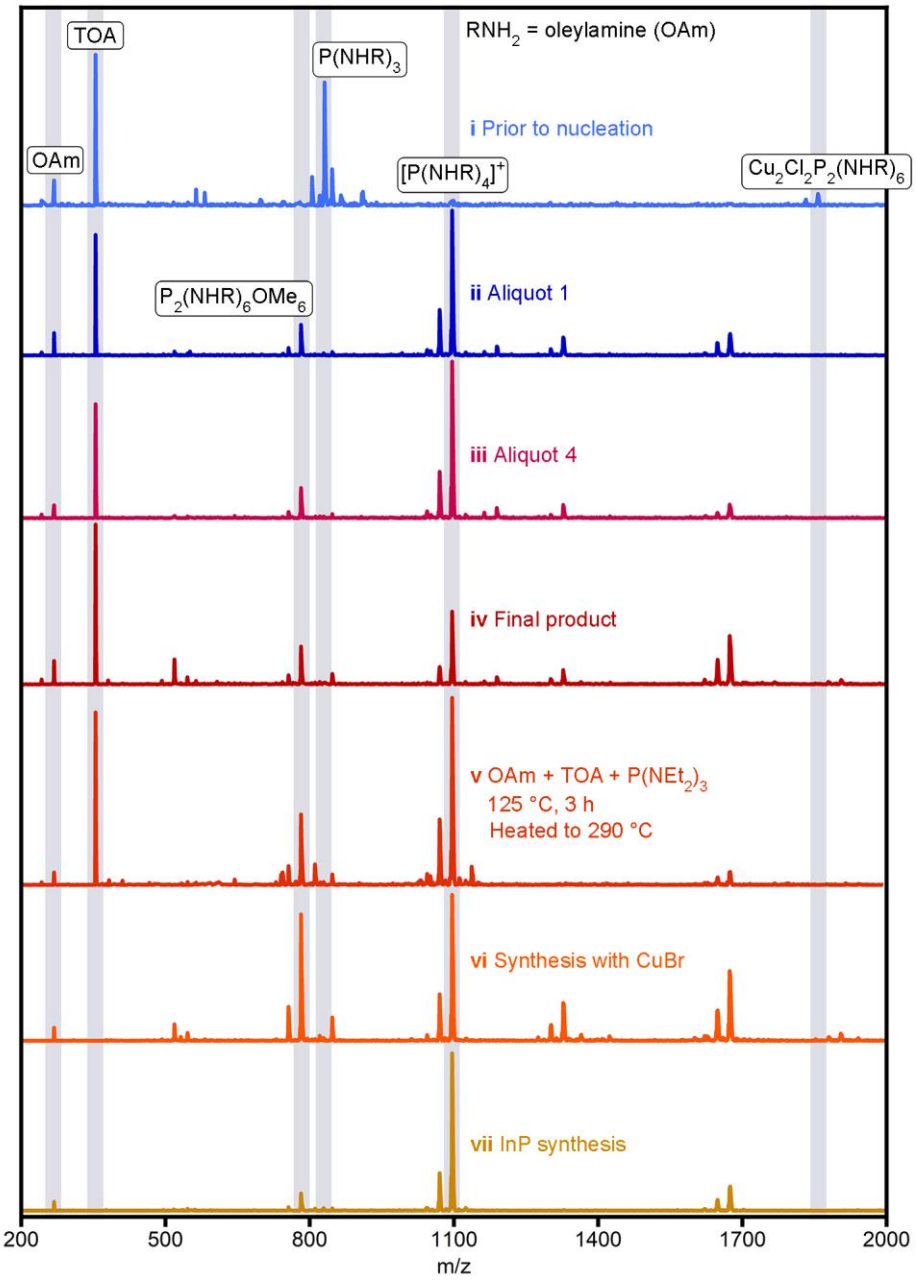

Figure S2. 6. Mass spectra (i–iv) One-pot synthesis of $Cu_{3-x}P$ nanocrystals ([Cu] = 0.100 M, OAm/P/Cu = 24.0/3.0/1.0, T_f = 300 °C; Figure 2.2): (i) Aliquot "0" collected prior to ramp-up from 125 °C, (ii) supernatant of aliquot 1, (iii) supernatant of aliquot 4 and (iv) the final supernatant. (v) OAm/TOA/$P(NEt_2)_3$ (8.0/2.6/1.0) degassed at 125 °C (3 h) and heated to 290 °C under Ar. (vi) Supernatant from a one-pot synthesis of $Cu_{3-x}P$ nanocrystals using CuBr ([Cu] = 0.100 M, OAm/P/Cu = 24.0/3.0/1.0, T_f = 295 °C). (vii) Supernatant from a hot-injection synthesis of InP ([In] = 0.100 M, OAm/P/In = 30.4/4.0/1.0, T_{inj} = 230 °C, T_f = 275 °C).

Section S2.1: Additional MS analysis

The solvents, OAm (267 g/mol) and TOA (354 g/mol) are present in the pre-nucleation solution and in the supernatants of all aliquots and the final product (Figure S2.6i–iv). Post-nucleation samples (Figure S2.6ii–iv) also contain $P_2(NHC_{18}H_{35})_2(OMe)_6$ (781 g/mol), which is generated by aminophosphine solvolysis of residual methanol[60] in the mass spectrometer.

Two additional peaks present in the spectra of post-nucleation samples (*m*/*z* = 1327, 1674) contain −26 and −52 side peaks, characteristic of oleyl groups. The species with peak at *m*/*z* = 1674 does not contain a metal or halogen, as this peak is also present in the mass spectra of the supernatants from $Cu_{3-x}P$ nanocrystals synthesized using CuBr instead of CuCl (Figure S2.6vi) and from InP nanocrystals synthesized via hot injection of $P(NEt_2)$ into $InCl_3$ in OAm (Figure S2.6vii). This species is tentatively assigned as $[(NHC_{18}H_{35})_3P(NC_{18}H_{35})P{=}O(NHC_{18}H_{35})_2]^+$. An analogous peak was observed at *m*/*z* = 1519 with the expected 6×(R–R′) mass difference of 156 *m*/*z* from using R′ = hexadecylamine[61] instead of R = OAm. Although the peak at *m*/*z* = 1327 could not be identified, it is likely unique to the formation of $Cu_{3-x}P$. Notably, this peak is present in the mass spectrum of the supernatant from $Cu_{3-x}P$ nanocrystals synthesized using CuBr instead of CuCl (Figure S2.6vi), but not present in the supernatant from InP nanocrystals synthesized via hot-injection of $P(NEt_2)$ into $InCl_3$ in OAm (Figure S2.6vii).

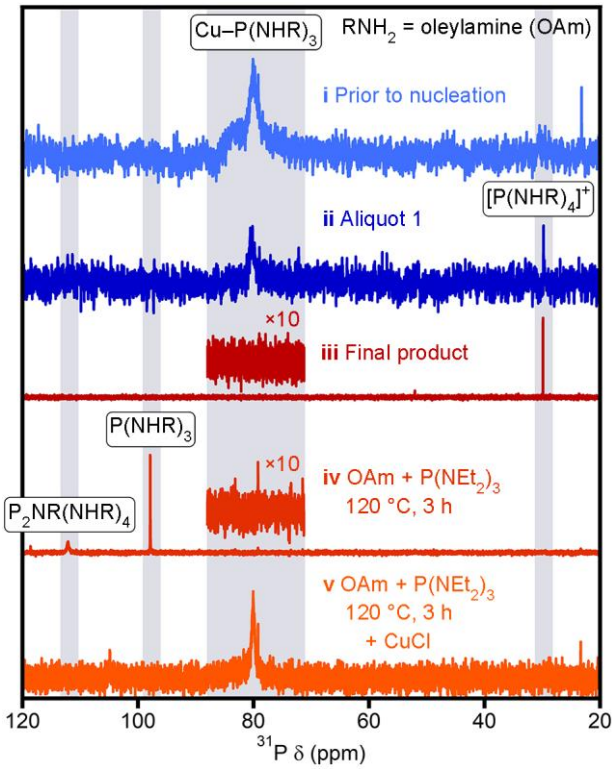

Figure S2. 7. ^{31}P-NMR spectra. (i–iii) One-pot synthesis of $Cu_{3-x}P$ nanocrystals ([Cu] = 0.100 M, OAm/P/Cu = 24.0/3.0/1.0, T_f = 300 °C; Figure 2.2): (i) aliquot "0" collected prior to ramp-up from 125 °C, (ii) the supernatant of aliquot 1 and (iii) the final supernatant. (iv) OAm/ $P(NEt_2)_3$ (22.8/3.0) degassed at 120 °C (3 h) to yield the transaminated phosphine, $P(NHR)_3$, to which (v) 0.25 equiv CuCl was added at room-temperature. These data suggest that the region centered at 80 ppm contains $P(NHR)_3$-coordinated Cu species ("Cu–$P(NHR)_3$"), such as $Cu_2Cl_2P_2(NHR)_6$ or $CuCl(P(NHR)_3)_2$.

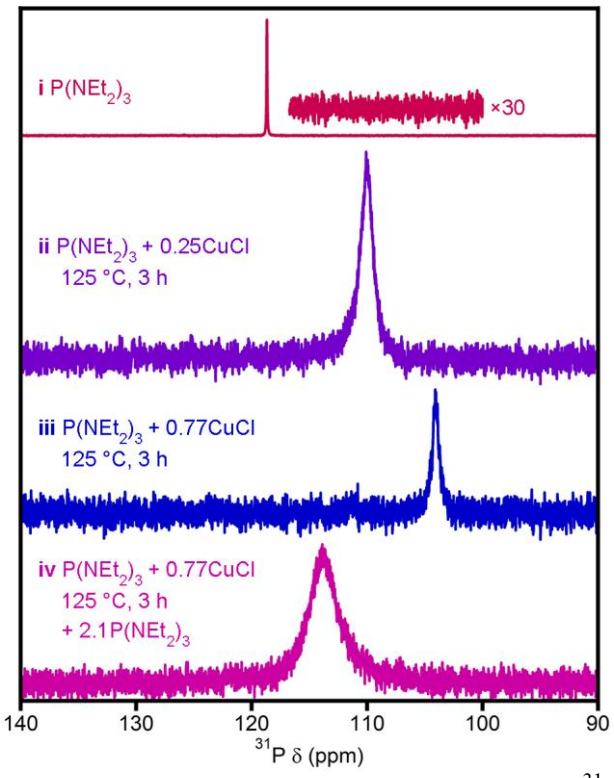

Figure S2. 8. Monitoring of Cu–phosphine complexation by ^{31}P-NMR. $P(NEt_2)_3$ (i) before and (ii, iii) after heating with 0.25, 0.77 equiv CuCl in octadecane at 125 °C for 3 h. Increasing addition of Cu results in an upfield shift of the $P(NEt_2)_3$ resonance. (iv) Addition of 2.1 equiv $P(NEt_2)_3$ shifts the resonance back downfield toward the free phosphine resonance.

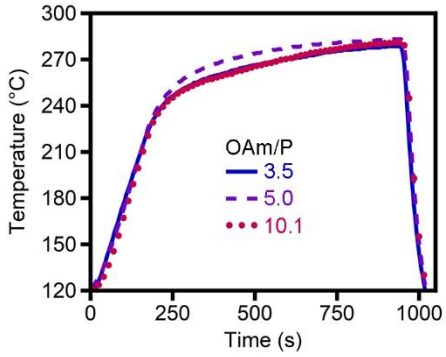

Figure S2. 9. Temperature profiles for the syntheses of $Cu_{3-x}P$ nanocrystals with varying OAm/P ratios ([Cu] = 0.100 M, P/Cu = 3.0; Figure 2.3).

Table S2. 2. Tabulated data for $Cu_{3-x}P$ nanocrystals synthesized with varying OAm/P ratios ([Cu] = 0.100 M, P/Cu = 3.0, $T_f \approx 280$ °C; Figures 2.1 and 2.3).

OAm/P	TOA/P	Duration of color change (s)	Lateral dimension (nm)	LSPR energy (meV)	Corresponding TEM figure
3.5	5.0	50	4 ± 1, 10.1 ± 0.9	737	2.3a
5.0	3.9	50	15 ± 1	737	2.3b
8.0	1.6	60	17 ± 1	776	2.1c
10.1	0	55	23 ± 3	786	2.3c

Table S2. 3. Yields of representative $Cu_{3-x}P$ syntheses with varying chemical conditions.

Chemical conditions	Yield[a] (% based on Cu)	Lateral dimension (nm)	Relative nucleation activity[b]	Corresponding TEM figure
OAm/P/Cu = 10.5/3.0/1.0; CuCl	82 ± 3	4 ± 1, 10.1 ± 0.9	5–30[c]	2.3a
OAm/P/Cu = 30.3/3.0/1.0; CuCl	85 ± 2	23 ± 3	1	2.3c
OAm/P/Cu = 11.2/1.4/1.0; CuCl	54 ± 2	11 ± 2	3	2.4a
OAm/P/Cu = 24.0/3.0/1.0; CuBr	51 ± 2	14 ± 1	2	S2.15

[a]Calculated as the percentage of Cu used in the reaction that was incorporated into the nanocrystal products

[b]Estimated as the ensemble particle count based on yield and lateral platelet dimension assuming a constant platelet thickness.

[c]Upper and lower bounds determined using the sizes of the smaller and larger subsets, respectively.

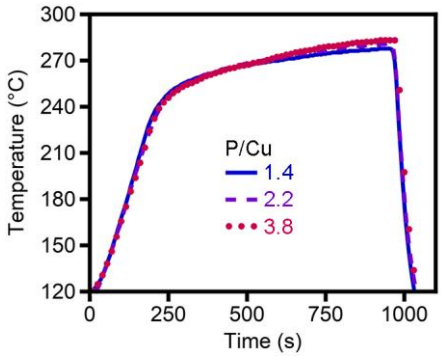

Figure S2. 10. Temperature profiles for the syntheses of $Cu_{3-x}P$ nanocrystals with varying P/Cu ratios ([Cu] = 0.100 M, OAm/P = 8.0; Figure 2.4).

Table S2. 4. Tabulated data for $Cu_{3-x}P$ nanocrystals synthesized with varying P/Cu ratios ([Cu] = 0.100 M, OAm/P = 8.0, $T_f \approx 280$ °C; Figures 2.1 and 2.4).

P/Cu	TOA/P	Duration of color change (s)	Lateral dimension (nm)	LSPR energy (meV)	Corresponding TEM figure
1.4	10.3	120	11 ± 2	861	2.4a
2.2	4.3	100	13 ± 2	828	2.4b
3.0	1.6	60	17 ± 1	776	2.1c
3.8	0	55	17 ± 1	761	2.4c

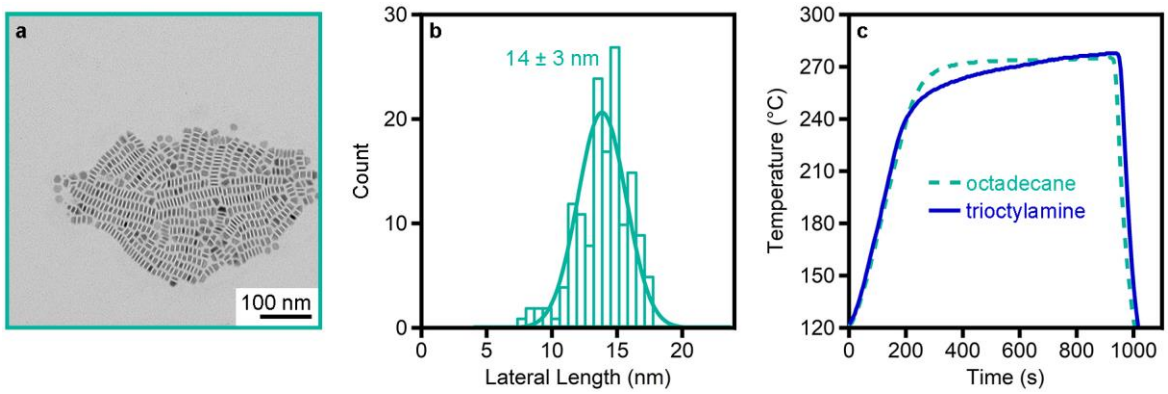

Figure S2. 11. Characterization of $Cu_{3-x}P$ nanocrystals synthesized using octadecane ([Cu] = 0.100 M, P/Cu = 1.4, OAm/octadecane/P = 7.6/15.0/1.0, T_f = 275 °C): **(a)** TEM image, **(b)** statistical analysis (n = 150) of lateral platelet dimension and **(c)** temperature profile compared to the analogous synthesis using TOA as the cosolvent ([Cu] = 0.100 M, P/Cu = 1.4, OAm/TOA/P = 8.0/10.3/1.0, T_f = 275 °C; Figures 4a, S10). The analogous synthesis with TOA yielded nanocrystals with an ensemble lateral dimension of 11 ± 2 nm.

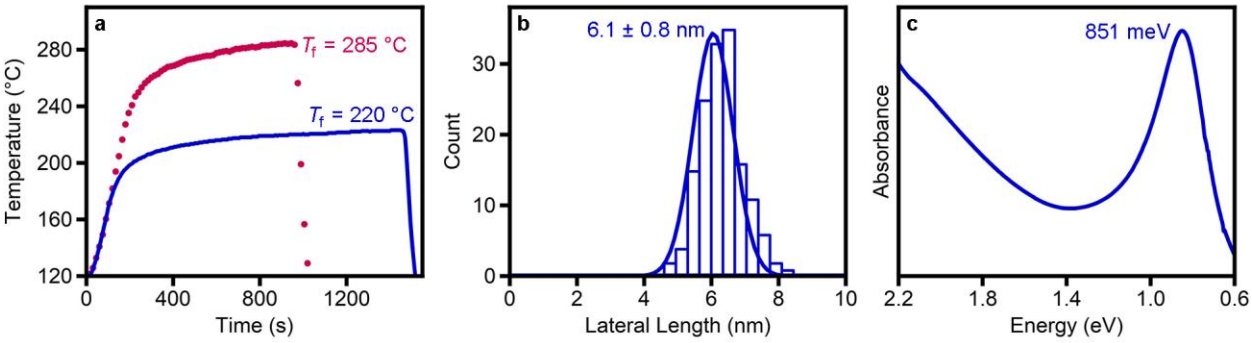

Figure S2. 12. Characterization of $Cu_{3-x}P$ nanocrystals synthesized with [Cu] = 0.100 M and OAm/P/Cu = 24.0/3.0/1.0 at low temperature (T_f = 220 °C, Figure 2.5): **(a)** Temperature profile compared to the one-pot high-temperature profile (reproduced from Figure 2.1c). **(b)** Statistical analysis of lateral platelet dimension and **(c)** absorption spectrum of the nanocrystal ensemble.

Table S2. 5. Tabulated data for $Cu_{3-x}P$ nanocrystals synthesized with varying temperature profiles ([Cu] = 0.100 M, OAm/P/Cu = 24.0/3.0/1.0; Figures 2.1c, 2.5, S2.1, S2.12 and S2.13).

T_f (°C)	Duration of color change (s)	Lateral dimension (nm)	LSPR energy (meV)	Corresponding TEM figure
285	60	17 ± 1	776	2.1c
220	240	6.1 ± 0.8	851	2.5a
275[a]	270	22 ± 2	855	S2.13b

[a]Reaction held at 225 °C for 18 min before ramping to 275 °C

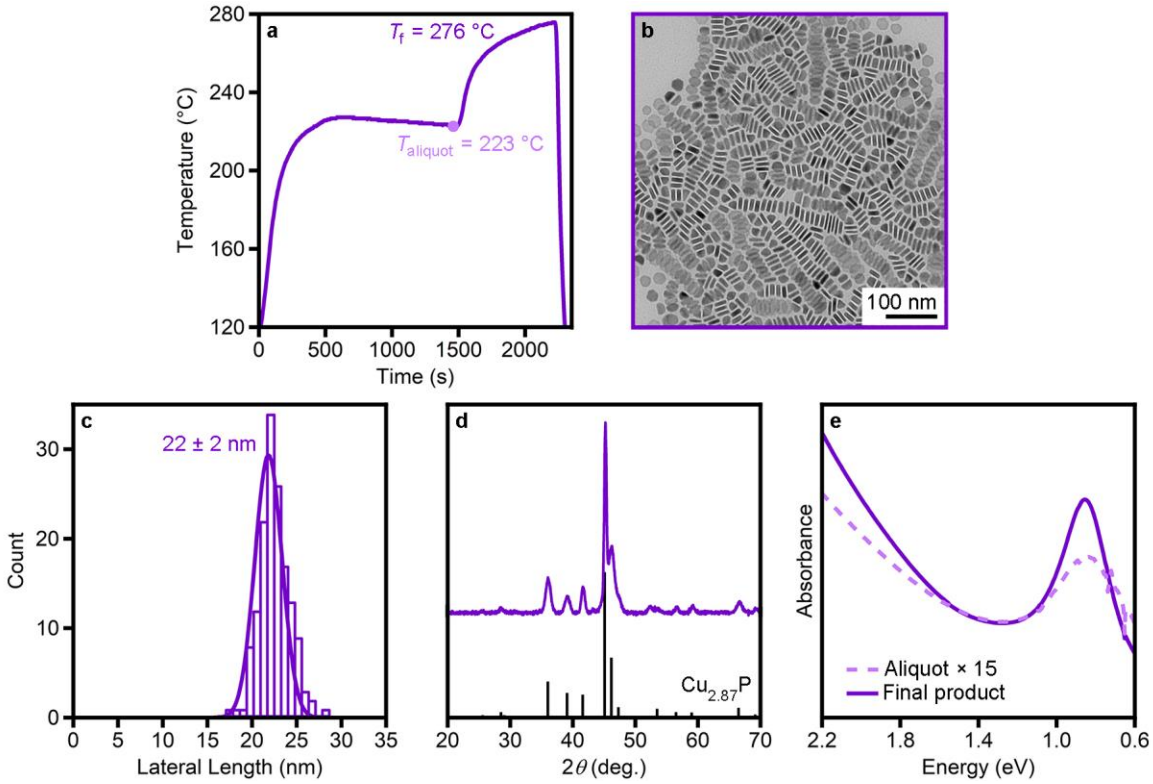

Figure S2. 13. Characterization of $Cu_{3-x}P$ nanocrystals synthesized by heating at 225 °C for 18 min followed by heating to T_f = 276 °C ([Cu] = 0.100 M, OAm/P/Cu = 24.0/3.0/1.0). **(a)** Temperature profile with aliquot withdrawal indicated (purple circle). **(b)** TEM image and **(c)** statistical analysis (n = 150) of lateral platelet dimension of the final nanocrystal product. **(d)** Powder X-ray diffraction pattern of the final product compared to that simulated for $P6_3cm$ $Cu_{2.87}P$ (ref. 36). **(e)** Quantitative absorption comparison of the aliquot and final product reveal ~15× lower yield in the aliquot.

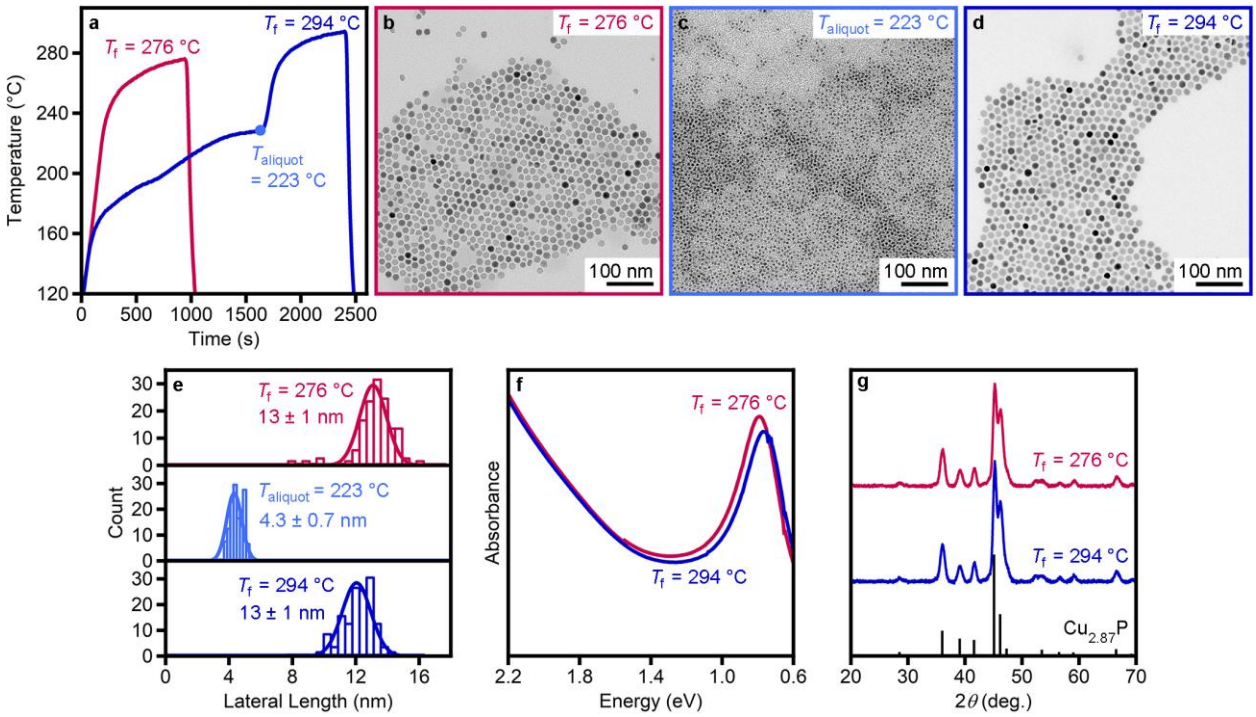

Figure S2. 14. Characterization of $Cu_{3-x}P$ nanocrystals from two separate syntheses with [Cu] = 0.100 M and OAm/P/Cu = 4.9/1.4/1.0 using different temperature profiles. **(a)** Temperature profiles for both reactions with aliquot withdrawal indicated (blue circle). TEM images of $Cu_{3-x}P$ nanocrystals from **(b)** a quick-ramp synthesis (T_f = 275 °C), **(c)** an aliquot ($T_{aliquot}$ = 223 °C) taken prior to ramp-up and **(d)** the final product (T_f = 294 °C) of the two-part synthesis. **(e)** Statistical analyses (n = 150) of lateral platelet dimension for each nanocrystal set. **(f)** Quantitative absorption comparison of the two syntheses suggests similar final yield. **(g)** Powder X-ray diffraction patterns compared to that simulated for $P6_3cm$ $Cu_{2.87}P$ (ref. 36).

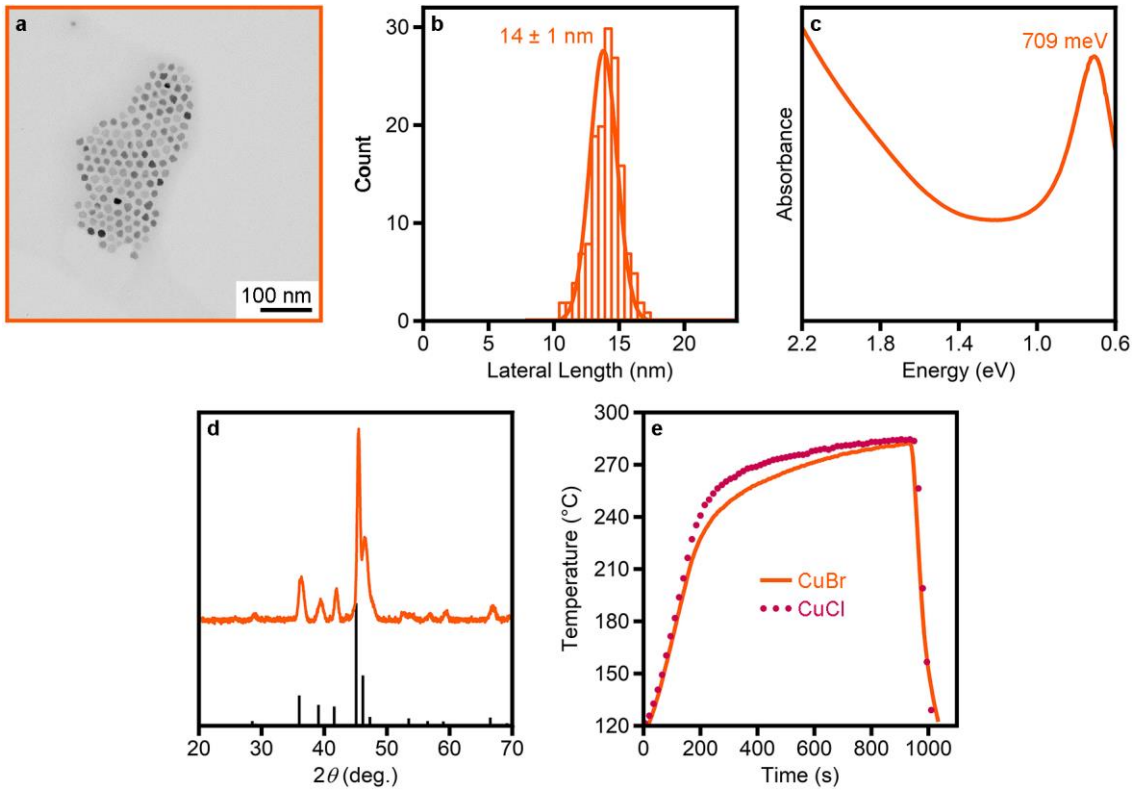

Figure S2. 15. Characterization of $Cu_{3-x}P$ nanocrystals synthesized using CuBr ([Cu] = 0.100 M, OAm/P/Cu = 24.0/3.0/1.0, T_f = 285 °C): **(a)** TEM image, **(b)** statistical analysis (n = 150) of lateral platelet dimension, **(c)** absorption spectrum, **(d)** powder X-ray diffraction pattern (compared to that simulated for $P6_3cm$ $Cu_{2.87}P$, ref. 36) and **(e)** temperature profile compared to the analogous synthesis using CuCl (Figure 2.1c).

Table S2. 6. Tabulated data for $Cu_{3-x}P$ nanocrystals synthesized using various copper halides ([Cu] = 0.100 M, OAm/P/Cu = 24.0/3.0/1.0 and T_f = 285 °C; Figures 2.1c and S2.15).

X^-	Duration of color change (s)	Lateral dimension (nm)	LSPR energy (meV)	Corresponding TEM figure
Cl^-	60	17 ± 1	770	2.1c
Br^-	50	14 ± 1	709	S2.15

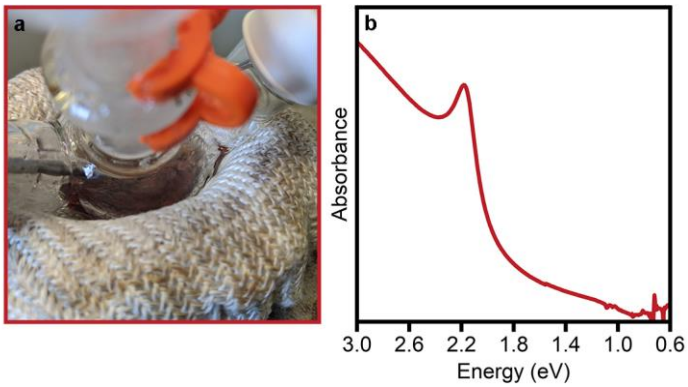

Figure S2. 16. Characterization of Cu(0) nanocrystals nucleated in a one-pot synthesis with high-OAm and low-$P(NEt_2)_3$ content ([Cu] = 0.100 M and OAm/P/Cu = 30.4/1.4/1.0): **(a)** Photograph of the red solution observed at 247 °C, signaling the initiation of Cu(0) formation and **(b)** absorption spectrum of an aliquot of Cu(0) nanocrystals withdrawn 60 s after the color-change. This red intermediate is not observed in other syntheses.

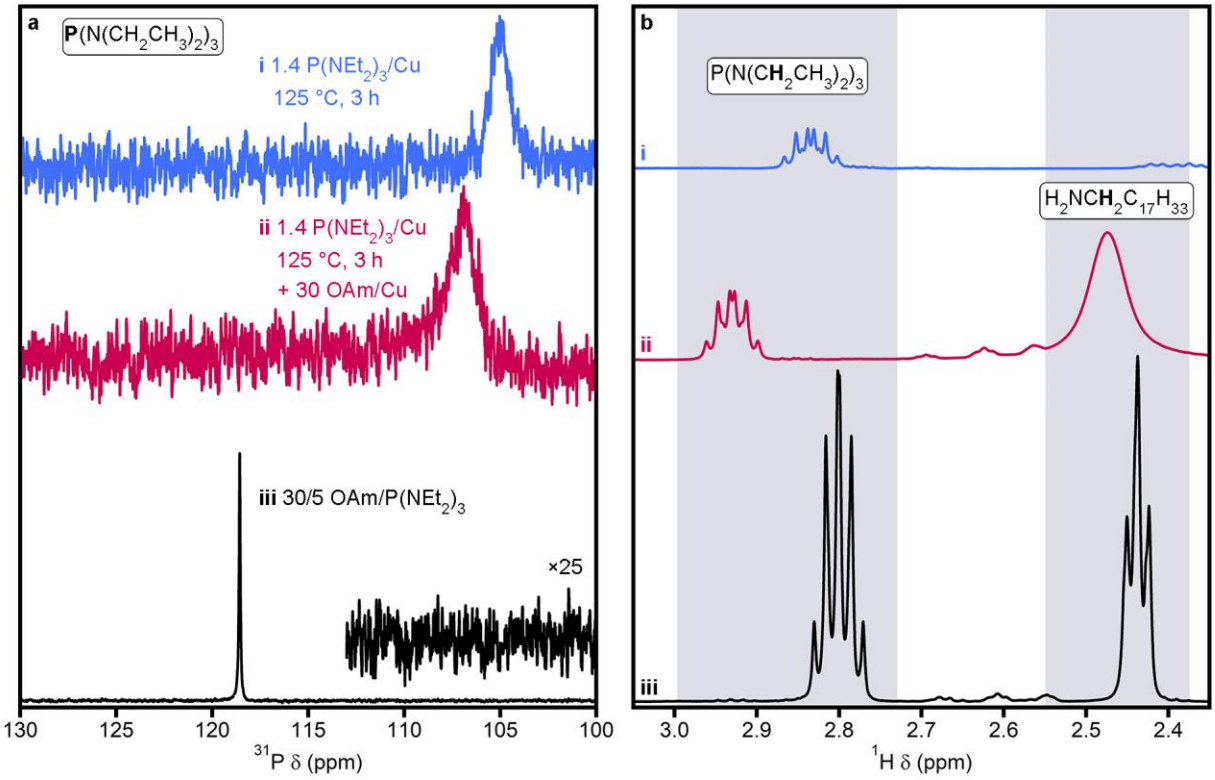

Figure S2. 17. **(a)** ^{31}P- and **(b)** ^{1}H-NMR spectra of 1.4 $P(NEt_2)_3$/Cu with (i) 0 and (ii) 30 equiv OAm. (iii) 30/5 OAm/ $P(NEt_2)_3$ is shown for reference.

Table S2. 7. Chemicals.

Chemical	Purity	Manufacturer
d^6-Benzene	99.5%	Cambridge Isotope Laboratories
Copper(I) chloride	>97%	Strem Chemicals
Copper(I) bromide	>98%	Strem Chemicals
Oleylamine (OAm)	>95%	Strem Chemicals
Octadecane	99%	Alfa Aesar
Tris(diethylamino)phosphine ($P(NEt_2)_3$)	95%	Acros Organics
Trioctylamine (TOA)	97%	Frontier Scientific

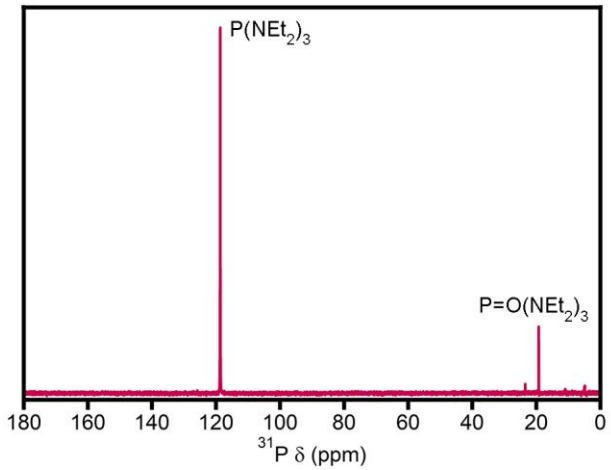

Figure S2. 18. ^{31}P-NMR spectrum of $P(NEt_2)_3$ after degassing and storage over molecular sieves (4 Å) for two days.

2.8 Acknowledgements

Chapter 2, in full, is a reprint of the material as it appears in "Colloidal Synthesis of Tunable Copper Phosphide Nanocrystals" *Chem. Mater.* **2021**, 33, 1394. The dissertation author was the primary author of this paper and gratefully acknowledges the contributions of coauthor Alina M. Schimpf. TEM imaging was performed at the National Center for Microscopy and Imaging Research at UC San Diego. ESI-TOF mass spectrometry was performed at the Molecular Mass Spectrometry Facility at University of California, San Diego. Powder X-ray diffraction measurements were performed at the UC San Diego Crystallography Facility.

2.9 References

1. Shim, M.; Guyot-Sionnest, P. n-Type Colloidal Semiconductor Nanocrystals. *Nature* **2000,** *407*, 981.

2. Vanmaekelbergh, D.; Liljeroth, P. Electron-Conducting Quantum Dot Solids: Novel Materials Based on Colloidal Semiconductor Nanocrystals. *Chem. Soc. Rev.* **2005,** *34*, 299.

3. Chikan, V. Challenges and Prospects of Electronic Doping of Colloidal Quantum Dots: Case Study of CdSe. *J. Phys. Chem. Lett.* **2011,** *2*, 2783.

4. Faucheaux, J. A.; Stanton, A. L. D.; Jain, P. K. Plasmon Resonances of Semiconductor Nanocrystals: Physical Principles and New Opportunities. *J. Phys. Chem. Lett.* **2014,** *5*, 976.

5. Schimpf, A. M.; Knowles, K. E.; Carroll, G. M.; Gamelin, D. R. Electronic Doping and Redox-Potential Tuning in Colloidal Semiconductor Nanocrystals. *Acc. Chem. Res.* **2015,** *48*, 1929.

6. Lhuillier, E.; Guyot-Sionnest, P. Recent Progresses in Mid Infrared Nanocrystal Optoelectronics. *IEEE J. Sel. Top. Quantum Electron.* **2017,** *23*.

7. Nutz, T.; zum Felde, U.; Haase, M. Wet-Chemical Synthesis of Doped Nanoparticles: Blue-Colored Colloids of n-Doped SnO_2 : Sb. *J. Chem. Phys.* **1999,** *110*, 12142.

8. Kanehara, M.; Koike, H.; Yoshinaga, T.; Teranishi, T. Indium Tin Oxide Nanoparticles with Compositionally Tunable Surface Plasmon Resonance Frequencies in the Near-IR Region. *J. Am. Chem. Soc.* **2009,** *131*, 17736.

9. Zhao, Y.; Pan, H.; Lou, Y.; Qiu, X.; Zhu, J.; Burda, C. Plasmonic $Cu_{2-x}S$ Nanocrystals: Optical and Structural Properties of Copper-Deficient Copper(I) Sulfides. *J. Am. Chem. Soc.* **2009,** *131*, 4253.

10. Buonsanti, R.; Llordes, A.; Aloni, S.; Helms, B. A.; Milliron, D. J. Tunable Infrared Absorption and Visible Transparency of Colloidal Aluminum-Doped Zinc Oxide Nanocrystals. *Nano Lett.* **2011,** *11*, 4706.

11. Rowe, D. J.; Jeong, J. S.; Mkhoyan, K. A.; Kortshagen, U. R. Phosphorus-Doped Silicon Nanocrystals Exhibiting Mid-Infrared Localized Surface Plasmon Resonance. *Nano Lett.* **2013,** *13*, 1317.

12. Fang, H. B.; Hegde, M.; Yin, P. H.; Radovanovic, P. V. Tuning Plasmon Resonance of In_2O_3 Nanocrystals throughout the Mid-Infrared Region by Competition between Electron Activation and Trapping. *Chem. Mater.* **2017,** *29*, 4970.

13. Marbella, L. E.; Gan, X. Y.; Kaseman, D. C.; Millstone, J. E. Correlating Carrier Density and Emergent Plasmonic Features in $Cu_{2-x}Se$ Nanoparticles. *Nano Lett.* **2017,** *17*, 2414.

14. Limpens, R.; Pach, G. F.; Mulder, D. W.; Neale, N. R. Size-Dependent Asymmetric Auger Interactions in Plasma-Produced n- and p-Type-Doped Silicon Nanocrystals. *J. Phys. Chem. C* **2019,** *123*, 5782.

15. Haase, M.; Weller, H.; Henglein, A. Photochemistry and Radiation-Chemistry of Colloidal Semiconductors. 23. Electron Storage on ZnO Particles and Size Quantization. *J. Phys. Chem.* **1988,** *92*, 482.

16. Liu, W. K.; Whitaker, K. M.; Smith, A. L.; Kittilstved, K. R.; Robinson, B. H.; Gamelin, D. R. Room-Temperature Electron Spin Dynamics in Free-Standing ZnO Quantum Dots. *Phys. Rev. Lett.* **2007,** *98*, 186804.

17. Palomaki, P. K. B.; Miller, E. M.; Neale, N. R. Control of Plasmonic and Interband Transitions in Colloidal Indium Nitride Nanocrystals. *J. Am. Chem. Soc.* **2013,** *135*, 14142.

18. Dorfs, D.; Härtling, T.; Miszta, K.; Bigall, N. C.; Kim, M. R.; Genovese, A.; Falqui, A.; Povia, M.; Manna, L. Reversible Tunability of the Near-Infrared Valence Band Plasmon Resonance in $Cu_{2-x}Se$ Nanocrystals. *J. Am. Chem. Soc.* **2011,** *133*, 11175.

19. Kriegel, I.; Jiang, C.; Rodríguez-Fernández, J.; Schaller, R. D.; Talapin, D. V.; da Como, E.; Feldmann, J. Tuning the Excitonic and Plasmonic Properties of Copper Chalcogenide Nanocrystals. *J. Am. Chem. Soc.* **2012,** *134*, 1583.

20. Niezgoda, J. S.; Harrison, M. A.; McBride, J. R.; Rosenthal, S. J. Novel Synthesis of Chalcopyrite $Cu_xIn_yS_2$ Quantum Dots with Tunable Localized Surface Plasmon Resonances. *Chem. Mater.* **2012,** *24*, 3294.

21. Xie, Y.; Riedinger, A.; Prato, M.; Casu, A.; Genovese, A.; Guardia, P.; Sottini, S.; Sangregorio, C.; Miszta, K.; Ghosh, S.; Pellegrino, T.; Manna, L. Copper Sulfide Nanocrystals with Tunable Composition by Reduction of Covellite Nanocrystals with Cu^{+} Ions. *J. Am. Chem. Soc.* **2013,** *135*, 17630.

22. Schimpf, A. M.; Thakkar, N.; Gunthardt, C. E.; Masiello, D. J.; Gamelin, D. R. Charge-Tunable Quantum Plasmons in Colloidal Semiconductor Nanocrystals. *ACS Nano* **2014,** *8*, 1065.

23. Urso, C.; Barawi, M.; Gaspari, R.; Sirigu, G.; Kriegel, I.; Zavelani-Rossi, M.; Scotognella, F.; Manca, M.; Prato, M.; De Trizio, L.; Manna, L. Colloidal Synthesis of Bipolar Off-Stoichiometric Gallium Iron Oxide Spinel-Type Nanocrystals with Near-IR Plasmon Resonance. *J. Am. Chem. Soc.* **2017,** *139*, 1198.

24. Luther, J. M.; Jain, P. K.; Ewers, T.; Alivisatos, A. P. Localized Surface Plasmon Resonances Arising from Free Carriers in Doped Quantum Dots. *Nat. Mater.* **2011,** *10*, 361.

25. Hsu, S.-W.; On, K.; Tao, A. R. Localized Surface Plasmon Resonances of Anisotropic Semiconductor Nanocrystals. *J. Am. Chem. Soc.* **2011,** *133*, 19072.

26. Hsu, S.-W.; Bryks, W.; Tao, A. R. Effects of Carrier Density and Shape on the Localized Surface Plasmon Resonances of $Cu_{2-x}S$ Nanodisks. *Chem. Mater.* **2012,** *24*, 3765.

27. Kriegel, I.; Rodriguez-Fernandez, J.; Wisnet, A.; Zhang, H.; Waurisch, C.; Eychmuller, A.; Dubavik, A.; Govorov, A. O.; Feldmann, J. Shedding Light on Vacancy-Doped Copper Chalcogenides: Shape-Controlled Synthesis, Optical Properties, and Modeling of Copper Telluride Nanocrystals with Near-Infrared Plasmon Resonances. *ACS Nano* **2013,** *7*, 4367.

28. Hartstein, K. H.; Brozek, C. K.; Hinterding, S. O. M.; Gamelin, D. R. Copper-Coupled Electron Transfer in Colloidal Plasmonic Copper-Sulfide Nanocrystals Probed by in Situ Spectroelectrochemistry. *J. Am. Chem. Soc.* **2018,** *140*, 3434.

29. Gan, X. Y.; Crawford, S. E.; Eikey, E. A.; Sen, R.; Killinger, J. R.; Millstone, J. E. Optoelectronic Impacts of Particle Size in Water-Dispersible Plasmonic Copper Selenide Nanoparticles. *J. Phys. Chem. C* **2020,** *124*, 4747.

30. Della Valle, G.; Scotognella, F.; Kandada, A. R. S.; Zavelani-Rossi, M.; Li, H.; Conforti, M.; Longhi, S.; Manna, L.; Lanzani, G.; Tassone, F. Ultrafast Optical Mapping of Nonlinear Plasmon Dynamics in $Cu_{2-x}Se$ Nanoparticles. *J. Phys. Chem. Lett.* **2013,** *4*, 3337.

31. Gan, X. Y.; Keller, E. L.; Warkentin, C. L.; Crawford, S. E.; Frontiera, R. R.; Millstone, J. E. Plasmon-Enhanced Chemical Conversion Using Copper Selenide Nanoparticles. *Nano Lett.* **2019,** *19*, 2384.

32. Scotognella, F.; Della Valle, G.; Srimath Kandada, A. R.; Dorfs, D.; Zavelani-Rossi, M.; Conforti, M.; Miszta, K.; Comin, A.; Korobchevskaya, K.; Lanzani, G.; Manna, L.; Tassone, F. Plasmon Dynamics in Colloidal $Cu_{2-x}Se$ Nanocrystals. *Nano Lett.* **2011,** *11*, 4711.

33. De Trizio, L.; Gaspari, R.; Bertoni, G.; Kriegel, I.; Moretti, L.; Scotognella, F.; Maserati, L.; Zhang, Y.; Messina, G. C.; Prato, M.; Marras, S.; Cavalli, A.; Manna, L. $Cu_{3-x}P$ Nanocrystals as a Material Platform for Near-Infrared Plasmonics and Cation Exchange Reactions. *Chem. Mater.* **2015,** *27*, 1120.

34. Bertoni, G.; Ramasse, Q.; Brescia, R.; De Trizio, L.; De Donato, F.; Manna, L. Direct Quantification of Cu Vacancies and Spatial Localization of Surface Plasmon Resonances in Copper Phosphide Nanocrystals. *ACS Mater. Lett.* **2019,** *1*, 665.

35. Riha, S. C.; Johnson, D. C.; Prieto, A. L. Cu_2Se Nanoparticles with Tunable Electronic Properties Due to a Controlled Solid-State Phase Transition Driven by Copper Oxidation and Cationic Conduction. *J. Am. Chem. Soc.* **2011,** *133*, 1383.

36. Olofsson, O. The Crystal Structure of Cu_3P. *Acta Chem. Scand.* **1972,** *26*, 2777.

37. Schlenger, H.; Jacobs, H.; Juza, R. Ternäre Phasen des Lithiums mit Kupfer und Phosphor. *Z. Anorg. Allg. Chem.* **1971,** *385*, 177.

38. Furo, I.; Bakonyi, I.; Tompa, K.; Zsoldos, E.; Heinmaa, I.; Alla, M.; Lippmaa, E. ^{31}P Nuclear Magnetic Resonance Knight Shift and Linewidth in Ni_3P and Cu_3P: A Magic-Angle Spinning Study. *J. Phys. Condens. Matter* **1990,** *2*, 4217.

39. Wolff, A.; Pallmann, J.; Boucher, R.; Weiz, A.; Brunner, E.; Doert, T.; Ruck, M. Resource-Efficient High-Yield Ionothermal Synthesis of Microcrystalline $Cu_{3-x}P$. *Inorg. Chem.* **2016,** *55*, 8844.

40. Wolff, A.; Doert, T.; Hunger, J.; Kaiser, M.; Pallmann, J.; Reinhold, R.; Yogendra, S.; Giebeler, L.; Sichelschmidt, J.; Schnelle, W.; Whiteside, R.; Nimal Gunaratne, H. Q.; Nockemann, P.; Weigand, J. J.; Brunner, E.; Ruck, M. Low-Temperature Tailoring of Copper-Deficient $Cu_{3-x}P$ — Electric Properties, Phase Transitions, and Performance in Lithium-Ion Batteries. *Chem. Mater.* **2018,** *30*, 7111.

41. Crosnier, O.; Nazar, L. F. Facile Reversible Displacement Reaction of Cu_3P with Lithium at Low Potential. *Electrochem. Solid St.* **2004,** *7*, A187.

42. Koh, S.; Kim, W. D.; Bae, W. K.; Lee, Y. K.; Lee, D. C. Controlling Ion-Exchange Balance and Morphology in Cation Exchange from $Cu_{3-x}P$ Nanoplatelets into InP Crystals. *Chem. Mater.* **2019,** *31*, 1990.

43. Wei, S.; Qi, K.; Jin, Z.; Cao, J.; Zheng, W.; Chen, H.; Cui, X. One-Step Synthesis of a Self-Supported Copper Phosphide Nanobush for Overall Water Splitting. *ACS Omega* **2016,** *1*, 1367.

44. Tappan, B. A.; Chen, K.; Lu, H.; Sharada, S. M.; Brutchey, R. L. Synthesis and Electrocatalytic HER Studies of Carbene-Ligated $Cu_{3-x}P$ Nanocrystals. *ACS Appl. Mater. Interfaces* **2020,** *12*, 16394.

45. Kumar, S.; Aziz, S. K. T.; Kumar, S.; Riyajuddin, S.; Yaniv, G.; Meshi, L.; Nessim, G. D.; Ghosh, K. Three-Dimensional Graphene-Decorated Copper-Phosphide (Cu_3P@3DG) Heterostructure as an Effective Electrode for a Supercapacitor. *Front. Mater.* **2020,** *7*, 30.

46. Sun, T.; Wang, Y.; Yu, W.; Wang, Y.; Dai, Z.; Liu, Z.; Shivananju, B. N.; Zhang, Y.; Fu, K.; Shabbir, B.; Ma, W.; Li, S.; Bao, Q. Flexible Broadband Graphene Photodetectors Enhanced by Plasmonic $Cu_{3-x}P$ Colloidal Nanocrystals. *Small* **2017,** *13*, 1701881.

47. Liu, Y.; Wu, J.; Jin, Y.; Zhen, W.; Wang, Y.; Liu, J.; Jin, L.; Zhang, S.; Zhao, Y.; Song, S.; Yang, Y.; Zhang, H. Copper(I) Phosphide Nanocrystals for In Situ Self-Generation Magnetic Resonance Imaging-Guided Photothermal-Enhanced Chemodynamic Synergetic Therapy Resisting Deep-Seated Tumor. *Adv. Funct. Mater.* **2019,** *29*, 1904678.

48. Sheets, E. J.; Yang, W.-C.; Balow, R. B.; Wang, Y.; Walker, B. C.; Stach, E. A.; Agrawal, R. An in Situ Phosphorus Source for the Synthesis of Cu_3P and the Subsequent Conversion to Cu_3PS_4 Nanoparticle Clusters. *J. Mater. Res.* **2015,** *30*, 3710.

49. Lee, J. M.; Kraynak, L. A.; Prieto, A. L. A Directed Route to Colloidal Nanoparticle Synthesis of the Copper Selenophosphate Cu_3PSe_4. *Angew. Chem. Int. Ed.* **2020,** *59*, 3038.

50. Su, H. L.; Xie, Y.; Li, B.; Liu, X. M.; Qian, Y. T. A Simple, Convenient, Mild Solvothermal Route to Nanocrystalline Cu_3P and Ni_2P. *Solid State Ionics* **1999,** *122*, 157.

51. Xie, Y.; Su, H. L.; Qian, X. F.; Liu, X. M.; Qian, Y. T. A Mild One-Step Solvothermal Route to Metal Phosphides (Metal = Co, Ni, Cu). *J. Solid State Chem.* **2000,** *149*, 88.

52. Liu, S.; Qian, Y.; Xu, L. Synthesis and Characterization of Hollow Spherical Copper Phosphide (Cu_3P) Nanopowders. *Solid State Commun.* **2009,** *149*, 438.

53. Henkes, A. E.; Schaak, R. E. Trioctylphosphine: A General Phosphorus Source for the Low-Temperature Conversion of Metals into Metal Phosphides. *Chem. Mater.* **2007,** *19*, 4234.

54. De Trizio, L.; Figuerola, A.; Manna, L.; Genovese, A.; George, C.; Brescia, R.; Saghi, Z.; Simonutti, R.; Van Huis, M.; Falqui, A. Size-Tunable, Hexagonal Plate-like Cu_3P and Janus-like Cu–Cu_3P Nanocrystals. *ACS Nano* **2012,** *6*, 32.

55. Manna, G.; Bose, R.; Pradhan, N. Semiconducting and Plasmonic Copper Phosphide Platelets. *Angew. Chem. Int. Ed.* **2013,** *52*, 6762.

56. Liu, Z.; Mu, H.; Xiao, S.; Wang, R.; Wang, W.; Wang, Y.; Zhu, X.; Lu, K.; Zhang, H.; Lee, S.-T.; Bao, Q.; Ma, W. Pulsed Lasers Employing Solution-Processed Plasmonic $Cu_{3-x}P$ Colloidal Nanocrystals. *Adv. Mater.* **2016,** *28*, 3535.

57. Liu, J.; Meyns, M.; Zhang, T.; Arbiol, J.; Cabot, A.; Shavel, A. Triphenyl Phosphite as the Phosphorus Source for the Scalable and Cost-Effective Production of Transition Metal Phosphides. *Chem. Mater.* **2018,** *30*, 1799.

58. Song, W.-S.; Lee, H.-S.; Lee, J. C.; Jang, D. S.; Choi, Y.; Choi, M.; Yang, H. Amine-Derived Synthetic Approach to Color-Tunable InP/ZnS Quantum Dots with High Fluorescent Qualities. *J. Nanopart. Res.* **2013,** *15*, 1750.

59. Tessier, M. D.; Dupont, D.; De Nolf, K.; De Roo, J.; Hens, Z. Economic and Size-Tunable Synthesis of InP/ZnE (E = S, Se) Colloidal Quantum Dots. *Chem. Mater.* **2015,** *27*, 4893.

60. Tessier, M. D.; De Nolf, K.; Dupont, D.; Sinnaeve, D.; De Roo, J.; Z, H. Aminophosphines: A Double Role in the Synthesis of Colloidal Indium Phosphide Quantum Dots. *J. Am. Chem. Soc.* **2016,** *138*, 5923.

61. Buffard, A.; Dreyffuss, S.; Nadal, B.; Heuclin, H.; Xu, X.; Patriarche, G.; Mézailles, N.; Dubertret, B. Mechanistic Insight and Optimization of InP Nanocrystals Synthesized with Aminophosphines. *Chem. Mater.* **2016,** *28*, 5925.

62. Laufersky, G.; Bradley, S.; Frécaut, E.; Lein, M.; Nann, T. Unraveling Aminophosphine Redox Mechanisms for Glovebox-Free InP Quantum Dot Syntheses. *Nanoscale* **2018,** *10*, 8752.

63. McMurtry, B. M.; Qian, K.; Teglasi, J. K.; Swarnakar, A. K.; De Roo, J.; Owen, J. S. Continuous Nucleation and Size Dependent Growth Kinetics of Indium Phosphide Nanocrystals. *Chem. Mater.* **2020,** *32*, 4358.

64. Mundy, M. E.; Ung, D.; Lai, N. L.; Jahrman, E. P.; Seidler, G. T.; Cossairt, B. M. Aminophosphines as Versatile Precursors for the Synthesis of Metal Phosphide Nanocrystals. *Chem. Mater.* **2018,** *30*, 5373.

65. Grigel, V.; Dupont, D.; De Nolf, K.; Hens, Z.; Tessier, M. D. InAs Colloidal Quantum Dots Synthesis via Aminopnictogen Precursor Chemistry. *J. Am. Chem. Soc.* **2016,** *138*, 13485.

66. Srivastava, V.; Janke, E. M.; Diroll, B. T.; Schaller, R. D.; Talapin, D. V. Facile, Economic and Size-Tunable Synthesis of Metal Arsenide Nanocrystals. *Chem. Mater.* **2016,** *28*, 6797.

67. Srivastava, V.; Dunietz, E.; Kamysbayev, V.; Anderson, J. S.; Talapin, D. V. Monodisperse InAs Quantum Dots from Aminoarsine Precursors: Understanding the Role of Reducing Agent. *Chem. Mater.* **2018,** *30*, 3623.

68. Zhao, T.; Oh, N.; Jishkariani, D.; Zhang, M.; Wang, H.; Li, N.; Lee, J. D.; Zeng, C.; Muduli, M.; Choi, H.-J.; Su, D.; Murray, C. B.; Kagan, C. R. General Synthetic Route to High-Quality Colloidal III–V Semiconductor Quantum Dots Based on Pnictogen Chlorides. *J. Am. Chem. Soc.* **2019,** *141*, 15145.

69. Ginterseder, M.; Franke, D.; Perkinson, C. F.; Wang, L.; Hansen, E. C.; Bawendi, M. G. Scalable Synthesis of InAs Quantum Dots Mediated through Indium Redox Chemistry. *J. Am. Chem. Soc.* **2020,** *142*, 4088.

70. Luiz, T.; Sudheendra Rao, M. N.; Varghese, B. Synthesis and X-ray Structural Characterization of (Diisopropylamino)(Morpholino)(Phenyl)Phosphine and its Dimeric Copper(I). *Synth. React. Inorg. M.* **2007,** *37*, 669.

71. Ganesamoorthy, C.; Balakrishna, M. S.; George, P. P.; Mague, J. T. Di- and Tetranuclear Copper(I) Complexes Containing Phenylaminobis(phosphonite), $PhN\{P(OC_6H_4OMe\text{-}o)_2\}_2$, and Their Reactivity toward Bipyridyl Ligands. *Inorg. Chem.* **2007,** *46*, 848.

72. Punji, B.; Mague, J. T.; Balakrishna, M. S. Group 11 Metal Complexes of the Mesocyclic Thioether Aminophosphonites [-$OC_{10}H_6$(μ-S)$C_{10}H_6O$-]PNC_4H_8E (E = O, NMe). *Eur. J. Inorg. Chem.* **2007,** *2007*, 720.

73. Luiz, T. ^{31}P NMR Spectroscopic Studies of Copper (I) Aminophosphine Complexes. *Rasayan J. Chem.* **2015,** *8*, 13.

74. Tarassoli, A.; Curtis Haltiwanger, R.; Norman, A. D. Isolation, X-Ray Structure and Solution Behavior of Tris(anilino)phosphine: $(C_6H_5NH)_3P$. *Inorganic and Nuclear Chemistry Letters* **1980,** *16*, 27.

75. Gopalakrishnan, J. Aminophosphines: Their Chemistry and Role as Ligands and Synthons. *Appl. Organomet. Chem.* **2009,** *23*, 291.

76. LaMer, V. K.; Dinegar, R. H. Theory, Production and Mechanism of Formation of Monodispersed Hydrosols. *J. Am. Chem. Soc.* **1950,** *72*, 4847.

77. Yin, Y.; Alivisatos, A. P. Colloidal Nanocrystal Synthesis and the Organic–Inorganic Interface. *Nature* **2005,** *437*, 664.

78. Whitehead, C. B.; Özkar, S.; Finke, R. G. LaMer's 1950 Model for Particle Formation of Instantaneous Nucleation and Diffusion-Controlled Growth: A Historical Look at the Model's Origins, Assumptions, Equations, and Underlying Sulfur Sol Formation Kinetics Data. *Chem. Mater.* **2019,** *31*, 7116.

79. Yang, H. R.; Hamachi, L. S.; Rreza, I.; Wang, W.; Chan, E. M. Design Rules for One-Step Seeded Growth of Nanocrystals: Threading the Needle between Secondary Nucleation and Ripening. *Chem. Mater.* **2019,** *31*, 4173.

80. Strach, M.; Mantella, V.; Pankhurst, J. R.; Iyengar, P.; Loiudice, A.; Das, S.; Corminboeuf, C.; van Beek, W.; Buonsanti, R. Insights into Reaction Intermediates to Predict Synthetic Pathways for Shape-Controlled Metal Nanocrystals. *J. Am. Chem. Soc.* **2019,** *141*, 16312.

81. Wade, S. R.; Willey, G. R. Co-ordination Studies of Tris(dimethylamino)phosphine Oxide: Reactions with the Covalent Metal Halides MCl_3 (M = Ti, V and Cr), MCl_4 (M = Ti, Zr, Hf and Sn) and SnI_4. *Journal of Inorganic and Nuclear Chemistry* **1980,** *42*, 1133.

82. Momma, K.; Izumi, F. VESTA 3 for Three-Dimensional Visualization of Crystal, Volumetric and Morphology Data. *J. Appl. Cryst.* **2011,** *44*, 1272.

83. Fulmer, G. R.; Miller, A. J. M.; Sherden, N. H.; Gottlieb, H. E.; Nudelman, A.; Stoltz, B. M.; Bercaw, J. E.; Goldberg, K. I. NMR Chemical Shifts of Trace Impurities: Common Laboratory Solvents, Organics, and Gases in Deuterated Solvents Relevant to the Organometallic Chemist. *Organometallics* **2010,** *29*, 2176.

CHAPTER 3. Redox Chemistries and Plasmonic Tunability of Vacancy-Doped Copper Phosphide Nanocrystals

3.1 Abstract

Copper phosphide ($Cu_{3-x}P$) nanocrystals are promising materials for nanoplasmonics due to their sub-stoichiometric composition, enabling the generation and stabilization of excess delocalized holes and leading to localized surface plasmon resonance (LSPR) absorption in the near-IR. We present three copper-coupled redox chemistries that allow post-synthetic modulation of the delocalized hole concentrations and corresponding LSPR absorption in colloidal $Cu_{3-x}P$ nanocrystals. Changes in the structural, optical, and compositional properties are evaluated by powder X-ray diffraction, electronic absorption spectroscopy, ^{31}P magic-angle spinning solid-state nuclear magnetic resonance spectroscopy and elemental analysis. The redox chemistries presented herein can be used to access nanocrystals with LSPR energies of 660–890 meV, a larger range than has been possible through synthetic tuning. In addition to utilizing previously reported redox chemistries used for copper chalcogenide nanocrystals, we show that largest structural and LSPR modulation is achieved through the use of a divalent metal halide and trioctylphosphine. Specifically, nanocrystals treated with zinc iodide and trioctylphosphine have the smallest reported unit-cell volume (295.2 $Å^3$) and most downfield ^{31}P chemical shift (+346 ppm) reported for $P6_3cm$ $Cu_{3-x}P$. Overall, these redox chemistries present valuable insight into controlling the optical and structural properties of $Cu_{3-x}P$.

3.2 Introduction

$Cu_{3-x}P$ has drawn increased attention in recent years for use in an array of applications including lithium-ion batteries,[1-2] catalysis,[3-4] photodetection,[5] supercapacitors,[6] chemodynamic therapy,[7] cation exchange,[8-9] and as a precursor to ternary copper chalcophosphates used in photovoltaics.[10-11] The intrinsic non-stoichiometry arising from copper vacancies in $Cu_{3-x}P$ has been computationally predicted to span a range of $0.17 < x < 0.33$,[8] consistent with compositions experimentally validated by elemental analysis.[12-13] The copper vacancies are charge-compensated by excess delocalized holes, which, at the nanoscale, yield an emergent localized surface plasmon resonance (LSPR) absorption in the near-IR.[8, 14-17] Despite this intrinsically hole-doped nature, strategies for dynamic redox tuning of the carrier density that have been widely demonstrated in other colloidal semiconductor nanocrystal systems[18-32] have not yet been applied to $Cu_{3-x}P$. The ability to modulate $Cu_{3-x}P$ carrier density may allow its extension to nanoplasmonic applications based on the plasmon-enhanced chemical conversion,[33] ultrafast optical switching,[34-35] and surface-enhanced Raman scattering[36] which have already been demonstrated for an analogous class of materials, copper chalcogenide (CuE or $Cu_{2-x}E$; E = S, Se, Te) nanocrystals.

Electronically doped colloidal semiconductor nanocrystals[18, 37-41] typically exhibit charge-carrier modulation upon post-synthetic redox or photo-redox manipulation,[18, 27, 37, 42-43] or via synthetically controlled defect incorporation and activation.[18-26] Carrier-density-tuning, most typically achieved through post-synthetic redox treatments, has been demonstrated for copper chalcogenides,[21, 25, 28-29, 31, 44-48] which also support delocalized holes to compensate copper vacancies. In contrast to the copper chalcogenides, which have shown phase-transformations with dynamic redox tuning,[49] $Cu_{3-x}P$ has only one copper-rich phase at ambient conditions. This phase-

stability as well as the potential for distinct surface chemistry make $Cu_{3-x}P$ a unique system for colloidal semiconductor nanoplasmonics.

Here, we develop three anaerobic, post-synthetic, redox chemistries for colloidal $Cu_{3-x}P$ nanocrystals and characterize the corresponding changes to their optical and structural properties using electronic absorption spectroscopy, powder X-ray diffraction, ^{31}P magic-angle spinning solid-state nuclear magnetic resonance (MAS SSNMR) spectroscopy and elemental analysis. Two of the post-synthetic chemistries, reduction with Cu^+-ion and oxidation with iodine, have been applied to obtain similar copper-coupled redox modulation in copper chalcogenide nanocrystals.[28, 31, 44, 50-52] Additionally, a new post-synthetic redox treatment, which utilizes a divalent metal halide and trioctylphosphine (TOP) is shown to yield the greatest structural and optical changes. The post-synthetic chemistries and characterizations detailed in this study provide the groundwork for broad tunability of the composition and associated carrier density and optical properties of $Cu_{3-x}P$ nanocrystals.

3.3 Results and Analysis

$Cu_{3-x}P$ nanocrystals (Figure 3.1a) were synthesized via a previously developed one-pot heat-up reaction.[16] In a typical synthesis, a solution of copper chloride (CuCl, 0.800 mmol), tris(diethylamino)phosphine ($P(NEt_2)_3$, 1.12 mmol), oleylamine (OAm, 3.93 mmol), and trioctylamine (TOA, 6.71 ml) was prepared such that OAm/P/Cu = 4.9/1.4/1.0 and [Cu] = 0.100 M (Table S3.1). The solution was degassed under vacuum at 125 °C for 3 h and subsequently heated to a final temperature of T_f = 273 °C (Figure S3.1). Transmission electron microscopy (TEM) imaging of the resulting nanocrystals (Figure 3.1a) revealed an ensemble of nanoplatelets with a lateral dimension of 12.4 ± 0.7 nm (Figure 3.1b). The $P6_3cm$ phase of $Cu_{3-x}P$ was verified by powder X-ray diffraction (Figure 3.1c) and the absorption spectrum (Figure 3.1d) contains a

LSPR feature at 740 ± 20 meV, characteristic of $Cu_{3-x}P$.[8, 15-17] Scherrer analysis of the powder X-ray diffraction data (Figure 3.1c) indicates a crystallite lateral dimension of 11.9 ± 0.1 nm, with size agreement between TEM imaging and Scherrer analysis suggesting nanoplatelet single-crystallinity for the samples presented in this study (Table S3.2).

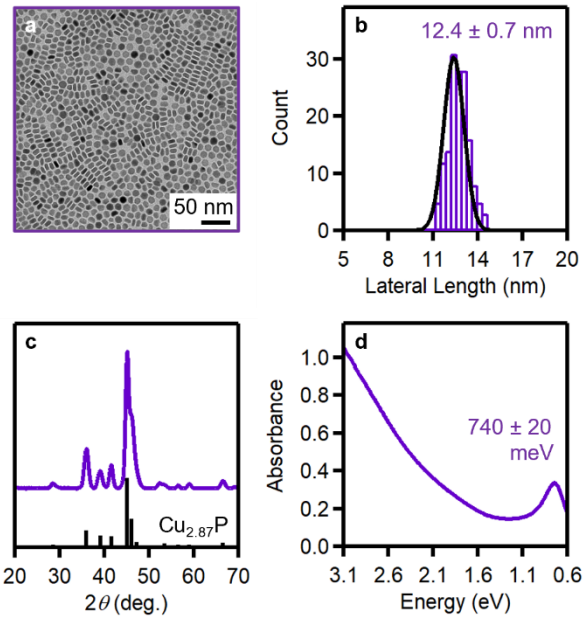

Figure 3. 1. Characterization of $Cu_{3-x}P$ nanocrystals (Synthesis 1, Table S3.1) synthesized with [Cu] = 0.100 M, OAm/P/Cu = 4.9/1.4/1.0 and T_f = 273 °C. **(a)** TEM image, **(b)** statistical analysis (n = 150) of lateral platelet dimension, **(c)** powder X-ray diffraction pattern (compared to that simulated for $P6_3cm$, ref. 12), and **(d)** average (n = 3) absorption spectrum.

Independent electronic absorption measurements on equal aliquots of the same $Cu_{3-x}P$ nanocrystal ensemble indicated non-negligible variation in the absorbance intensity (Figure S3.2). Although the concentrated $Cu_{3-x}P$ nanocrystal suspensions appeared as colloidal inks with no visible scattering or settling of solids, we hypothesize that aggregative platelet-stacking interactions led to suspension heterogeneity at the nanoscale, especially in more concentrated suspensions. More reliable intensities for the quantitative optical analyses of this study are thus reported as n = 3 average spectra (as with Figure 3.1d). To determine yield, $Cu_{3-x}P$ nanocrystals

were quantitatively digested in nitric acid and Cu^{2+} content was determined using the $^2E_g \rightarrow {}^2T_{2g}$ absorption (Figure S3.3). Synthesis 1 (Figure 3.1) had a yield of 75 ± 3% (based on Cu; Table S3.1), which is in agreement with elemental analysis of similarly synthesized $Cu_{3-x}P$ nanocrystals.[16] This yield was used to determine the extinction coefficient based on Cu of $\varepsilon_{3.1eV}^{Cu}$ = $2100 \pm 200 \frac{L}{mol\ Cu \times cm}$.

Measures taken to minimize inter-ensemble variation included the use of a reproducible reaction heating profile (Figure S3.1) and identical reaction composition (Table S3.1), within massing error, as these variables are known to influence nanocrystal size and/or LSPR energy in aminophosphine-based $Cu_{3-x}P$ syntheses.[16] The yields, average absorption spectra, and lateral dimensions for the ensembles (Table S3.1, Syntheses 1–5; Figures S3.4, S3.5i, S3.6a) were the same, within experimental error of < 12%, justifying the formulation of post-redox cross-ensemble comparisons.

The first redox chemistry investigated was oxidation by iodine (I_2), as it has been established to act as a copper-coupled oxidant of copper chalcogenide nanocrystals.[44, 51-52] In contrast to previous studies in which I_2 and nanocrystals were mixed as solutions on the cuvette-scale, a toluene suspension of an entire batch of $Cu_{3-x}P$ nanocrystals was oxidized with I_2 solid under static vacuum for 20 h without direct contact (Figure S3.7). The oxidized $Cu_{3-x}P$ nanocrystals were purified by addition of acetonitrile (MeCN) and collection by centrifugation. After oxidation, the $Cu_{3-x}P$ nanocrystal ensemble exhibited a blueshift of 80 meV with respect to the as-synthesized LSPR energy of the same ensemble (Figures 3.2a, S3.8i; Table S3.3), indicating an increase in the delocalized hole concentration. TEM images of the purified nanocrystals reveal that the size and morphology were unchanged after oxidation (Figure S3.5a). Powder X-ray diffraction indicated retention of the *P*6$_3$*cm* $Cu_{3-x}P$ phase after oxidation with I_2 (Figure S3.9i).

The purified nanocrystals were quantitatively digested, and absorption spectra of the resulting solutions were used to determine that the Cu-content of the oxidized nanocrystals was 93 ± 10 % of the sample prior to oxidation (Figure S3.10a, Table S3.3), suggesting that 7% of Cu atoms were removed from the lattice. This loss of Cu atoms is consistent with an increase in the concentration of delocalized holes evidenced by the blueshift of the LSPR absorption (Figure 3.2a). To corroborate this analysis, the supernatant collected during nanocrystal purification was evaporated and the resulting residue analyzed. Powder X-ray diffraction (Figure S3.11) revealed the presence of copper(I) iodide (CuI). Similar CuI formation was reported during the copper-coupled oxidation of copper sulfide nanocrystals.[44] Digestion and optical analysis of the residue indicates that 6.6% of Cu atoms were removed from the $Cu_{3-x}P$ nanocrystals and reacted to form CuI (Section S3.1, Figure S3.12), consistent with the amount of Cu lost based on analysis of the digested nanocrystals. These results indicate that oxidation with I_2 creates additional Cu vacancies that lead to delocalized holes without damaging the $Cu_{3-x}P$ nanocrystals.

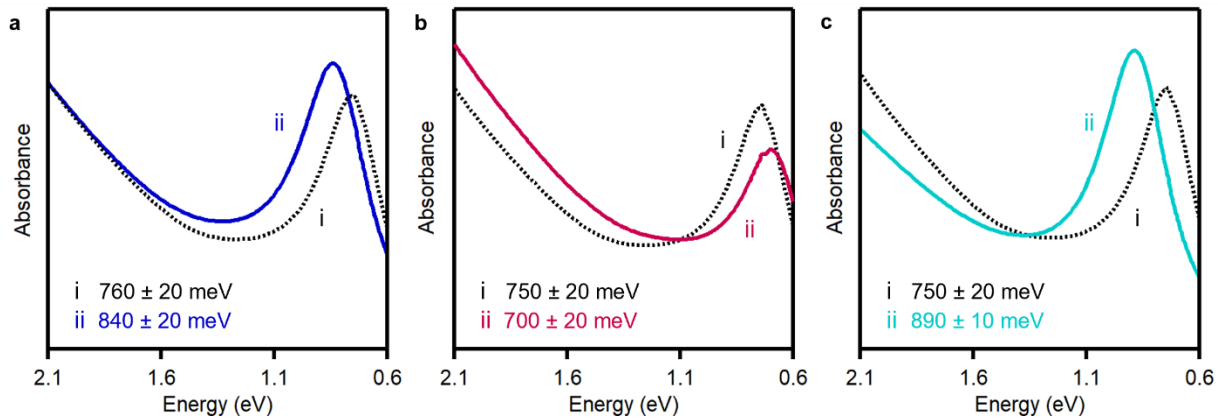

Figure 3. 2. Average (n = 3) absorption spectra of $Cu_{3-x}P$ nanocrystals **(i)** before and **(ii)** after **(a)** oxidation with I_2, **(b)** reduction with Cu^+, and **(c)** oxidation with ZnI_2/TOP. Ensembles from Syntheses 2−4 (Table S3.1) were used for these experiments.

The second redox treatment investigated was reduction with Cu^+, as tetrakis(acetonitrile)copper(I) hexafluorophosphate ($[Cu(MeCN)_4]PF_6$) has been shown to act as a copper-coupled reductant for copper chalcogenide nanocrystals.[28, 31, 50] In a modification of a previously reported procedure,[31] methanol (MeOH), OAm, and $[Cu(MeCN)_4]PF_6$ solid were added directly to a diluted $Cu_{3-x}P$ nanocrystal suspension ($[Cu_{total}]$ = 0.043 M, MeOH/OAm/Cu_{PF6}/Cu_{Cu3-xP} = 7.84/0.48/0.24/1.00) and stirred at ambient temperature for 20 h. The reduced $Cu_{3-x}P$ nanocrystals were purified by precipitation with MeCN and collection via centrifugation. After reaction with Cu^+, the $Cu_{3-x}P$ nanocrystal ensemble exhibited a redshift of 50 meV with respect to the as-synthesized LSPR energy for the same ensemble (Figures 3.2b, S3.8ii; Table S3.3). TEM revealed that $Cu_{3-x}P$ nanoplatelet size and morphology were unchanged after reduction (Figure S3.5b). The $P6_3cm$ phase of $Cu_{3-x}P$ was maintained by powder X-ray diffraction after reduction (Figure S3.9ii). The purified nanocrystals were digested and analyzed to yield a post-reduction Cu-atom content of 94 ± 13 % relative to the original ensemble (Figure S3.10b, Table S3.3). The supernatant collected following purification was concentrated to give an oil. Surprisingly, electronic absorption spectroscopy of the oil (Figure S3.13a) did not reveal Cu^{2+}, which has been observed as a byproduct when copper sulfide nanocrystals were reduced with Cu^+.[31] When this solution was exposed to air, Cu^{2+} was observed (Figure S3.13b), indicating that the anaerobic supernatant contained primarily Cu^+. Quantitative analysis of this absorption feature (Section S3.2, Figure S3.14) indicated a loss of Cu atoms relative to the amount of $[Cu(MeCN)_4]PF_6$ added to the solution. This loss suggests that Cu atoms were inserted into the nanocrystals upon reduction, corresponding to an increase in Cu-content of 2.5%. The supernatant oil was also analyzed by ^{31}P and ^{19}F NMR spectroscopy to probe the PF_6^- environment (Figure S3.15). When the oil was intentionally exposed to air, signal broadening was observed for the

resonance in both the ^{31}P and ^{19}F spectra, corroborating the oxidation of diamagnetic Cu^{+} to paramagnetic Cu^{2+} upon air-exposure.

The third redox chemistry presented is an apparent oxidation that occurs when $Cu_{3-x}P$ nanocrystals are heated in the presence of both zinc iodide (ZnI_2) and TOP. TOP has previously been shown to extract Cu atoms from $Cu_{3-x}P$ nanocrystals.[8-9] Additionally, Z-type ligands have recently been demonstrated to passivate hole traps of indium phosphide nanocrystal surfaces.[53] In this treatment, a mixture of $Cu_{3-x}P$ nanocrystals, OAm, ZnI_2, and TOP ([Cu] = 0.078 M, TOP/Zn/OAm/Cu = 16.0/4.0/3.0/1.0) was stirred at 100 °C for 20 h. The $Cu_{3-x}P$ nanocrystals were purified by precipitation with MeCN and collection via centrifugation. After reaction with ZnI_2/TOP, the nanocrystal ensemble exhibited a blueshift of 140 meV with respect to the as-synthesized LSPR energy for the same ensemble (Figures 3.2c, S3.8iii; Table S3.3). This blueshift is indicative of the generation of additional delocalized holes, consistent with oxidation of the nanocrystals. TEM of the treated $Cu_{3-x}P$ nanocrystals indicated that the size and morphology were unchanged (Figure S3.5c). Powder X-ray diffraction revealed that the $Cu_{3-x}P$ nanocrystals retained their $P6_3cm$ phase after being treated with ZnI_2 and TOP (Figure S3.9iii). The purified nanocrystals were digested and analyzed, revealing a post-redox Cu-atom content of 74 ± 12% relative to the original ensemble (Figure S3.10c, Table S3.3). Again, the loss of Cu atoms is consistent with an increase in delocalized hole concentration evidenced by absorption spectroscopy (Figure 3.2c). The supernatant collected during purification was concentrated, and the resulting oil was analyzed for Cu content. In this case, no Cu^{2+} could be detected by absorption spectroscopy, even after intentional air-exposure (Figure S3.16i). This observation alone does not rule out the possibility of copper-coupled oxidation and Cu-atom extraction, as it is likely that any Cu is ligated by TOP, keeping it in the +1 oxidation state. This assertion is supported by the absence of Cu^{2+} absorption

when a control solution containing CuI and TOP is exposed to air (Figure S3.16ii). Furthermore, ^{31}P NMR experiments on the supernatant indirectly suggest the presence of Cu (Section S3.3, Figure S3.17). The unchanged nanoplatelet size together with a statistically significant loss of Cu following treatment are indicators that oxidation using ZnI_2 and TOP is possibly copper-coupled. More direct evidence of Cu-atom extraction is provided by analysis of the structural data (*vide infra*).

$Cu_{3-x}P$ has been proposed as an anode material for lithium-ion batteries on account of its ability to accommodate, to an extent, the electrochemical insertion of Li^+ without substantial reorganization of the P-sublattice.[1-2] We expected that Li^+-compensated chemical reduction of $Cu_{3-x}P$ nanocrystals would be energetically favorable, given the driving force of 3.8 V, based on the Li/Li^+ reduction potential and reported valence band potential of $Cu_{3-x}P$.[15] Furthermore Li^+-compensated reduction may be expected to support more extensive chemical reduction than that attainable with copper-coupled reactions due to the differences in the bulk material compositions of copper phosphide and its ternary phase with lithium. Specifically, the entire $Cu_{3-x}P$ homogeneity range is predicted to be sub-stiochiometric by density function theory (DFT),[8] whereas Li_2CuP is fully stiochiometric.[13, 54] Attempts to heterogeneously reduce $Cu_{3-x}P$ nanocrystals with Li^0 in a toluene suspension yielded no LSPR shift after 72 h, although colloidal stability was retained. Since toluene may not facilitate Li^+-transfer, we then attempted a similar reduction in 1:6.8 THF:toluene since ethers are known to coordinate to Li^+.[55] This reduction in toluene/THF led to irreversible aggregation after 20 h and exhibited only a statistically insignificant redshift of the LSPR prior to aggregation (Figure S3.18). TEM revealed that $Cu_{3-x}P$ nanoplatelet size and morphology were unchanged following reduction in toluene/THF (Figure S3.6). After optical characterization, the $Cu_{3-x}P$ nanocrystals were purified by precipitation with MeCN and collection

via centrifugation. Powder X-ray diffraction revealed (1) that the $Cu_{3-x}P$ nanocrystals retained their $P6_3cm$ phase after reduction with Li^0 and (2) that the purification did not fully remove lithium chloride (LiCl) formed during the reduction (Figure S3.19). The nanocrystals were digested and analyzed, revealing a post-redox Cu-atom content of 95 ± 12% (Figure S3.10d, Table S3.3). These results indicate that reduction with Li^0 leads to aggregation, but not disintegration of the $Cu_{3-x}P$ nanocrystals. Homogeneous treatment of the nanocrystals with n-butyllithium (nBuLi) induced instantaneous aggregation after the addition of just 0.03 nBuLi/Cu, suggesting that aggregation is induced above a certain threshold of reduction, which is reached more rapidly in a homogeneous reaction. The aggregation problem was eliminated when nanocrystals were reduced with Li^0 in 1:28 OAm:toluene (OAm/Cu = 1.5), yielding nanocrystals in which the LSPR was redshifted 90 meV relative to the original ensemble. This redshift, however, spontaneously and rapidly reversed with a blueshift of 90 meV upon removal of excess Li metal (Figure S3.20), precluding reliable structural characterization of the reduced product.

Alternative oxidation chemistries with use of cerium(IV) and ferrocenium, which have been demonstrated for copper chalcogenides,[28, 44] also yield a LSPR peak blueshift for $Cu_{3-x}P$ nanocrystals with varying degrees of LSPR intensity loss (Figure S3.21a–c). These oxidation chemistries readily aggregated the $Cu_{3-x}P$ nanocrystals (Figure S3.21d,e) and were difficult to extend beyond the cuvette-scale. The remainder of our studies will thus focus only on the first three described treatments (oxidation with I_2, reduction with Cu^+ and oxidation with ZnI_2/TOP). Simplified Drude–Lorentz calculations (Section S3.4) were used to estimate a carrier-concentration range of N_h = 3.0–4.8 × 10^{21} cm^{-3} for the as-synthesized and redox-treated nanocrystals (Table 3.1), which agrees well with N_h = 3.8 × 10^{21} cm^{-3} determined from Hall measurements on bulk $Cu_{3-x}P$ films.[56]

Table 3. 1. Lattice parameters (*a* and *c*), unit-cell volumes, Cu/P molar ratios, LSPR maxima, delocalized hole carrier concentrations, and ^{31}P MAS SSNMR chemical shifts for $Cu_{3-x}P$ nanocrystal ensembles.

	E_{LSPR} (meV)	Drude N_h (10^{21} cm^{-3})[a]	a (Å)[b]	c (Å)[c]	Unit-Cell Volume (Å^3)	Cu/P[d]	V_{Cu} N_h (10^{21} cm^{-3})[e]	^{31}P δ (ppm)
Cu(I)	700 ± 20	3.0	6.970 ± 0.004	7.152 ± 0.006	300.9 ± 0.3	2.93 ± 0.02	1.5	+101
As-synthesized	740 ± 20	3.4	6.961 ± 0.001	7.154 ± 0.001	300.2 ± 0.1	2.90 ± 0.02	2.0	+186
I_2	840 ± 20	4.4	6.943 ± 0.003	7.150 ± 0.005	298.5 ± 0.3	2.82 ± 0.02	3.6	+256
ZnI_2/TOP	890 ± 10	4.8	6.917 ± 0.002	7.125 ± 0.003	295.2 ± 0.2	2.67 ± 0.02	6.7	+346

[a]Estimated from optical data and modelling (Section S3.4)
[b]Calculated using *d*-spacing of (3 0 0) reflection at $2\theta \approx 45°$
[c]Calculated using *a*-parameter and *d*-spacing of (2 −1 2) reflection at $2\theta \approx 36°$
[d]Estimated using the unit-cell volume and bulk $Cu_{3-x}P$ data (Figure S3.22)
[e]Estimated from diffraction-derived composition, unit-cell volume and assumption of 1 h^+/V_{Cu}

The removal/insertion of Cu in copper chalcogenides[21, 25, 28-29] and bulk $Cu_{3-x}P$ samples[1, 57] has been shown to lead to lattice contraction/expansion. Figure 3.3a shows the (300) reflection for the as-synthesized and redox-treated nanocrystals. Importantly, for nanocrystals that are expected to contain less Cu (i.e. are more oxidized), this reflection shifts to higher 2θ, indicating a lattice contraction. Analysis of the unit-cell parameters revealed that the lattice is more contracted for nanocrystals that show a higher-energy LSPR (Table 3.1). The calculated lattice parameters span a larger range for *a* than *c* (Table 3.1), which agrees with previously reported structural data for bulk $Cu_{3-x}P$.[12, 57] The calculated unit-cell volume range of 295.2–300.9 Å^3 (Table 3.1) contains the entire known bulk $P6_3cm$ $Cu_{3-x}P$ unit-cell volume range[1, 12] of 295.9–300.3 Å^3.

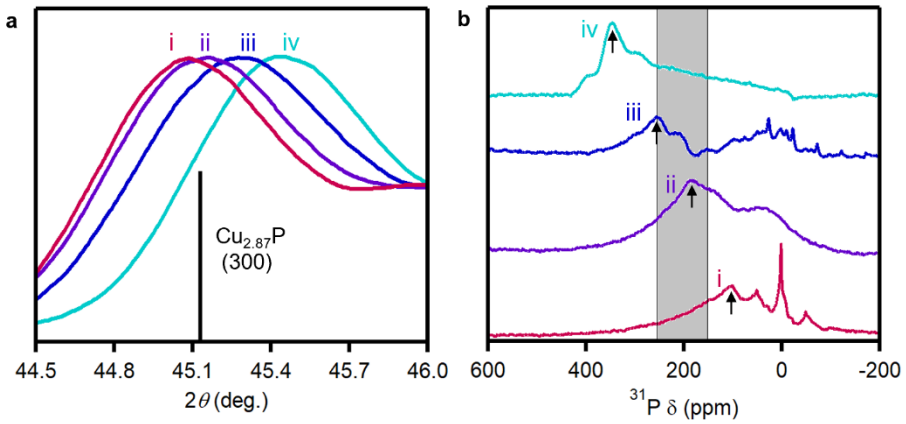

Figure 3. 3. (a) Magnified powder X-ray diffraction patterns (compared to that simulated for *P*6$_3$*cm*, ref. 12) and **(b)** ^{31}P MAS SSNMR spectra for $Cu_{3-x}P$ nanocrystal ensembles: (i) reduced-with-Cu^+, (ii) as-synthesized, (iii) oxidized-with-I_2, and (iv) oxidized-with-ZnI_2/TOP. Ensembles from Syntheses 1−4 (Table S3.1) were used for these experiments. The arrows indicate the chemical shifts where T_1 was measured. The shaded region corresponds to the bulk $Cu_{3-x}P$ Knight shift range reported in ref. 1.

As the lattice contraction is expected to depend directly on the number of Cu vacancies, the powder X-ray diffraction data can be used to extract compositional information, as has been demonstrated for Cu/Se ratios in substoichimetric copper selenide nanocrystals.[25] Unlike methods that rely on elemental analysis of digested nanocrystal samples, compositional analysis based on diffraction data should reflect only the crystalline domain of the nanocrystal core and neglect contributions from amorphous surface regions. In other words, the diffraction data is expected to largely be blind to whether the nanocrystal surfaces are Cu- or P-rich, and therefore provide vacancy concentrations that are representative of contributions to the LSPR energy. To extract compositional data, the relationship between unit-cell volume and Cu/P was derived empirically from values previously reported for bulk $Cu_{3-x}P$ (Figure S3.22).[12] This relationship was used to determine Cu/P values of the as-synthesized and redox-treated nanocrystals (Table 3.1). The estimated Cu/P range of 2.67–2.93 is consistent with that predicted by DFT calculations (2.67–2.83),[8] particularly at the copper-deficient limit. The assumption of one delocalized hole per

vacancy yields a delocalized-hole-density range of N_h = 1.5–6.7 × 10^{21} cm^{-3}, agreeing well with values based on optical modelling and Hall measurements on bulk films (*vide supra*).

SSNMR spectroscopy has recently been demonstrated as a sensitive technique for probing delocalized carrier densities in degenerately doped semiconductor nanocrystals, even when LSPR absorption is undetectable.[25] Specifically, ^{77}Se SSNMR was used to show that increased copper vacancies, or increased delocalized hole densities, led to a downfield Knight shift in substoichiometric copper selenide nanocrystals. Additionally, the nanocrystals exhibited Korringa behavior across a wide composition range. To our knowledge, nanoscale $Cu_{3-x}P$ has not yet been characterized by ^{31}P SSNMR, but an analogous downfield Knight shift for increased copper vacancies[1, 57] and Korringa behavior[58] have been demonstrated for bulk $Cu_{3-x}P$. Here, we use ^{31}P magic-angle spinning (MAS) SSNMR spectroscopy to provide additional correlation of structural and optical changes in as-synthesized and redox-treated $Cu_{3-x}P$ nanocrystals (Figure 3.3b). As expected, the nanocrystal spectra are broadened relative to those of the bulk.[1, 57] Furthermore, additional, often sharper resonances are present in the spectra of redox-treated nanocrystals, likely due to contributions from residual molecular redox and surface P-species. In the spectrum of the as-synthesized $Cu_{3-x}P$ nanocrystals (Figure 3.3bii), the most intense peak at +186 ppm falls within the reported chemical shift range for bulk $Cu_{3-x}P$.[1] Saturation recovery experiments performed at 300 K fit well to a single-exponential at 186 ppm (Figure S3.23a), yielding a spin–lattice relaxation time of T_1 = 15.5 ± 0.7 ms (Table S3.4). This value agrees well with that reported for bulk $Cu_{3-x}P$ (T_1 = 16 ms).[58] We thus assign the broad intense resonance indicated by the arrows (Figure 3.3b) to the nanocrystal "core."

The core resonance of redox-treated nanocrystals follows the expected Knight behavior; specifically, nanocrystals that are more oxidized, and thus have higher carrier densities, display a

more downfield shift of the core resonance (Figure 3.3b, Table 3.1). Saturation recovery experiments performed on redox-treated $Cu_{3-x}P$ nanocrystals (Figure S3.23b) at the indicated peaks did not fit well to single-exponential behavior, likely due to overlap with surface species formed during redox treatments, which preclude reliable extraction of spin–lattice relaxation times. Although the data could be fit to double-exponentials (Table S3.4) in which the fast component is likely derived primarily from the nanocrystal core, the extracted spin–lattice relaxation times do not follow the expected trend of decreasing T_1 with increasing ^{31}P δ (or increasing carrier density).

In systems with well-defined spin–lattice relaxation times, the ratio of carrier densities for two different compositions (N_h^a/N_h^b) can be determined from the inverse ratio of the corresponding spin–lattice relaxation times (T_1^b/T_1^a, Equation 3.1).[25, 59-61] Based on optical (Figure 3.2), structural (Figure 3.3a) and chemical shift data (Figure 3.3b), the largest difference in carrier density from the as-synthesized (ii) nanocrystals is expected to be seen in nanocrystals oxidized with ZnI_2 and TOP (iv). These oxidized nanocrystals have an estimated spin–lattice relaxation time of T_1^{iv} = 10.8 ± 0.4 ms, suggesting that the delocalized hole concentration is twice that of the as-synthesized nanocrystals ($N_h^{iv}/N_h^{ii} = 2.0$).

$$\frac{N_h^a}{N_h^b} = \left(\frac{T_1^b}{T_1^a}\right)^{3/2} \tag{3.1}$$

It is worth noting that characterizations of nanocrystals reduced with Li^0 in toluene/THF (Figures S3.18, S3.19, S3.23a, S3.24) indicate negligible redox with similar unit-cell volume, LSPR energy, and ^{31}P MAS SSNMR chemical shift and T_1 (Tables 3.1, S3.4) to the as-synthesized sample (Figures 3.1, 3.3ii).

The oxidation with ZnI_2 and TOP produced a notably larger LSPR energy shift, lattice parameter change, and ^{31}P SSNMR chemical shift than reduction with Cu^+ (Figures 3.2, 3.3; Table

3.1). The most likely explanation for this asymmetry is that the as-synthesized $Cu_{3-x}P$ nanocrystal composition with the standard synthetic conditions (Syntheses 1–8, Table S3.1) is closer to the copper-rich limit of the *P*6$_3$*cm* stoichiometry range. If the extent of copper-coupled redox is dependent on the as-synthesized nanocrystal copper content, then sufficiently copper-deficient $Cu_{3-x}P$ nanocrystals should exhibit a larger optical and structural change for reduction than oxidation. We have previously demonstrated that higher LSPR energy (corresponding to a more copper-deficient composition) can be attained by decreasing the synthesis temperature to decrease the reactivity during $Cu_{3-x}P$ nanocrystal nucleation.[16] To test our prediction, a low-temperature synthesis (20 h at T = 200 °C) of $Cu_{3-x}P$ nanocrystals with the standard reaction composition ([Cu] = 0.100 M, OAm/P/Cu = 4.9/1.4/1.0) was carried out (Synthesis 10, Table S3.1), and its product ensemble was used for post-synthetic redox experiments. In line with prediction, the resulting $Cu_{3-x}P$ nanocrystals, with as-synthesized LSPR energy of 880 meV, exhibited no LSPR shift upon oxidation with ZnI_2 and TOP and a substantial LSPR redshift of 120 meV upon reduction with Cu^+ (Figure S3.25a). Interestingly, in addition to retention of crystallinity after the redox experiments (Figure S3.25b), powder X-ray diffraction revealed a lattice contraction for the oxidation with ZnI_2/TOP (Figure S3.25c), despite the unchanged LSPR peak position. This suggests the possibility that some of the lattice contraction observed upon ZnI_2/TOP-treatment of the standard $Cu_{3-x}P$ nanocrystals (Figure 3.3aiv) might not be accompanied by vacancy-compensated delocalized hole formation. TEM imaging confirmed that nanoplatelet size and morphology were unchanged by the redox treatments (Figure S3.26).

An important feature of carrier-doped nanocrystals is the potential for reversible tuning of the carrier density. To demonstrate reversibility of oxidative treatments, $Cu_{3-x}P$ nanocrystals were oxidized with I_2 or ZnI_2/TOP, purified, and back-reduced with Cu^+. Figure 3.4 presents

characterization of the reversibility experiments of the most extensive oxidation treatment, ZnI_2/TOP. Similar to the oxidation shown in Figure 3.2c, the initial oxidation led to a 120-meV blueshift of the LSPR, from 740 ± 20 to 860 ± 10 (Figure 3.4a). Back-reduction with Cu^+ yielded a 160-meV-redshift of the LSPR to 700 ± 20 meV (Figure 3.4a). This final LSPR energy is consistent with that observed when as-synthesized nanocrystals were reduced with Cu^+ (Figure 3.2b), indicating that (1) oxidation with ZnI_2/TOP is reversible and (2) there is an intrinsic limit to the level of reduction feasible with a particular treatment (i.e. $E_{\mathrm{LSPR}}^{\mathrm{Cu,final}}$, rather than $\Delta E_{\mathrm{LSPR}}^{\mathrm{Cu}}$, is constant). Powder X-ray diffraction shows that crystallinity and the $P6_3cm$ phase are retained throughout oxidation and back-reduction (Figure 3.4b), and TEM revealed that $Cu_{3-x}P$ nanoplatelet size and morphology were unchanged following oxidation and back-reduction (Figure S3.27). The oxidation and reduction are accompanied by a lattice contraction and re-expansion (Figure 3.4c, Table S3.5), further indicating the reversibility of the ZnI_2/TOP oxidation. An analogous reversibility experiment was performed in which nanocrystals were oxidized with I_2 and back-reduced with Cu^+. These treatments also led to a reversible LSPR shift (Figure S3.28a) as well as lattice contraction and re-expansion (Figure S3.28b). $Cu_{3-x}P$ crystallinity and nanoplatelet size and morphology were unchanged, as evidenced by powder X-ray diffraction (Figure S3.28c) and TEM imaging (Figure S3.28d,e), respectively.

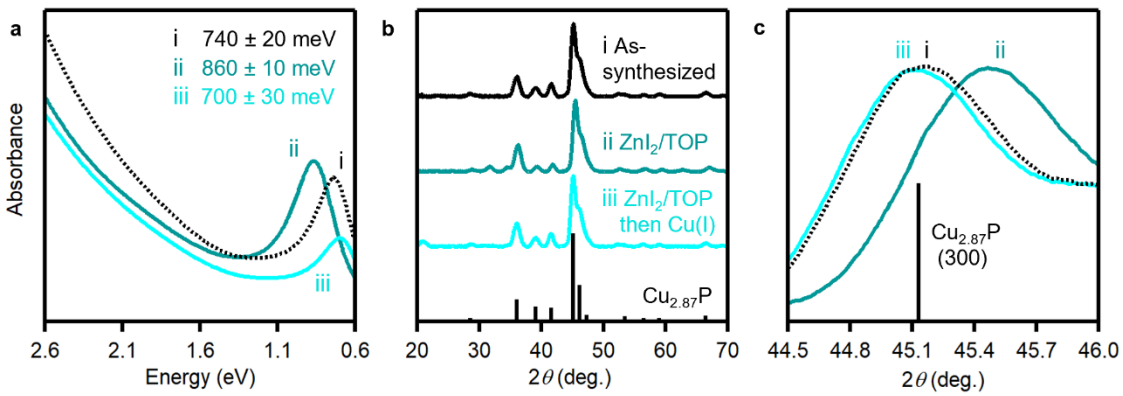

Figure 3. 4. Optical and structural characterization of $Cu_{3-x}P$ nanocrystals from an oxidation reversibility experiment using ZnI_2/TOP and Cu^+. **(a)** Absorption spectra and **(b)** full-scale and **(c)** magnified powder X-ray diffraction patterns compared to that simulated for *P*6$_3$*cm*, ref. 12. Data presented for (i) as-synthesized, (ii) ZnI_2/TOP-oxidized, and (iii) Cu^+-back-reduced ensembles. Nanocrystals from Synthesis 6 (Table S3.1) were used for this experiment.

Surprisingly, when the order of redox treatments was reversed (reduction followed by back-oxidation), reversibility was not maintained. Reduction with Cu^+, followed by back-oxidation with I_2, led to $Cu_{3-x}P$ degradation, as indicated by loss of crystallinity (Figure S3.29a), LSPR absorption (Figure S3.29b), and reduced particle contrast by TEM (Figure S3.29). An even more extensive degradation occurred when a Li/OAm-reduced-sample was re-oxidized with I_2 (Figure S3.30). These findings indicate that, while changes to the "core" of the $Cu_{3-x}P$ nanocrystals are, in principle reversible, incompatibility between successive redox experiments can lead to nanocrystal degradation, likely due to altered surfaces and leftover impurities from previous chemistries.

The reduced Cu-atom content of $Cu_{3-x}P$ nanocrystals after oxidation with ZnI_2 and TOP (Table S3.3), together with the retention of nanocrystal size and morphology (Figure S3.5c), correlated structural, optical, and ^{31}P SSNMR changes (Figures 3.2c, 3.3iv, S3.8), and reversible redox (Figure 3.4) suggest that the ZnI_2/TOP treatment is a copper-coupled oxidation. It is likely that Cu-atom removal is facilitated by TOP coordination to form copper(I) phosphine molecular

complexes, based as TOP is known to extract Cu from $Cu_{3-x}P$ nancorystals.[8-9] It is not expected, however, that either ZnI_2 or TOP are capable of oxidizing $Cu_{3-x}P$ nanocrystals. A set of control experiments indicated that the combined use of both TOP and a divalent metal salt is necessary for $Cu_{3-x}P$ oxidation. Specifically, a series of post-synthetic MX_2 (M = Zn, Cd; X = Cl, I, acetate) and/or TOP treatments were performed in which the M and X were changed, TOP and/or MX_2 were omitted, or fewer equiv of MX_2 and TOP were used. Detailed conditions are provided in Table S3.6. All nine experiments used the same ensemble (Synthesis 7, Table S3.1) and were heated in parallel at 100 °C for 20 h. TEM imaging revealed that $Cu_{3-x}P$ nanoplatelet size and morphology were unchanged for all MX_2 and TOP treatments (Figure S3.31) and powder X-ray diffraction verified the retention of crystallinity and the $P6_3cm$ phase for all experiments (Figure S3.32). It is worth noting that treatment with any zinc halide salt resulted in an additional, unassigned reflection in the powder X-ray diffraction pattern at $2\theta = 31.7°$ (Figure S3.9iii, Figure 3.4bii, Figure S3.32i,iv,vi). Attempts to oxidize with zinc acetate failed due to irreversible nanocrystal aggregation, precluding optical characterization.

Figure S3.33 presents the absorption spectra for the as-synthesized ensemble as well as each of the nine treatments. The largest blueshifts in the LSPR occurred for treatments with both MX_2 and TOP (TOP/M/Cu ≈ 15.5/3.9/1) and were independent of MX_2 identity (Figure S3.33i,ii,vi,vii). To highlight the differences among treatments, Figures 3.5a and S3.34a present the corresponding difference spectra with respect to the as-synthesized sample. The difference spectra for all MX_2/TOP treatments (Figures 3.5ai,ii, S3.34vi,vii) contain a positive-difference peak at higher energy, which is lower in intensity with smaller excess (Figure 3.5aiii) and absent with omission of MX_2 and/or TOP (Figures 3.5aiv, S3.34viii,ix). These data confirm a distinct optical response upon concerted oxidation with both MX_2 and TOP. Powder X-ray diffraction

revealed a lattice contraction upon oxidation, which increases with LSPR blueshift (Figures 3.5b, S3.34b, Table S3.5).

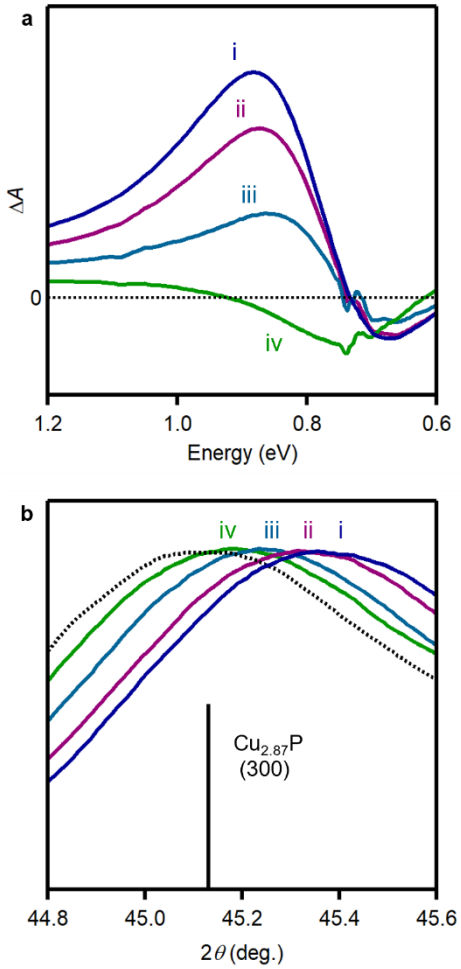

Figure 3. 5. Optical and structural characterizations for four highlighted cases of the nine post-synthetic MX_2/TOP (M = Zn, Cd; X = Cl, I) experiments (compositions detailed in Table S3.6). **(a)** Absorption difference spectra ($\Delta A = A_{\text{after oxidation}} - A_{\text{no redox}}$; no normalization) and **(b)** magnified powder X-ray diffraction patterns compared to that simulated for $P6_3cm$, ref. 12. Data presented for ensembles treated with: (i) ZnI_2/TOP (3.9 Zn/Cu), (ii) CdI_2/TOP, (iii) ZnI_2/TOP (0.5 Zn/Cu) and (iv) ZnI_2 (no TOP). The as-synthesized powder X-ray diffraction is provided as a dashed line for reference. Full-scale powder X-ray diffraction patterns and absorption spectra are shown in Figure S3.32 and S3.33, respectively. Ensemble from Synthesis 7 (Table S3.1) was used for all experiments.

To gain insight into the role of the divalent metal salt, a select number of MX_2/TOP-treated nanocrystals were further characterized using mass-spectrometry-detected inductively coupled

plasma (ICP–MS) and scanning TEM with energy dispersive X-ray spectroscopy (STEM–EDS) mapping. The chosen experiments utilized MI_2 (those of Figure 3.4ii, Figure 3.5i,ii) to avoid the confounding effect of chloride, which is likely present on the nancrystal surface from synthesis.[53, 62] ICP–MS on dried, purified nanocrystal solids revealed that both CdI_2/TOP and ZnI_2/TOP oxidations lead to Cu-atom extractions from the nanocrystals of 12–15%. Additionally, the amounts of Zn or Cd are comparable to the amounts of extracted Cu atoms (i.e. $M/\Delta Cu = 0.5–0.9$, Table S3.7). STEM–EDS mapping was used to determine the spatial distribution of Zn, Cd, and I atoms in MX_2/TOP-oxidized $Cu_{3-x}P$ nanocrystal ensembles. As expected for the as-synthesized sample, there was co-localization of the Cu-Kα signal with the nanoplatelets and an absence of Zn-Kα, Cd-Lα and I-Lα signal above the noise limit (Figure S3.35). STEM–EDS mapping of the ZnI_2/TOP-oxidized nanocrystals revealed the presence of nanoscale domains of Zn and I orthogonally localized with respect to the Cu-Kα signal and the $Cu_{3-x}P$ nanocrystals (Figures S3.36, S3.37). These regions may correspond to the additional species detected in the powder X-ray diffraction patterns of ZnX_2-treated samples (Figure 3.3aiv, Figure 3.4bii, Figure S3.32i,iv,vi). In contrast, STEM–EDS mapping of the CdI_2/TOP-oxidized nanocrystals revealed co-localization of both Cd-Lα and I-Lα signals with the $Cu_{3-x}P$ nanocrystals and no indication of separate domains (Figures S3.38, S3.39). Unfortunately, higher-resolution, single-particle mapping was not possible due to nanocrystal degradation by the electron beam.

3.4 Discussion

The data presented in this study show that solution-phase redox chemistries can be leveraged to post-synthetically tailor the plasmonics of colloidal $Cu_{3-x}P$ nanocrystals on the scale of an entire synthesis ensemble. This post-synthetic tuning represents a valuable extension of the LSPR control previously demonstrated through modulation of nanocrystal formation reactivity in

aminophosphine-based syntheses.[16] Anaerobic LSPR tuning is especially important for $Cu_{3-x}P$ nanocrystals, as metal phosphide surfaces have been shown to readily form a substantial amount of oxidized phosphate defects.[63] For example, $Cu_{3-x}P$ nanocrystals were substantially altered by aerobic oxidation, as indicated by the observation of thicker lower-contrast "shells" in TEM images with increasing air exposure time (Figure S3.40).

While two of the copper-coupled redox chemistries investigated in this study, reduction with Cu^+ and oxidation with I_2, have been demonstrated with an analogous class of nanomaterials, copper chalcogenides,[28, 31, 44, 50-52] the oxidation protocol using I_2 was newly adapted to a larger scale (Figure S3.7). The previously unreported oxidation chemistry with ZnI_2 and TOP was associated with the greatest change in Cu vacancy concentration, LSPR shift, spin–lattice relaxation, and Knight shift (Figure 3.3, Table 3.1), which, taken all together, indicate the largest modulation of the carrier density. The three highlighted anaerobic redox chemistries leave $Cu_{3-x}P$ nanocrystal size and morphology by TEM (Figures S3.5, S3.26–28, S3.31) unchanged. Additionally, crystallite sizes estimated by Scherrer analysis of powder X-ray diffraction data (Table S3.2) indicate that nanoparticle single-crystallinity remains intact after redox.

Correlations among Optical, Structural, and Electronic Properties. LSPR absorption is an emergent phenomenon with nanoscaling, and accordingly, there is no literature-reported quantitative correlation between optical and structural (or optical and ^{31}P SSNMR chemical shift) properties for $Cu_{3-x}P$ nanocrystals as a function of their compositional variance. Building a framework for the optical–structural correlation, in particular, is valuable due to the phase-stability of $P6_3cm$ $Cu_{3-x}P$ as the sole reported copper-rich phase of copper phosphide under ambient conditions, which contrasts with the cascade of phase changes observed in copper chalcogenides with redox tuning.[49] The 24 $Cu_{3-x}P$ nanocrystal samples characterized by both electronic

absorption spectroscopy and powder X-ray diffraction in this work are compared and reveal an approximately linear relationship between unit-cell volume and E_{LSPR}^2 (Figure 3.6a). This observed trend is expected because an increase in Cu^+ vacancies, and the concomitant unit cell contraction, should lead to the introduction of more delocalized holes for charge compensation, thereby increasing the free carrier concentration, N_h, which correlates with E_{LSPR}^2, according to the Drude–Lorentz model. Interestingly, the samples treated with MX_2/TOP systematically exhibited lower-than-expected LSPR energy for their unit-cell volumes compared to the linear fit, whereas the opposite is true for the samples oxidized with I_2. Relatedly, treatment with MX_2/TOP led to a lattice contraction but no change in the LSPR peak energy for the low-temperature-synthesized ensemble (Figure S3.25). Finally, ensembles treated with either TOP or MX_2 (but not both) exhibited lattice contraction without changes to their LSPR peak energy (Figures 3.5iv, S3.34viii, S3.33iv,viii). An interpretation of these results is that treatment with MX_2/TOP leads to a greater portion of surface-mediated charge-compensation of Cu vacancies, possibly by M^{2+}-cation-containing species.

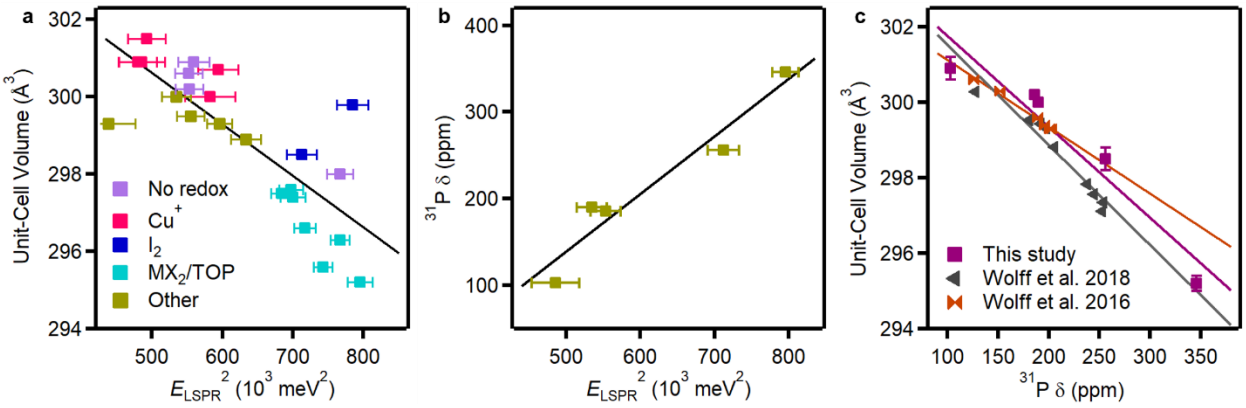

Figure 3. 6. Correlational relationships among structural, optical, and electronic properties for $Cu_{3-x}P$ nanocrystals. **(a)** Unit-cell volume vs. square of LSPR maximum for all redox experiments characterized by powder X-ray diffraction, **(b)** ^{31}P MAS SSNMR chemical shift vs. square of LSPR maximum for Table 3.1 data, and **(c)** unit-cell volume vs. ^{31}P MAS SSNMR chemical shift for Table 3.1 data, compared to those from ref. 1 and 57. Solid lines are lines of best fit with separate trendlines for data from other studies (Figure 3.6c).

For the five $Cu_{3-x}P$ nanocrystal samples characterized by ^{31}P MAS SSNMR, the observed ^{31}P chemical shift increases linearly with E_{LSPR}^2 (Figure 3.6b), corroborating the interpretation that the change in chemical shift arises from a Knight shift and a change in the delocalized hole concentration. The trend relating unit-cell volume and ^{31}P chemical shift (Figure 3.6c) agrees well with values reported for bulk counterparts,[1, 57] indicating that nanoscaling, to the extent demonstrated in this study, does not profoundly alter the electronic or structural properties of $Cu_{3-x}P$.

Cu Vacancies and Delocalized Hole Carriers. The diffraction-estimated core composition range extracted for $Cu_{3-x}P$ nanocrystal ensembles of this study is Cu/P = 2.67–2.93 (Table 3.1). If the corresponding Cu vacancies are each compensated by a delocalized hole, this corresponds to N_h = 1.5–6.7 × 10^{21} cm^{-3}. Drude estimates from optical data (Table 3.1, Section S3.3) indicate N_h = 3.0–4.8 × 10^{21} cm^{-3}. The overlap among these two independently-derived carrier concentration estimates, and estimates from Hall measurements of bulk $Cu_{3-x}P$ (N_h = 3.8 × 10^{21} cm^{-3}),[56]

corroborates their accuracy and confirms that Cu vacancies are charge-compensated by delocalized hole carriers, as has been previously asserted.[8, 14] While SSNMR spin–lattice relaxation data cannot give absolute carrier concentrations without comparison to a sufficiently similar reference material,[25] relative comparisons for the samples of the study (Table 3.1) using Equation 3.1 indicate differences in N_h consistent with optical Drude estimates. The larger range in N_h from diffraction-estimates as compared to optical Drude estimates suggests that the number of delocalized holes per Cu vacancy is less than unity (~0.4 h^+/V_{Cu}). One possible explanation for this is that surface-mediated charge compensation of Cu vacancies by cationic species competes with delocalized hole formation. In contrast, the estimation of hole concentration from diffraction is lower ($N_h = 1.5 \times 10^{21}$ cm^{-3}) than the optical estimate ($N_h = 3.0 \times 10^{21}$ cm^{-3}) for the most reduced $Cu_{3-x}P$ nanocrystal sample (Figure 3.3i, Table 3.1).

Oxidation Chemistry with MX_2 and TOP. Since treatment with MX_2/TOP produces the most profound change in $Cu_{3-x}P$ structural and optical properties, an understanding of the redox mechanism could enable extension to greater carrier densities or to other plasmonic nanomaterials. It is likely that the oxidation is copper-coupled based on the joint observation of lattice-contraction (Figures 3.3a, 3.4c, 3.5b, S3.34b, Tables 3.1, S3.5) and decreased Cu atom content in post-redox nanocrystals by elemental analysis with both ICP–MS (Table S3.7) and Cu^{2+} optical analysis of nitric acid-digested nanocrystals (Figures S3.3, S3.10c, Table S3.3). A possible model of Cu-atom extraction is that Cu leaves the nanocrystal as a TOP-ligated copper(I) complex with a halide counteranion, which may come from either MX_2 or the Cl^- already on the nanocrystal surface from synthesis.[53, 62] This idea is supported by a previous observation that Cu-atom extraction from $Cu_{3-x}P$ nanocrystals during cation-exchange was controlled by the relative amount of TOP.[9] The component of the oxidation mechanism with no simple explanation is the loss of electrons from

the nanocrystals. It is inferred, however, that the oxidant is derived from MX_2, as reaction with just TOP (and OAm) does not induce the full oxidation (Figures S3.32, S3.33, S3.34viii). Unlike the oxidation with I_2, the halogen atoms in the oxidation treatment with MX_2/TOP are anionic prior to redox. A mechanism of halogen reduction can thus be ruled out during treatment with MX_2/TOP. It thus seems likely that Cd^{2+} or Zn^{2+} react with the $Cu_{3-x}P$ nanocrystals during redox. This idea is corroborated by elemental analysis, which reveals the presence of Zn and Cd atoms in the purified post-oxidation nanocrystal samples in amounts consistent with the number extracted Cu atoms (which only corresponds to 2–3 % of total MX_2 used in the reaction; Table S3.7).

One possible explanation for the increase in delocalized hole concentration with the MX_2/TOP treatment is that MX_2 binds undercoordinated P-atoms at the nanocrystal surface as a Z-type ligand. There is precedent for this in a recent study, which posits the existence of Z-type ligation of aminophosphine-synthesized indium phosphide nanocrystals after reaction with $ZnCl_2$ at 100 °C.[53] The same study used DFT calculations to reveal that P-atom passivation by $ZnCl_2$ eliminates hole surface-traps. If this phenomenon translates to $Cu_{3-x}P$ nanocrystals, it becomes clearer why reaction with MX_2 might lead to an increase in delocalized hole carrier concentration, especially in the presence of Cu-extracting TOP, which would expose additional under-coordinated surface P atoms. Experiments to probe surface-association of MX_2 by STEM–EDS elemental mapping (Figures S3.35–39) were inconclusive. While the CdI_2/TOP-treated $Cu_{3-x}P$ nanocrystals have Cd colocalized with the nanocrystals (Figures S3.38, S3.39), ligand-shell physisorption of Cd-containing species could not be ruled out due to the inability to measure at higher-resolution without destroying the particles. An additional confounding result was the observation of Zn-containing (and Cu-free) nanoscale domains in the STEM–EDS mapping of ZnI_2/TOP-oxidized nanocrystals (Figure S3.36, S3.37). It is unlikely that the domains are

unreacted zinc halide, as the additional diffraction peak observed with ZnX_2-reacted samples (both X = Cl and I; Figure 3.4bii, Figure S3.9iii, Figure S3.32i,iv,vi) does not match any known phase of $ZnCl_2$ or ZnI_2. While the additional peak nearly coincides with the (220) reflection of α-Zn_3P_2,[64] other reflections of α-Zn_3P_2 which were not observed. This impurity reflection also does not match known phases of Cu(0), Zn(0), or copper halide salts. The fact that the diffraction peak is observed also in the absence of TOP and minimal nanocrystal oxidation (Figures 3.5iv, S3.32iv) suggests that the corresponding species is probably generated by a non-productive side reaction.

Practical Considerations for Using Solution-Phase Redox. Some key limitations of the solution-phase $Cu_{3-x}P$ nanocrystal redox chemistries presented in this study include co-precipitation of insoluble species during purification and nanoplatelet aggregation. Insoluble molecular impurities coprecipitated with $Cu_{3-x}P$ nanocrystals during purification after reduction with Cu^+. This was determined by the observation of a substantially larger powder mass during sample preparation for ^{31}P MAS SSNMR, as well as the sharp resonances in the corresponding measurement near 0 ppm (Figure 3.3bi). It is likely that these molecular impurities reacted with I_2 to degrade $Cu_{3-x}P$ nanocrystals during an attempted reversibility experiment (Figure S3.29).

Irreversible aggregation of $Cu_{3-x}P$ nanocrystals was most problematic with the Li/THF treatment (Figures S3.6, S3.18, S3.19, S3.24). The presence of LiCl impurities in the powder X-ray diffraction pattern of the Li/THF treatment (Figure S3.19) suggests that adventitious species in the reaction mixture oxidize Li(0), which then strips off Cl^- passivating species from the $Cu_{3-x}P$ nanocrystal surface to form LiCl. The existence of Cl^- as a surface-bound species is inferred from its precedent as a co-passivant, along with OAm, on the surface of metal chloride- and aminophosphine-synthesized metal phosphides.[53, 62] The nanocrystal surface destabilization from Cl^- removal is likely the driving force for particle aggregation.

The MX_2/TOP treatment from this study represents a promising opportunity for further study of the electrochemical lithiation mechanism for *P*6$_3$*cm* $Cu_{3-x}P$. The electrochemical lithiation of bulk $Cu_{3-x}P$ is known to extrude crystalline Cu(0) through (partial) substitution reactions that accompany the formation of ternary phases Li_2CuP and Li_3P with increasing negative potential.[65] The initial discharge step is controversial, with conflicting literature accounts of whether or not monophasic Li-intercalation is possible without cation exchange[65-66] at less negative potentials prior to formation of Li_2CuP. Recent work from Wolff and coworkers has suggested that initially copper-deficient *P*6$_3$*cm* $Cu_{3-x}P$ undergoes a different lithiation pathway than the more copper-rich counterpart, as indicated by differential capacity measurements.[1] Their interpretation of this result was that the Cu-deficient composition does not extrude Cu(0) prior to reaching the potential at which Li_2CuP begins to form. The MX_2/TOP oxidation chemistry of this study, which, to our knowledge, yields the smallest *P*6$_3$*cm* $Cu_{3-x}P$ unit-cell volume reported in the literature (Figure 3.6c, Table 3.1), allows access of a uniquely Cu-deficient $Cu_{3-x}P$ composition. Accordingly, the MX_2/TOP-oxidized $Cu_{3-x}P$ nanocrystal thin films would be ideal candidates for fundamental electrochemical lithiation studies. If monophasic, reductive Li^+-intercalation without Cu(0) extrusion is indeed possible for sufficiently copper-deficient *P*6$_3$*cm* $Cu_{3-x}P$ films, it could be used to access rapid and reversible plasmonic tunability while also avoiding the aforementioned limitations of solution-phase redox chemistry.

3.5 Summary and Conclusions

We have developed three post-synthetic chemistries for the anaerobic copper-coupled redox modulation of plasmonic $Cu_{3-x}P$ nanocrystals which yield correlated changes to their structural and optoelectronic properties. Similar to copper chalcogenides, post-synthetic reactions with Cu^+ and I_2 lead to nanocrystal reduction and oxidation, respectively, as demonstrated through

observation of the LSPR energy shift by electronic absorption spectroscopy, lattice parameter change by powder X-ray diffraction, and a ^{31}P MAS SSNMR Knight shift. A previously unreported copper-coupled oxidation chemistry with MX_2 and TOP accesses an expansion of the previously demonstrated ranges of $P6_3cm$ $Cu_{3-x}P$ structural and electronic properties. $Cu_{3-x}P$ nanocrystals oxidized with MX_2 and TOP can be back-reduced with Cu^+, indicating that the new oxidation chemistry permits reversible carrier density tuning and does not irrevocably change the material. Additionally, control experiments allowed us to determine that MX_2 identity is generalizable to zinc- and cadmium- halide salts and that MX_2 and TOP are both needed for the full oxidative effect. The three redox chemistries and corresponding characterization presented will inform future endeavors to leverage the optical, structural, and compositional tunability of $Cu_{3-x}P$ nanocrystals.

3.6 Experimental Methods

3.6.1 Chemicals

The manufacturers and purities of the chemicals used in this study are given in Table S3.8. Toluene, tetrahydrofuran (THF), and acetonitrile (MeCN) were dried and deoxygenated according to standard procedures[67] and stored over molecular sieves (3 Å) for two days before use. Methanol (MeOH) was deoxygenated with several freeze–pump–thaw cycles and stored over molecular sieves (3 Å) for two days before use. Oleylamine (OAm), trioctylamine (TOA), and tris(diethylamino)phosphine ($P(NEt_2)_3$) were degassed upon receipt and stored over molecular sieves (4 Å) for two days before use. All zinc and cadmium salts were dried under vacuum at 120 °C for two hours before use. Nitric acid and copper metal were used as received and handled in air. All other chemicals were handled and stored exclusively in a nitrogen-filled glovebox. Lithium metal (Li^0) was opened in a nitrogen-filled glovebox and promptly transferred to rubber-septum-

capped vials, which were evacuated and stored under static vacuum to limit the formation of lithium nitride.

3.6.2 Synthesis

Synthesis and workup of $Cu_{3-x}P$ nanocrystals were conducted under inert atmosphere to avoid aerobic oxidation, either with a nitrogen-equipped Schlenk line or in a nitrogen-filled glovebox.

One-pot syntheses of $Cu_{3-x}P$ nanocrystals with TOA as a cosolvent. The synthesis of $Cu_{3-x}P$ nanocrystals was adapted from a previous study.[16] For the syntheses reported herein, the reaction mixture compositions were identical within the measurement limitations (Table S3.1). For Syntheses 9 and 10, the temperature-profiles and reaction-times were different than those of Syntheses 1–8.

In a typical synthesis (Syntheses 1–8, 10), a three-neck, 25-ml round-bottom flask was loaded with CuCl (79.2 mg, 0.800 mmol), $P(NEt_2)_3$ (277 mg, 1.12 mmol), OAm (1.05 g, 1.29 ml, 3.93 mmol), and TOA (5.43 g, 6.71 ml). This gave a total volume of 8.00 ml with OAm/P/Cu = 4.9/1.4/1.0 and [Cu] = 0.100 M. The flask was equipped with a condenser and two septa through which glass sheathes containing 2 cm silicone oil. To the sheathes were added a thermocouple to control the temperature and an Omega data logger to measure the temperature. The mixture was stirred and degassed at ~125 °C for 3 h. At this point, the pressure over the flask was equal to the equilibrium, closed-vacuum-line pressure, indicating full removal of $HNEt_2$ that was generated by transamination of $P(NEt_2)_3$. The resulting pale, straw-colored solution was placed under nitrogen and was heated as outlined in the heating methods section below after first equilibrating to a starting temperature of 105 °C. Following the reaction, the heating mantle was removed and the flask allowed to slowly cool. The room-temperature reaction flask was transferred to a nitrogen-

filled glovebox. To the flask was added 15 ml THF and 7 ml MeCN. The resulting suspension was transferred to two test tubes and the nanocrystals were collected via centrifugation at 2000 rpm for 5 min. The nanocrystals were resuspended in 3000 μl toluene to form concentrated stock solutions.

For Synthesis 9, the reaction conditions were the same with the exception of a few changes made to account for the smaller scale and lower total volume of 4.97 ml. The flask was loaded with CuCl (49.1 mg, 0.496 mmol), $P(NEt_2)_3$ (173 mg, 0.699 mmol), OAm (0.662 g, 0.814 ml, 2.47 mmol), and TOA (3.35 g, 4.14 ml). 10 ml THF and 6 ml MeCN were added to the mixture prior to centrifugation and the nanocrystals were resuspended in 2000 μl toluene after collection by centrifugation. The ensemble from Synthesis 9 was used for a single oxidation-with-I_2 experiment solely for the purpose of verifying CuI formation by powder X-ray diffraction (Figure S3.11). Characterization of the Synthesis 9 ensemble by TEM, absorption spectroscopy, and powder X-ray diffraction (Figure S3.41) reveals similar $Cu_{3-x}P$ nanocrystals to those isolated from Syntheses 1–8, despite the altered temperature-profile of the former from its lower reaction volume.

Heating methods. For syntheses 1–9, the reaction-temperature during degassing was controlled with a 25-ml heating mantle connected to a PID. After the degassing step, the heating mantle was instead controlled with a contact voltage regulator (Volteq, $TDGC_2$–500VA). The desired heating profile was achieved through a stepwise, two-voltage scheme. For syntheses 1–8, a starting voltage of 120 V was used to set the maximum ramp-rate ($dT/dt \approx 22$ °C/min) with a starting temperature of 105 °C. When the temperature reached ~230 °C after 7 min, the voltage was lowered to 90 V to set the asymptotic temperature of ~272 °C for the remaining 10 min of the reaction. This two-step constant voltage heading method led to reproducible temperature profiles across multiple syntheses (Figure S3.1). For Synthesis 9, a starting voltage of 120 V was used to set the maximum ramp-rate ($dT/dt = 35$ °C/min) with a starting temperature of 115 °C. When the

temperature reached 205 °C after 3.5 min, the voltage was lowered to 90 V for the remaining 13 min of the reaction to reach T_f = 276 °C (Figure S3.42). The lower reaction volume of 4.96 ml for Synthesis 9 (Table S3.1) was the cause for the different temperature-profile as compared to Syntheses 1–8. For Synthesis 10 (low-temperature), the heating mantle was entirely controlled with a PID. Following degassing, the reaction mixture was heated (maximum ramp-rate $dT/dt \approx$ 19 °C/min) to T_f = 200 °C with an initial temperature-overshoot of T_{max} = 215 °C (Figure S3.43) and held for a total reaction time of 21 h.

Quantification of the reaction-temperature. The reaction-temperature was stored digitally with an Omega data logger (OM-EL-USB-TC-LCD) at five-second intervals for Syntheses 1–9. The reaction-temperature was recorded by hand at sixty-second intervals for Synthesis 10. The raw temperature was adjusted to a corrected temperature with a temperature-dependent empirical quadratic function which was generated by calibration against an external mercury thermometer.

3.6.3 Post-Synthetic Redox Experiments

All post-synthetic redox treatments of $Cu_{3-x}P$ nanocrystals were conducted under inert atmosphere to avoid aerobic oxidation, either with a nitrogen-equipped Schlenk line or in a nitrogen-filled glovebox. After each post-synthetic redox treatment, nanocrystals were resuspended in toluene without additional washes to avoid aggregation. Subsequent washes were performed immediately prior to characterization, and are described in the corresponding sections.

Oxidation of $Cu_{3-x}P$ nanocrystals with I_2. In a nitrogen-filled glovebox, a three-neck, 25-ml round-bottom flask was loaded with a stock solution of $Cu_{3-x}P$ nanocrystals (from Synthesis 2; 2.97 ml, 0.65 mmol Cu). The flask was equipped with a reflux condenser and two rubber septa and transferred to a Schlenk line. Under high nitrogen flow, the rubber septum on one side-neck was replaced with a Merlic solid-addition adapter loaded with I_2 (5.0 g, 20 mmol). With stirring, the

flask was subjected to ten cycles of 5 s dynamic vacuum followed by 55 s static vacuum. The reaction was left under static vacuum for 20 h with vigorous stirring. This reaction setup, which maintained physical separation of the solid I_2 from the nanocrystal suspension is shown in Figure S3.7. The oxidation was terminated by replacement of the iodine-filled adapter with a rubber septum under high nitrogen flow. Remaining volatiles were removed from the flask under vacuum for 30 min. The flask was transferred back to the glovebox, where nanocrystals were resuspended in 2970 μl toluene to form a concentrated stock solution. The washing procedures for subsequent characterizations are described in the corresponding sections. All supernatants from these washes were combined and concentrated under vacuum to give a waxy, white residue. The residue was quantitatively digested to determine the Cu-content by electronic absorption spectroscopy.

For the oxidation-with-I_2 experiment using the ensemble from Synthesis 9, the reaction conditions were the same with the exception of a few differences. The stock solution of $Cu_{3-x}P$ nanocrystals used had lower volume and lower concentration (1.00 ml, 0.18 mmol Cu). After the oxidation, the nanocrystals were resuspended in 1000 μl toluene. Without the addition of MeCN, the toluene suspension was transferred to a single, counter-balanced test tube and a white solid was collected via centrifugation at 2000 rpm for 1 min. This white solid was characterized by powder X-ray diffraction and found to contain CuI.

Reduction of $Cu_{3-x}P$ nanocrystals with Cu^+. The procedure to reduce $Cu_{3-x}P$ nanocrystals with Cu^+ was adapted from a previous report.[31] In a nitrogen-filled glovebox, a 20-ml scintillation vial was loaded with $Cu_{3-x}P$ nanocrystals in a toluene suspension (from Synthesis 3; 2.97 ml, 0.64 mmol Cu), THF (15 ml), OAm (100 μl, 0.3 mmol), $[Cu(MeCN)_4]PF_6$ (56 mg, 0.15 mmol), and MeOH (200 μl, 4.94 mmol). The mixture was vigorously stirred for 20 h at ambient temperature. The reduction was terminated by the addition of 800 μl OAm (to prevent aggregation) and 2 ml

MeCN (to precipitate nanocrystals) to the mixture. The nanocrystals were transferred to two test tubes, collected via centrifugation at 2000 rpm for 5 min, and resuspended in 2970 μl toluene. The washing procedures for subsequent characterizations are described in the corresponding sections. All supernatants from these washes were added to the supernatant collected from this initial wash. The combined supernatant was concentrated under vacuum to yield an oil, which was analyzed by electronic absorption and solution NMR spectroscopies.

For the reduction-with-Cu^+ experiment using the Synthesis 10 ensemble, the scale was reduced to ~30% with otherwise identical conditions. A 20-ml scintillation vial was loaded with $Cu_{3-x}P$ nanocrystals in a toluene suspension (900 μl, 0.20 mmol Cu), THF (4.5 ml), OAm (30 μl, 0.09 mmol), $[Cu(MeCN)_4]PF_6$ (17 mg, 0.047 mmol), and MeOH (60 μl, 1.5 mmol). The reduction was terminated with only 300 μl OAm and 600 ml MeCN. The nanocrystals were resuspended in 900 μl toluene.

Treatment of $Cu_{3-x}P$ nanocrystals with MX_2/TOP (M = Zn, Cd; X = Cl, I, acetate). For the standard ZnI_2/TOP condition, in a nitrogen-filled glovebox, a 20-ml scintillation vial was loaded with $Cu_{3-x}P$ nanocrystals in a toluene suspension (from Synthesis 4; 2.97 ml, 0.67 mmol Cu), ZnI_2 (0.809 g, 2.53 mmol), TOP (3.76 g, 4.52 ml, 10.1 mmol), and OAm (0.508 g, 0.63 ml, 1.90 mmol). The vial was sealed with a Teflon-lined cap and heated to 100 °C with vigorous stirring for 20 h. The oxidation was terminated by the addition of 12 ml THF (for miscibility) and 6 ml MeCN (for precipitation) to the mixture. The slurry was transferred to two test-tubes and nanocrystals were collected via centrifugation at 2000 rpm for 5 min and resuspended in 2970 μl toluene. The washing procedures for subsequent characterizations are described in the corresponding sections. All supernatants from these washes were added to the supernatant collected from this initial wash.

The combined supernatant was concentrated under vacuum to yield an oil, which was analyzed by electronic absorption and solution NMR spectroscopies.

For the oxidation-with-ZnI_2/TOP experiment using the Synthesis 10 ensemble, the scale was reduced to ~30% with otherwise identical conditions. A 20-ml scintillation vial was loaded with $Cu_{3-x}P$ nanocrystals in a toluene suspension (900 µl, 0.20 mmol Cu), ZnI_2 (0.245 g, 0.767 mmol), TOP (1.14 g, 1.37 ml, 3.08 mmol), and OAm (0.16 g, 0.20 ml, 0.60 mmol). The oxidation was terminated with only 4 ml THF and 2 ml MeCN. The nanocrystals were resuspended in 900 µl toluene.

For the remaining experiments using the Synthesis 7 ensemble (corresponding to Figures 3.5, S3.31–34), the most important differences in the reaction conditions involved changing the identity or concentration of MX_2 or omitting TOP and/or MX_2, with use of additional toluene to maintain [Cu] ≈ 0.080 M (Table S3.6). These 9 oxidation reactions were carried out in parallel to ensure consistent heating among the experiments. Another substantial difference is that the MX_2/TOP/OAm/toluene mixtures were first heated to 100 °C for 3 h in the absence of $Cu_{3-x}P$ nanocrystals to verify solubilization of the MX_2 salt prior to the oxidation. A toluene suspension of $Cu_{3-x}P$ nanocrystals (300 µl, 0.066 mmol Cu) was added to bring the solution to [Cu] ≈ 0.080 M, which was then heated for an additional 20 h. The oxidations were each terminated with only 3 ml THF and 1.5 ml MeCN. The nanocrystal ensembles from the oxidation experiments were separately each resuspended in 300 µl toluene.

Reduction of $Cu_{3-x}P$ nanocrystals with lithium in the presence of THF. In a nitrogen-filled glovebox, a 20-ml scintillation vial was loaded with $Cu_{3-x}P$ nanocrystals in a toluene suspension (from Synthesis 5; 2.97 ml, 0.62 mmol Cu), THF (0.33 ml, 4.1 mmol), and Li^0 (0.15 g, 22 mmol). The mixture was vigorously stirred at ambient temperature for 20 h and monitored via electronic

absorption spectroscopy. After 20 h, when it became necessary to reconstitute colloidal stability $Cu_{3-x}P$ nanocrystals for absorption spectroscopy, the aggregated suspension was decanted to a vial separate from the Li^0 granules. For electronic absorption measurements, colloidal stability was reconstituted through the addition of the nanocrystal mixture to OAm-containing solutions of THF/toluene (0.4 % OAm, 49.8% THF, 49.8% toluene by volume in the final suspension). Sample preparation for powder X-ray diffraction and SSNMR was performed on the same day to avoid reversal of lithiation by minimizing post-redox time in the solution-state.

Reduction of $Cu_{3-x}P$ nanocrystals with lithium in the presence of OAm. In a nitrogen-filled glovebox, a 20-ml scintillation vial was loaded with $Cu_{3-x}P$ nanocrystals in a toluene suspension (from Synthesis 6; 600 µl, 0.13 mmol Cu), OAm (66 µl, 0.20 mmol) and Li^0 (30 mg, 4.3 mmol). The mixture was vigorously stirred at ambient temperature, and it appeared colloidally stability throughout the reaction. The reduction was terminated after 96 h by decanting the colloidally stable $Cu_{3-x}P$ nanocrystal suspension to a vial separate from the Li^0 granules. The nanocrystal suspension was diluted with 2 ml toluene and 10 ml THF (for miscibility) and 8 ml MeCN (for precipitation). and the nanocrystals were subsequently precipitated with the addition of 8 ml MeCN. The slurry was transferred to a test tube and nanocrystals were collected via centrifugation at 2000 rpm for 5 min. The nanocrystals were resuspended in 600 µl toluene. Absorption spectroscopy was performed immediately upon resuspension of the nanocrystals, as the observed reduction was easily reversible. The product from this same experiment was used for a reduction reversibility experiment with I_2 (see below).

Redox reversibility experiments. The reversibility experiments were performed at reduced scale with use of 600 µl $Cu_{3-x}P$ nanocrystal stock solution (0.13 mmol Cu) for each experiment to allow use of the same ensemble (from Synthesis 6) for all of them. The individual redox

experiments were performed as noted above and identical components of the protocols are not repeated. The following is an example of how two redox experiments were performed sequentially, using the case of the oxidation-with-ZnI_2/TOP reversibility experiment (of Figure 3.4). A 20-ml scintillation vial was loaded with $Cu_{3-x}P$ nanocrystals in a toluene suspension (600 µl, 0.13 mmol Cu), ZnI_2 (0.164 g, 0.514 mmol), TOP (0.745 g, 0.897 ml, 2.01 mmol), and OAm (0.118 g, 0.145 ml, 0.441 mmol). After the oxidation, 3 ml THF and 1.5 ml MeCN were added to the mixture. The slurry was transferred to two test-tubes and nanocrystals were collected via centrifugation at 2000 rpm for 5 min and resuspended in 600 µl toluene. Half of the resulting stock solution (300 µl) was kept for TEM, absorbance, and powder X-ray diffraction characterization of the mid-point product. The remaining 300 µl were used for the reduction reversibility with Cu^+. A 20-ml scintillation vial was loaded with 300 µl stock solution of $Cu_{3-x}P$ nanocrystals, THF (1.5 ml), OAm (10 µl, 0.03 mmol), $[Cu(MeCN)_4]PF_6$ (6.1 mg, 0.016 mmol), and MeOH (20 µl, 0.49 mmol). The reduction was terminated by the addition of 80 µl OAm and 200 µl MeCN to the mixture. The nanocrystals were transferred to two test tubes, collected via centrifugation at 2000 rpm for 5 min, and resuspended in 300 µl toluene.

Similar to the oxidation-with-ZnI_2/TOP reversibility experiment, the remaining 3 reversibility experiments were conducted at 20% scale (600 µl stock solution) for the initial redox treatment and 10% scale (300 µl stock solution) for the subsequent reversibility experiment with a single centrifugation-purification step between the two experiments.

Synthesis and isolation of ferrocenium triflate (FcOTf). In a nitrogen-filled glovebox, a 20-ml scintillation vial was loaded with silver triflate (0.205 g, 0.778 mmol), ferrocene (0.148 g, 0.796 mmol), THF (3 ml) and MeCN (1 ml, 19 mmol). The solution was vigorously stirred at ambient

temperature for 12 h and the metallic silver was filtered off. The dark blue solution was concentrated under vacuum to give FcOTf as a dark blue powder (0.247 g, 94.7 % yield).

Cuvette-scale oxidation of $Cu_{3-x}P$ nanocrystals with cerium(IV) ammonium nitrate (CAN). In a nitrogen-filled glovebox, a toluene suspension of $Cu_{3-x}P$ nanocrystals (from Synthesis 6; 10 µl, 2.1 µmol Cu), THF (400 µl) and toluene (390 µl) were added to a 2-mm quartz screw-cap cuvette. The absorption was monitored prior to redox and after each successive addition of 3 µl MeOH solution of CAN (0.101 M) up to a total of 9 µl. The full oxidation corresponds to 0.43 CAN/Cu. Once the oxidation was complete, 400 µl MeCN was added, and the slurry was transferred to a plastic, o-ring, screw-cap tube (Axygen, SCT-200-SS-C). The nanocrystals were collected via centrifugation at 4000 rpm for 5 min. and subsequently resuspended in 800 µl 1/1 toluene/THF (by volume) for TEM imaging.

Cuvette-scale oxidation of $Cu_{3-x}P$ nanocrystals with FcOTf and TBAI. In a nitrogen-filled glovebox, a toluene suspension of $Cu_{3-x}P$ nanocrystals (from Synthesis 6; 10 µl, 2.1 µmol Cu), THF (400 µl) and toluene (390 µl) were added to a 2-mm quartz screw-cap cuvette. The absorption was monitored prior to redox and after each successive addition of 3 µl of both (1) MeCN solution of TBAI (0.066 M) and (2) MeCN solution of FcOTf (0.059 M) up to a total of 9 µl each. The full oxidation corresponds to 0.28 TBA/Cu and 0.25 Fc/Cu. Once the oxidation was complete, 400 µl MeCN was added, and the slurry was transferred to a plastic, o-ring, screw-cap tube (Axygen, SCT-200-SS-C). The nanocrystals were collected via centrifugation at 4000 rpm for 5 min and subsequently resuspended in 800 µl 1/1 toluene/THF (by volume) for TEM imaging.

Cuvette-scale oxidation of $Cu_{3-x}P$ nanocrystals with FcOTf only. In a nitrogen-filled glovebox, a toluene suspension of $Cu_{3-x}P$ nanocrystals (from Synthesis 6; 10 µl, 2.1 µmol Cu), THF (400 µl) and toluene (390 µl) were added to a 2-mm quartz screw-cap cuvette. The absorption

was monitored prior to redox and after cumulative additions of 3 and 12 µl MeCN solution of FcOTf (0.059 M). The full oxidation corresponds to 0.34 Fc/Cu.

3.6.4 Characterization

All sample preparations for characterization were conducted under inert atmosphere in a nitrogen-filled glovebox to mitigate aerobic oxidation prior to measurement.

Transmission electron microscopy (TEM). Sample grid preparation involved preparing a dilute $Cu_{3-x}P$ nanocrystal solution by the addition of 10 µl toluene stock solution (~2.1 µmol Cu) to 790 µl 39/40 toluene/THF (by volume). 25 µl of this dilute $Cu_{3-x}P$ nanocrystal solution was drop-cast onto a 100-mesh copper grid coated with Formvar and carbon (Electron Microscopy Sciences). The copper grid was suspended in air with reverse action tweezers to allow the entire 25 µl droplet to evaporate directly from the grid. Imaging was performed on the same day as grid-preparation to avoid particle oxidation. Images were collected on a FEI Tecnai Spirit operating at 120 kV. The lateral dimension was taken to be the longest line that could be drawn along the two-dimensional projection of a nanoplatelet. The size distributions were derived from the analysis of 150 nanocrystals with the use of $13(\sqrt{150}+1)$ constant-width bins spanning the ensemble range.

Electronic absorption spectroscopy of $Cu_{3-x}P$ nanocrystals. In a nitrogen-filled glovebox, a 2-mm quartz screw-cap cuvette (Starna Cells 18F-Q-10-Gl14-C) was loaded with $Cu_{3-x}P$ nanocrystals in a toluene suspension (10 µl, ~2.1 µmol Cu), 390 µl toluene, and 400 µl THF. Spectra were collected using a Cary 5000 spectrometer in transmission mode. A background spectrum of 1/1 THF/toluene (by volume) in the same cuvette was subtracted from each spectrum. The LSPR energies were estimated by local fitting of the near-IR absorbance peak to a Gaussian function with use of a linear background to account for non-plasmonic near-IR baseline absorption.

Powder X-ray diffraction. From the concentrated toluene stock solution, 300 μl (~0.064 mmol Cu) was transferred to a plastic, o-ring, screw-cap tube (Axygen, SCT-200-SS-C) and precipitated with 300 μl MeCN. The precipitated nanocrystals were collected via centrifugation at 4000 rpm for 5 min. The nanocrystals were resuspended in 300 μl THF, precipitated with 300 μl MeCN and collected via centrifugation at 4000 rpm for 5 min. Residual solvent was removed under vacuum and the pellets (~5 mg) were stored under nitrogen until just before the measurement.

Powder diffraction patterns were measured using a transmission-mode diffractometer equipped with a Bruker Apex II detector and Cu Kα radiation source (λ = 1.5418 Å). In a typical measurement, a 200-μm-diameter piece of pellet was quickly picked out under a light microscope and mounted onto the diffractometer goniometer head and kept under a dry nitrogen stream (T = 280 K; 5 l/min flow rate) to minimize air exposure. For the as-synthesized Synthesis 1 ensemble and post-redox Syntheses 2–5 ensembles, samples were measured in triplicate, with different pellet pieces each time. Three frames centered at 2θ = 30°, 45°, and 60°, respectively, were collected with a detector distance of 150 mm, spinning φ, and 240-s exposure-time per image. The Debye rings obtained from the three frames were merged and radially integrated in a cone with γ range 80–100° using Diffrac.eva software. The resulting powder patterns were fit in the range of 2θ = 20–70° with a cubic baseline and Gaussian peaks using the Wavemetrics Multi-Peak Fitting Package in Igor. An external standard of bulk lanthanum hexaboride was used to correct systematic errors in 2θ. For comparison, the powder diffraction pattern of $Cu_{2.87}P$ was simulated from single-crystal data[12] using VESTA.[68] Platelet lateral dimensions were estimated for each ensemble through Scherrer analyses of the (300) reflection, as it is the sharpest reflection and the only reflection without contribution from nanoplatelet height in the *c*-direction.

Cu-atom-quantification by Cu^{2+} absorption. In a nitrogen-filled glovebox, 50 μl stock solution (~0.011 mmol Cu) was transferred to a plastic, o-ring, screw-cap tube (Axygen, SCT-200-SS-C), diluted with 300 μl THF and precipitated with 600 μl MeCN. The precipitated nanocrystals were collected via centrifugation at 4000 rpm for 5 min. The nanocrystals were resuspended in 300 μl THF, precipitated with 600 μl MeCN and collected via centrifugation at 4000 rpm for 5 min. This process of withdrawing and washing 50 μl of the stock solution was repeated a total of three times to give three separate pellets. The pellets were left in air to allow residual solvent evaporation, after which they were individually digested overnight in the sealed o-ring, screw-cap tube with 800 μl 70% HNO_3 (Fisher Chemical, certified ACS plus). The resulting solutions were filtered with a 0.22 μm PVDF syringe filter and transferred to a 2-mm path-length cuvette. Absorption spectra were collected using a Cary 5000 spectrometer in transmission mode. A background of 70% HNO_3 was subtracted from each spectrum. To determine [Cu^{2+}], the extinction coefficient under these conditions was determined by generating a calibration line using analogously digested Cu^0 (Figure S3.44). Rather than using a single-energy extinction coefficient for [Cu^{2+}] quantification, an integrated energy range of 1.378–1.550 eV was used. It was assumed that all Cu from the digested $Cu_{3-x}P$ nanocrystals were oxidized to Cu^{2+}. This Cu-atom-quantification was used to extract synthesis yields based on Cu^{2+}/Cu for Syntheses 1 and 10. This procedure was also used to extract post-redox Cu-atom content for the redox experiments using ensembles from Syntheses 2–5 (Figures 3.2, S3.18). The average $Cu_{3-x}P$ nanocrystal absorption spectra (from Figures 3.1d, 3.2ii, S3.18ii, S3.25aii) and Cu^{2+} digested solution spectra (from Figures S3.3, S3.10, S3.45) were used to calculate Cu-based extinction coefficients at 3.1 eV ($\varepsilon_{3.1\mathrm{eV}}^{\mathrm{Cu}}$). This value ranged from 2000–2200 M^{-1} cm^{-1} (Table S3.9) with no statistically significant

differences between the 6 samples evaluated, despite their substantially different LSPR peak energies.

^{31}P magic-angle spinning solid-state nuclear magnetic resonance (MAS SSNMR) spectroscopy. In a nitrogen-filled glovebox, 2400 μl (~0.51 mmol Cu) stock solution was transferred to a test-tube and precipitated with 1500 μl MeCN. The precipitated nanocrystals were collected via centrifugation at 2000 rpm for 5 min. The resulting pellet was resuspended in 2000 μl toluene, precipitated with 1000 μl MeCN and collected by centrifugation at 2000 rpm for 5 min. The resulting pellet was dried under vacuum, pulverized, and stored under static vacuum in rubber septum-capped test-tubes until the measurement. In a typical workup, the pellet mass was ~40–50 mg. The pellet of nanocrystals reduced with Cu^{+}, however, was 86 mg.

All MAS SSNMR experiments were performed with a 600 MHz (14.1 Tesla) Bruker AVANCE-IIIHD spectrometer equipped with a Bruker 3.2 mm HPC MAS probe. In a nitrogen-filled glovebox, 3.2 mm rotors were center packed with Teflon tape and nanocrystalline $Cu_{3-x}P$ powder in a glovebox. ^{31}P direct polarization experiments were conducted with 12 kHz MAS and collected with 128 scans. The π/2 pulse length was 2 μs and the recycle delay was 3 s. ^{31}P T_1 values were determined using saturation recovery experiments with 12 kHz MAS and collected with 128 scans with variable delay times from 0.0005–1.0 s. ^{31}P chemical shifts were referenced externally to $Ca_3(PO_4)_2$ (upfield resonance at −1.66 ppm relative to 85% phosphoric acid).

Elemental analysis by inductively coupled plasma – mass spectrometry (ICP–MS). The same solid pellets used for powder X-ray diffraction were subsequently used for ICP–MS. The remainder of the pellets was digested overnight in a sealed in a plastic, o-ring, screw-cap tube (Axygen, SCT-200-SS-C) with 800 μl 70% HNO_3 (Fisher Chemical, TraceMetal). The following day, the solutions were filtered with a 0.22 μm PVDF syringe filter, diluted with 5/95

HNO_3/ultrapure water (by volume), and analyzed using a Thermo iCAP RQ ICP–MS. The ultrapure water was collected from a Barnstead Nanopure Water Purification System (Thermo Fisher). Serial dilution was used to prepare three solutions for each sample with cumulative dilution factors of 4167, 8333, and 16667. For each sample, element quantification is reported as an average for all values which fall within the calibration range.

Solution NMR spectroscopy. In a typical preparation, 100 µl supernatant and 600 µl benzene-d_6 were added to a screw-cap NMR tube (Wilmad-Labglass). All but two NMR spectra were collected on a Varian Mercury Plus 400 MHz spectrometer (Oxford NMR AS400 Magnet) with ^{1}H decoupling. The spectra of Figure S3.17i,iii were instead collected on a JEOL ECA 500 MHz spectrometer. ^{31}P NMR spectra of solutions containing TOP were collected with 1024 scans with relaxation delay = 0.5 s and processed in Mestrenova using 2-Hz apodization. ^{31}P NMR spectra of solutions containing PF_6^- were collected with 64 scans, relaxation delay = 1 s and processed using 5-Hz apodization. ^{19}F NMR spectra were collected with 16 scans, relaxation delay = 1 s and processed using 5-Hz apodization. Chemical shifts for ^{31}P NMR spectra were externally referenced to 85 % H_3PO_4 (δ = 0 ppm).

Scanning transmission electron microscopy – energy-dispersive X-ray spectroscopy (STEM–EDS). Sample grid preparation involved preparing a dilute $Cu_{3-x}P$ nanocrystal solution by the addition of 10 µl toluene stock solution (~2.1 µmol Cu) to 790 µl toluene. 25 µl of this dilute $Cu_{3-x}P$ nanocrystal solution was drop-cast onto a 400-mesh gold grid coated with Lacey Carbon and without Formvar (Ted Pella, Inc.). The gold grid was suspended in air with reverse action tweezers to allow the entire 25 µl droplet to evaporate directly from the grid. STEM images and spatially correlated EDS spectra were collected on a JEM-ARM300F Grand Arm operating at 300kV. STEM images, EDS color maps, and intensity integration area scans were processed with

Gatan DigitalMicrograph software. 3D EDS surface plots were generated in MATLAB after processing the EDS color map images with pixel-wise adaptive Wiener noise-removal filtering (the ‘wiener2’ function from the Image Processing Toolbox).

3.7 Appendix: Supplementary Information

Table S3. 1. Details of all $Cu_{3-x}P$ nanocrystal syntheses used herein.

Synthesis	OAm/P/Cu	[Cu] (M)	Volume (ml)	T_f (°C)	% Yield (Cu)[a]	LSPR max (meV)	Figures
1	4.91/1.40/1.00	0.100	8.06	273	75 ± 3	740 ± 20	3.1, 3.3ii
2	4.90/1.40/1.00	0.100	8.21	273	80 ± 8	760 ± 20	3.2a, 3.3iii
3	4.92/1.40/1.00	0.100	8.06	272	80 ± 9	750 ± 20	3.2b, 3.3i
4	4.93/1.40/1.00	0.100	8.05	272	84 ± 10	750 ± 20	3.2c, 3.3iv
5	4.93/1.41/1.00	0.100	8.09	272	77 ± 9	750 ± 20	S3.18,19
6	4.92/1.41/1.00	0.100	8.04	272	78 ± 8	740 ± 20	3.4, S3.27–S30
7	4.92/1.40/1.00	0.100	8.05	271	82 ± 8	750 ± 20	3.5, S3.31–34
8	4.95/1.40/1.00	0.100	8.12	273	85 ± 9	750 ± 20	S3.40
9	4.95/1.41/1.00	0.100	4.96	276	73 ± 7	770 ± 20	S3.11,41
10	4.93/1.41/1.00	0.100	8.13	200	81 ± 4	880 ± 20	S3.25,26

[a]Based on CuCl used in the synthesis. Cu-atom content for Syntheses 1 and 10 was determined following quantitative digestion of the nanocrystals in nitric acid, after which the Cu^{2+}-concentration was determined via the $^2E_g \rightarrow {}^2T_{2g}$ absorption. This analysis provided a Synthesis 1 extinction coefficient for the LSPR absorption feature of $\varepsilon_{3.1eV}^{Cu} = 2100 \pm 200 \frac{L}{mol\ Cu \times cm}$, which was used to determine the copper content and corresponding yield for Syntheses 2–9.

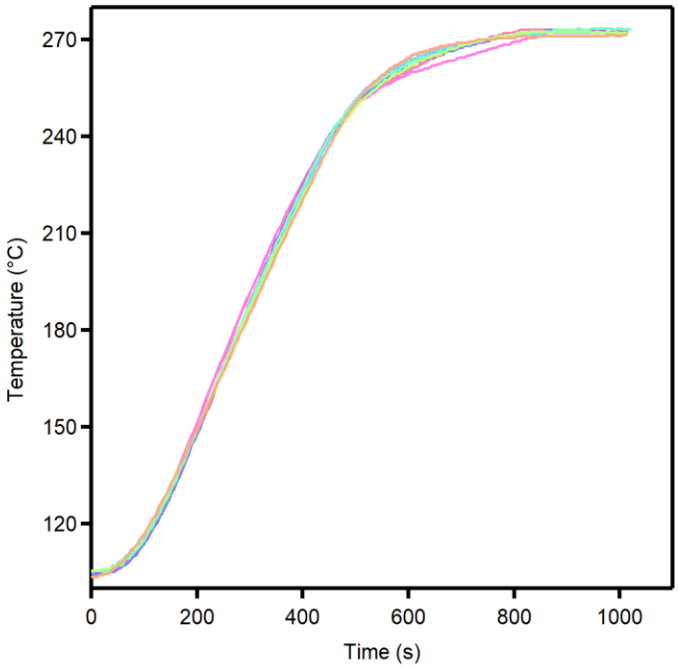

Figure S3. 1. Temperature-profiles for the standard $Cu_{3-x}P$ nanocrystal heat-up syntheses (1–8, Table S3.1), which were heated with a contact voltage regulator. The maximum ramp-rate of $dT/dt \approx 22$ °C/min and asymptotic temperature of $T_f \approx 272$ °C were reproducibly achieved.

Table S3. 2. $Cu_{3-x}P$ nanocrystal lateral platelet dimensions as measured by TEM imaging and/or calculated through Scherrer analysis of powder X-ray diffraction data.

Synthesis	Redox Experiment	TEM lateral dimension (nm)	Scherrer lateral dimension (nm)
1	As-synthesized	12.4 ± 0.7	11.9 ± 0.1
2	I_2	12.2 ± 0.6	11.0 ± 0.1
3	Cu(I)	12.9 ± 0.8	12.6 ± 0.6
4	ZnI_2/TOP	13.2 ± 0.7	12.2 ± 0.1
5	Li/THF	12.1 ± 0.8	11.2 ± 0.1
6	As-synthesized	12.7 ± 0.8	11.6
6	ZnI_2/TOP		11.0
6	ZnI_2/TOP then Cu(I)	12.3 ± 0.7	11.8
6	I_2		10.6
6	I_2 then Cu(I)	12.8 ± 0.7	12.0
6	Cu(I)		11.7
6	Cu(I) then I_2	11.8 ± 0.8	
6	Li/OAm		11.3
6	Li/OAm then I_2	11.6 ± 1.0	
7	As-synthesized	13.1 ± 0.6	11.4
7	ZnI_2/TOP (3.9 Zn/Cu)	12.9 ± 0.7	11.3
7	$ZnCl_2$/TOP	12.9 ± 0.7	11.1
7	CdI_2/TOP	12.9 ± 0.7	11.3
7	$CdCl_2$/TOP	13.0 ± 0.7	11.1
7	TOP no MX_2		11.4
7	ZnI_2 no TOP		11.4
7	$Zn(OAc)_2$/TOP	12.9 ± 0.7	10.5
7	ZnI_2/TOP (0.5 Zn/Cu)		11.5
9	As-synthesized	13.3 ± 0.9	12.2
10	As-synthesized	15 ± 1	14.3
10	Cu(I)	15 ± 1	14.3
10	ZnI_2/TOP	14 ± 1	14.0

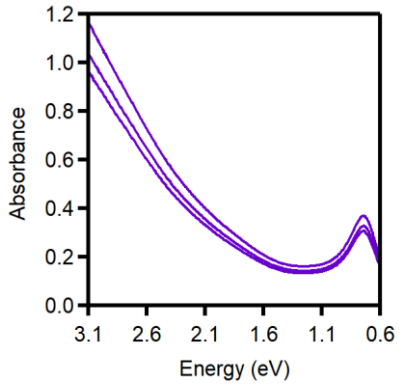

Figure S3. 2. Three independently measured absorption spectra of as-synthesized $Cu_{3-x}P$ nanocrystals for Synthesis 1 (Table S3.1, Figure 3.1). Each spectrum was collected by diluting 10 µl stock solution in 390 µl toluene and 400 µl tetrahydrofuran (THF).

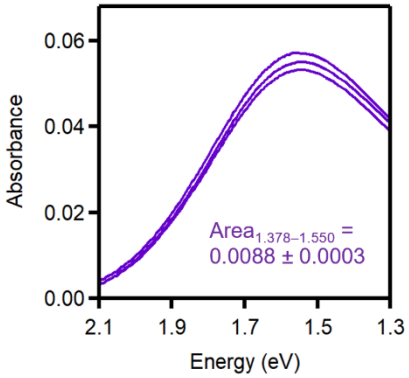

Figure S3. 3. Three independently measured absorption spectra of Cu^{2+} in nitric acid solutions from digestions of $Cu_{3-x}P$ nanocrystals for Synthesis 1 (Table S3.1, Figure 3.1). Each spectrum was collected by addition of 800 µl nitric acid to a purified $Cu_{3-x}P$ nanocrystal pellet prepared from 60 µl stock solution.

Table S3. 3. Post-redox Cu-atom content and LSPR shifts for $Cu_{3-x}P$ nanocrystal ensembles for various post-synthetic redox treatments.

Synthesis	Post-synthetic redox treatment	Post-redox Cu (%)[a]	LSPR shift (meV)[b]	Corresponding Figures
2	I_2 oxidation	93 ± 10	+80 ± 30	3.2a
3	Cu^+ reduction	94 ± 13	−50 ± 30	3.2b
4	ZnI_2/TOP oxidation	74 ± 12	+140 ± 20	3.2c
5	Li/THF treatment	95 ± 12	−20 ± 30	S3.18

[a]Based on estimated initial Cu-atom content from post-synthesis yields of Table S3.1. Cu-atom content was determined via the $^2E_g \rightarrow {}^2T_{2g}$ absorption of solutions made from digested pellets collected from post-redox purification.
[b]Positive (negative) values indicate a LSPR blueshift (redshift).

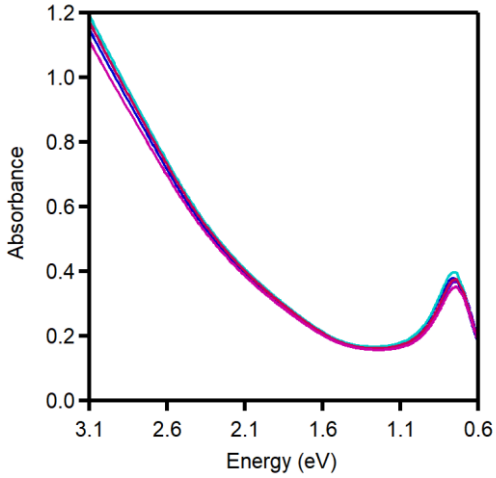

Figure S3. 4. Average (n = 3) absorption spectra of as-synthesized $Cu_{3-x}P$ nanocrystals for Syntheses 1–5 (Table S3.1). Each spectrum is the average of 3 spectra collected by diluting 10 µl stock solution in 390 µl toluene and 400 µl THF.

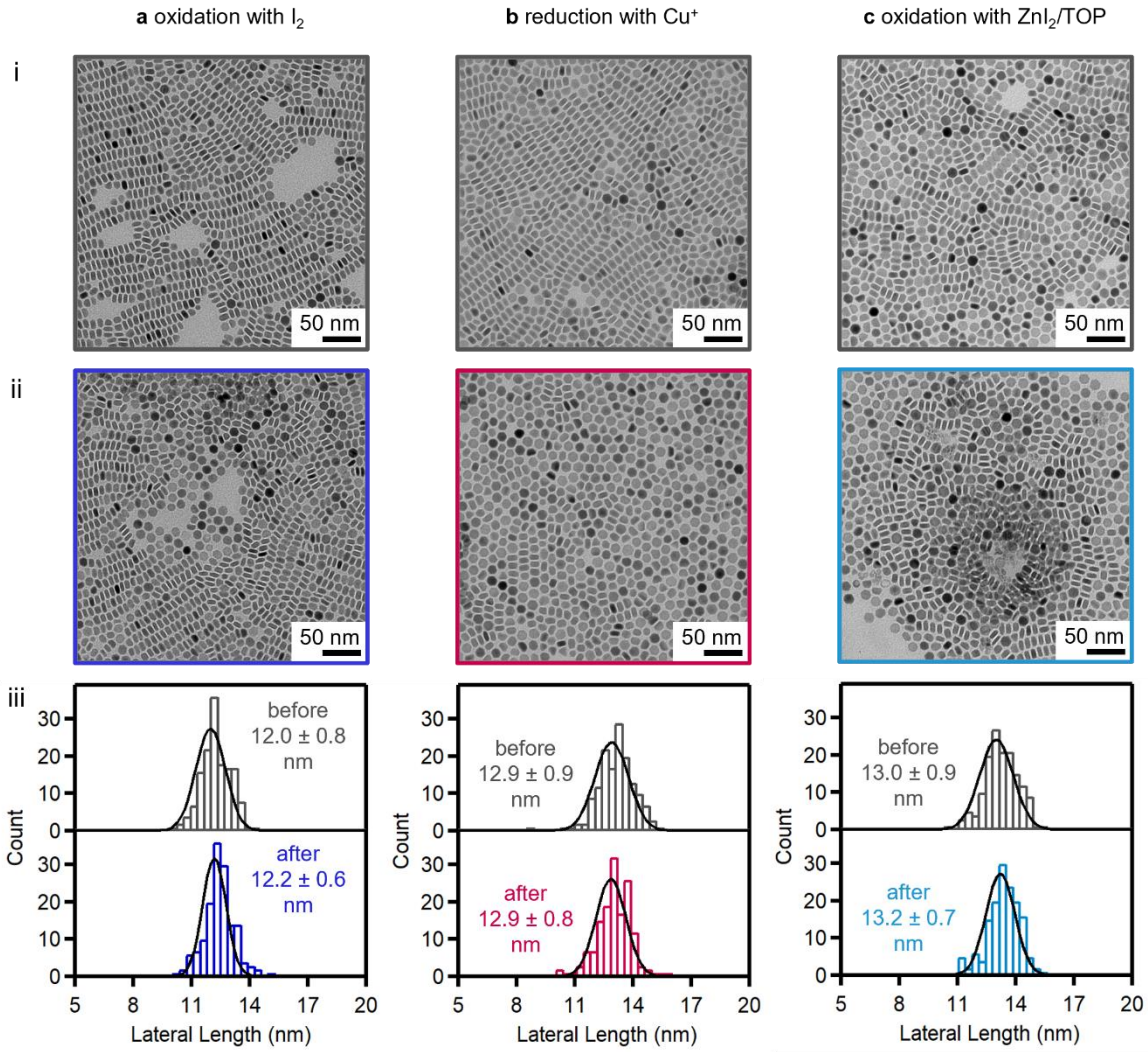

Figure S3. 5. TEM characterization of $Cu_{3-x}P$ nanocrystals (i) before and (ii) after **(a)** oxidation with I_2 **(b)** reduction with Cu^+ and **(c)** oxidation with ZnI_2 and TOP**.** (iii) Statistical analyses (n = 150) of lateral platelet dimension for each of the treatments.

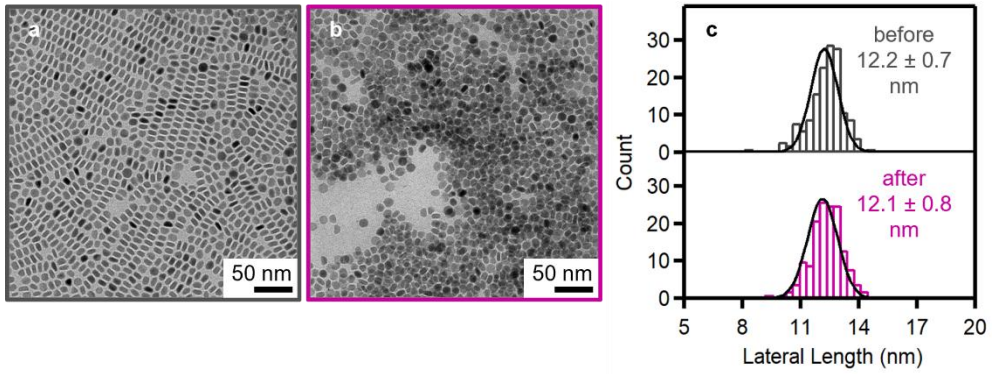

Figure S3. 6. TEM characterization of $Cu_{3-x}P$ nanocrystals **(a)** before and **(b)** after stirring with Li^0 in 1:6.8 THF:toluene (same experiment as Figure S3.18). **(c)** Statistical analyses (n = 150) of lateral platelet dimension.

Figure S3. 7. Photographs of different stages of the oxidation-with-I_2 experiment. **(a)** The initial physical separation between the nanocrystal toluene suspension in the round-bottom flask and the iodine solid in the Merlic adapter. **(b)** Red co-condensate droplets of toluene and iodine in the Merlic adapter observed at intermediate times. **(c)** White copper iodide (CuI) solids spotting the nanocrystal film which formed after evacuating the flask at the end of the oxidation.

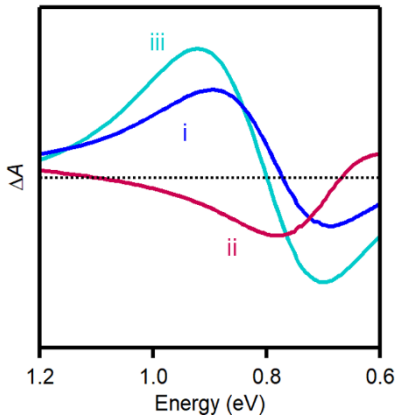

Figure S3. 8. Absorption difference spectra ($\Delta A = A_{\text{after redox}} - A_{\text{no redox}}$) upon (i) oxidation with I_2 (from Figure 3.2a), (ii) reduction with Cu^+ (from Figure 3.2b), and (iii) oxidation with ZnI_2 and TOP (from Figure 3.2c).

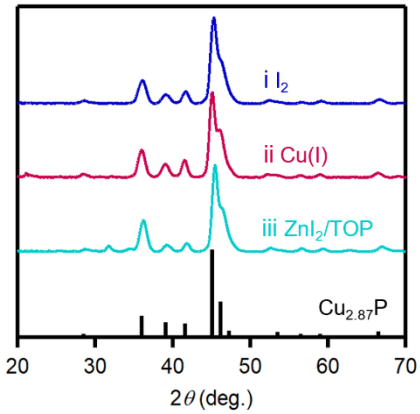

Figure S3. 9. Powder X-ray diffraction patterns of $Cu_{3-x}P$ nanocrystal ensembles after redox (from Figure 3.2): (i) oxidized with I_2, (ii) reduced with Cu^+, and (iii) oxidized with ZnI_2 and TOP. The simulated pattern for $P6_3cm$ $Cu_{2.87}P$ (ref. 12) is shown for comparison.

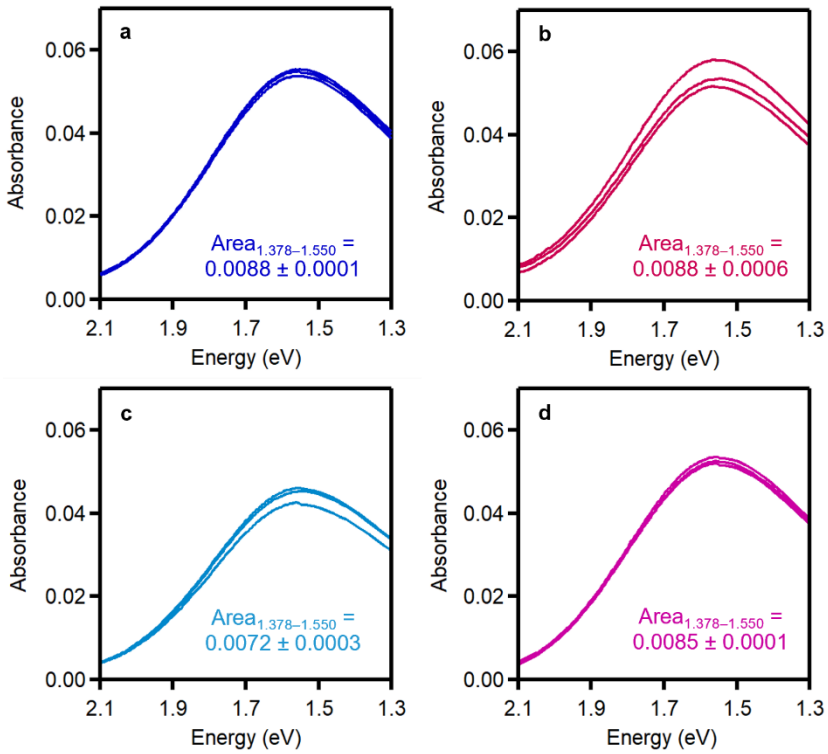

Figure S3. 10. Absorption spectra of Cu^{2+} in nitric acid solutions from digestions of $Cu_{3-x}P$ nanocrystals after the post-synthetic experiments of Figures 2 and S18. These data were used for post-redox Cu content determination (Table S3.2). n = 3 measurements and the integrated absorbance in the 1.378–1.550 eV range for: **(a)** oxidation with I_2, **(b)** reduction with Cu^+, **(c)** oxidation with ZnI_2/TOP, and **(d)** Li/THF-treatment. Each spectrum was collected by addition of 800 µl nitric acid to a purified $Cu_{3-x}P$ nanocrystal pellet prepared from 60 µl stock solution.

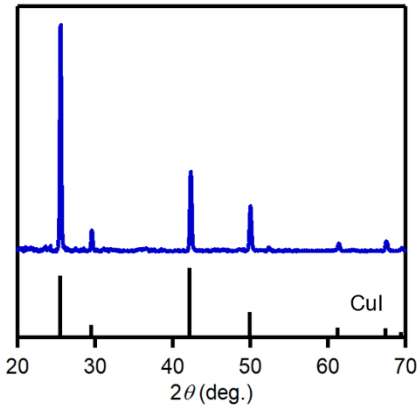

Figure S3. 11. Powder X-ray diffraction pattern of the oxidation-with-I_2 supernatant residue (using the ensemble from Synthesis 9, Table S3.1) compared to that simulated for sphalerite CuI (ref. 69)

Section S3.1: Supernatant analysis for oxidation using I_2

The supernatants from all centrifugation-separation purifications of $Cu_{3-x}P$ nanocrystals after oxidation with I_2 were combined and concentrated under vacuum to give a waxy white residue. According to previous redox studies[44, 51-52] of copper chalcogenide nanocrystals, CuI forms as an oxidation byproduct when extracted Cu reacts with reduced I_2 (Equation S3.1):

$$I_2 + 2Cu^+ + 2e^- \rightarrow 2CuI \qquad \text{(S3.1)}$$

For one oxidation-with-I_2 experiment (that of Figure S3.11; using Synthesis 10 of Table S3.1), the supernatant residue was confirmed to contain CuI by powder X-ray diffraction. For a different oxidation-with-I_2 experiment (that of Figure 3.2a; using Synthesis 2 of Table S3.1), the residue from an entire ensemble supernatant (20.2 mg) was digested in nitric acid (2000 μl) to quantify the amount of CuI which forms upon Cu-atom extraction from $Cu_{3-x}P$ nanocrystals during oxidation with I_2. The absorption spectrum of the digested supernatant residue (Figure S3.12a) reveals the characteristic Cu^{2+} peak near E = 1.6 eV. Quantitative analysis of this peak yields an estimate of 0.043 mmol Cu-atom extraction, corresponding to 6.6% of the post-synthesis Cu-atom yield (Table S3.1). This is in good agreement with the 93 ± 10% Cu-atom content from post-redox nanocrystal digestion analysis (Table S3.2). This calculation suggests that the residue is 41%-by-mass CuI.

The iodide anion in the supernatant residue was also oxidized by nitric acid. Control absorption measurements were performed to verify that the peak at E = 2.54 eV from iodine has no spectral overlap with the 1.378–1.550 eV region used for Cu^{2+}-quantification. The absorption spectra of nitric acid solutions of I_2 only (Figure S3.12bi), I_2 and OAm (Figure S3.12bii), and OAm only

(Figure S3.12biii) all indicate negligible absorption from 1.378–1.550 eV. Using the extinction coefficient based on I of $\varepsilon^{\mathrm{I}}_{2.54\mathrm{eV}} = 174\ \frac{\mathrm{L}}{\mathrm{mol\ I} \times \mathrm{cm}}$ derived from the I_2-only-nitric-acid standard, the supernatant residue is estimated to have atomic ratio I/Cu = 0.97. This suggests (1) that almost all Cu atoms in the supernatant residue were present as CuI and (2) that the post-oxidation vacuum step removes excess I_2 from the reaction flask.

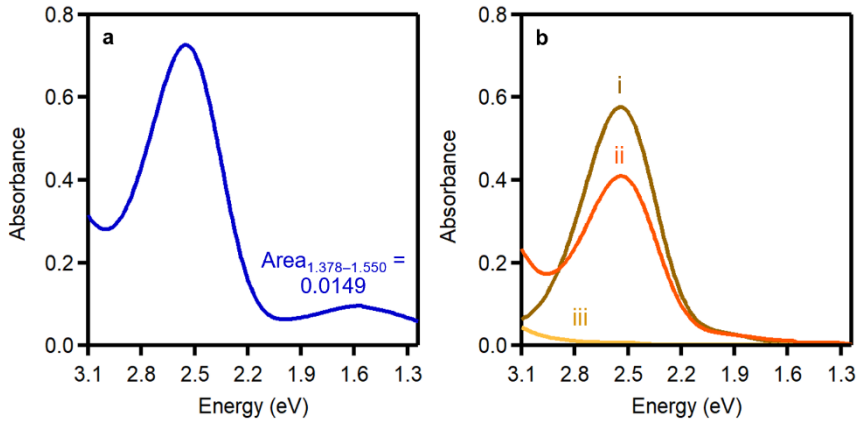

Figure S3. 12. Absorption spectra of nitric acid solutions of **(a)** digested supernatant residue (using the ensemble from Synthesis 2, Table S3.1) and **(b)** control standards: (i) [I_2] = 0.0083 M, (ii) **[**I_2] = 0.0083 M and [OAm] = 0.042 M, and (iii) [OAm] = 0.042 M.

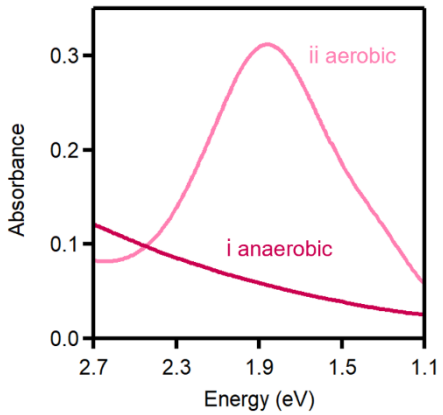

Figure S3. 13. Absorption spectra of the concentrated supernatant oil from reduction with Cu^+ (same experiment as Figure 3.2b; using Synthesis 3, Table S3.1): (i) before and (ii) after exposure to air. The solution was prepared as a 1/5 OAm/THF (by volume) solution (see Section S3.2 for further details).

Section S3.2: Supernatant analysis for reduction using Cu^+

The supernatant from centrifugation-separation purification of $Cu_{3-x}P$ nanocrystals after reduction with Cu^+ was concentrated under vacuum to give a colorless oil, consisting of mostly OAm, with colorless crystals forming at ambient temperature due to the low solubility of the molecular Cu^+ species. It was anticipated that this oil could be homogenized with heat and analyzed for Cu^{2+} content to quantify the amount of Cu atoms inserted into the $Cu_{3-x}P$ nanocrystals, according to the findings of a previous study[31] on Cu^+-reduced copper sulfide nanocrystals. The expected balanced redox reactions for the analogous disproportionation mechanism are:

$$Cu_{3-x}P + \gamma Cu^+ + \gamma e^- \rightarrow Cu_{3-x+\gamma}P \quad \text{(S3.2)}$$

$$\gamma Cu^+ \rightarrow \gamma Cu^{2+} + \gamma e^- \quad \text{(S3.3)}$$

$$Cu_{3-x}P + 2\gamma Cu^+ \rightarrow Cu_{3-x+\gamma}P + \gamma Cu^{2+} \quad \text{(S3.4)}$$

Surprisingly, the anaerobic supernatant oil revealed no Cu^{2+} peak by absorption spectroscopy (Figure S3.13i) until after deliberate exposure to air (Figure S3.13ii). These observations do not rule out the previously established disproportion reduction mechanism, as the byproduct Cu^{2+} species may have been subsequently reduced. It is possible that Cu^{2+} generated from the reduction was subsequently reduced by the majority solvent THF, based on its precedence as an electron donor.[70]

An alternative analysis was devised to estimate Cu atom insertion into the reduced $Cu_{3-x}P$ nanocrystals (those from Figure 3.2b; corresponding to Synthesis 3 of Table S3.1), with 5 min air bubbling of the concentrated supernatant oil and absorption quantification of the resulting Cu^{2+}. A standard solution with [Cu, PF_6] = 0.022 M was prepared by addition of $[Cu(MeCN)_4]PF_6$ (36 mg,

0.098 mmol) to OAm (730 µl) and heating at 100 °C under vacuum to remove MeCN. This mixture, scattery but macroscopically homogenized, was added to 500 µl THF (600 µl total volume). The mixture became a clear blue solution instantly upon air bubbling and its absorption spectrum (Figure S3.14a) was analyzed to calculate an extinction coefficient of $\varepsilon_{1.88\mathrm{eV}}^{\mathrm{Cu}}$ = 82 $\frac{\mathrm{L}}{\mathrm{mol\ Cu} \times \mathrm{cm}}$.

Dilution and air bubbling of 100 µl (14 % of the total 730 µl volume) of the concentrated reduction supernatant oil also yielded a clear blue solution. The absorption spectrum of the aerobic reduction supernatant oil (Figure S3.13ii) suggests that 45% of the Cu atoms added in the form of $[Cu(MeCN)_4]PF_6$ during the reduction experiment were absent from the supernatant, assuming equal extinction to the standard. With consideration of the limited solubility of $[Cu(MeCN)_4]PF_6$, it is unreasonable to assume that the full amount of missing Cu atoms was inserted into $Cu_{3-x}P$ nanocrystal lattice.

A control test was carried out to estimate the extent of molecular Cu co-precipitation. The protocol from reduction with Cu^+ was followed with the exclusion of $Cu_{3-x}P$ nanocrystals as the sole modification. Centrifugation was used to collect a beige solid instead of the usual $Cu_{3-x}P$ nanocrystal pellet. The control supernatant was prepared, measured (Figure S3.14b) and analyzed analogously to the reduction supernatant, with an estimated precipitation of 35% of Cu atoms as the beige insoluble solid. Using the assumption that the same 35% proportion of molecular Cu co-precipitated with $Cu_{3-x}P$ nanocrystals, it is estimated that 0.015 mmol Cu atoms were inserted into $Cu_{3-x}P$ nanocrystals, corresponding to 2.5% of the post-synthesis Cu-atom yield (Table S3.1).

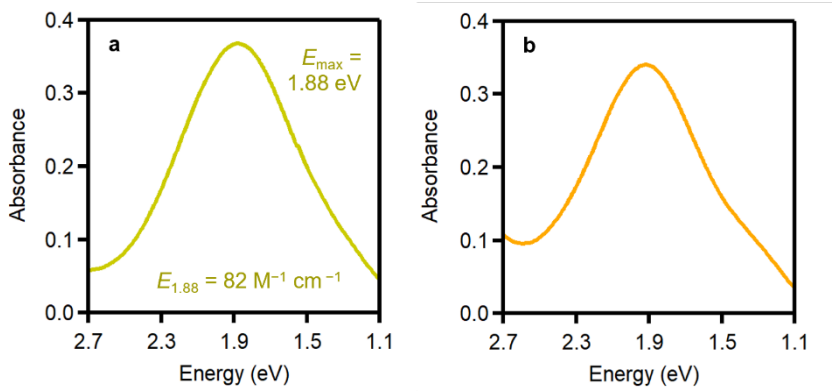

Figure S3. 14. Aerobic absorption spectra of: **(a)** [Cu, PF_6] = 0.022 M standard and **(b)** supernatant oil from $Cu_{3-x}P$-free solubility control test. Both spectra were collected using 1/5 OAm/THF (by volume) as the cuvette solvent (see Section S3.2 for further details).

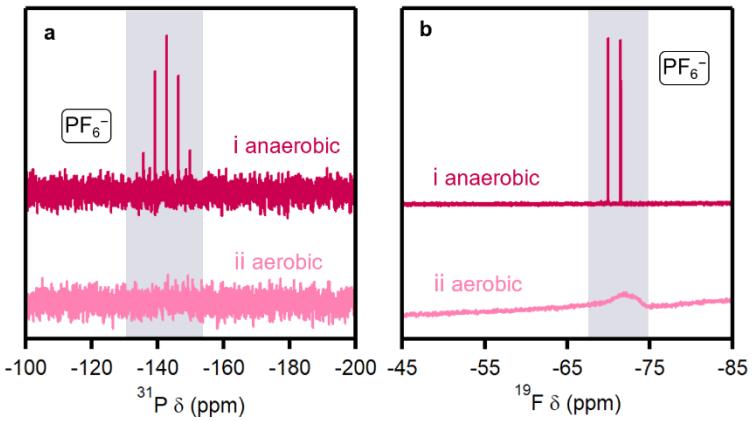

Figure S3. 15.: NMR spectra of the concentrated supernatant oil from reduction with Cu^+ (same experiment as Figure 3.2b; using Synthesis 3, Table S3.1): **(a)** ^{31}P-NMR spectra and **(b)** ^{19}F-NMR spectra (i) before and (ii) after exposure to air.

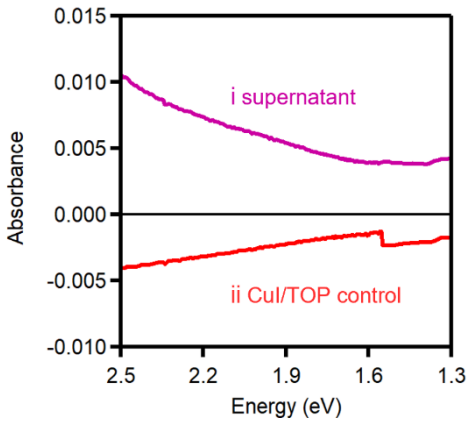

Figure S3. 16. Absorption spectra in air of: (i) the concentrated supernatant oil from oxidation with ZnI_2 and TOP (same experiment as Figure 3.2c; using Synthesis 4, Table S3.1) and (ii) a control solution with CuI and TOP ([Cu] = 0.0063 M, TOP/Cu = 52). Both spectra were collected using 1:5 TOP/THF (by volume) as cuvette solvent.

Section S3.3: Supernatant analysis for oxidation using ZnI_2 and TOP

Unlike the redox experiments using I_2 and Cu^+, the ZnI_2/TOP experiment has no intuitive or literature basis for being a redox reaction. The substantial LSPR blueshift (Figure 3.2c), pXRD lattice contraction (Figure 3.3aiv), and downfield ^{31}P-SSNMR Knight shift (Figure 3.3biv), however, collectively suggest that the ZnI_2/TOP treatment yields a Cu-coupled oxidation of the nanocrystals. Such an oxidation would be expected to lead to an extraction of Cu atoms from nanocrystals into the supernatant.

The supernatant collected during purification after treatment with ZnI_2 and TOP was colorless, as expected for a solution with the d^{10} metal ions Cu^+ and Zn^{2+}. Efforts to oxidize the evaporated supernatant oil in air (as done in Section S3.2) were unsuccessful (Figure S3.16i), likely due to the propensity of copper complexes with alkylphosphine ligands to adopt a 1^+ copper oxidation state. Attempts to oxidize the oil with nitric acid (as done in Section S3.1) failed due to the immiscibility between TOP and nitric acid. These limitations precluded an optical analysis of supernatant Cu content by Cu^{2+} quantification.

An alternative analysis was devised to support the assertion of Cu atom extraction from the oxidized $Cu_{3-x}P$ nanocrystals (for the experiment corresponding to Figure 3.5v), using solution ^{31}P-NMR spectroscopy to empirically determine how Cu perturbs the TOP-derived resonance in the presence of excess Zn/Cu. The supernatant oil was diluted with benzene-d_6 in a 1:6 volume ratio. Four controls were prepared with 4.0 TOP/ZnI_2, three with varying [Zn] and no Cu and the fourth containing 0.083 CuI/ZnI_2 ([Cu+Zn] = 6.8 mM). A sharper peak at −30.4 ppm from unbound TOP[71] is present in the ^{31}P-NMR spectra (Figure S3.17) of the four control solutions and the supernatant, as expected. An additional broader peak, likely from bound TOP, is also present in all three spectra but with a chemical shift which appears to vary with solution Cu content. The

most upfield shift of −31.5 ppm was observed with the Cu-free standards (Figure S3.17i–iii) and the most downfield shift of −30.9 ppm with the 0.083 Cu/Zn ratio standard (Figure S3.22v). If this shift of the broad peak arises from the presence of Cu, the intermediate chemical shift of −31.2 ppm for the supernatant broad peak (Figure S3.22iv) implies that the supernatant has Cu/Zn < 0.083.

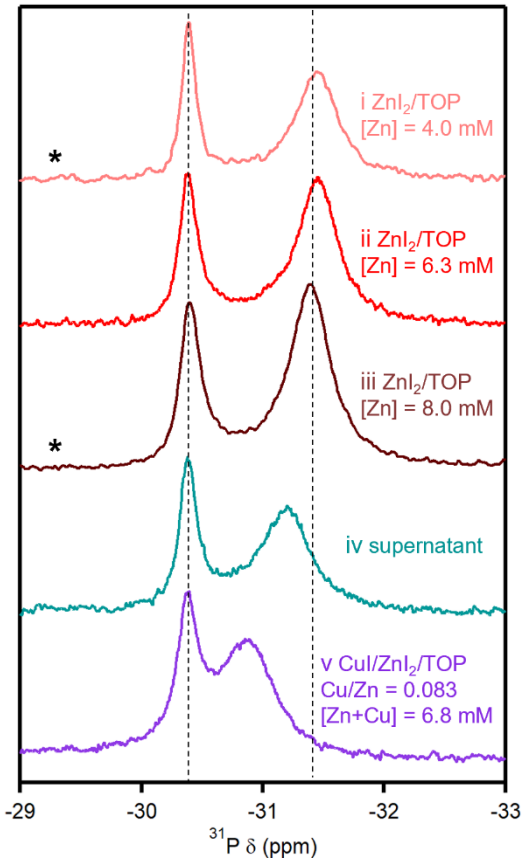

Figure S3. 17. ^{31}P-NMR spectra of: (i–iii) Cu-free control solutions with ZnI_2 and TOP with TOP/Zn = 4.0 (i) [Zn] = 4.0 mM, (ii) [Zn] = 6.3 mM, and (iii) [Zn] = 8.0 mM. (iv) oxidation-with-ZnI_2/TOP supernatant (same experiment as Figure 3.5i, [TOP] ~ 24 mM). (v) control CuI/ZnI_2/TOP solution ([Zn+Cu] = 6.8 mM, TOP/Zn/Cu = 4.0/1.0/0.083). The dotted lines are guides to the eye. Spectra indicated with * were collected using a different spectrometer (JEOL ECA 500 MHz).

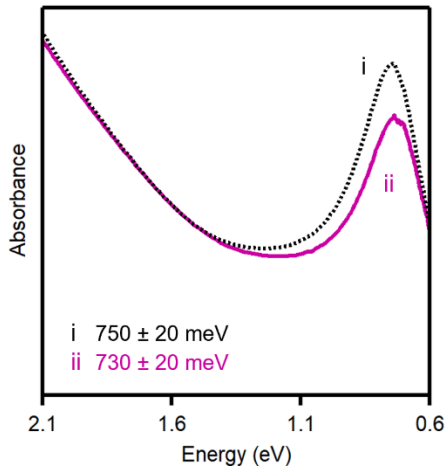

Figure S3. 18. (a) Average (n = 3) absorption spectra of $Cu_{3-x}P$ nanocrystals (i) before and (ii) after reaction with Li^0 in 1:6.8 THF:toluene solution. The ensemble from Synthesis 5 (Table S3.1) was used for this experiment.

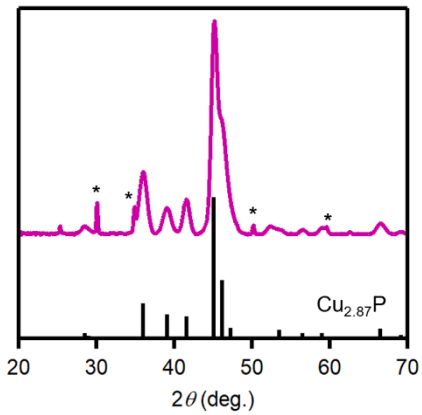

Figure S3. 19. Powder X-ray diffraction pattern of Li/THF-treated $Cu_{3-x}P$ nanocrystals (of Figure S3.18). The simulated pattern for $P6_3cm$ $Cu_{2.87}P$ (ref. 12) is shown for comparison. Asterisks indicate impurity LiCl reflections, ref. 72. The ensemble from Synthesis 5 (Table S3.1) was used for this experiment.

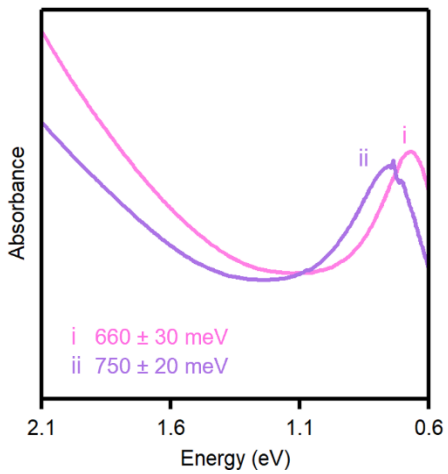

Figure S3. 20. Absorption spectra of $Cu_{3-x}P$ nanocrystals after reduction with Li^0 in 1:28 OAm:toluene solution after (i) 30 min and (ii) 48 h of storage in Li-free toluene. The ensemble from Synthesis 6 (Table S3.1) was used for this experiment.

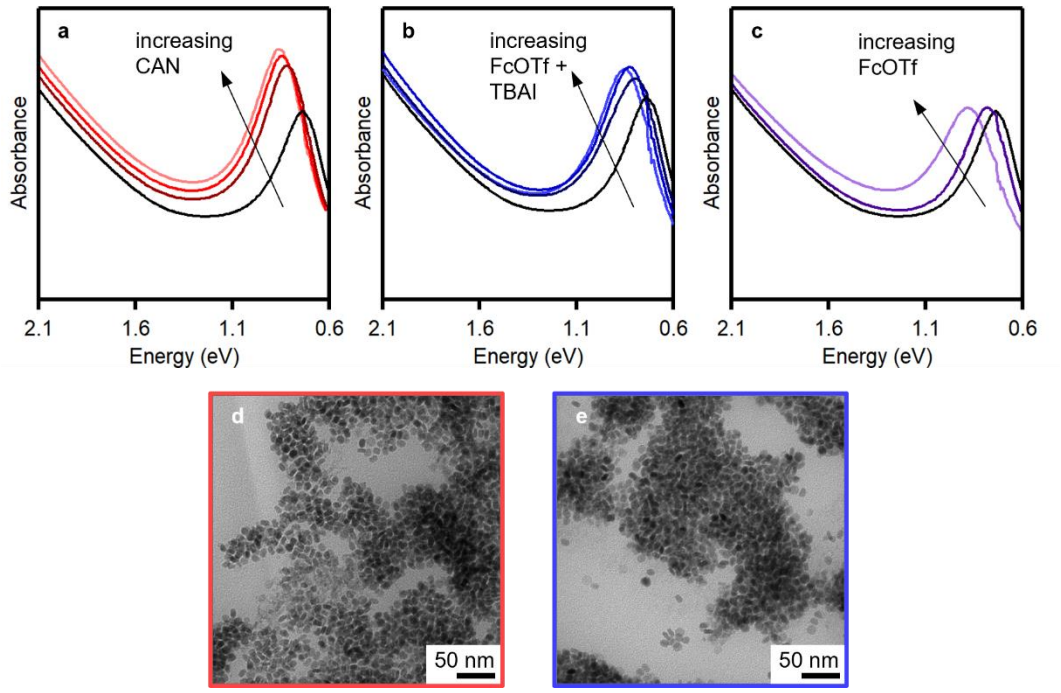

Figure S3. 21. Characterization of as-synthesized $Cu_{3-x}P$ nanocrystals reacted with alternative oxidants on the cuvette-scale. Absorption spectra after addition of up to: **(a)** 0.43 equivalents (equiv) CAN to Cu atoms, **(b)** 0.25 equiv FcOTf and 0.28 equiv TBAI to Cu atoms, and **(c)** 0.34 equiv FcOTf only to Cu atoms. TEM images after oxidation with **(d)** 0.42 equiv CAN to Cu and **(e)** 0.25/0.28 equiv FcOTf/TBAI to Cu. All experiments from this Figure 3.used the same ensemble (Synthesis 6, Table S3.1).

Section S3.4: Drude–Lorentz modelling of optical data

In plasmonic nanocrystals, the observed LSPR frequency, ω_{sp}, correlates with charge carrier concentration, N_h, and also depends on the dielectric constant, ε_m, of the solvent environment and the carrier collision frequency, γ, which is experimentally estimated as the LSPR full width at half maximum. With the assumption that the dielectric function of $Cu_{3-x}P$ in the LSPR region is dominated by free carriers,[48] the bulk plasma frequency, ω_p, can be calculated using Equation S3.5.

$$\omega_p = \sqrt{(\omega_{sp}{}^2 + \gamma^2)(1 + 2\varepsilon_m)} \tag{S3.5}$$

For the 50/50 toluene/THF (by volume) solvent system used for optical measurements in this study, ε_m is approximated as 5.33, which is the corresponding arithmetic mole average of the dielectric constants for toluene (2.38) and THF (7.58). Using the as-synthesized example from Figure 3.1d (ω_{sp} = 744 meV, γ = 233 meV), Equation S3.5 gives ω_p = 2.66 eV (or 4.04 x 10^{15} rad/s). ω_p correlates with N_h, and also depends on the hole effective mass, m_h*, which has been recently calculated for bulk $Cu_{3-x}P$ as a function of transport direction.[56] N_h can be calculated from ω_p and m_h*, using Equation S3.6.

$$N_h = \left(\omega_p{}^2 \varepsilon_0 m_h{}^*\right) \Big/ e^2 \tag{S3.6}$$

m_h* is approximated as $0.67m_e$, where m_e is the electron mass, which was determined by taking the harmonic mean of the calculated ab-plane and c-axis effective masses.[56] Continuing with the use of the as-synthesized example and ω_p = 4.04 x 10^{15} rad/s, use of Equation S3.6 yields an

estimate of N_h = 3.4 x 10^{21} cm^{-3}. Drude–Lorentz calculations using the high frequency dielectric constant, ε_∞,[73] which is approximated as 2.5, from DFT-calculated dielectric function at photon energy = 7 eV for bulk $Cu_{3-x}P$,[56] yield an estimate of N_h = 3.9 x 10^{21} cm^{-3}. The 13% increase is sufficiently small and Equation S3.5 is used for calculation of bulk plasma frequency for the charge carrier concentrations reported in Table 3.1.

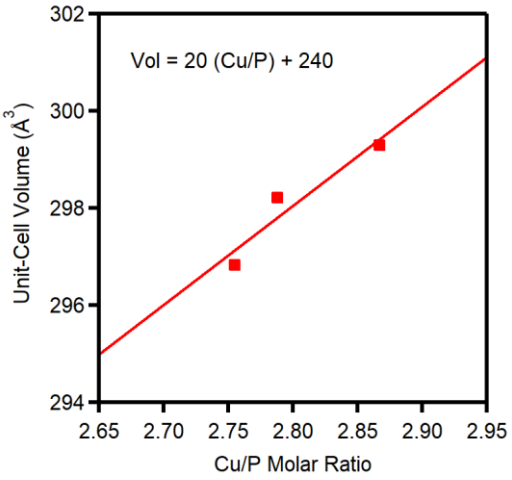

Figure S3. 22. Unit-cell volumes and corresponding compositions of bulk $Cu_{3-x}P$ as reported in ref. 12. The linear regression line-of-best-fit for the three points is plotted. The predicted values and standard errors for the Cu/P molar ratios reported in Tables 3.1 and S3.4 were calculated using the correlation coefficient between unit-cell volume and Cu/P molar ratio and the means and standard deviations for each variable.

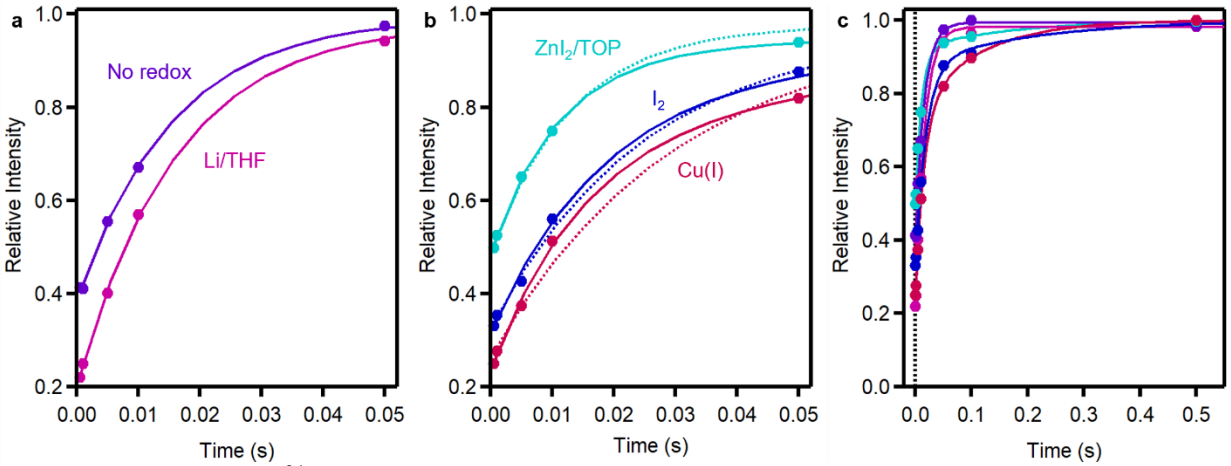

Figure S3. 23. ^{31}P-NMR saturation-recovery T_1 relaxation data (at T = 300 K) and corresponding exponential fits (parameters in Tables 3.1 and S3.3). **(a)** Single-exponential fits for as-synthesized (of Figure 3.3ii) and Li/THF-treated (of Figure S3.18) samples. **(b)** Biexponential (solid) and single exponential (dotted) fits for reduced-with-Cu^+, oxidized-with-I_2, and oxidized-with-ZnI_2/TOP (of Figure 3.3i,iii,iv) samples. **(c)** Overlaid and full-time-scale best fits from (a) and (b).

Table S3. 4. ^{31}P-NMR saturation-recovery T_1 relaxation parameters (at T = 300 K) derived from single-exponential and biexpontial fitting (Figure S3.18).

Experiment	^{31}P δ (ppm)[a]	τ_{single} (ms)	τ_{fast} (ms)	τ_{slow}(ms)	I_{fast} (%)[b]
Cu(I)	101	30 ± 5	15 ± 2	110 ± 40	67
Li/THF	187	16.0 ± 0.8	--	--	--
No redox	186	15.5 ± 0.7	--	--	--
I_2	256	25 ± 4	18 ± 5	200 ± 300	82
ZnI_2/TOP	346	13 ± 2	10.8 ± 0.4	160 ± 40	85

[a]Chemical shift assigned to nanocrystal "core" that was used for saturation-recovery experiments to measure T_1.
[b]$100I_{fast}/(I_{fast} + I_{slow})$

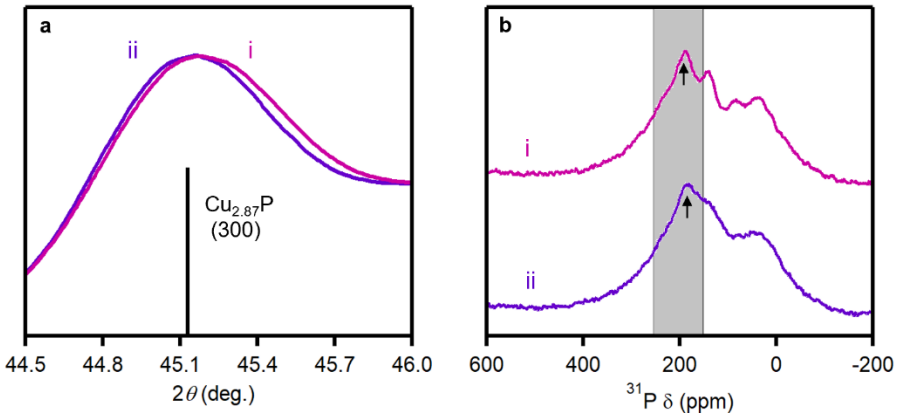

Figure S3. 24. (a) Magnified powder X-ray diffraction patterns (compared to that simulated for *P*6$_3$*cm*, ref. [12]) and **(b)** ^{31}P MAS SSNMR spectra for Cu$_{3-x}$P nanocrystal ensembles: (i) Li/THF-treated and (ii) as-synthesized (reprinted from Figure 3.3ii). Ensembles from Syntheses 5 and 1 (Table S3.1), respectively, were used for these experiments. The arrows indicate the chemical shifts where T_1 was measured. The shaded region corresponds to the bulk Cu$_{3-x}$P Knight shift range reported in ref. 1.

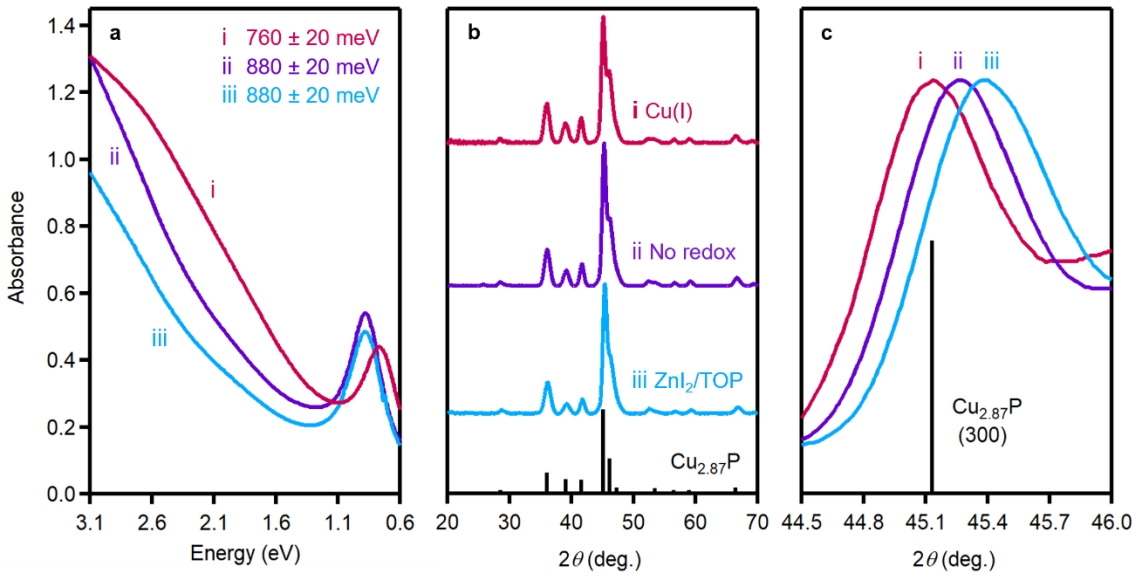

Figure S3. 25. Optical and structural characterization of Cu$_{3-x}$P nanocrystals from the low-temperature synthesis (Synthesis 10, Table S3.1) and its post-synthetic redox products. **(a)** Average (n = 3) absorption spectra and **(b)** full-scale and **(c)** magnified powder X-ray diffraction patterns compared to that simulated for P6$_3$*cm*, ref. 12. Data presented for: (i) Cu$^+$-reduced, (ii) as-synthesized and (iii) ZnI$_2$/TOP-oxidized ensembles.

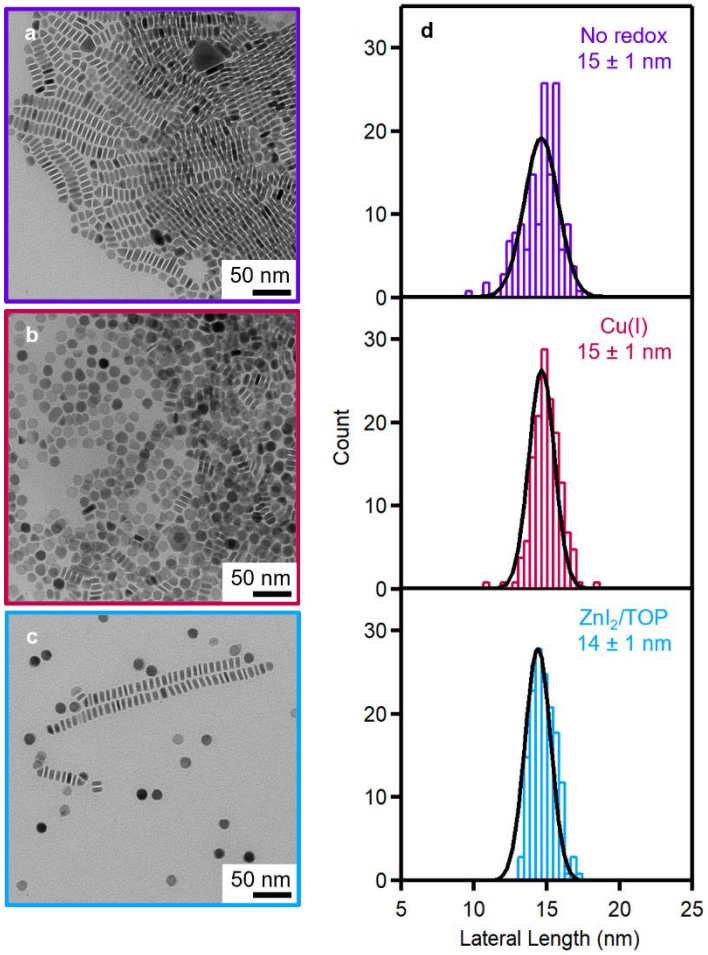

Figure S3. 26. TEM characterization of $Cu_{3-x}P$ nanocrystals from the low-temperature synthesis (Synthesis 10, Table S3.1) and the post-synthetic redox products. TEM images of **(a)** as-synthesized, **(b)** Cu^{+}-reduced, and **(c)** ZnI_2/TOP-oxidized ensembles. **(d)** Statistical analyses (n = 150) of lateral platelet dimension.

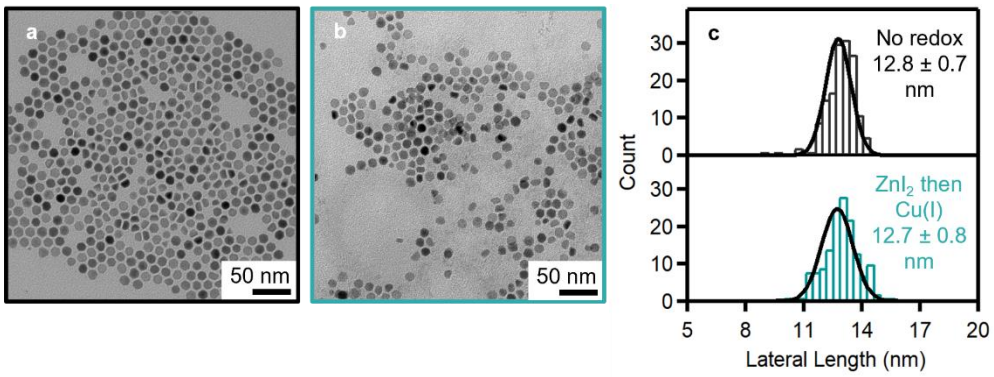

Figure S3. 27. TEM images of $Cu_{3-x}P$ nanocrystals from the ZnI_2/TOP reversibility experiment of Figure 3.4 **(a)** before and **(b)** after oxidation with ZnI_2 and TOP followed by back-reduction with Cu^+. **(c)** Statistical analyses (n = 150) of lateral platelet dimension.

Table S3. 5. $Cu_{3-x}P$ nanocrystal unit-cell volumes, Cu/P molar ratios, and changes to nanocrystal core Cu-atom content for all experiments involving characterization with powder X-ray diffraction.

Synthesis	Redox Experiment	Unit-Cell Volume ($Å^3$)[a]	Cu/P[a]	ΔCu (%) (X-ray)[b]
1	As-synthesized	300.2	2.90	
2	I_2	298.5	2.82	−2
3	Cu(I)	300.9	2.93	+1
4	ZnI_2/TOP	295.2	2.67	−8
5	Li/THF	300.0	2.89	< 1
6	As-synthesized	300.6	2.91	
6	ZnI_2/TOP	295.6	2.69	−8
6	ZnI_2/TOP then Cu(I)	300.9	2.93	< 1
6	I_2	299.8	2.88	−1
6	I_2 then Cu(I)	300.7	2.92	< 1
6	Cu(I)	301.5	2.95	+1
6	Li/OAm	299.3	2.86	−2
7	As-synthesized	300.9	2.93	
7	ZnI_2/TOP (3.9 Zn/Cu)	296.6	2.74	−7
7	$ZnCl_2$/TOP	297.4	2.77	−5
7	CdI_2/TOP	297.5	2.77	−5
7	$CdCl_2$/TOP	297.6	2.78	−5
7	TOP no MX_2	299.3	2.86	−3
7	ZnI_2 no TOP	299.5	2.87	−2
7	$Zn(OAc)_2$/TOP	299.2	2.85	−3
7	ZnI_2/TOP (0.5 Zn/Cu)	298.9	2.84	−2
10	As-synthesized	298.0	2.80	
10	Cu(I)	300.0	2.89	+3
10	ZnI_2/TOP	296.3	2.72	−3

[a]Calculated analogously to Table 3.1 using diffraction data.
[b]Calculated from Cu/P molar ratio change assuming constant P.

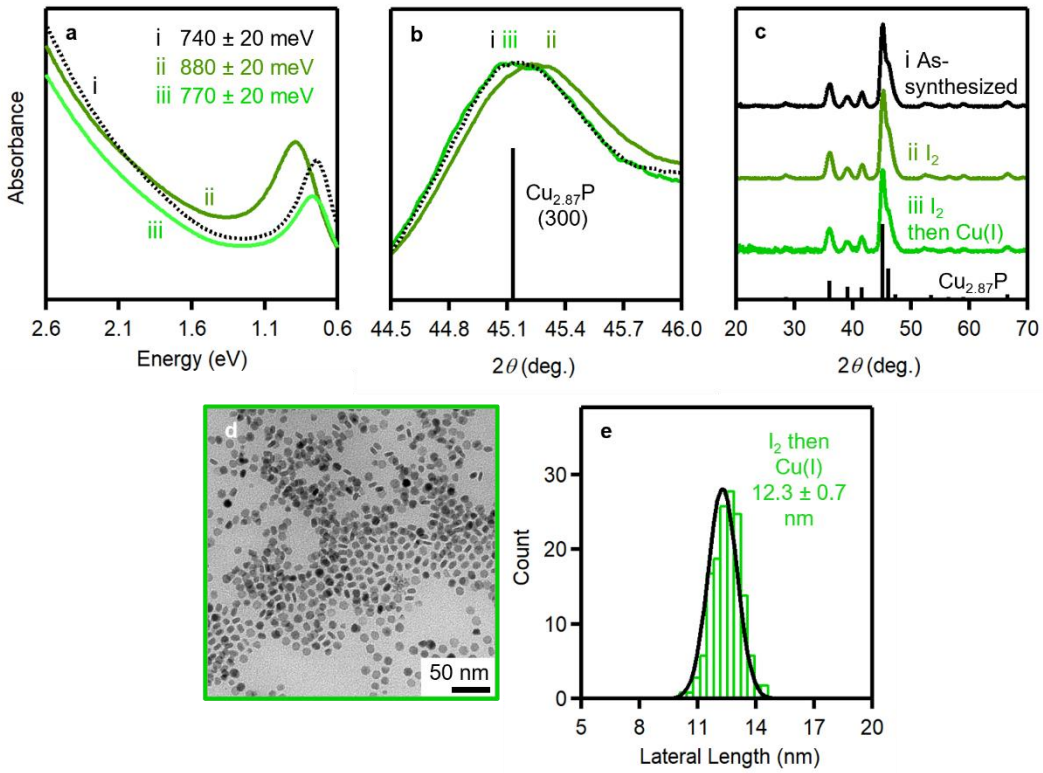

Figure S3. 28. Optical and structural characterization of $Cu_{3-x}P$ nanocrystals from an oxidation reversibility experiment using I_2 and Cu^+. **(a)** Absorption spectra and **(b)** magnified and **(c)** full-scale powder X-ray diffraction patterns compared to that simulated for $P6_3cm$, ref. 12. Data presented for (i) as-synthesized (reprinted from Figure 3.4i), (ii) I_2-oxidized and (iii) Cu^+-back-reduced ensembles. **(d)** TEM image after oxidation with I_2 followed by back-reduction with Cu^+ and **(e)** Statistical analysis (n = 150) of lateral platelet dimension. Nanocrystals from Synthesis 6 (Table S3.1) were used for this experiment. As-synthesized TEM and statistical analysis are presented in Figure S3.27a,c.

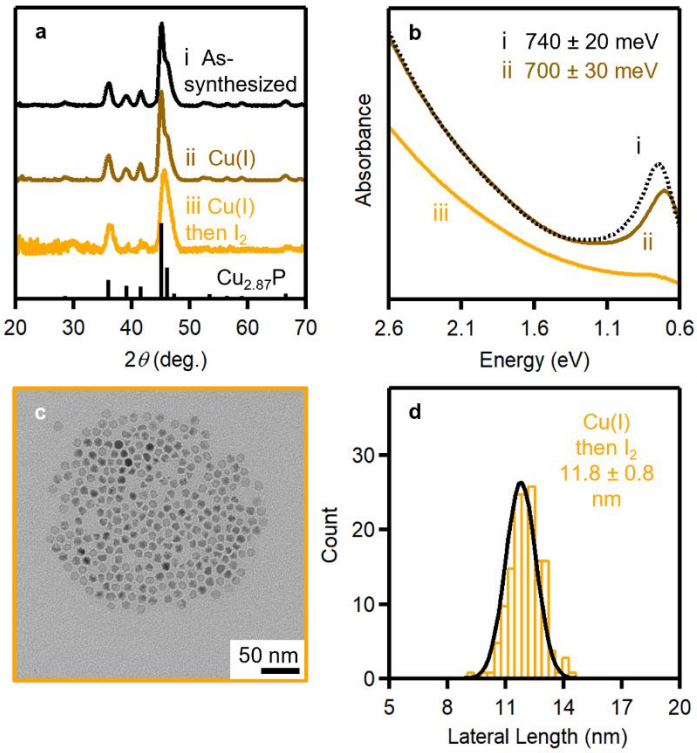

Figure S3. 29. Optical and structural characterization of $Cu_{3-x}P$ nanocrystals from a reduction reversibility experiment using Cu^+ and I_2. **(a)** Powder X-ray diffraction patterns compared to that simulated for $P6_3cm$, ref. 12 and **(b)** absorption spectra. Data presented for (i) as-synthesized (reprinted from Figure 3.4i), (ii) Cu^+-reduced and (iii) I_2-back-oxidized ensembles. **(c)** TEM image after reduction with Cu^+ followed by back-oxidation with I_2 and **(d)** Statistical analysis (n = 150) of lateral platelet dimension. Nanocrystals from Synthesis 6 (Table S3.1) were used for this experiment. As-synthesized TEM and statistical analysis are presented in Figure S3.27a,c.

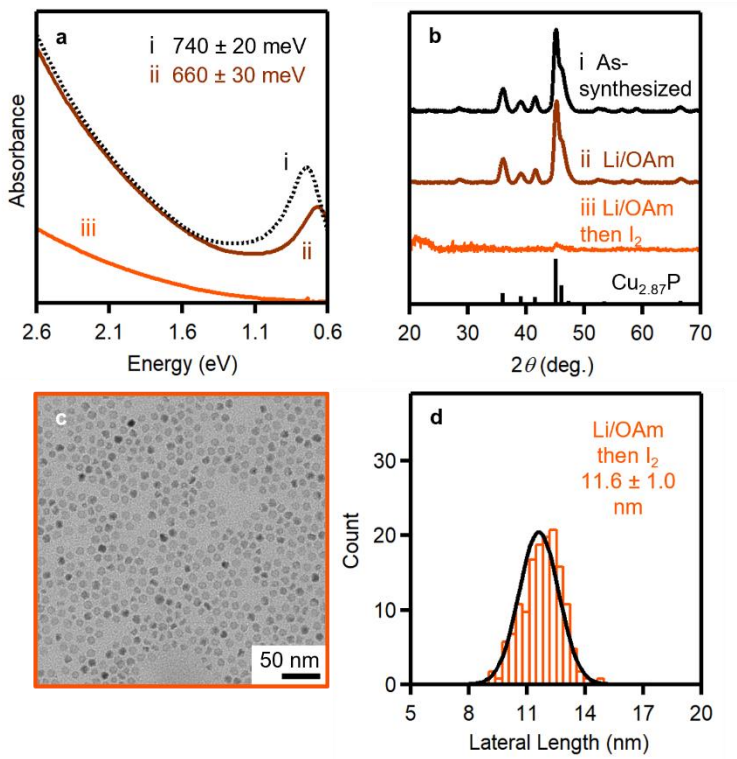

Figure S3. 30. Optical and structural characterization of $Cu_{3-x}P$ nanocrystals from a reduction reversibility experiment using Li/OAm and I_2. **(a)** Absorption spectra and **(b)** powder X-ray diffraction patterns compared to that simulated for $P6_3cm$, ref. 12. Data presented for (i) as-synthesized (reprinted from Figure 3.4i), (ii) Li/OAm-reduced (Figure S3.30aii reprinted from Figure S3.20i) and (ii) I_2-back-oxidized ensembles. **(c)** TEM image after reduction with Li/OAm followed by back-oxidation with I_2 and **(d)** Statistical analysis (n = 150) of lateral platelet dimension. Nanocrystals from Synthesis 6 (Table S3.1) were used for this experiment. As-synthesized TEM and statistical analysis are presented in Figure 3.27a,c.

Table S3. 6. Reaction compositions for post-synthetic MX_2/TOP (M = Zn, Cd; X = Cl, I, OAc) experiments (Figures 3.5, S3.31–34). Amounts of MX_2 salt, TOP, and OAm are given as molar ratios to estimated amounts of Cu atoms in the $Cu_{3-x}P$ nanocrystals. All experiments from this table used the same as-synthesized ensemble (Synthesis 7, Table S3.1).

Post-Synthetic Experiment	M/Cu (M = Zn, Cd)	TOP/Cu	OAm/Cu	[Cu] (M)	Figures
ZnI_2/TOP (3.9 Zn/Cu)	3.9	15.5	3.0	0.081	3.5i, S3.31b
CdI_2/TOP	3.8	15.5	2.9	0.081	3.5ii, S3.31d
ZnI_2/TOP (0.5 Zn/Cu)	0.5	1.9	2.9	0.081	3.5iii
ZnI_2 no TOP	3.9	0	2.9	0.081	3.5iv
$ZnCl_2$/TOP	3.8	15.5	3.1	0.080	S3.34i, S3.31c
$CdCl_2$/TOP	3.8	15.5	3.0	0.081	S3.34ii, S3.31e
TOP no MX_2	0	15.5	2.9	0.081	S3.34iii
OAm only	0	0	2.9	0.081	S3.34iv
$Zn(OAc)_2$/TOP	3.8	15.5	2.9	0.081	S3.31f

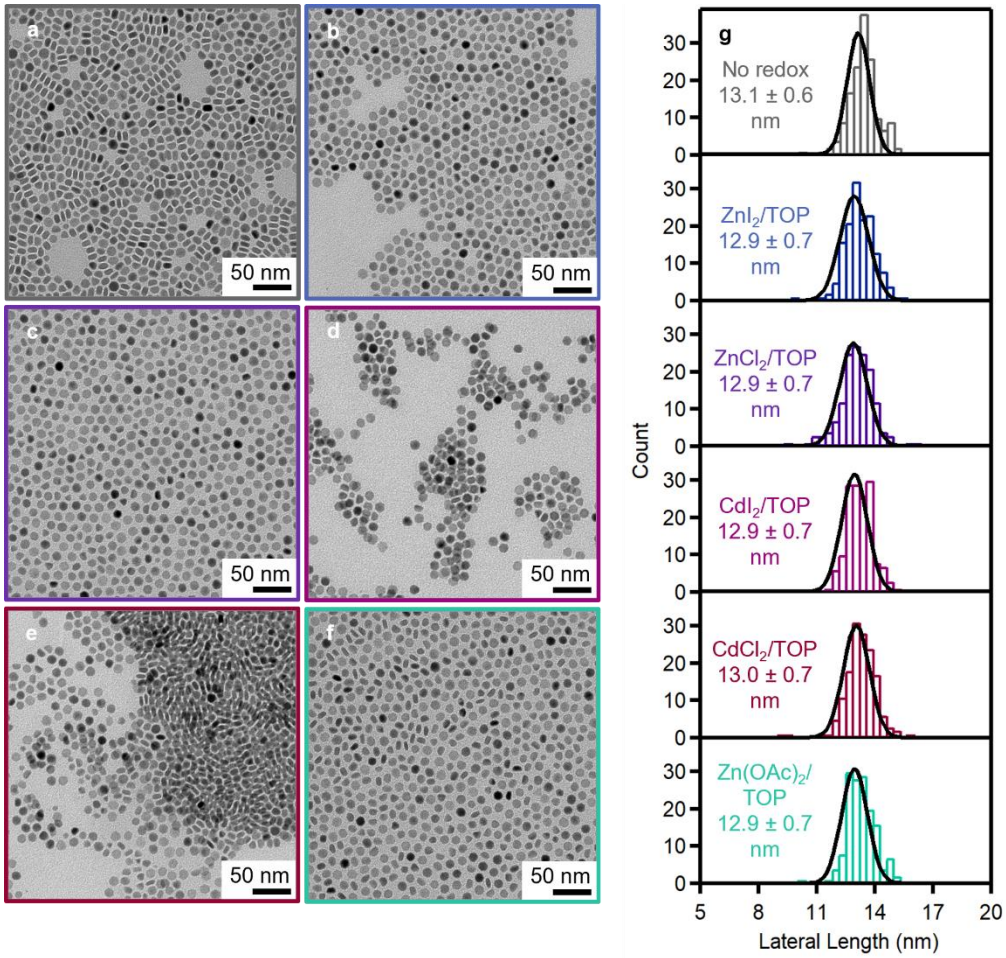

Figure S3. 31. TEM characterization of $Cu_{3-x}P$ nanocrystals from MX_2/TOP (M = Zn, Cd; X = Cl, I, OAc) oxidation experiments of Figure 3.5. TEM images of **(a)** as-synthesized, **(b)** ZnI_2/TOP-oxidized (3.9 Zn/Cu), **(c)** $ZnCl_2$/TOP-oxidized, **(d)** CdI_2/TOP-oxidized, **(e)** $CdCl_2$/TOP-oxidized and **(f)** $Zn(OAc)_2$/TOP-reacted ensembles. **(g)** Statistical analyses (n = 150) of lateral platelet dimension. All experiments used the same as-synthesized ensemble (Synthesis 7, Table S3.1).

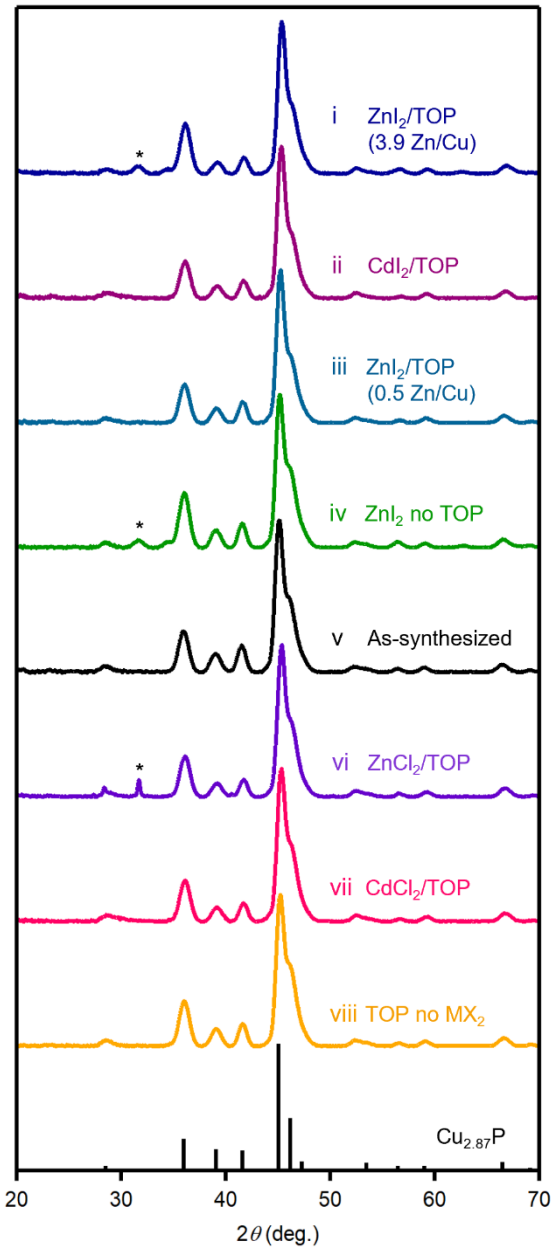

Figure S3. 32. Powder X-ray diffraction patterns for post-synthetic MX_2/TOP (M = Zn, Cd; X = Cl, I) experiments (equivalents and reagents given in Table S3.6) compared to that simulated for $P6_3cm$, ref. 12. Data presented for the following ensembles: (i) ZnI_2/TOP (3.9 Zn/Cu), (ii) CdI_2/TOP, (iii) ZnI_2/TOP (0.5 Zn/Cu), (iv) ZnI_2 (no TOP), (v) as-synthesized, (vi) $ZnCl_2$/TOP, (vii) $CdCl_2$/TOP and (viii) TOP (no MX_2). Asterisks indicate an unindexed peak.

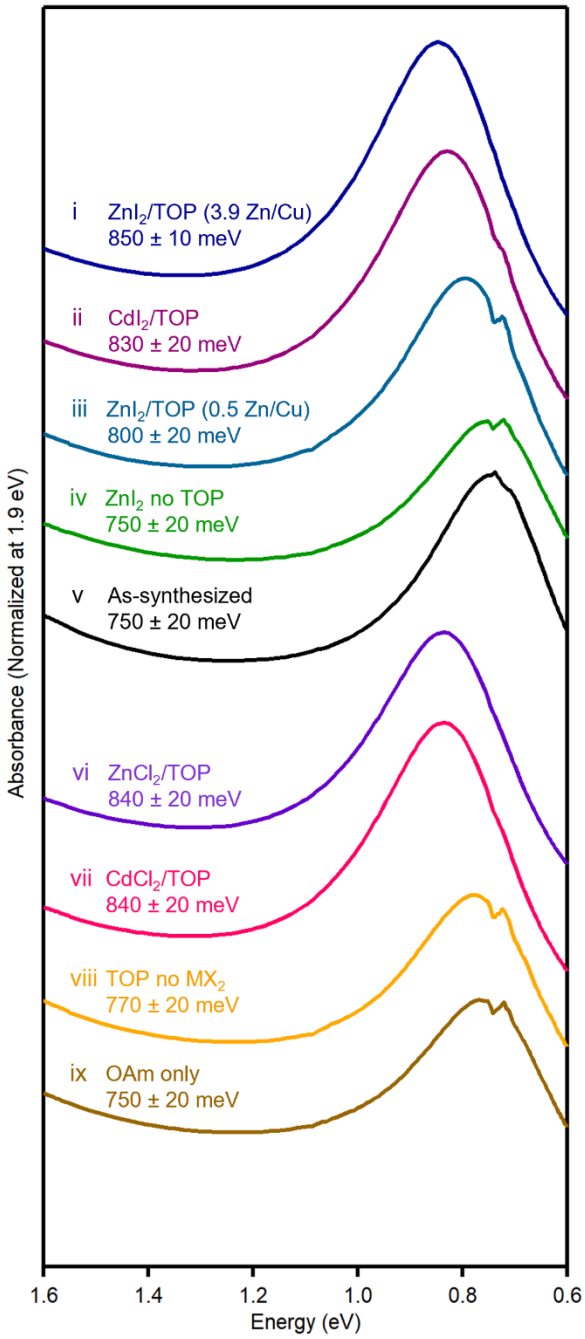

Figure S3. 33. Absorption spectra for post-synthetic MX_2/TOP (M = Zn, Cd; X = Cl, I) experiments (equivalents and reagents given in Table S3.6) compared to that simulated for $P6_3cm$, ref. 12. Data presented for the following ensembles: (i) ZnI_2/TOP (3.9 Zn/Cu), (ii) CdI_2/TOP, (iii) ZnI_2/TOP (0.5 Zn/Cu), (iv) ZnI_2 (no TOP), (v) as-synthesized, (vi) $ZnCl_2$/TOP, (vii) $CdCl_2$/TOP, (viii) TOP (no MX_2) and (ix) OAm only.

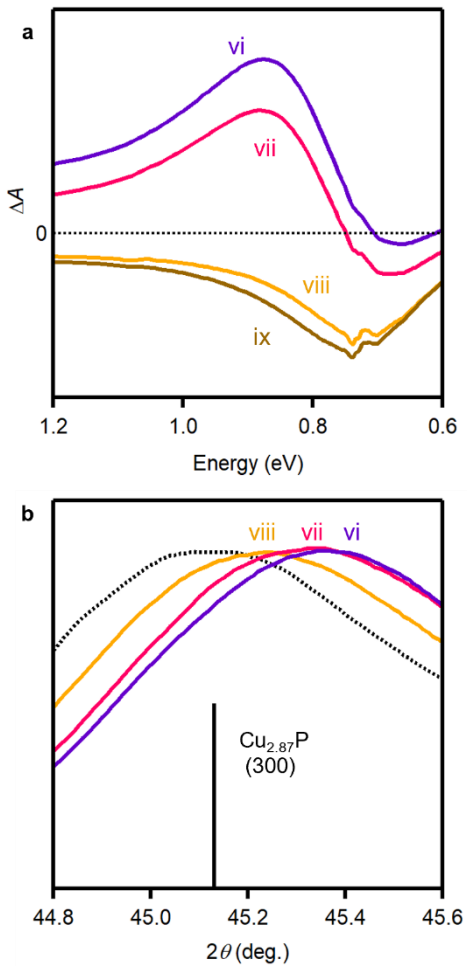

Figure S3. 34. Optical and structural characterizations four of the remaining nine post-synthetic MX_2/TOP (M = Zn, Cd; X = Cl, I) experiments (compositions detailed in Table S3.6). **(a)** Absorption difference spectra ($\Delta A = A_{\text{after oxidation}} - A_{\text{no redox}}$; no normalization) and **(b)** magnified powder X-ray diffraction patterns compared to that simulated for $P6_3cm$, ref. 12. Data presented for ensembles treated with: (vi) $ZnCl_2$/TOP, (vii) $CdCl_2$/TOP, (viii) TOP (no MX_2) and (ix) OAm only. The as-synthesized powder X-ray diffraction is provided as a dashed line for reference. Full-scale powder X-ray diffraction patterns and absorption spectra are shown in Figure S3.32 and S3.33, respectively. Ensemble from Synthesis 7 (Table S3.1) was used for all experiments.

Table S3. 7. ICP–MS elemental analysis of select MX_2/TOP-oxidized and as-synthesized $Cu_{3-x}P$ nanocrystal samples.

Redox Treatment	Synthesis	As-synthesized Cu/P (atom)	Post-redox Cu/P (atom)	M/P (M = Zn, Cd) (atom)	ΔCu/P[a]	| M/ΔCu |
ZnI_2/TOP	6	1.78 ± 0.02	1.51 ± 0.02	0.20 ± 0.01	−0.27 ± 0.03	0.7 ± 0.1
	7	1.81 ± 0.02	1.60 ± 0.02	0.20 ± 0.02	−0.22 ± 0.03	0.9 ± 0.2
	Average	1.80 ± 0.03	1.56 ± 0.04	0.20 ± 0.01	−0.24 ± 0.03	0.8 ± 0.1
CdI_2/TOP	7	1.81 ± 0.02	1.51 ± 0.03	0.14 ± 0.01	−0.30 ± 0.04	0.5 ± 0.1

[a]Calculated with the assumption that P-atom content is unchanged after redox. This assumption is reasonable because the decrease in Cu-atom content by ICP–MS for the Synthesis 7 samples for ZnI_2/TOP and CdI_2/TOP treatments (compared to as-synthesized) are −12 ± 2 % and −14 ± 2 %, respectively.

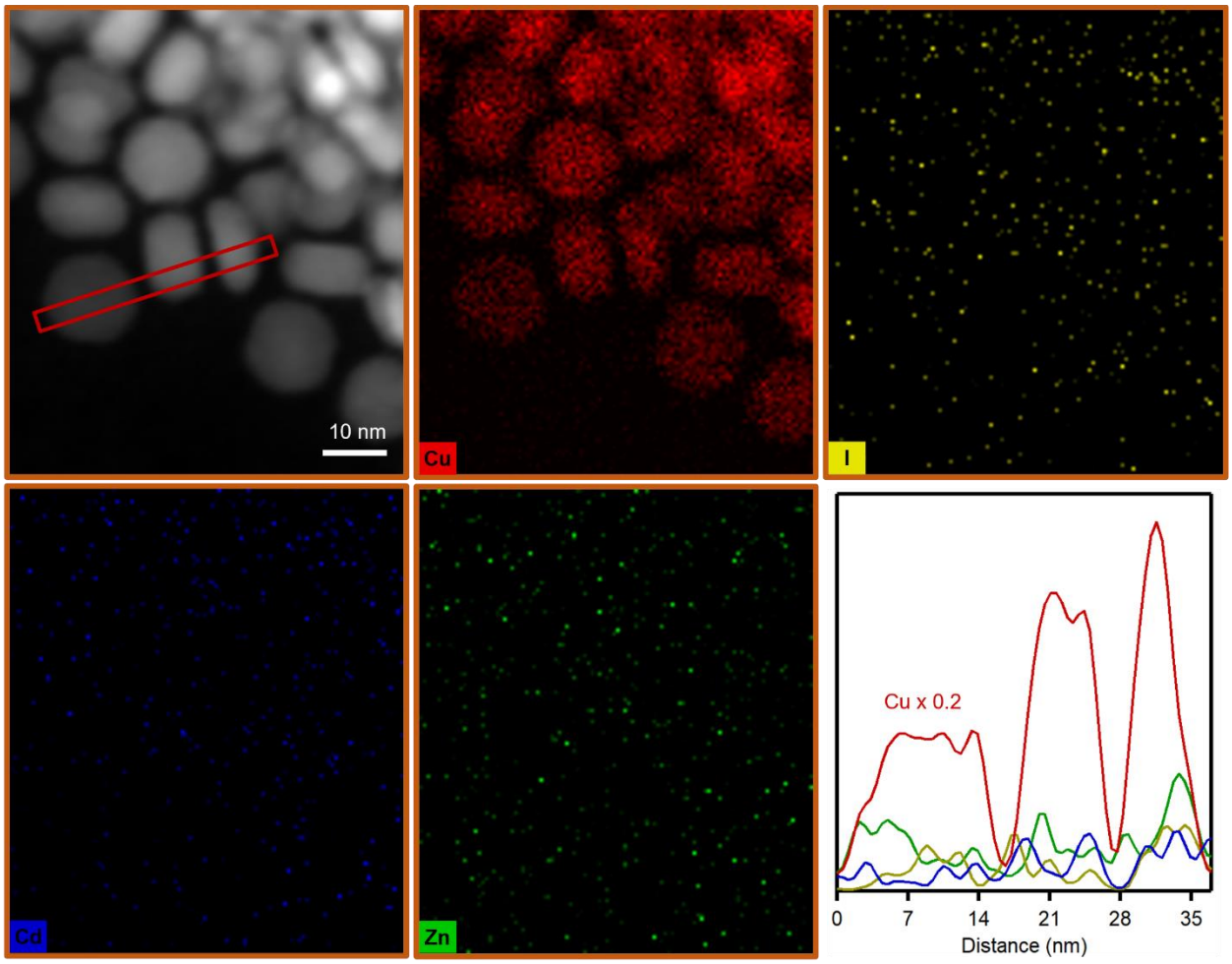

Figure S3. 35. STEM–EDS mapping images and corresponding line-scan of as-synthesized $Cu_{3-x}P$ nanocrystals (Synthesis 7, Table S3.1). Line-scan noise was reduced through binomial smoothing over a 1-nm range of pixels. Mapping reveals the expected result that Cu-Kα signal localizes with the nanoplatelets from the dark-field STEM image. The background Zn-Kα, Cd-Lα and I-Lα signals are also quantified.

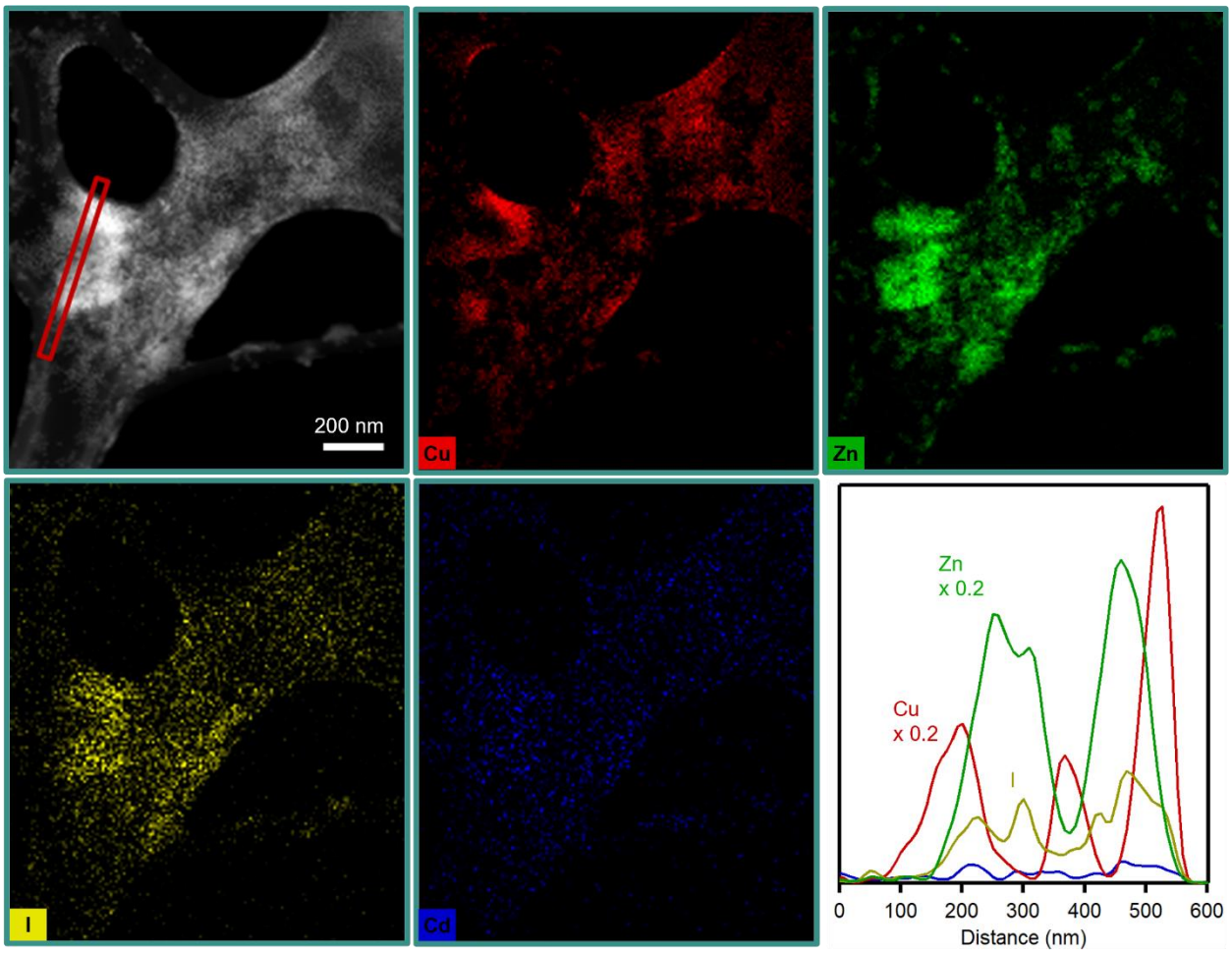

Figure S3. 36. STEM–EDS mapping images and corresponding line-scan of ZnI_2/TOP-oxidized $Cu_{3-x}P$ nanocrystals (Figure 3.5i; Synthesis 7, Table S3.1). Line-scan noise was reduced through binomial smoothing over a 16-nm range of pixels. Lower-resolution mapping reveals Zn aggregation.

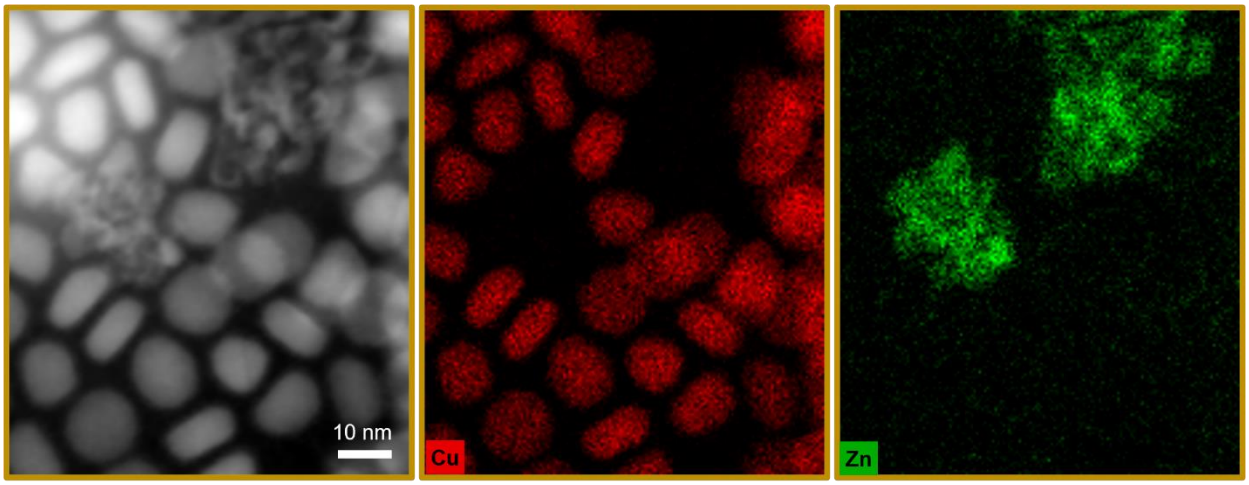

Figure S3. 37. STEM–EDS mapping images of ZnI_2/TOP-oxidized $Cu_{3-x}P$ nanocrystals (Figure 3.5i; Synthesis 7, Table S3.1). Higher-magnification mapping allows confirmation of independent localization for Zn-Kα signal with respect to the nanoplatelet Cu-Kα signal.

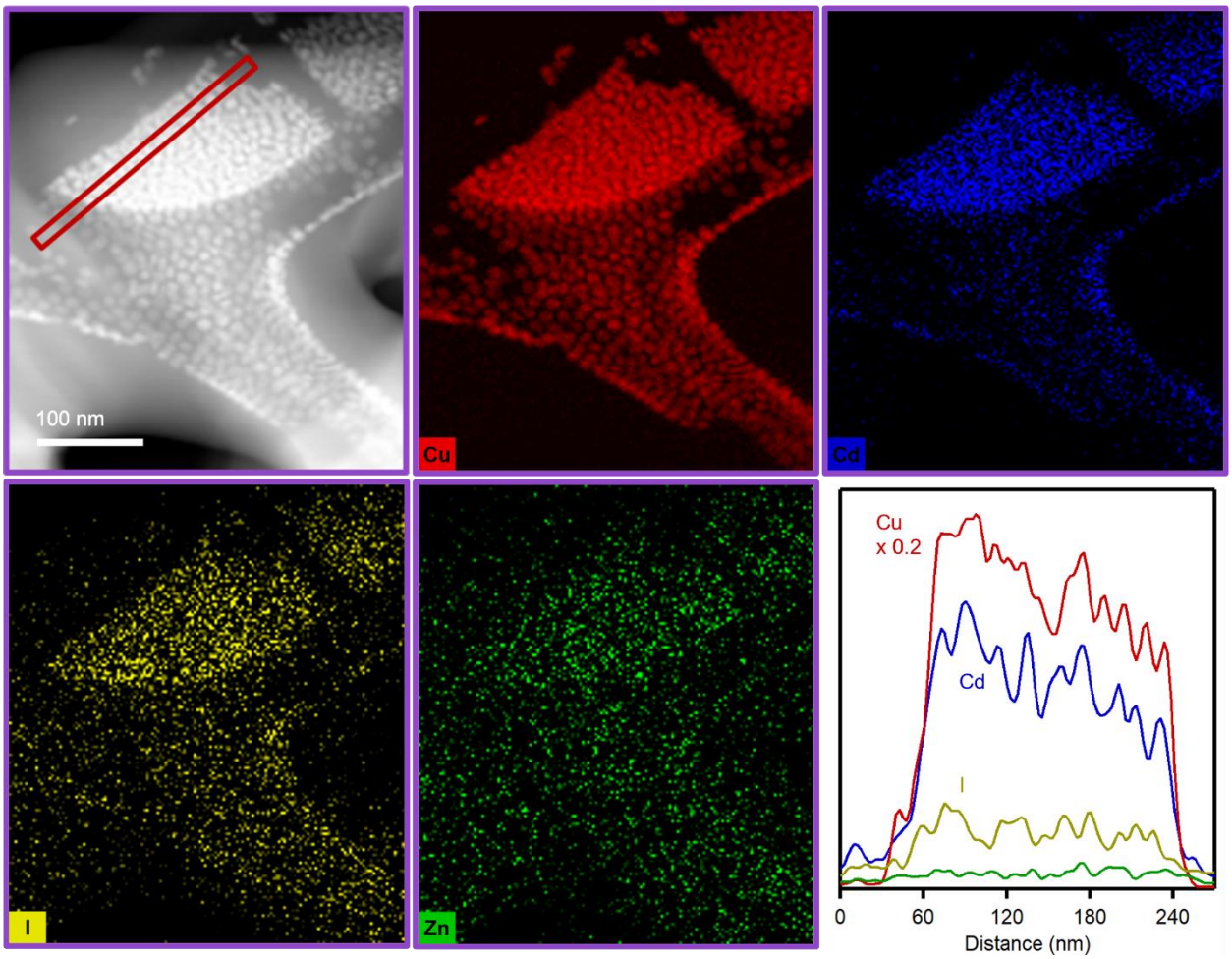

Figure S3. 38. STEM–EDS mapping images and corresponding line-scan of CdI_2/TOP-oxidized $Cu_{3-x}P$ nanocrystals (Figure 3.5ii; Synthesis 7, Table S3.1). Line-scan noise was reduced through binomial smoothing over a 5-nm range of pixels. Mapping reveals a co-localization of Cd-Lα and I-Lα signal with the Cu-Kα signal from the nanoplatelets.

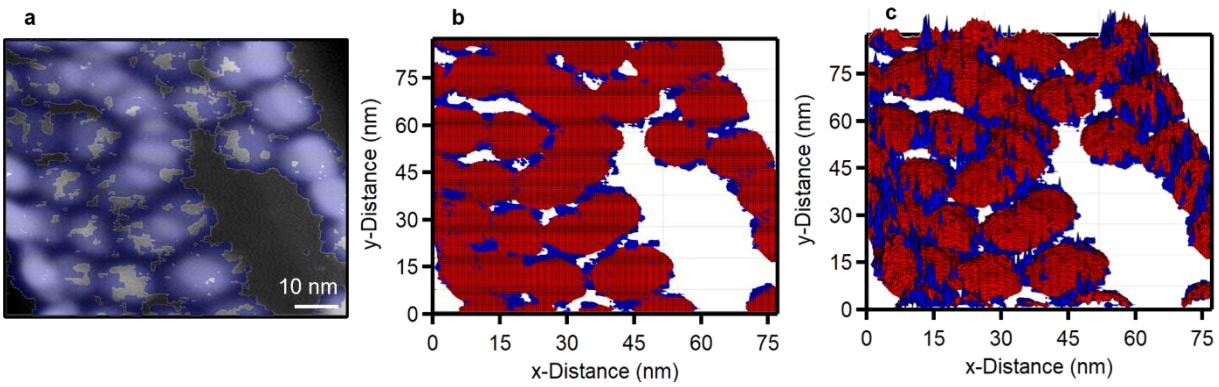

Figure S3. 39. STEM–EDS maps of CdI_2/TOP-oxidized $Cu_{3-x}P$ nanocrystals (Figure 3.5ii; Synthesis 7, Table S3.1) after application of a pixel-wise adaptive low-pass Wiener filter using 5x5 pixel bins (514 pm pixel-length, 6.6 nm^2 area) and exclusion of signal below a noise z-limit. **(a)** top-down 2D-projection Cd-Lα-only map overlaid with its corresponding dark-field STEM image. The corresponding **(b)** top-down 2D-projection and **(c)** 3D map with arbitrarily scaled Cu-Kα signal (red) and Cd-Lα signal (blue).

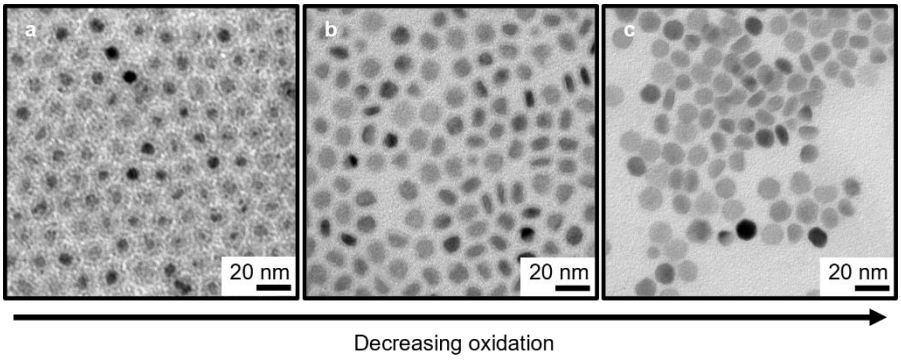

Figure S3. 40. Qualitative TEM assessment of $Cu_{3-x}P$ nanocrystal surface oxidation by observation of low-contrast outer "shells" as a function of time out in air as a dropcast film and number of additional centrifugation purifications. TEM images after **(a)** 4 months in air with 0 extra purifications (Synthesis 1, Table S3.1) and 42 h in air with **(b)** 0 and **(c)** 3 extra purifications (Synthesis 8, Table S3.1). More complete purification and reduced time in air decrease nanocrystal oxidation.

Table S3. 8. Chemicals

Chemical	Purity	Manufacturer
Chemicals used in $Cu_{3-x}P$ nanocrystal synthesis		
Copper(I) chloride (CuCl)	>97%	Strem Chemicals
Oleylamine (OAm)	>98%	Sigma Aldrich
Tris(diethylamino)phosphine ($P(NEt_2)_3$)	97%	Alfa Aesar
Trioctylamine (TOA)	97%	Frontier Scientific
Chemicals used for post-synthetic redox experiments		
n-Butyllithium (nBuLi)	-	Oakwood Chemical (1.6 M, hexane)
Cadmium chloride ($CdCl_2$)	>99%	Fisher Chemical (certified ACS)
Cadmium iodide (CdI_2)	98%	Alfa Aesar
Cerium(IV) ammonium nitrate (CAN)	>98.0%	TCI Chemicals
Copper(II) triflate ($Cu(OTf)_2$)	98%	Oakwood Chemical
Ferrocene	99%	Alfa Aesar
Ferrocenium hexafluorophosphate ($FcPF_6$)	97%	Sigma Aldrich
Lithium metal (Li^0)	>99%	Thermo Scientific Chemicals
Methanol (MeOH)	99.8%	Sigma Aldrich (anh.)
Silver triflate (AgOTf)	99%	Strem Chemicals
Tetrabutylammonium iodide (TBAI)	>98%	TCI Chemicals
Tetrakis(acetonitrile)copper(I) hexafluorophosphate ($[Cu(MeCN)_4]PF_6$)	>98%	Strem Chemicals
Trioctylphosphine (TOP)	>97%	Strem Chemicals
Zinc acetate dihydrate ($Zn(OAc)_2•2H_2O$)	-	Fisher Chemical (cryst./certified)
Zinc chloride ($ZnCl_2$)	99%	Sigma Aldrich (bioreagent)
Zinc iodide (ZnI_2)	>98%	Acros Organics
Other chemicals		
Benzene-d^6	99.5%	Cambridge Isotope Laboratories
Copper metal	99%	Alfa Aesar (−50+70 mesh, semisph.)
Copper(I) iodide (CuI)	98%	Strem Chemicals
Nitric acid (HNO_3)	70% bv	Fisher Chemical (certified ACS plus)
Nitric acid (HNO_3)	70% bv	Fisher Chemical (TraceMetal)

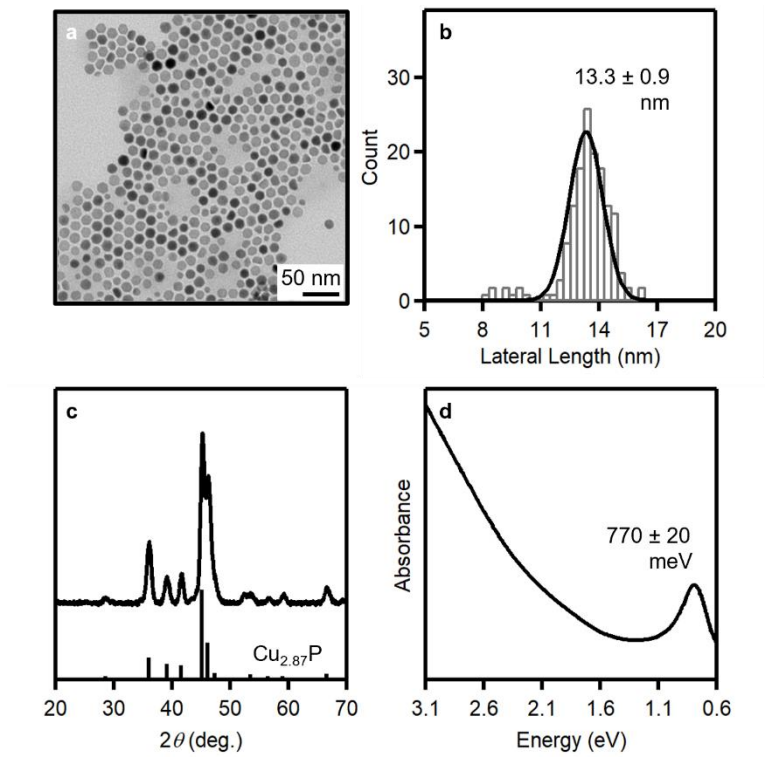

Figure 3. 41. Characterization of as-synthesized $Cu_{3-x}P$ nanocrystals from Synthesis 9 (Table S3.1). **(a)** TEM image, **(b)** statistical analysis (n = 150) of lateral platelet dimension, **(c)** powder X-ray diffraction pattern (compared to that simulated for $P6_3cm$, ref. 12), and **(d)** absorption spectrum.

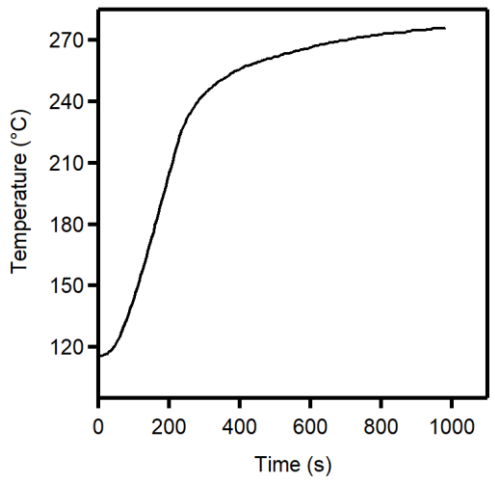

Figure S3. 42. Temperature-profile for the low-volume $Cu_{3-x}P$ nanocrystal heat-up synthesis (9, Table S3.1), which was heated with a contact voltage regulator. The maximum ramp-rate was $dT/dt \approx 35$ °C/min with T_f = 276 °C.

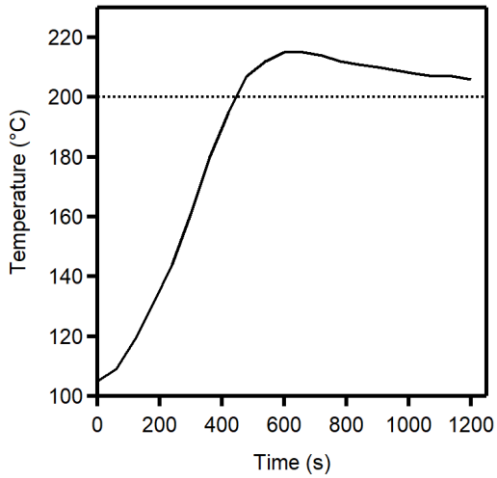

Figure S3. 43. Temperature-profile for the first 10 min of the low-temperature $Cu_{3-x}P$ nanocrystal heat-up synthesis (10, Table S3.1), which was heated with a PID. The maximum ramp-rate was $dT/dt \approx 19$ °C/min and an asymptotic reaction-temperature was $T_f = 200$ °C.

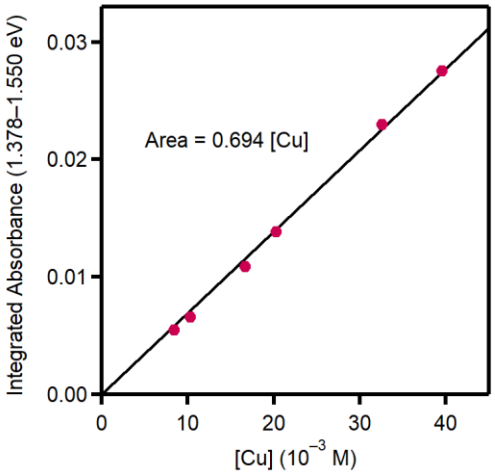

Figure S3. 44. Electronic absorption calibration line for Cu^{2+} quantification with use of nitric acid-digested copper metal as the standard. This relation was used to calculate yields (for Syntheses 1 and 10) or post-redox Cu content (for ensembles from Syntheses 2–5) from Cu^{2+} absorption spectra of digested $Cu_{3-x}P$ nanocrystal solutions. It was also used to estimate Cu content of the supernatant residue from the oxidation-with-I_2 experiment of Figure 3.2a (Section S3.1).

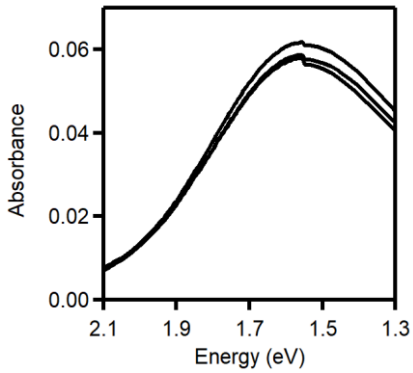

Figure S3. 45. Three independently measured absorption spectra of Cu^{2+} in nitric acid solutions from digestions of $Cu_{3-x}P$ nanocrystals for Synthesis 10 (Table S3.1, Figures S3.25–26). Each spectrum was collected by addition of 800 µl nitric acid to a purified $Cu_{3-x}P$ nanocrystal pellet prepared from 60 µl stock solution.

Table S3. 9. Cu-based extinction coefficients for $Cu_{3-x}P$ nanocrystal ensembles and their respective LSPR peak energies.

Synthesis	Post-Synthetic Redox Treatment	$\varepsilon_{3.1eV}^{Cu}$ $(\frac{L}{mol\ Cu \times cm})$	E_{LSPR} (meV)
1	As-synthesized	2100 ± 200	740 ± 20
2	I_2	2200 ± 100	840 ± 20
3	Cu(I)	2200 ± 200	700 ± 20
4	ZnI_2/TOP	2200 ± 100	890 ± 10
5	Li/THF	2000 ± 100	730 ± 20
10	As-synthesized	2000 ± 300	880 ± 20

3.8 Acknowledgements

Chapter 3, in part, is currently being prepared for imminent submission for publication of the material. The dissertation author was the primary author of this paper and gratefully acknowledges the contributions of coauthors Kevin R. Chalek, Mingjie Xu, Gregory P. Holland, and Alina M. Schimpf. This research was primarily supported by the National Science Foundation through the UC San Diego Materials Research Science and Engineering Center (DMR-2011924). TEM imaging was performed at the National Center for Microscopy and Imaging Research at UC San Diego. Powder X-ray diffraction measurements were performed at the UC San Diego Crystallography Facility with the welcome technical guidance of Dr. Milan Gembicky. STEM–EDS imaging and mapping were performed at the Irvine Materials Research Institute. The authors thank Haeun Chang for assistance with ICP–MS data collection, which was performed at the Environmental and Complex Analysis Laboratory at UC San Diego.

3.9 References

1. Wolff, A.; Doert, T.; Hunger, J.; Kaiser, M.; Pallmann, J.; Reinhold, R.; Yogendra, S.; Giebeler, L.; Sichelschmidt, J.; Schnelle, W.; Whiteside, R.; Nimal Gunaratne, H. Q.; Nockemann, P.; Weigand, J. J.; Brunner, E.; Ruck, M. Low-Temperature Tailoring of Copper-Deficient $Cu_{3-x}P$ — Electric Properties, Phase Transitions, and Performance in Lithium-Ion Batteries. *Chem. Mater.* **2018,** *30*, 7111.

2. Crosnier, O.; Nazar, L. F. Facile Reversible Displacement Reaction of Cu_3P with Lithium at Low Potential. *Electrochem. Solid St.* **2004,** *7*, A187.

3. Wei, S.; Qi, K.; Jin, Z.; Cao, J.; Zheng, W.; Chen, H.; Cui, X. One-Step Synthesis of a Self-Supported Copper Phosphide Nanobush for Overall Water Splitting. *ACS Omega* **2016,** *1*, 1367.

4. Tappan, B. A.; Chen, K.; Lu, H.; Sharada, S. M.; Brutchey, R. L. Synthesis and Electrocatalytic HER Studies of Carbene-Ligated $Cu_{3-x}P$ Nanocrystals. *ACS Appl. Mater. Interfaces* **2020,** *12*, 16394.

5. Sun, T.; Wang, Y.; Yu, W.; Wang, Y.; Dai, Z.; Liu, Z.; Shivananju, B. N.; Zhang, Y.; Fu, K.; Shabbir, B.; Ma, W.; Li, S.; Bao, Q. Flexible Broadband Graphene Photodetectors Enhanced by Plasmonic $Cu_{3-x}P$ Colloidal Nanocrystals. *Small* **2017,** *13*, 1701881.

6. Kumar, S.; Aziz, S. K. T.; Kumar, S.; Riyajuddin, S.; Yaniv, G.; Meshi, L.; Nessim, G. D.; Ghosh, K. Three-Dimensional Graphene-Decorated Copper-Phosphide (Cu_3P@3DG) Heterostructure as an Effective Electrode for a Supercapacitor. *Front. Mater.* **2020,** *7*, 30.

7. Liu, Y.; Wu, J.; Jin, Y.; Zhen, W.; Wang, Y.; Liu, J.; Jin, L.; Zhang, S.; Zhao, Y.; Song, S.; Yang, Y.; Zhang, H. Copper(I) Phosphide Nanocrystals for In Situ Self-Generation Magnetic Resonance Imaging-Guided Photothermal-Enhanced Chemodynamic Synergetic Therapy Resisting Deep-Seated Tumor. *Adv. Funct. Mater.* **2019,** *29*, 1904678.

8. De Trizio, L.; Gaspari, R.; Bertoni, G.; Kriegel, I.; Moretti, L.; Scotognella, F.; Maserati, L.; Zhang, Y.; Messina, G. C.; Prato, M.; Marras, S.; Cavalli, A.; Manna, L. $Cu_{3-x}P$ Nanocrystals as a Material Platform for Near-Infrared Plasmonics and Cation Exchange Reactions. *Chem. Mater.* **2015,** *27*, 1120.

9. Koh, S.; Kim, W. D.; Bae, W. K.; Lee, Y. K.; Lee, D. C. Controlling Ion-Exchange Balance and Morphology in Cation Exchange from $Cu_{3-x}P$ Nanoplatelets into InP Crystals. *Chem. Mater.* **2019,** *31*, 1990.

10. Sheets, E. J.; Yang, W.-C.; Balow, R. B.; Wang, Y.; Walker, B. C.; Stach, E. A.; Agrawal, R. An in Situ Phosphorus Source for the Synthesis of Cu_3P and the Subsequent Conversion to Cu_3PS_4 Nanoparticle Clusters. *J. Mater. Res.* **2015,** *30*, 3710.

11. Lee, J. M.; Kraynak, L. A.; Prieto, A. L. A Directed Route to Colloidal Nanoparticle Synthesis of the Copper Selenophosphate Cu_3PSe_4. *Angew. Chem. Int. Ed.* **2020,** *59*, 3038.

12. Olofsson, O. The Crystal Structure of Cu_3P. *Acta Chem. Scand.* **1972,** *26*, 2777.

13. Schlenger, H.; Jacobs, H.; Juza, R. Ternäre Phasen des Lithiums mit Kupfer und Phosphor. *Z. Anorg. Allg. Chem.* **1971,** *385*, 177.

14. Bertoni, G.; Ramasse, Q.; Brescia, R.; De Trizio, L.; De Donato, F.; Manna, L. Direct Quantification of Cu Vacancies and Spatial Localization of Surface Plasmon Resonances in Copper Phosphide Nanocrystals. *ACS Mater. Lett.* **2019,** *1*, 665.

15. Manna, G.; Bose, R.; Pradhan, N. Semiconducting and Plasmonic Copper Phosphide Platelets. *Angew. Chem. Int. Ed.* **2013,** *52*, 6762.

16. Rachkov, A. G.; Schimpf, A. M. Colloidal Synthesis of Tunable Copper Phosphide Nanocrystals. *Chem. Mater.* **2021,** *33*, 1394.

17. Liu, Z.; Mu, H.; Xiao, S.; Wang, R.; Wang, W.; Wang, Y.; Zhu, X.; Lu, K.; Zhang, H.; Lee, S.-T.; Bao, Q.; Ma, W. Pulsed Lasers Employing Solution-Processed Plasmonic $Cu_{3-x}P$ Colloidal Nanocrystals. *Adv. Mater.* **2016,** *28*, 3535.

18. Schimpf, A. M.; Knowles, K. E.; Carroll, G. M.; Gamelin, D. R. Electronic Doping and Redox-Potential Tuning in Colloidal Semiconductor Nanocrystals. *Acc. Chem. Res.* **2015,** *48*, 1929.

19. Nutz, T.; zum Felde, U.; Haase, M. Wet-Chemical Synthesis of Doped Nanoparticles: Blue-Colored Colloids of n-Doped SnO_2 : Sb. *J. Chem. Phys.* **1999,** *110*, 12142.

20. Kanehara, M.; Koike, H.; Yoshinaga, T.; Teranishi, T. Indium Tin Oxide Nanoparticles with Compositionally Tunable Surface Plasmon Resonance Frequencies in the Near-IR Region. *J. Am. Chem. Soc.* **2009,** *131*, 17736.

21. Zhao, Y.; Pan, H.; Lou, Y.; Qiu, X.; Zhu, J.; Burda, C. Plasmonic $Cu_{2-x}S$ Nanocrystals: Optical and Structural Properties of Copper-Deficient Copper(I) Sulfides. *J. Am. Chem. Soc.* **2009,** *131*, 4253.

22. Buonsanti, R.; Llordes, A.; Aloni, S.; Helms, B. A.; Milliron, D. J. Tunable Infrared Absorption and Visible Transparency of Colloidal Aluminum-Doped Zinc Oxide Nanocrystals. *Nano Lett.* **2011,** *11*, 4706.

23. Rowe, D. J.; Jeong, J. S.; Mkhoyan, K. A.; Kortshagen, U. R. Phosphorus-Doped Silicon Nanocrystals Exhibiting Mid-Infrared Localized Surface Plasmon Resonance. *Nano Lett.* **2013,** *13*, 1317.

24. Fang, H. B.; Hegde, M.; Yin, P. H.; Radovanovic, P. V. Tuning Plasmon Resonance of In_2O_3 Nanocrystals throughout the Mid-Infrared Region by Competition between Electron Activation and Trapping. *Chem. Mater.* **2017,** *29*, 4970.

25. Marbella, L. E.; Gan, X. Y.; Kaseman, D. C.; Millstone, J. E. Correlating Carrier Density and Emergent Plasmonic Features in $Cu_{2-x}Se$ Nanoparticles. *Nano Lett.* **2017,** *17*, 2414.

26. Limpens, R.; Pach, G. F.; Mulder, D. W.; Neale, N. R. Size-Dependent Asymmetric Auger Interactions in Plasma-Produced n- and p-Type-Doped Silicon Nanocrystals. *J. Phys. Chem. C* **2019,** *123*, 5782.

27. Palomaki, P. K. B.; Miller, E. M.; Neale, N. R. Control of Plasmonic and Interband Transitions in Colloidal Indium Nitride Nanocrystals. *J. Am. Chem. Soc.* **2013,** *135*, 14142.

28. Dorfs, D.; Härtling, T.; Miszta, K.; Bigall, N. C.; Kim, M. R.; Genovese, A.; Falqui, A.; Povia, M.; Manna, L. Reversible Tunability of the Near-Infrared Valence Band Plasmon Resonance in $Cu_{2-x}Se$ Nanocrystals. *J. Am. Chem. Soc.* **2011,** *133*, 11175.

29. Kriegel, I.; Jiang, C.; Rodríguez-Fernández, J.; Schaller, R. D.; Talapin, D. V.; da Como, E.; Feldmann, J. Tuning the Excitonic and Plasmonic Properties of Copper Chalcogenide Nanocrystals. *J. Am. Chem. Soc.* **2012,** *134*, 1583.

30. Niezgoda, J. S.; Harrison, M. A.; McBride, J. R.; Rosenthal, S. J. Novel Synthesis of Chalcopyrite $Cu_xIn_yS_2$ Quantum Dots with Tunable Localized Surface Plasmon Resonances. *Chem. Mater.* **2012,** *24*, 3294.

31. Xie, Y.; Riedinger, A.; Prato, M.; Casu, A.; Genovese, A.; Guardia, P.; Sottini, S.; Sangregorio, C.; Miszta, K.; Ghosh, S.; Pellegrino, T.; Manna, L. Copper Sulfide Nanocrystals with Tunable Composition by Reduction of Covellite Nanocrystals with Cu^+ Ions. *J. Am. Chem. Soc.* **2013,** *135*, 17630.

32. Schimpf, A. M.; Thakkar, N.; Gunthardt, C. E.; Masiello, D. J.; Gamelin, D. R. Charge-Tunable Quantum Plasmons in Colloidal Semiconductor Nanocrystals. *ACS Nano* **2014,** *8*, 1065.

33. Gan, X. Y.; Keller, E. L.; Warkentin, C. L.; Crawford, S. E.; Frontiera, R. R.; Millstone, J. E. Plasmon-Enhanced Chemical Conversion Using Copper Selenide Nanoparticles. *Nano Lett.* **2019,** *19*, 2384.

34. Della Valle, G.; Scotognella, F.; Kandada, A. R. S.; Zavelani-Rossi, M.; Li, H.; Conforti, M.; Longhi, S.; Manna, L.; Lanzani, G.; Tassone, F. Ultrafast Optical Mapping of Nonlinear Plasmon Dynamics in $Cu_{2-x}Se$ Nanoparticles. *J. Phys. Chem. Lett.* **2013,** *4*, 3337.

35. Scotognella, F.; Della Valle, G.; Srimath Kandada, A. R.; Dorfs, D.; Zavelani-Rossi, M.; Conforti, M.; Miszta, K.; Comin, A.; Korobchevskaya, K.; Lanzani, G.; Manna, L.; Tassone, F. Plasmon Dynamics in Colloidal $Cu_{2-x}Se$ Nanocrystals. *Nano Lett.* **2011,** *11*, 4711.

36. Li, W.; Zamani, R.; Rivera Gil, P.; Pelaz, B.; Ibáñez, M.; Cadavid, D.; Shavel, A.; Alvarez-Puebla, R. A.; Parak, W. J.; Arbiol, J.; Cabot, A. CuTe Nanocrystals: Shape and Size Control, Plasmonic Properties, and Use as SERS Probes and Photothermal Agents. *J. Am. Chem. Soc.* **2013,** *135*, 7098.

37. Shim, M.; Guyot-Sionnest, P. n-Type Colloidal Semiconductor Nanocrystals. *Nature* **2000,** *407*, 981.

38. Chikan, V. Challenges and Prospects of Electronic Doping of Colloidal Quantum Dots: Case Study of CdSe. *J. Phys. Chem. Lett.* **2011,** *2*, 2783.

39. Vanmaekelbergh, D.; Liljeroth, P. Electron-Conducting Quantum Dot Solids: Novel Materials Based on Colloidal Semiconductor Nanocrystals. *Chem. Soc. Rev.* **2005,** *34*, 299.

40. Lhuillier, E.; Guyot-Sionnest, P. Recent Progresses in Mid Infrared Nanocrystal Optoelectronics. *IEEE J. Sel. Top. Quantum Electron.* **2017,** *23*.

41. Faucheaux, J. A.; Stanton, A. L. D.; Jain, P. K. Plasmon Resonances of Semiconductor Nanocrystals: Physical Principles and New Opportunities. *J. Phys. Chem. Lett.* **2014,** *5*, 976.

42. Liu, W. K.; Whitaker, K. M.; Smith, A. L.; Kittilstved, K. R.; Robinson, B. H.; Gamelin, D. R. Room-Temperature Electron Spin Dynamics in Free-Standing ZnO Quantum Dots. *Phys. Rev. Lett.* **2007,** *98*, 186804.

43. Haase, M.; Weller, H.; Henglein, A. Photochemistry and Radiation-Chemistry of Colloidal Semiconductors. 23. Electron Storage on ZnO Particles and Size Quantization. *J. Phys. Chem.* **1988,** *92*, 482.

44. Hartstein, K. H.; Brozek, C. K.; Hinterding, S. O. M.; Gamelin, D. R. Copper-Coupled Electron Transfer in Colloidal Plasmonic Copper-Sulfide Nanocrystals Probed by in Situ Spectroelectrochemistry. *J. Am. Chem. Soc.* **2018,** *140*, 3434.

45. Hsu, S.-W.; On, K.; Tao, A. R. Localized Surface Plasmon Resonances of Anisotropic Semiconductor Nanocrystals. *J. Am. Chem. Soc.* **2011,** *133*, 19072.

46. Hsu, S.-W.; Bryks, W.; Tao, A. R. Effects of Carrier Density and Shape on the Localized Surface Plasmon Resonances of $Cu_{2-x}S$ Nanodisks. *Chem. Mater.* **2012,** *24*, 3765.

47. Kriegel, I.; Rodriguez-Fernandez, J.; Wisnet, A.; Zhang, H.; Waurisch, C.; Eychmuller, A.; Dubavik, A.; Govorov, A. O.; Feldmann, J. Shedding Light on Vacancy-Doped Copper Chalcogenides: Shape-Controlled Synthesis, Optical Properties, and Modeling of Copper Telluride Nanocrystals with Near-Infrared Plasmon Resonances. *ACS Nano* **2013,** *7*, 4367.

48. Luther, J. M.; Jain, P. K.; Ewers, T.; Alivisatos, A. P. Localized Surface Plasmon Resonances Arising from Free Carriers in Doped Quantum Dots. *Nat. Mater.* **2011,** *10*, 361.

49. Riha, S. C.; Johnson, D. C.; Prieto, A. L. Cu_2Se Nanoparticles with Tunable Electronic Properties Due to a Controlled Solid-State Phase Transition Driven by Copper Oxidation and Cationic Conduction. *J. Am. Chem. Soc.* **2011,** *133*, 1383.

50. Lee, M.; Yang, J.; Lee, H.; Lee, J. I.; Koirala, A. R.; Park, J.; Jo, H.; Kim, S.; Park, H.; Kwak, J.; Yoo, H.; Huh, W.; Kang, M. S. Stoichiometric Doping of Highly Coupled $Cu_{2-x}S$ Nanocrystal Assemblies. *ACS Appl. Mater. Interfaces* **2021,** *13*, 26330.

51. Jain, P. K.; Manthiram, K.; Engel, J. H.; White, S. L.; Faucheaux, J. A.; Alivisatos, A. P. Doped Nanocrystals as Plasmonic Probes of Redox Chemistry. *Angew. Chem. Int. Ed.* **2013,** *52*, 13671.

52. Elimelech, O.; Liu, J.; Plonka, A. M.; Frenkel, A. I.; Banin, U. Size Dependence of Doping by a Vacancy Formation Reaction in Copper Sulfide Nanocrystals. *Angew. Chem. Int. Ed.* **2017,** *56*, 10335.

53. Dümbgen, K. C.; Leemans, J.; De Roo, V.; Minjauw, M.; Detavernier, C.; Hens, Z. Surface Chemistry of InP Quantum Dots, Amine–Halide Co-Passivation, and Binding of Z-Type Ligands. *Chem. Mater.* **2023,** *35*, 1037.

54. Crosnier, O.; Mounsey, C.; Herle, P. S.; Taylor, N.; Nazar, L. F. Crystal Structure and Electrochemical Behavior of Li_2CuP: a Surprising Reversible Crystalline−Amorphous Transformation. *Chem. Mater.* **2003,** *15*, 4890.

55. Blint, R. J. Binding of Ether and Carbonyl Oxygens to Lithium Ion. *J. Electrochem. Soc.* **1995,** *142*, 696.

56. Crovetto, A.; Unold, T.; Zakutayev, A. Is $Cu_{3-x}P$ a Semiconductor, a Metal, or a Semimetal? *Chem. Mater.* **2023,** *35*, 1259.

57. Wolff, A.; Pallmann, J.; Boucher, R.; Weiz, A.; Brunner, E.; Doert, T.; Ruck, M. Resource-Efficient High-Yield Ionothermal Synthesis of Microcrystalline $Cu_{3-x}P$. *Inorg. Chem.* **2016,** *55*, 8844.

58. Furo, I.; Bakonyi, I.; Tompa, K.; Zsoldos, E.; Heinmaa, I.; Alla, M.; Lippmaa, E. ^{31}P Nuclear Magnetic Resonance Knight Shift and Linewidth in Ni_3P and Cu_3P: A Magic-Angle Spinning Study. *J. Phys. Condens. Matter* **1990,** *2*, 4217.

59. Levin, E. M.; Cook, B. A.; Ahn, K.; Kanatzidis, M. G.; Schmidt-Rohr, K. Electronic Inhomogeneity and Ag:Sb Imbalance of $Ag_{1-y}Pb_{18}Sb_{1+z}Te_{20}$ High-Performance Thermoelectrics Elucidated by ^{125}Te and ^{207}Pb NMR. *Phys. Rev. B* **2009,** *80*, 115211.

60. Levin, E. M. Effects of Ge Substitution in GeTe by Ag or Sb on the Seebeck Coefficient and Carrier Concentration Derived from ^{125}Te NMR. *Phys. Rev. B* **2016,** *93*, 045209.

61. Selbach, H.; Kanert, O.; Wolf, D. NMR Investigation of the Diffusion and Conduction Properties of the Semiconductor Tellurium. I. Electronic Properties. *Phys. Rev. B* **1979,** *19*, 4435.

62. Leemans, J.; Dümbgen, K. C.; Minjauw, M. M.; Zhao, Q.; Vantomme, A.; Infante, I.; Detavernier, C.; Hens, Z. Acid–Base Mediated Ligand Exchange on Near-Infrared Absorbing, Indium-Based III–V Colloidal Quantum Dots. *J. Am. Chem. Soc.* **2021,** *143*, 4290.

63. Stein, J. L.; Holden, W. M.; Venkatesh, A.; Mundy, M. E.; Rossini, A. J.; Seidler, G. T.; Cossairt, B. M. Probing Surface Defects of InP Quantum Dots Using Phosphorus Kα and Kβ X-ray Emission Spectroscopy. *Chem. Mater.* **2018,** *30*, 6377.

64. Zanin, I. E.; Aleinikova, K. B.; Afanasiev, M. M.; Antipin, M. Y. Structure of Zn_3P_2. *J. Struct. Chem.* **2004,** *45*, 844.

65. Mauvernay, B.; Doublet, M. L.; Monconduit, L. Redox Mechanism in the Binary Transition Metal Phosphide Cu_3P. *J. Phys. Chem. Solids* **2006,** *67*, 1252.

66. Bichat, M. P.; Politova, T.; Pascal, J. L.; Favier, F.; Monconduit, L. Electrochemical Reactivity of Cu_3P with Lithium. *J. Electrochem. Soc.* **2004,** *151*, A2074.

67. Pangborn, A. B.; Giardello, M. A.; Grubbs, R. H.; Rosen, R. K.; Timmers, F. J. Safe and Convenient Procedure for Solvent Purification. *Organometallics* **1996,** *15*, 1518.

68. Momma, K.; Izumi, F. VESTA 3 for Three-Dimensional Visualization of Crystal, Volumetric and Morphology Data. *J. Appl. Cryst.* **2011,** *44*, 1272.

69. Shan, Y.; Li, G.; Tian, G.; Han, J.; Wang, C.; Liu, S.; Du, H.; Yang, Y. Description of the Phase Transitions of Cuprous Iodide. *Journal of Alloys and Compounds* **2009,** *477*, 403.

70. Melikyan, G. G.; Deravakian, A. Tetrahydrofuran as an One-Electron Donor: Highly Diastereoselective Coupling of Cobalt-Complexed Propargyl Alcohol. *J. Organomet. Chem.* **1997,** *544*, 143.

71. Lim, S. J.; Kim, W.; Shin, S. K. Surface-Dependent, Ligand-Mediated Photochemical Etching of CdSe Nanoplatelets. *J. Am. Chem. Soc.* **2012,** *134*, 7576.

72. Ievină, A.; Straumanis, M.; Karlsons, K. Praezisionsbestimmung von Gitterkonstanten hygroskopischer Verbindungen (LiCl, NaBr). *Z. Phys. Chem.* **1938,** *40B*, 146.

73. Agrawal, A.; Cho, S. H.; Zandi, O.; Ghosh, S.; Johns, R. W.; Milliron, D. J. Localized Surface Plasmon Resonance in Semiconductor Nanocrystals. *Chem. Rev.* **2018,** *118*, 3121.

CHAPTER 4. Considerations for Use of Copper Phosphide as a Model System for Mechanistic Investigations of Metal Pnictide Colloidal Synthesis

4.1 Introduction

Aminopnictines represent a promising class of easy-to-handle precursors for the colloidal synthesis of high-quality, low-polydispersity metal pnictide nanocrystals. Tris(amino)phosphines and tris(amino)arsines have been utilized in the past decade for the synthesis of colloidal nanocrystals of InP,[1-5] Cd_3P_2,[6] CoP,[6] CoP_2,[6] Ni_2P,[6] Zn_3P_2,[6] InAs,[7-10] and Cd_3As_2.[9] The study outlined in Chapter 2 of this dissertation represents the first extension of aminophosphine chemistry to use with copper salts for the synthesis of $P6_3cm$ $Cu_{3-x}P$ nanocrystals. In that work, a pathway was proposed for Cu–P bond-formation (Scheme 4.1) which extends the redox disproportionation[4] outlined by Buffard and coworkers to the spectroscopically observed *in situ* copper–phosphorus precursor. The empirical observations of reduced $Cu_{3-x}P$ growth reactivity with P/Cu < 3 (see Chapter 2) and the need for use of P/In ≥ 4 to obtain full nanocrystal yield[3] (In-atom basis) lend credence to the proposed disproportionation pathway of Scheme 4.1 and its InP analogue.[4] It is important to note, however, that the disproportionation pathway has not been directly confirmed. One could easily conceive of an alternative pathway to the phosphonium cation, such as the nucleophilic attack of metal-bound aminophosphine by amine, followed by metal hydride formation and acid elimination to generate reactive metal-containing anionic species (Scheme 4.2).

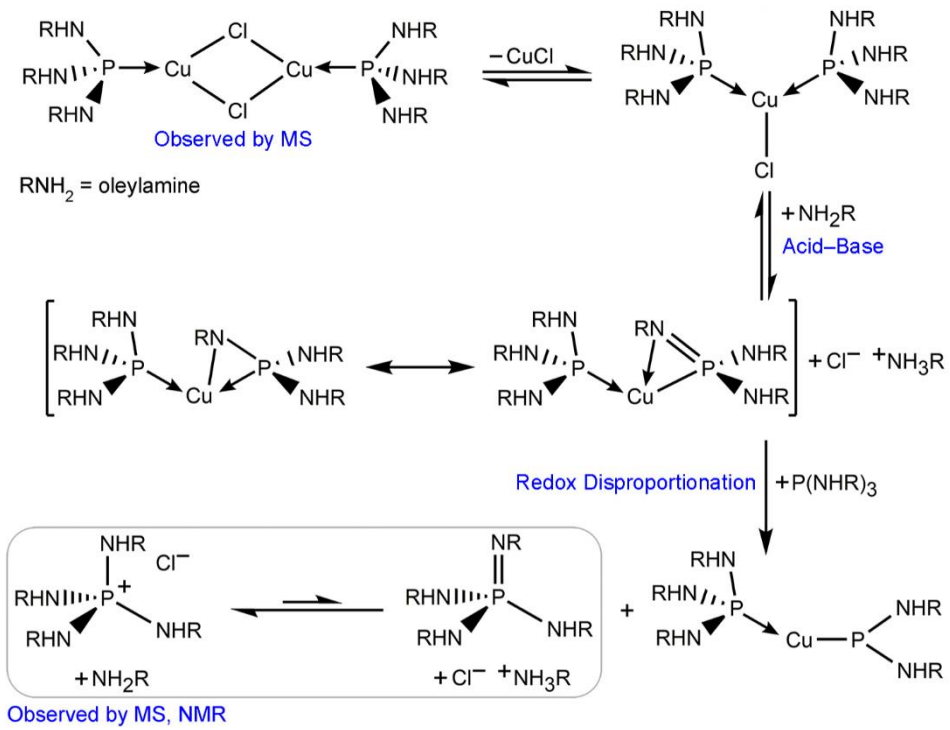

Scheme 4. 1. Pathway for Cu–P bond-formation in aminophosphine synthesis based on that previously proposed for In–P; reproduced from Scheme 2. 2. for reader's convenience.

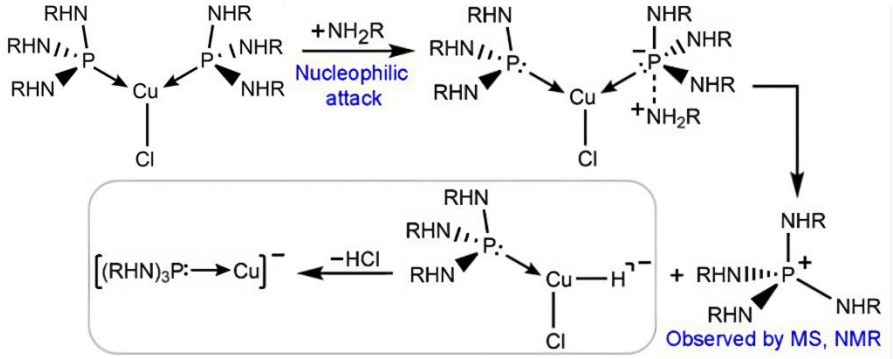

Scheme 4. 2. Alternative, hypothetical pathway for Cu–P bond-formation in aminophosphine synthesis based on metal hydride complex formation and subsequent acid elimination.

Even if the disproportionation pathway is indeed the route to metal pnictide nanocrystal formation, it is unclear, in the case of pre-transaminated reactions, such as the one-pot heat-up $Cu_{3-x}P$ synthesis, whether the acid–base reaction preceding the disproportionation or the disproportionation itself is the rate-limiting step for Cu–P bond formation. It is imperative to

elucidate the reaction mechanism underlying the aminopnictine chemistry for metal pnictide nanocrystal formation, as that knowledge can then be exploited to formulate general synthetic design principles for a more targeted tailoring of metal pnictide nanocrystal reaction products.

The colloidal synthesis of $P6_3cm$ $Cu_{3-x}P$ developed in Chapter 2 represents a valuable platform for systematic mechanistic investigations on account of its observable, and potentially isolable, prenucleation intermediates, which have not been observed in other aminopnictine-based metal pnictide syntheses. By changing the precursor identities, modular colloidal synthesis may be accessed with tailored amine acidity (and P–N bond strength) or copper–counteranion bond strength (Scheme 4.3). This modular synthesis would, in principle, allow interrogation of the chemical processes underlying $Cu_{3-x}P$ formation, in a similar manner to a recent Hammett study of substituted-thiourea precursor conversion to lead sulfide nanocrystals.[11]

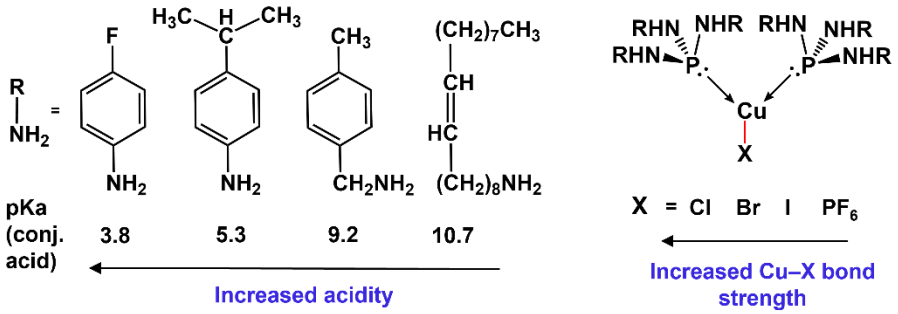

Scheme 4. 3. Modular colloidal aminophosphine-based synthesis of $Cu_{3-x}P$ nanocrystals accessible by tailoring amine acidity and copper–counteranion bond strength of reaction precursors.

In this chapter, $Cu_{3-x}P$ is evaluated as a model system that extends aminophosphine chemistry for nanocrystal formation beyond the use of metal halide salts, tris(diethylamino)phosphine ($P(NEt_2)_3$), and long-chain alkylamines like oleylamine (OAm). Preliminary findings are presented for the investigation of the synthetic roles of aminophosphine amide and metal salt counteranion identity. Key challenges to the extension of aminopnictine-

based nanocrystal synthesis are discussed. Of particular note are (1) the complications arising from replacement of OAm, which crucially serves a dual-role as nanocrystal surfactant and aminophosphine amide, and (2) the formation of zerovalent metal, which may occur from use of tertiary amines as the reaction solvent.

4.2 Results and Discussion

4.2.1 Aminophosphine Precursors Derived from Small, Rigid Amines

In the one-pot heat-up synthesis developed in Chapter 2, which uses CuCl, $P(NEt_2)_3$, OAm, and trioctylamine (TOA), the active aminophosphine precursor, $P(NHC_{18}H_{35})_3$, was formed by *in situ* transamination of $P(NEt_2)_3$ by OAm in the presence of CuCl under vacuum at 125 °C for 3 h. That approach is problematic for small, rigid primary amines (such as those of Scheme 4.3), which are volatile and easily lost *in vacuo* at 125 °C. An alternative approach, adapted from previous work,[12] was used in which the primary amine (NH_2R = 4-methylbenzylamine (4-MBA), p-toluidine, p-phenetidine, or 4-decylaniline) was stirred together with $P(NEt_2)_3$ at 70 °C under nitrogen atmosphere for 20 h. This lower-temperature reaction under ambient pressure yielded quantitative transamination for the small primary amines, even without use of excess primary amine as shown with the case of p-toluidine. This was confirmed, in part, by the disappearance of the $P(NEt_2)_3$ resonance at 119 ppm in the corresponding ^{31}P NMR spectra (Figure 4.1). In the case of 4-MBA (Figure 4.1ii), a resonance at 99 ppm arises from the $P(NHC_8H_9)_3$ monophosphine, at chemical shift close to that of $P(NHC_{18}H_{35})_3$ (Figure 4.1iii). In the case of the three arylamines (Figure 4.1iv–vi), the $P(NHR)_3$ monophosphine corresponds to the resonances in the 75–78 ppm range and the $P_2(NR)(NHR)_4$ diphosphine corresponds to the resonances in the 68–72 ppm range, assignments which match those from a previous report on the synthesis of aryl phosphorus triamides using phenylamine.[12] The substantially different ^{31}P NMR chemical shift relative to

$P(NHC_{18}H_{35})_3$ for the arylamine-derived aminophosphines is expected as the arylamines have N-atom participation in the aromaticity of the phenyl ring, which is not true for OAm or 4-MBA.

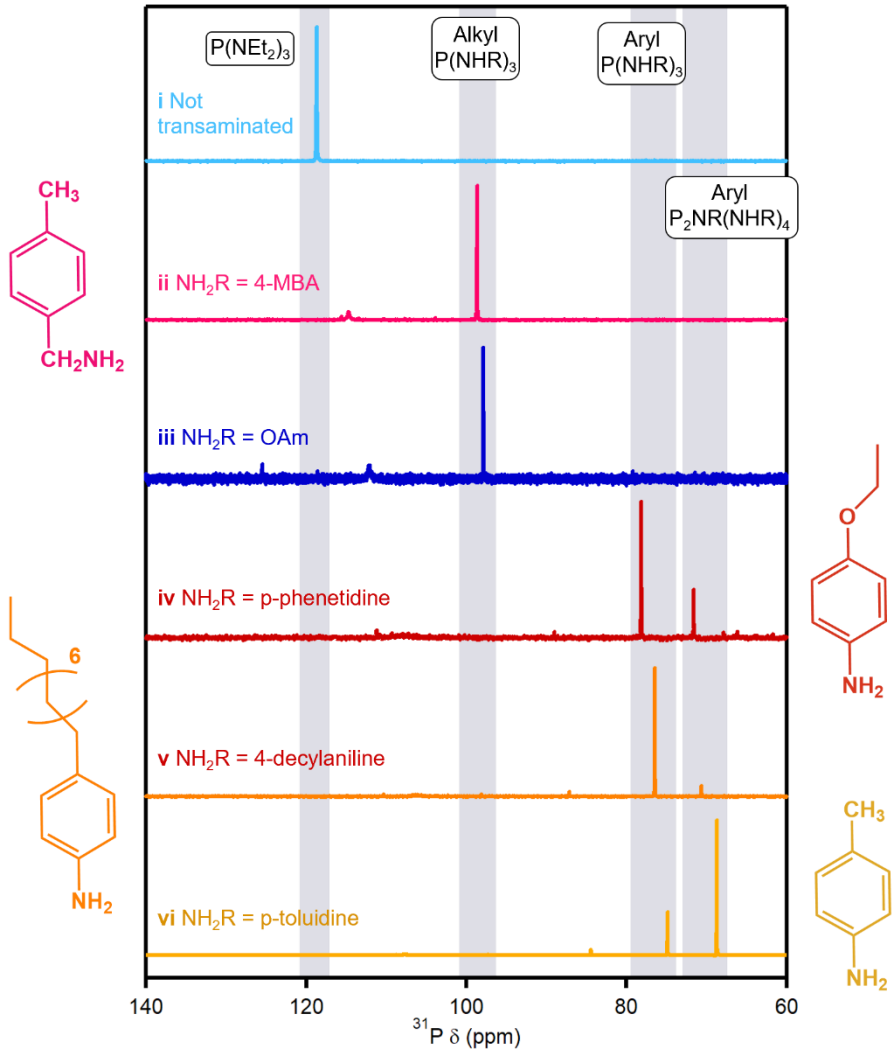

Figure 4. 1. ^{31}P-NMR spectra of transamination products from reaction of $P(NEt_2)_3$ with excess (or stoichiometric) primary amine (NH_2R). (i) Without transamination (reprinted from Figure S2.8i) and after reaction with: (ii) 5.0 equiv 4-methylbenzylamine (4-MBA), (iii) 7.6 equiv OAm (reprinted from Figure S2.7iv), (iv) 6.0 equiv p-phenetidine, (v) 4.0 equiv 4-decylaniline, and (vi) 3.0 equiv p-toluidine.

Sufficiently concentrated TOA solutions with $P(NEt_2)_3$ and CuCl with heat-assisted dissolution yielded crystals suitable for characterization by single-crystal X-ray diffraction upon slow cooling. The crystals were comprised of molecules of $Cu_4Cl_4P(NEt_2)_3$ adopting a distorted,

"cubane" confirmation (Structure **1**, Figure 4.2a, Table S4.1), similar to what has been previously reported for triphenylphosphine-ligated CuCl in the solid-state.[13] This Cu_4Cl_4 core is a dimer of the $P(NEt_2)_3$ analogue of the *in situ* dinuclear synthesis intermediate ($Cu_2Cl_2P_2(NHC_{18}H_{35})_6$) identified by MS in Chapter 2. This finding suggests that it should be possible to isolate and crystallize aminophosphine-ligated CuCl molecules derived from small, rigid primary amines, which could then be used as single-source precursors for $Cu_{3-x}P$ nanocrystal synthesis.

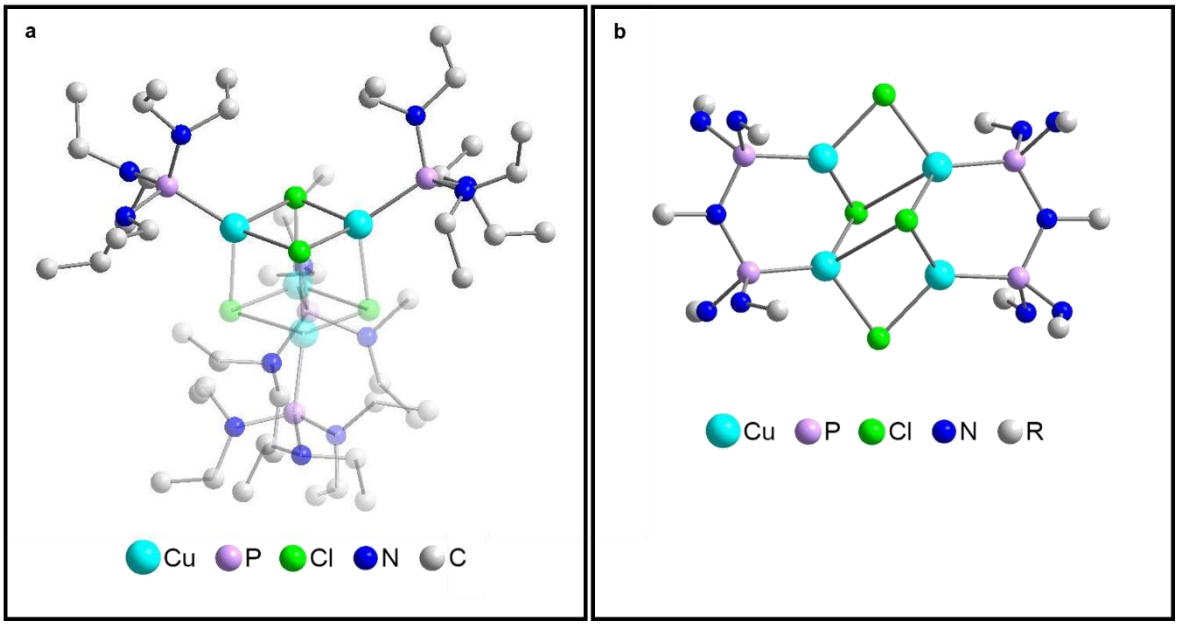

Figure 4. 2. Solid-state structures of **(a)** $Cu_4Cl_4(P(NEt_2)_3)_4$ (Structure **1**, Table S4.1; H atoms omitted) and **(b)** $Cu_4Cl_4(P_2NR(NHR)_4)_2$ where NH_2R = p-toluidine (Structure **2b**, Table S4.1; p-tolyl moieties omitted).

One key difference between $P(NEt_2)_3$ and $P(NHR)_3$ is that the latter undergoes aminophosphine condensation to form diphosphine ($P_2(NR)(NHR)_4$) and release amine.[12, 14] This diphosphine exists in an equilibrium with the monophosphine ($P(NHR)_3$), with relative amounts modulated by the degree of excess amine. A portion of tetrahydrofuran (THF) solution with (p-toluidino)phosphine was concentrated under vacuum. The resulting crystals contained diphosphine molecules (Structure **2a**, Figure S4.1, Table S4.1), as expected from the large relative amount of

diphosphine in the ^{31}P NMR spectrum of the pre-crystallization solution (Figure 4.1.vi). A different portion of the THF solution with (p-toluidino)phosphine was reacted with an acetonitrile (MeCN) solution of CuCl to yield a white powder, which was recrystallized from boiling THF. Similar to **1**, the resulting crystals were comprised of Cu_4Cl_4 molecules but instead with diphosphine coordination of 2 P_2N_5 ligands per Cu_4Cl_4 core (Structure **2b**, Figure 4.2a, Table S4.1). Crystals of aminophosphine–Cu_2Cl_2 polymers were also found (Structures **3, 4**, Figures S4.2, S4.3, Table S4.1), but these are expected to be less useful as single-source precursors on account of their limited solubility.

4.2.2 Metallic Cu(0): An Obstacle to Probing Role of Aminophosphine Amide

In order to use aminophosphine-ligated CuCl single-source precursors for meaningful kinetic analyses, it is necessary to first identify OAm-free reaction conditions that give well-defined, phase-pure $P6_3cm$ $Cu_{3-x}P$ nanocrystals. It was predicted that N,N-dimethylhexadecylamine (DMHDAm) might be a suitable surfactant substitute for OAm, as it is a long-chain tertiary amine with two minimally bulky methyl substituents that cannot undergo transamination. One-pot, heat-up reactions of post-transamination aminophosphine mixtures and CuCl in mixed DMHDAm and TOA solvent led to extensive Cu(0) formation by powder X-ray diffraction (Figure 4.3) with use of aminophosphines derived from p-phenetidine, 4-decylaniline, and 4-MBA. While the relative amount of Cu(0), as compared to $P6_3cm$ $Cu_{3-x}P$, was greater with increased amine acidity, this trend is not necessarily meaningful as all three reactions became insoluble upon being heated above 200 °C and underwent inhomogeneous reactivity. The identification of reaction conditions that disfavor reduction of Cu is thus necessary in order to access reactivity regimes amenable to mechanistic studies of $Cu_{3-x}P$ formation.

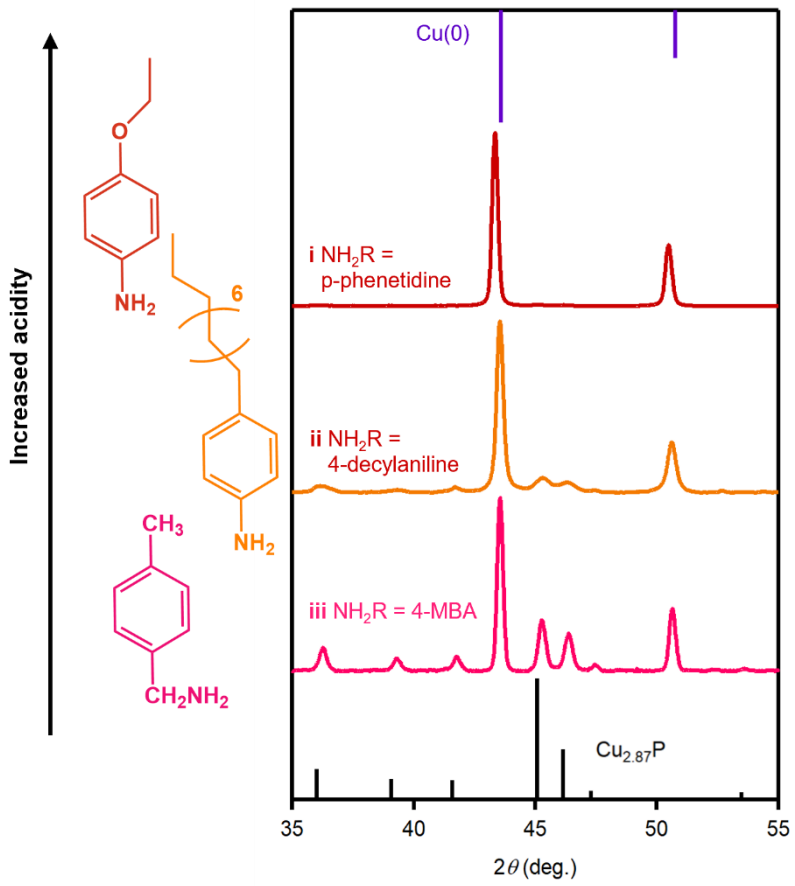

Figure 4. 3. Powder X-ray diffraction patterns of the insoluble solid products from the one-pot, heat-up reactions with different primary amines, NH_2R, in the complete absence of OAm ([Cu] = 0.020 M, TOA/DMHDAm/NH_2R/P/CuCl = 107/10/*x*/3/1, $T_f \approx 240$ °C). The corresponding primary amines: (i) p-phenetidine (*x* = 14), (ii) 4-decylaniline (*x* = 18), and (iii) 4-MBA (*x* = 14). The phosphorus was delivered to the reaction in the form of post-transamination aminophosphine mixture with excess of the corresponding primary amine. The simulated patterns for $P6_3cm$ $Cu_{2.87}P$ (ref. 15) and fcc Cu (ref. 16) are shown for comparison.

4.2.3 Reaction Design Strategies for Prevention of Zerovalent Metal Formation

Amines are capable of reducing cationic precursors to form zerovalent metallic nanoparticles.[17] The extensive formation of Cu(0) in reactions using small, rigid amines and mixed DMHDAm/TOA solvent might be explained by DMHDAm acting as a better reducing agent than TOA due to its lower steric bulk. A control one-pot, heat-up OAm-based synthesis using CuCl and post-transamination aminophosphine mixture with 10 equiv DMHDAm/Cu formed colloidal

$Cu_{3-x}P$ nanocrystals with no visual indication of Cu(0) formation (Figure 4.4a). In contrast, if DMHDAm was used as the sole solvent (120 equiv DMHDAm/Cu and complete removal of TOA), the signature red color-change indicating Cu(0) nanocrystal formation was observed (Figure 4.4b). These results together indicate that DMHDAm is a more effective reducing agent than TOA for the formation of Cu(0) in these one-pot, heat-up reactions. It is also likely, however, that OAm-based aminophosphine syntheses are more resistant to Cu(0) formation than their small-amine-based analogues, potentially due to the greater CuCl solubility afforded by the OAm surfactant.

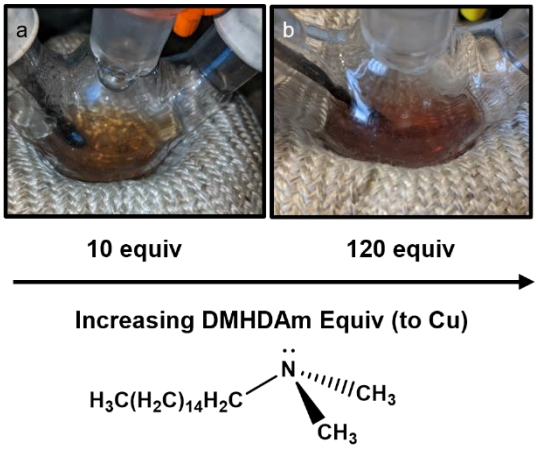

Figure 4. 4. Visual indication of Cu(0) nanocrystal formation with observation of red color change in one-pot, heat-up reactions with increased DMHDAm. **(a)** No observation of Cu(0) with 10 equiv DMHDAm (TOA/DMHDAm/OAm/P/CuCl = 98/10/12/3/1, [Cu] = 0.020 M) and **(b)** observation of Cu(0) with 120 equiv DMHDAm (TOA/DMHDAm/OAm/P/CuCl = 0/120/12/3/1, [Cu] = 0.020 M). The phosphorus was delivered to the reaction in the form of pre-transaminated tris(oleylamino)phosphine with some excess of free OAm.

If it is the case that small-amine-based one-pot, heat-up reactions are more susceptible to Cu(0) formation, it may be that excess TOA is also responsible for reducing Cu^+ species to Cu(0) in the reactions of Figure 4.3. It is inevitable that some amine will always be present in any primary-amine-based aminophosphine synthesis due to the diphosphine condensation

equilibrium.[12, 14] To minimize the amount of amine, however, the large excess of amine solvent typically used in the colloidal metal phosphide syntheses[1-6, 18] should be easily replaceable with a more inert solvent such as an alkane. Solvent substitution with alkane is expected give decreased Cu(0) formation by removing excess reducing agent without impacting the aminophosphine chemistry leading to $Cu_{3-x}P$ nanocrystal formation. Indeed, a one-pot, heat-up reaction using 4-MBA with 50 equiv DMHDAm/CuCl and hexadecane as the primary solvent yielded phase-pure $P6_3cm$ $Cu_{3-x}P$ by powder X-ray diffraction (Figure 4.5). It should be noted, however, that unlike with OAm-based syntheses, the $Cu_{3-x}P$ product was heterogeneous and insoluble throughout the reaction. This indicates that DMHDAm is not suitable as a substitute for OAm stabilization of $Cu_{3-x}P$ nanocrystal surfaces and that uncontrolled growth is occurring.

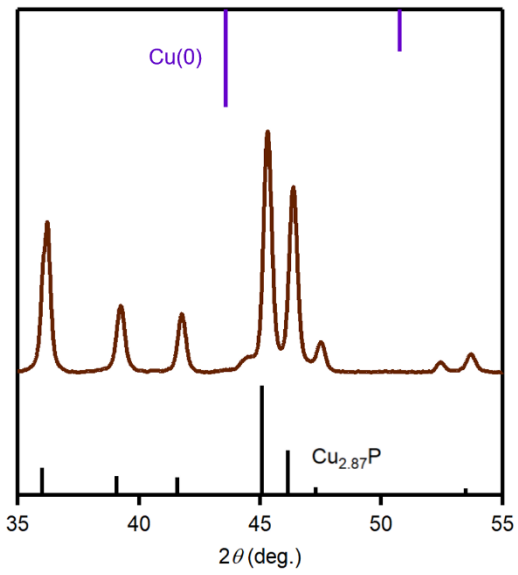

Figure 4. 5. Powder X-ray diffraction pattern of the insoluble $Cu_{3-x}P$ product from the one-pot, heat-up reactions with 4-MBA as primary amine in hexadecane ([Cu] = 0.010 M, DMHDAm/4-MBA/P/CuCl = 50/12/3/1, $T_f \approx 250$ °C). The phosphorus was delivered to the reaction in the form of pre-transaminated tris(4-methylbenzylamino)phosphine with slight excess of free 4-MBA. The simulated patterns for fcc Cu (ref. 16) and $P6_3cm$ $Cu_{2.87}P$ (ref. 15) are shown for comparison.

Precursor solubilization is another important consideration for mitigating Cu(0) formation during one-pot, heat-up reactions of Cu salts. As an example, an *in situ* trioctylphosphine(TOP)-ligated CuBr precursor formed in hexadecane solvent ([Cu] = 0.080 M, TOP/Cu = 2.0) does not form Cu(0), even after being heated at 270 °C for 1 h. Subsequent addition of 22 equiv OAm/Cu to this TOP/CuBr solution (dilution to [Cu] = 0.049 M) did not induce Cu(0) formation either after further heating at 260 °C for 30 min. These observations contrast with results from a recently reported synthesis of Cu(0) nanospheres in which Cu(0) nucleates just 7 min after addition of TOP to a OAm/CuBr solution (OAm/TOP/CuBr = 35/2/1, [Cu] = 0.080 M) at 150 °C.[19] It is thus anticipated that zerovalent metal formation can be further mitigated by proper solubilization of metal salt precursors, which requires a sufficiently high (but not too high) temperature, judicious choice of ligand/solvent, and sufficiently long "solubilization time" prior to heating beyond the threshold temperature for zerovalent metal nucleation.

The importance of developing design strategies for the prevention of zerovalent metal formation is crucial for even more synthetically challenging metal phosphide targets, such as the phosphorus-rich AgP_2. It is likely that zerovalent metal is formed when metal-cation-reduction outcompetes metal phosphide formation reactivity, as first discussed in Chapter 2. There are two factors that lead to increased zerovalent metal formation with attempts to synthesize AgP_2 even more so than for $Cu_{3-x}P$: (1) the 0.28 V greater driving-force for Ag^+ reduction as compared to Cu^+ reduction and (2) the harsher conditions and higher temperatures typically required to crystallize phosphorus-rich metal phosphides on account of their increased P–P covalency.[20] Even with use of hexadecane solvent and extended heating at 125 °C for 3 h for solubilization, a one-pot, heat-up reaction with AgCl and OAm-derived aminophosphine ([Ag] = 0.020 M, 28/8/1 OAm/P/Ag) yielded only nanocrystalline Ag(0) with no AgP_2 observable by powder X-ray

diffraction (Figure 4.6a). The absorption spectrum of the Ag(0) nanocrystals (Figure 4.6b) contains a highly broadened localized surface plasmon resonance (LSPR) feature compared to that typically observed for pristine Ag(0) nanocrystals, indicating potential P-atom incorporation into the Ag(0) lattice. It is clear that additional reaction design strategies are needed to fully suppress Ag(0) formation at the conditions needed for AgP_2 crystallization.

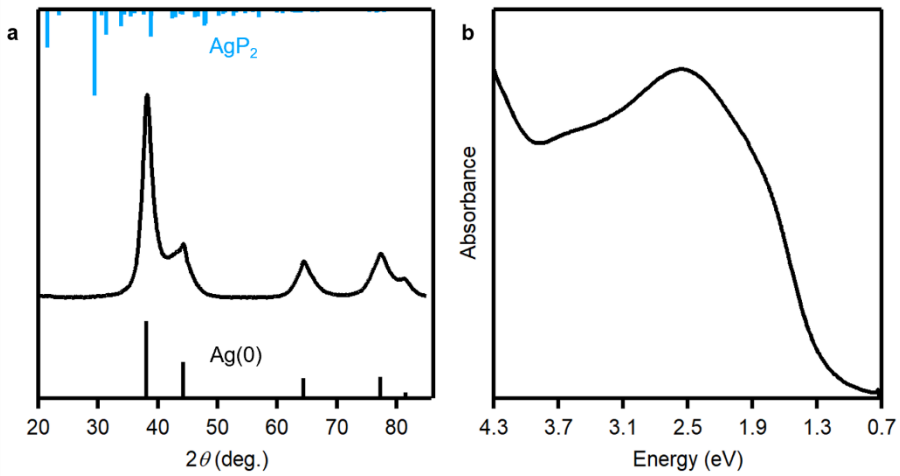

Figure 4. 6. Characterization of a one-pot, heat-up reaction with AgCl, $P(NEt_2)_3$, and OAm in hexadecane solvent ([Ag] = 0.020 M, 28/8/1 OAm/P/Ag, $T_f \approx 230$ °C). **(a)** Powder X-ray diffraction pattern compared to those simulated for fcc Ag (ref. 21) and $P2_1/c$ AgP_2 (ref. 22) and **(b)** absorption spectrum of the resulting colloidal nanocrystal product.

4.2.4 Synthetic Complications with Decreased Amounts of OAm

As discussed above, the $Cu_{3-x}P$ products formed during one-pot, heat-up reactions of CuCl and aminophoshine in the total absence of OAm are not colloidally stable (*vide infra*). TEM imaging of the reaction product from one such synthesis (Figure 4.7a) reveals poorly-defined aggregates, instead of the well-defined nanoplatelets observed for $Cu_{3-x}P$ syntheses using OAm. It may be possible, however, to still use OAm as a surfactant for well-defined $Cu_{3-x}P$ nanocrystals but in sufficiently low quantities (sub-stoichiometric for phosphorus amide replacement, OAm/P < 3) and with pre-transamination using a different primary amine such that the other primary

amine/amide dictates the aminophosphine reactivity rather than OAm. To test one aspect of this idea, a one-pot, heat-up reaction was carried out with [Cu] = 0.020 M and 15/4/3/1 4-MBA/OAm/P/CuCl using hexadecane as the primary solvent. TEM imaging of the resulting product (Figure 4.7b) indicates that the use of small OAm quantities relative to the other primary amine can still stabilize well-defined $Cu_{3-x}P$ nanocrystals.

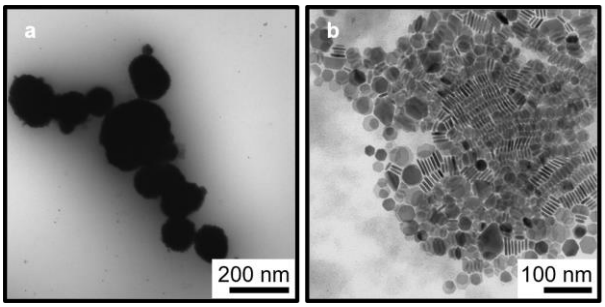

Figure 4. 7. TEM images of $Cu_{3-x}P$ reaction products from separate one-pot, heat-up reactions with different amine composition ([Cu] = 0.020 M, 15/3/1 4-MBA/P/CuCl with hexadecane as the primary solvent): **(a)** with 50 equiv DMHDAm and 0 equiv OAm and **(b)** with 0 equiv DMHDAm and 4 equiv OAm.

The aspect of the proposed sub-stochiometric OAm reaction scheme which cannot be readily evaluated by TEM or powder X-ray diffraction using a single experiment is whether the other primary amine present, rather than OAm, dictates the aminophosphine reactivity. An amide scrambling experiment was devised in which aminophosphines derived from 4-decylaniline (4-decylaniline/P = 4.0; where 4-decylaniline refers to the sum of free amine and bound amide) were heated at 150 °C for 4 h in the presence of OAm (with OAm/P = 4.0). The ^{31}P NMR spectra before and after the heating (Figure 4.8) reveal extensive amide scrambling with 13% 4-decylanilide and 87% oleylamide (Table S4.2) in the final aminophosphine mixture. The fact that there is more oleylamide than 4-decylanilide despite both amines being present in equimolar quantities indicates that it is a poor assumption that the other amine besides OAm will dictate the majority of the precursor-conversion reactivity. The identification of a suitable surfactant replacement for OAm

is thus imperative if modular aminophosphine-ligated CuCl single-source precursors are to be used meaningful, quantitative kinetic analyses of $Cu_{3-x}P$ formation reactivity. Briefly, preliminary synthetic efforts to completely substitute OAm with alternative surfactants such as TOP or N-heterocyclic carbenes[23] yielded neither $P6_3cm$ $Cu_{3-x}P$ nor Cu(0) at the typical temperature range of 200–250 °C, indicating that these ligands bind Cu too tightly and suppress Cu reactivity with aminophosphine. It is inadvisable to exceed temperatures of 250 °C for metal phosphide nanocrystal nucleation in aminophosphine-based syntheses as aminophosphines form insoluble solids above that threshold even in the absence of metal salts.

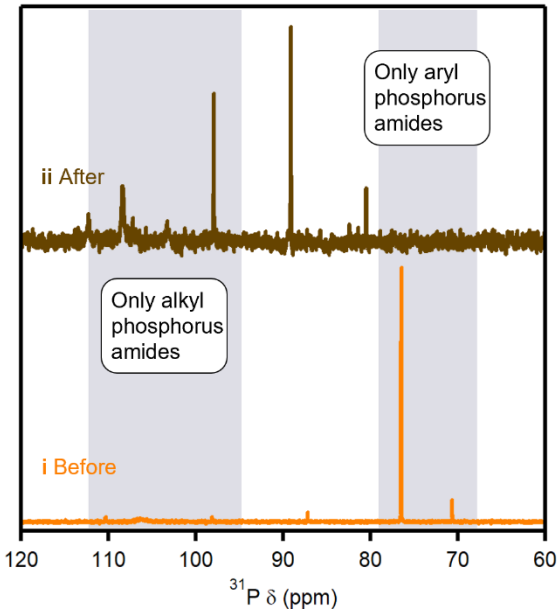

Figure 4. 8. ^{31}P-NMR spectra (i) before (reprinted from Figure 4.1v) and (ii) after an amide scrambling reaction of a Cu-free 4-decylaniline-transaminated aminophosphine mixture with OAm/P = 4.0 for 4 h at 150 °C. Equimolar quantities of OAm and 4-decylaniline (the sum of both free amine and phosphorus-bound amide) were used.

4.2.5 Preliminary Investigations into the Role of the Copper Salt Counteranion

Modular $Cu_{3-x}P$ nanocrystal synthesis with variation of copper salt counteranion identity has the logistical benefit of not fundamentally relying on the identification of a surfactant substitute

for OAm. It is expected that different copper salts would have varying copper–anion bond strengths (Scheme 4.3), which could impact aminophosphine-based nanocrystal formation chemistry if cleavage of the copper–anion bond is a rate-limiting step. While metal halides have been exclusively used for metal phosphide nanocrystal syntheses thus far,[1-6, 18] it is anticipated that it should be possible to form $Cu_{3-x}P$ nanocrystals through the use of other copper salts such as tetrakis(acetonitrile)copper(I) hexafluorophosphate ($[Cu(MeCN)_4]PF_6$). A one-pot, heat-up synthesis with $[Cu(MeCN)_4]PF_6$ in hexadecane solvent ([Cu] = 5.0 mM, 15/5/1 = OAm/P/Cu) heated to T = 248 °C (Figure S4.4) yielded an ensemble of pseudo-spherical $Cu_{3-x}P$ nanocrystals (Figure 4.9a) with a diameter of 3.6 ± 0.2 nm (Figure 4.9b). The $P6_3cm$ phase of $Cu_{3-x}P$ was verified by powder X-ray diffraction (Figure 4.9c) and the absorption spectrum (Figure 4.9d) contains a LSPR feature characteristic $Cu_{3-x}P$.[18, 24-26] The $Cu_{3-x}P$ LSPR peak energy is higher than previously observed for larger $Cu_{3-x}P$ nanocrystals, suggesting the possibility of quantum-confined plasmonics for $Cu_{3-x}P$ crystallite diameters below 4 nm. The $Cu_{3-x}P$ nanocrystal yield is estimated to be 68% using a $Cu_{3-x}P$ extinction coefficient based on Cu, $\varepsilon_{3.1eV}^{Cu}$ = 2100 ± 200 M^{-1} cm^{-1} (see Chapter 3). This result indicates that the nucleation activity is an order of magnitude greater than similar CuCl-based synthesis (Chapter 2) as estimated by the quotient of nanocrystal yield over volume (calculated with platelet lateral dimension from TEM and constant, arbitrary platelet height). The greater nucleation activity is qualitatively corroborated by a color-change indicating $Cu_{3-x}P$ formation at lower temperatures (T = 190 °C) for the $[Cu(MeCN)_4]PF_6$-based synthesis compared to CuCl-based syntheses (T ~ 220 °C; Chapter 2). It is possible that the high $Cu_{3-x}P$ nanocrystal formation reactivity for syntheses with $[Cu(MeCN)_4]PF_6$ is due to the weak ionic bond between Cu^+ and PF_6^-, as compared to covalent Cu–halide bonds. Alternatively, the PF_6^- may react with aminophosphine to generate a more reactive P species, as it is known that

aminophosphines spontaneously cleave the C–Cl bonds of chlorocarbons.[14] Further studies using other weakly bound counteranions are necessary to make a definitive conclusion.

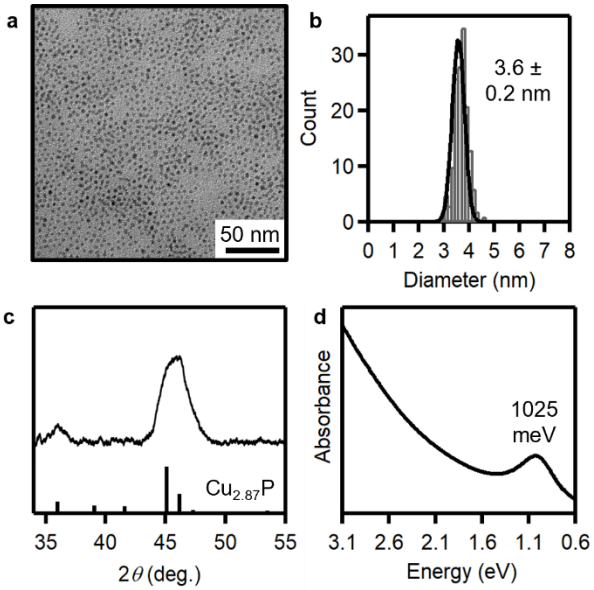

Figure 4. 9. Characterization of $Cu_{3-x}P$ nanocrystals from a one-pot, heat-up synthesis using $[Cu(MeCN)_4]PF_6$ as the Cu salt precursor instead of CuCl ([Cu] = 5.0 mM, 15/5/1 = OAm/P/Cu with hexadecane as the primary solvent). **(a)** TEM image of the resulting nanocrystals, **(b)** statistical analysis (n = 150) of nanocrystal diameter, and the corresponding **(c)** powder X-ray diffraction pattern (compared to that simulated for $P6_3cm$ $Cu_{2.87}P$, ref. 15) and **(d)** absorption spectrum.

It is known from previous studies that metal bromide and metal iodide salts can be used in aminophosphine-based metal phosphide nanocrystal syntheses for size tuning.[2, 6, 18] These studies did not, however, indicate whether the observed metal-halide size tuning is atom-efficient and due to different nucleation activities or merely from different nanocrystal yields. A one-pot, heat-up reaction series with CuX (X = Cl^-, Br^-, I^-) and OAm-derived aminophosphine ([Cu] = 0.020 M, 25/5/1 OAm/P/CuX, with hexadecane solvent) with carefully controlled reaction temperature (Figure S4.5) was used to probe the effect of halide on $Cu_{3-x}P$ nanocrystal formation reactivity. TEM images of the resulting nanocrystals indicate increasing maximum nanocrystal size for larger halides (Figure 4.10). It should be noted, however, that for the reaction with CuI (Figure 4.10c),

there is considerable ensemble polydispersity with strange "crescent"-shaped platelets which together suggest extensive particle dissolution and Ostwald ripening.[27] The increased particle "monomer" solubility could be due to the high P/Cu = 5 and/or the low [Cu] = 0.020 M. From the results with these unoptimized reaction conditions, it is not possible to determine reliable relative nucleation activities as a function of halide identity. Nevertheless, these preliminary results suggest that halide identity likely has a substantive effect on aminophosphine precursor conversion under certain reaction conditions and further study is needed to elucidate it.

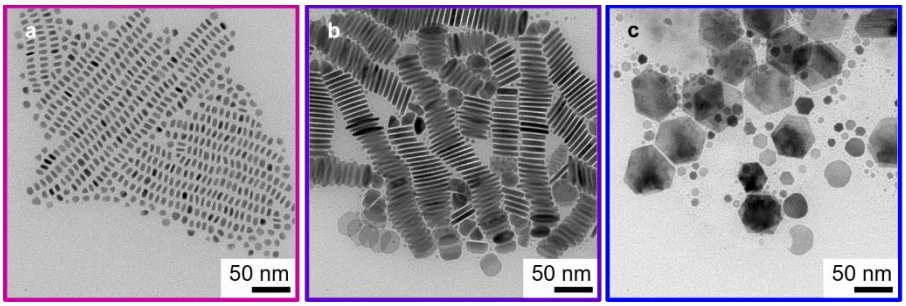

Figure 4. 10. TEM images of $Cu_{3-x}P$ nanocrystals from a series of one-pot, heat-up syntheses with different Cu(I) halide CuX salts ([Cu] = 0.020 M, 25/5/1 OAm/P/Cu using hexadecane as the primary solvent): **(a)** X = Cl^-, **(b)** X = Br^-, and **(c)** X = I^-.

4.2.6 A Strategy for Amide- and Counteranion-Substitution Kinetic Studies

Once suitable reaction conditions for the copper halide series and a surfactant substitute for OAm are identified, it will be possible to test the effect of the amide and copper counteranion identity on precursor-conversion reactivity during $Cu_{3-x}P$ nanocrystal synthesis. A simple strategy is proposed for the quantification of nanocrystal nucleation and growth reactivity as a function of these precursor substitutions. If a one-pot, heat-up reaction with copper salt, aminophosphine, and hexadecane solvent is carried out at a constant temperature that is sufficiently low such that nanocrystal formation takes place on the order of ~1 h (such as T = 225 °C), then aliquots of the reaction mixture can be withdrawn throughout the synthesis. These aliquots can be divided for (1)

characterization by TEM and (2) post-purification digestion in nitric acid for optical Cu^{2+} yield analysis. The yield *vs* time aliquot points can be fit to extract a growth-reactivity rate-constant. Select aliquots imaged by TEM can be used to estimate relative nucleation activities by the quotient of nanocrystal yield over volume. This framework is demonstrated with data from a one-pot, heat-up reaction with CuCl and OAm-derived aminophosphine (Figure 4.11; [Cu] = 0.040 M, 18/3/1 = OAm/P/Cu). A single-exponential fit to the yield *vs* time aliquot points (Figure 4.11a) indicates a first-order nanocrystal growth rate constant of 0.031 min^{-1}. The nanoplatelet lateral dimensions of aliquots 2 and 5 and their corresponding yields can be used to estimate relative nucleation activities of 0.15 ± 0.03 and 0.13 ± 0.02, respectively (calculated as % yield divided by the square of lateral platelet dimension in nm).

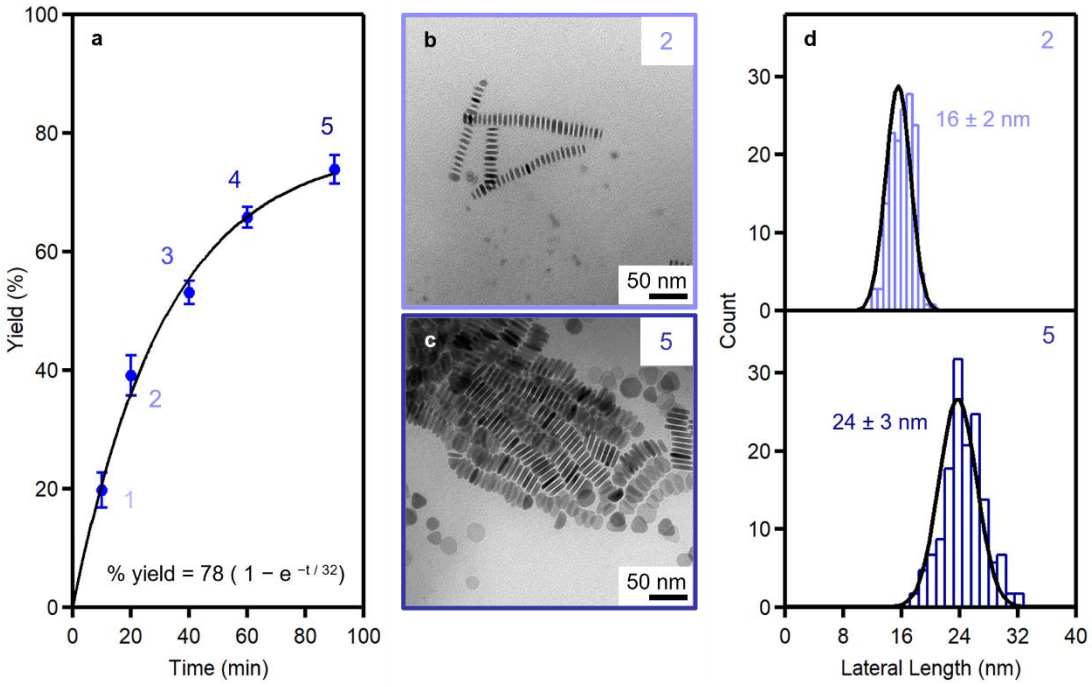

Figure 4. 11. (a) Nanocrystal yield (Cu-atom basis) over time in a $Cu_{3-x}P$ nanocrystal synthesis with CuCl and OAm at T = 225 °C ([Cu] = 0.040 M, 18/3/1 = OAm/P/Cu, with hexadecane as the primary solvent). TEM images of aliquots taken **(b)** 20 min (2) and **(c)** 90 min (5) after the start of nucleation. **(d)** Statistical analyses (n = 150) of lateral platelet dimensions of (top to bottom) aliquots 2 and 5.

4.3 Summary & Conclusions

$Cu_{3-x}P$ is presented as a model system for the systematic mechanistic study of aminophosphine chemistry for nanocrystal formation. It is anticipated that knowledge of the mechanisms of nitrogen–phosphorus and copper–anion bond cleavage and copper–phosphorus bond formation would be generalizable to the improvement of other metal pnictide nanocrystal syntheses which also use aminopnictine precursors. Copper–phosphorus precursors derived from aminophosphines with small, rigid primary amide moieties are synthesized, isolated, and crystallized and are anticipated to be useful as single-source precursors for investigation into the synthetic role of aminophosphine amide identity. Some obstacles to use of these single-source precursors, such as amine-mediate metal cation reduction and incomplete solubilization, have been addressed and resolved. However, the outstanding challenges of identifying a suitable surfactant replacement for OAm and further mitigation of zerovalent metal formation, for more challenging synthetic metal phosphide targets such as AgP_2, remain. Investigations into the synthetic role of metal counteranions are expected to be fruitful based on the preliminary indication of increased nucleation activity and atom-efficient size reduction with use of the ionic $[Cu(MeCN)_4]PF_6$ precursor. A general strategy is proposed for the quantification of nanocrystal nucleation and growth reactivity which can be utilized once the issues complicating use of different phosphorus amides and copper counteranions are resolved. $Cu_{3-x}P$ represents a valuable platform for deeper interrogation of aminopnictine chemistry for the synthesis of solid-state inorganic nanomaterials with much work yet to be done.

4.4 Experimental Methods

4.4.1 Chemicals

The manufacturers and purities of the chemicals used in this study are given in Table S4.3. Toluene, THF, and MeCN were dried and deoxygenated according to standard procedures[28] and stored over molecular sieves (3 Å) for two days before use. OAm, TOA, $P(NEt_2)_3$, hexadecane, and DMHDAm were degassed upon receipt and stored over molecular sieves (4 Å) for two days before use. All primary amines other than OAm and copper- and silver-halide salts were handled and stored exclusively in a nitrogen-filled glovebox. Nitric acid (HNO_3) was used as received and handled in air.

4.4.2 Synthesis

All manipulations for the synthesis and workup of $Cu_{3-x}P$ nanocrystals were conducted under inert atmosphere to avoid aerobic oxidation, either with a nitrogen-equipped Schlenk line or in a nitrogen-filled glovebox.

Quantification of reaction temperature. For all reactions, the flask mixture temperature was measured using a thermocouple probe with the tip submerged in 1 cm of silicone oil and sheathed in a glass cover to avoid contamination. The temperature output was stored digitally with an Omega data logger (OM-EL-USB-TC-LCD) at five second intervals. The raw temperature was adjusted to a corrected temperature with a temperature-dependent empirical quadratic function which was generated by calibration against an external mercury thermometer.

Heating methods. Reaction temperature, for all syntheses with the exception of the one from Figure 4.11, was controlled through use of a 25-ml heating mantle connected to a contact voltage regulator (Volteq, $TDGC_2$–500VA). The desired heating profile was achieved through either a constant voltage or stepwise, two-voltage scheme. For the constant-temperature synthesis

of the kinetic experiment corresponding to Figure 4.11, reaction temperature was instead controlled through use of a PID controller. The reaction mixture was heated (ramp-rate $dT/dt \approx 15$ °C/min) to the set point of 225 °C and held for a total reaction time of 90 min. t = 0 m for this synthesis of Figure 4.11 was taken as the moment that T = 225 °C was reached.

One-pot heat-up reactions. The general reaction scheme was adapted from the successful synthesis of $Cu_{3-x}P$ nanocrystals from a previous study using aminophosphines.[18] A substantial difference was that aminophosphine was transaminated separately from metal salts prior to the heat-up (*vide infra*). Common variations for the one-pot heat-up reactions involved (1) changing solvent composition with use of TOA, hexadecane and/or DMHDAm, (2) partial or complete substitution of OAm with short-chain rigid primary amines, (3) replacement of CuCl with other copper- or silver- salts.

In an example synthesis (that of Figure 4.3iii), a 25-ml round-bottom flask was loaded with CuCl (10.5 mg, 0.106 mmol), a pre-transaminated aminophosphine mixture (0.189 g, 0.34 mmol P, 1.47 mmol 4-MBA, where '4-MBA' includes the sum of the bound amide and free amine forms), DMHDAm (289 mg, 0.36 ml, 1.07 mmol), and TOA (3.77 g, 4.66 ml). This represents a 5.22 ml total volume with [Cu] = 0.020 M and TOA/DMHDAm/4-MBA/P/CuCl = 107/10/14/3/1. The mixture was stirred and degassed under vacuum at ~125 °C for 30 min, to remove any adventitious oxygen and water, and subsequently heated at 125 °C under nitrogen atmosphere for another 90 min, to solubilize the mixture. The resulting pale, straw-colored solution was heated as outlined in the *heating methods* section (in this example, heated up to T_f = 242 °C). After slowly cooling in air, the reaction flask was transferred to the glovebox. If the product was insoluble, it was collected via centrifugation at 2000 rpm for 2 min, washed once more by addition of 2 ml toluene to the resulting pellet, and collected yet again via centrifugation at 2000 rpm for 2 min. If

the product was colloidally stable, the nanocrystal mixture was first diluted with 15 ml THF, and then the nanocrystals were precipitated with the addition of 7 ml MeCN and collected via centrifugation at 2000 rpm for 5 min. The nanocrystals were resuspended in 3 ml toluene.

Transamination of $P(NEt_2)_3$ with primary amines. In an example transamination (that of Figure 4.1iii), a 25-ml round-bottom flask was loaded with $P(NEt_2)_3$ (0.804 g, 3.25 mmol) and 4-MBA (1.974 g, 16.29 mmol). The mixture was heated under nitrogen atmosphere in an oil bath held at T = 70 °C for 20 h. The flask was evacuated under vacuum to remove residual diethylamine. Completeness of transamination was verified by ^{31}P NMR spectroscopy and mass loss. It should be noted that only partial transamination with OAm occurs with heating at 70 °C for 20 h under nitrogen and that 3 hr degas under vacuum at 125 °C is necessary for a complete transamination. 4-decylaniline, p-phenetidine, and p-toluidine transamination protocols were identical to that of 4-MBA.

4.4.3 Aminophosphine Precursor Isolation and Crystallization

This section details the protocols used to isolate and crystallize Structures 1–5 of Table S4.1.

*Crystallization of **1** ($C_{48}H_{120}Cl_4Cu_4N_{12}P_4$).* A concentrated mixture of CuCl (49.5 mg, 0.500 mmol), $P(NEt_2)_3$ (0.177 g, 0.716 mmol), and TOA (0.700 ml) ([Cu] = 0.56 M, P/Cu = 1.4) was heated to 100 °C for 10 min to fully solubilize the CuCl. The hot solution was cooled to ambient temperature slowly to yield colorless crystals, which were observed 5 h later. The corresponding crystal structure is shown in Figure 4.2a.

*Crystallization of **2a** ($C_{39}H_{47}N_5OP_2$).* $P(NEt_2)_3$ (1.486 g, 6.006 mmol) was transaminated (*vide supra*) with p-toluidine (1.932 g, 18.03 mmol). The resulting viscous liquid was dissolved in

6 ml THF. Half of the solution (3.41 g) was concentrated with gentle heating under vacuum to ~80% of the starting volume, at which point a slight opacity indicating supersaturation was observed. After 20 h, several multi-mm, colorless crystals were observed, with the corresponding crystal structure of Figure S4.1.

*Isolation and Crystallization of **2b** ($C_{43}H_{55}Cl_2Cu_2N_5O_2P_2$).* CuCl (0.300 g, 3.03 mmol) was added to 8 ml MeCN. The copper oxychloride impurities from the resulting mixture were removed via centrifugation at 2000 rpm for 5 min; the supernatant was decanted for further use. The remaining half of the (p-toluidino)phosphine THF solution (3.41 g, ~2.6 mmol P, ~6.5 mmol p-toluidine) was added slowly to the CuCl MeCN solution over 2 min. The mixture was stirred for 20 h and the white solids which formed were collected via centrifugation at 2000 rpm for 5 min (0.401 g, 33% yield).

For the growth of crystals suitable for single-crystal powder X-ray diffraction, some of the product (39 mg) was recrystallized from 7 ml boiling THF after stirring for 30 min (closed system, no solvent loss). The hot solution was cooled to ambient temperature slowly to yield colorless crystals, which were observed 20 h later. The corresponding crystal structure is shown in Figure 4.2b.

*Crystallization of **3** ($C_{24}H_{30}ClCuN_3P$).* CuCl (0.166 g, 1.68 mmol) and pre-transaminated (4-methylbenzylamino)phosphine solution (2.303 g, ~3.4 mmol P, ~18 mmol 4-MBA) were solubilized upon addition to 2 ml THF, 4 ml tol, and 5 ml TOA with heating at 100 °C for 30 min. MeCN (1 ml) was added to the resulting solution to precipitate a white powder which was collected via centrifugation at 2000 rpm for 5 min. This powder was recrystallized from 1 ml boiling THF after stirring for 30 min (closed system, no solvent loss). The hot solution was cooled to ambient

temperature slowly to yield colorless crystals, which were observed 20 h later. The corresponding crystal structure is shown in Figure S4.2.

*Crystallization of Structure **4** (*$C_{16}H_{18}ClCuN_3P$*).* A pre-transaminated (p-toluidino)phosphine solution (1.443 g, ~1.3 mmol P, ~3.8 mmol p-toluidine) was diluted with 2 ml THF. A purified, oxychloride-free CuCl MeCN solution (1.233 g, ~1.3 mmol Cu; see isolation of **2b** above) was added slowly to the aminophosphine/THF solution over 2 min. The solution was allowed to sit unperturbed at ambient temperature for 16 days to yield colorless crystals. The corresponding crystal structure is shown in Figure S4.3.

4.4.4 Characterization

All sample preparations for characterization were conducted under inert atmosphere in a nitrogen-filled glovebox to mitigate aerobic oxidation prior to measurement.

Transmission electron microscopy (TEM). Sample grid preparation for TEM involved the drop-casting of nanocrystal suspensions in 50:50 bv THF/toluene onto a 100-mesh copper grid coated with Formvar and carbon (Electron Microscopy Sciences). TEM images were collected on a FEI Tecnai Spirit operating at 120 kV. If applicable, nanoplatelet lateral dimension was determined via statistical analysis of those TEM images. Particles were analyzed with mitigated orientation bias by taking lateral dimension of the platelet to be the longest line that could be drawn along the particle's two-dimensional projection. The size distributions were derived from the analysis of 150 particles with the use of 13($\sqrt{150}$+1) constant-width bins spanning the ensemble range.

Electronic absorption spectroscopy of $Cu_{3-x}P$ nanocrystals. Concentrated nanocrystal toluene suspension (10 µl, 1/300th of total sample), 390 µl toluene, and 400 µl THF were anaerobically added to a quartz screw-cap cuvette (2-mm path-length). Spectra were collected

using a Cary 5000 spectrometer in transmission mode and background corrected using the spectrum of 50:50 bv THF/toluene in the same cuvette. LSPR energy was estimated by local fitting of the near-infrared absorbance peak to a Gaussian function.

Powder X-ray diffraction. Samples were prepared from dried pellets collected by centrifugation. produced from two additional washes of the nanocrystals. Powder diffraction patterns were measured using a transmission-mode diffractometer equipped with a Bruker APEX-II Ultra CCD detector and Cu Kα radiation source ($\lambda_{\alpha 1}$ = 1.5406 Å, $\lambda_{\alpha 2}$ = 1.5444 Å).[29] For each individual measurement, a 200-μm-diameter piece of pellet was quickly picked out under a light microscope and mounted on a Cryoloop with Fomblin Y oil. Three frames centered at 2θ = 30°, 45°, and 60°, respectively, were collected with a detector distance of 150 mm, spinning φ, and 240 s exposure time per image. The Debye rings obtained from the three frames were merged and radially integrated in a cone with γ range 80–100° using Diffrac.eva software. For comparison, the powder diffraction patterns of $Cu_{2.87}P$, AgP_2, fcc Ag, and fcc Cu were simulated from single-crystal data[15-16, 21-22] using VESTA.[30]

Single-crystal X-ray diffraction. Single-crystal X-ray diffraction was performed using a Bruker APEX-II Ultra CCD diffractometer equipped with either Cu Kα (λ = 1.5406 Å) or Mo Kα radiation (λ = 0.7107 Å). Crystals were mounted on a Cryoloop with Fomblin Y oil. Data were collected in a nitrogen gas stream at 100 (or 273) K using Φ and ω scans. Crystal-to-detector distance was 45 mm and exposure time was 10 s per frame using a scan width of 0.75°. The data were integrated using the Bruker SAINT software program and scaled using the SADABS software program. Solution by direct methods (SHELXT[31]) produced a complete phasing model consistent with the proposed structure.

$^{31}P\{^{1}H\}$ NMR spectroscopy. The aminophosphine/amine solutions and a minimum of 350 μl benzene-d_6 were added to a screw-cap NMR tube (Wilmad-Labglass) with a minimum total volume of 650 μl. ^{31}P NMR spectra were collected on a JEOL ECA 500 MHz spectrometer with ^{1}H decoupling (32 scans, relaxation delay = 20 s) and processed in Mestrenova using 2-Hz apodization. Chemical shifts were externally referenced to 85 % H_3PO_4 (δ = 0 ppm).

Yield determination by Cu^{2+} quantification for reaction aliquots. For the kinetic experiment corresponding to Figure 4.11, aliquots of ~1 ml volume were withdrawn at 10 min, 20 min, 40 min, 60 min, and 90 min time-points after reaching T = 225 °C. These aliquots were further divided into four sub-aliquots, which were each quantitatively weighed using an analytical balance. One sub-aliquot was saved for TEM and the remaining three were digested with nitric acid for yield determination. Each sub-aliquot was purified twice by addition of 0.25 ml toluene and 1.25 ml acetone and pellet collection via centrifugation at 8000 rpm for 3 min. Accordingly, each aliquot yielded three separate pellets for digestion and yield quantification. After the evaporation of residual solvent, each dry pellet was digested for 22 h with 800 μl 70% HNO_3 while kept sealed in a plastic, o-ring, screw-cap tube (Axygen, SCT-200-SS-C) to prevent volume change. The following day, the solutions were filtered with a 0.22 μm PVDF syringe filter and [Cu^{2+}] was quantified by measurement of absorption spectra in a 2-mm path-length cuvette using a Cary 5000 spectrometer in transmission mode with background correction using neat HNO_3. A calibration line was made using analogously digested copper metal as a standard (see Appendix of Chapter 3). Rather than using a single-energy extinction coefficient for [Cu^{2+}] quantification, an energy range of 1.378–1.550 eV nm was integrated instead. For yield calculations, it was assumed that all Cu atoms from the digested $Cu_{3-x}P$ nanocrystals were oxidized to Cu^{2+}. Additionally,

aliquot masses relative to the total synthesis mass are used for back-calculation of yield, which is reported relative to CuCl used in the synthesis.

4.5 Appendix: Supplementary Information

Table S4. 1. Crystallographic parameters of an aminophosphine molecule, aminophosphine–Cu_4Cl_4 clusters, and aminophosphine–Cu_nCl_n polymers.

Structure	**1**	**2b**	**2a**	**3**	**4**
Figure	4.2a	4.2b	S4.1	S4.2	S4.3
Empirical formula	$C_{48}H_{120}$ Cl_4Cu_4 $N_{12}P_4$	$C_{43}H_{55}$ Cl_2Cu_2 $N_5O_2P_2$	$C_{39}H_{47}$ N_5OP_2	$C_{24}H_{30}$ ClCu N_3P	$C_{16}H_{18}$ ClCu N_3P
Formula weight	1384.73	933.52	663.79	489.49	382.31
Crystal system	Monoclinic	Triclinic	Monoclinic	Triclinic	Monoclinic
Space group	$P2_1/n$	P1	Cc	P1	C2/c
c (Å)	22.6033(4)	16.058(2)	17.822(7)	17.4377(14)	16.732(2)
α (°)	90	66.515(5)	90	76.560(4)	90
β (°)	100.031(1)	72.427(4)	120.127(9)	88.386(6)	121.806(2)
γ (°)	90	79.016(4)	90	69.053(6)	90
Volume ($Å^3$)	13824.0(5)	2407.4(5)	3605(2)	1161.9(2)	3722.6(8)
Z	8	2	4	2	8
ρ_{calc} (g/cm^3)	1.215	1.248	1.223	1.399	1.491
μ (mm^{-1})	3.979	1.105	0.158	1.140	1.409
Goodness-of-fit on F^2	1.069	1.071	1.020	1.103	1.043
Reflections collected	160802	72965	9334	8859	14787
Independent reflections	25115	9820	5026	4209	3821
R_1	0.0465	0.0459	0.0483	0.0556	0.0370
wR_2	0.1490	0.1208	0.1065	0.1581	0.0946
Temperature (K)	100	100	100	273	100
Radiation	CuK_α	MoK_α	MoK_α	MoK_α	MoK_α

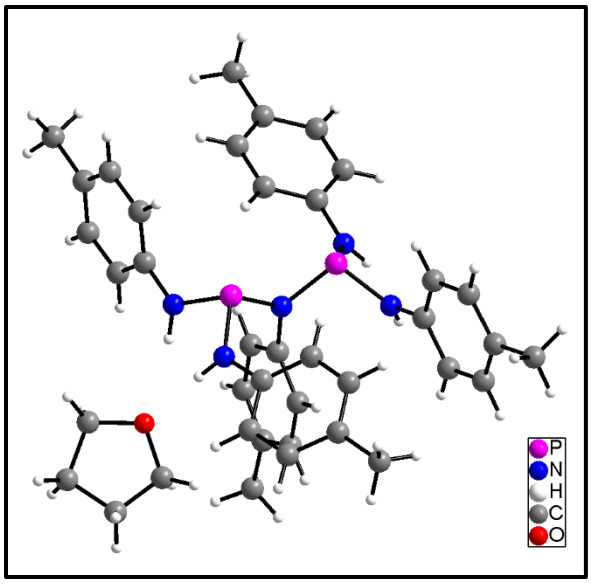

Figure S4. 1. Solid-state structure (**2a**, Table S4.1) of diphosphine $P_2NR(NHR)_4$ co-crystallized with THF as a solvent, where NH_2R = p-toluidine.

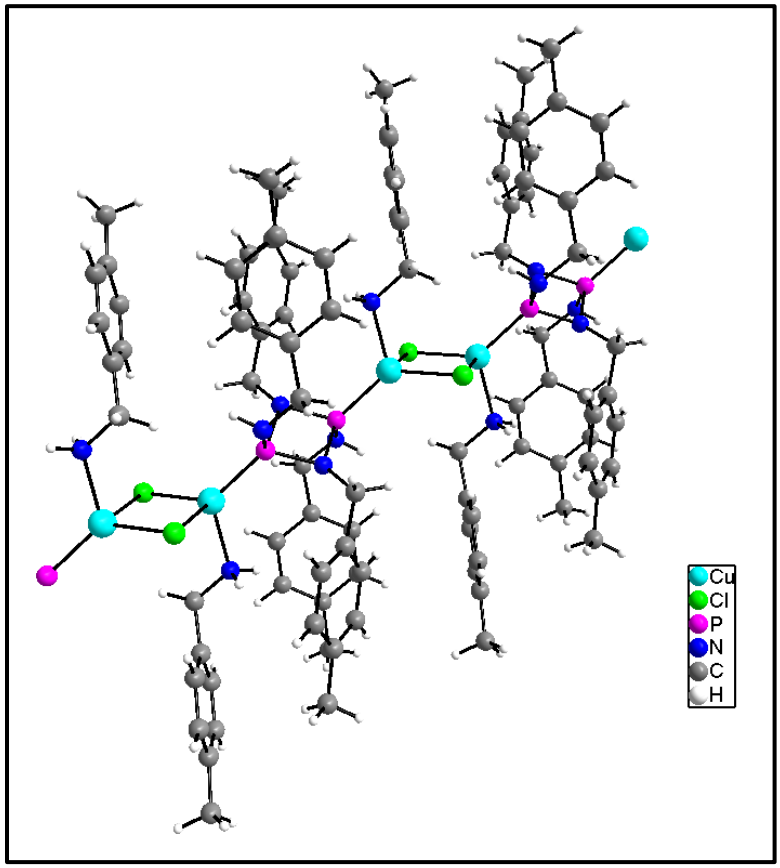

Figure S4. 2. Solid-state structure (**3**, Table S4.1) of polymer with repeating units of alternating $Cu_2Cl_2(NH_2R)_2$ and diphosphine $P_2(NR)_2(NHR)_2$, where NH_2R = 4-MBA.

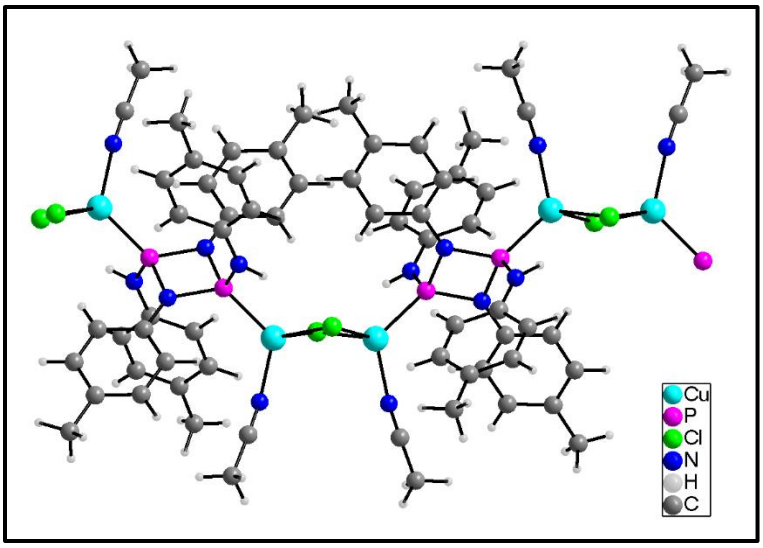

Figure S4. 3. Solid-state structure (**4**, Table S4.1) of polymer with repeating units of alternating $Cu_2Cl_2(MeCN)_2$ and diphosphine $P_2(NR)_2(NHR)_2$, where NH_2R = p-toluidine.

Table S4. 2. The peak assignments, positions, and relative areas from the ^{31}P NMR spectra of the phosphorus amide scrambling experiment of Figure 4.8.

Species*	**^{31}P δ (ppm)**	**Relative Area (Before)**	**Relative Area (After)**
$P_2NR'(NHR')_4$	108.4	0.0	47.0
$P(NHR')_3$	98.1	0.0	23.5
$P(NHR')_2(NHR)_1$	89.1	0.0	23.9
$P(NHR')_1(NHR)_2$	80.5	0.0	5.6
$P(NHR)_3$	76.5	89.3	0.0
$P_2NR(NHR)_4$	70.7	10.7	0.0

*NH_2R = 4-decylaniline; NH_2R' = OAm

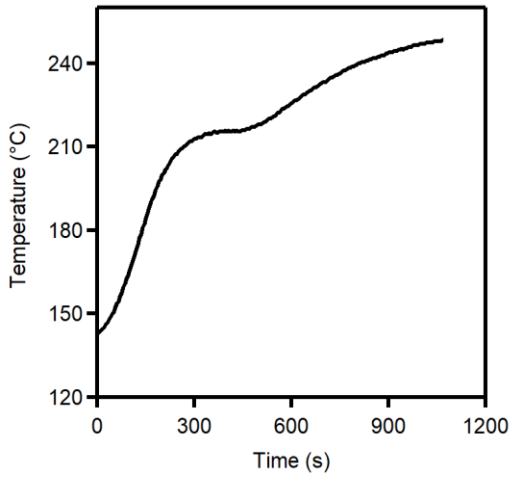

Figure S4. 4. Temperature profile of the $Cu_{3-x}P$ nanocrystal heat-up synthesis using $[Cu(MeCN)_4]PF_6$ as the Cu salt precursor (corresponding to Figure 4.9).

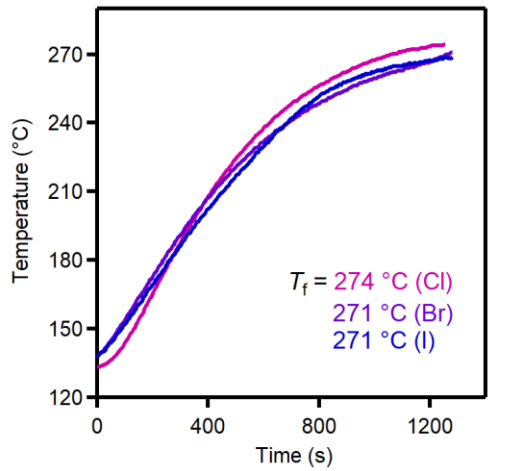

Figure S4. 5. Temperature profiles for the $Cu_{3-x}P$ nanocrystal heat-up synthesis series with varied Cu(I) halide identity (corresponding to Figure 4.10).

Table S4. 3. Chemicals.

Chemical	Purity	Manufacturer
d^6-Benzene	99.5%	Cambridge Isotope Laboratories
Copper(I) chloride (CuCl)	>97%	Strem Chemicals
Copper(I) bromide (CuBr)	>98%	Strem Chemicals
Copper(I) iodide (CuI)	98%	Strem Chemicals
4-Decylaniline	98%	Alfa Aesar
N,N-Dimethylhexadecylamine (DMHDAm)	>98%	TCI Chemicals
Hexadecane	>98%	TCI Chemicals
4-Methylbenzylamine (4-MBA)	98%	Alfa Aesar
Nitric acid (HNO_3)	70% bv	Fisher Chemical (certified ACS)
Oleylamine (OAm)	>95%	Strem Chemicals
p-Phenetidine	>98%	TCI Chemicals
Silver(I) chloride (AgCl)	99.9%	Strem Chemicals
Tetrakis(acetonitrile)copper(I) hexafluorophosphate ($[Cu(MeCN)_4]PF_6$)	>98%	Strem Chemicals
p-Toluidine	99%	Acros Organics
Tris(diethylamino)phosphine ($P(NEt_2)_3$)	95%	Acros Organics
Trioctylamine (TOA)	97%	Frontier Scientific

4.6 Acknowledgements

Chapter 4 is comprised of unpublished work which may eventually be published in some form in the more distant future. The dissertation author was the primary author of this chapter and gratefully acknowledges the contributions of advisor Alina M. Schimpf. This research was primarily supported by the National Science Foundation through the UC San Diego Materials Research Science and Engineering Center (DMR-2011924). TEM imaging was performed at the National Center for Microscopy and Imaging Research at UC San Diego. Single-crystal and powder X-ray diffraction measurements were performed at the UC San Diego Crystallography Facility with the welcome technical guidance of Dr. Milan Gembicky.

4.7 References

1. Song, W.-S.; Lee, H.-S.; Lee, J. C.; Jang, D. S.; Choi, Y.; Choi, M.; Yang, H. Amine-Derived Synthetic Approach to Color-Tunable InP/ZnS Quantum Dots with High Fluorescent Qualities. *J. Nanopart. Res.* **2013,** *15*, 1750.

2. Tessier, M. D.; Dupont, D.; De Nolf, K.; De Roo, J.; Hens, Z. Economic and Size-Tunable Synthesis of InP/ZnE (E = S, Se) Colloidal Quantum Dots. *Chem. Mater.* **2015,** *27*, 4893.

3. Tessier, M. D.; De Nolf, K.; Dupont, D.; Sinnaeve, D.; De Roo, J.; Z, H. Aminophosphines: A Double Role in the Synthesis of Colloidal Indium Phosphide Quantum Dots. *J. Am. Chem. Soc.* **2016,** *138*, 5923.

4. Buffard, A.; Dreyffuss, S.; Nadal, B.; Heuclin, H.; Xu, X.; Patriarche, G.; Mézailles, N.; Dubertret, B. Mechanistic Insight and Optimization of InP Nanocrystals Synthesized with Aminophosphines. *Chem. Mater.* **2016,** *28*, 5925.

5. Laufersky, G.; Bradley, S.; Frécaut, E.; Lein, M.; Nann, T. Unraveling Aminophosphine Redox Mechanisms for Glovebox-Free InP Quantum Dot Syntheses. *Nanoscale* **2018,** *10*, 8752.

6. Mundy, M. E.; Ung, D.; Lai, N. L.; Jahrman, E. P.; Seidler, G. T.; Cossairt, B. M. Aminophosphines as Versatile Precursors for the Synthesis of Metal Phosphide Nanocrystals. *Chem. Mater.* **2018,** *30*, 5373.

7. Grigel, V.; Dupont, D.; De Nolf, K.; Hens, Z.; Tessier, M. D. InAs Colloidal Quantum Dots Synthesis via Aminopnictogen Precursor Chemistry. *J. Am. Chem. Soc.* **2016,** *138*, 13485.

8. Srivastava, V.; Dunietz, E.; Kamysbayev, V.; Anderson, J. S.; Talapin, D. V. Monodisperse InAs Quantum Dots from Aminoarsine Precursors: Understanding the Role of Reducing Agent. *Chem. Mater.* **2018,** *30*, 3623.

9. Srivastava, V.; Janke, E. M.; Diroll, B. T.; Schaller, R. D.; Talapin, D. V. Facile, Economic and Size-Tunable Synthesis of Metal Arsenide Nanocrystals. *Chem. Mater.* **2016,** *28*, 6797.

10. Ginterseder, M.; Franke, D.; Perkinson, C. F.; Wang, L.; Hansen, E. C.; Bawendi, M. G. Scalable Synthesis of InAs Quantum Dots Mediated through Indium Redox Chemistry. *J. Am. Chem. Soc.* **2020,** *142*, 4088.

11. Hendricks, M. P.; Campos, M. P.; Cleveland, G. T.; Jen-La Plante, I.; Owen, J. S. A Tunable Library of Substituted Thiourea Precursors to Metal Sulfide Nanocrystals. *Science* **2015,** *348*, 1226.

12. Tarassoli, A.; Haltiwanger, R. C.; Norman, A. D. Synthesis and Structural Characterization of the Primary-Amine-Substituted Phosphines $(C_6H_5NH)_3P$ and $[(C_6H_5N_H)_2P]_2NC_6H_5$. *Inorg. Chem.* **1982,** *21*, 2684.

13. Churchill, M. R.; Kalra, K. L. Tetrameric Phosphinecopper(I) Halides. X-Ray Crystallographic Evidence for a "Cubane" Structure for the Cu_4Cl_4 core of $(PPh_3CuCl)_4$ and a "Step" Structure for the Cu_4Br_4 core in Crystalline $(PPh_3CuBr)_4 \cdot 2CHCl_3$. *J. Am. Chem. Soc.* **1973,** *95*, 5772.

14. Gopalakrishnan, J. Aminophosphines: Their Chemistry and Role as Ligands and Synthons. *Appl. Organomet. Chem.* **2009,** *23*, 291.

15. Olofsson, O. The Crystal Structure of Cu_3P. *Acta Chem. Scand.* **1972,** *26*, 2777.

16. Shkvarina, E. G.; Titov, A. A.; Shkvarin, A. S.; Plaisier, J. R.; Gigli, L.; Titov, A. N. Thermal Stability of the Layered Modification of $Cu_{0.5}ZrTe_2$ in the Temperature Range 25–900 °C. *Acta Crystallogr. C Struct. Chem.* **2018,** *74*, 1020.

17. Newman, J. D. S.; Blanchard, G. J. Formation of Gold Nanoparticles Using Amine Reducing Agents. *Langmuir* **2006,** *22*, 5882.

18. Rachkov, A. G.; Schimpf, A. M. Colloidal Synthesis of Tunable Copper Phosphide Nanocrystals. *Chem. Mater.* **2021,** *33*, 1394.

19. Strach, M.; Mantella, V.; Pankhurst, J. R.; Iyengar, P.; Loiudice, A.; Das, S.; Corminboeuf, C.; van Beek, W.; Buonsanti, R. Insights into Reaction Intermediates to Predict Synthetic Pathways for Shape-Controlled Metal Nanocrystals. *J. Am. Chem. Soc.* **2019,** *141*, 16312.

20. Carenco, S.; Portehault, D.; Boissière, C.; Mézailles, N.; Sanchez, C. Nanoscaled Metal Borides and Phosphides: Recent Developments and Perspectives. *Chem. Rev.* **2013,** *113*, 7981.

21. Spreadborough, J.; Christian, J. W. High-Temperature X-Ray Diffractometer. *J. Sci. Instrum.* **1959,** *36*, 116.

22. Møuller, M. H.; Jeitschko, W. Darstellung, Eigenschaften und Kristallstruktur von Cu_2P_7 und Strukturverfeinerungen von CuP_2 und AgP_2. *Z. anorg. allg. Chem.* **1982,** *491*, 225.

23. Tappan, B. A.; Chen, K.; Lu, H.; Sharada, S. M.; Brutchey, R. L. Synthesis and Electrocatalytic HER Studies of Carbene-Ligated $Cu_{3-x}P$ Nanocrystals. *ACS Appl. Mater. Interfaces* **2020,** *12*, 16394.

24. De Trizio, L.; Gaspari, R.; Bertoni, G.; Kriegel, I.; Moretti, L.; Scotognella, F.; Maserati, L.; Zhang, Y.; Messina, G. C.; Prato, M.; Marras, S.; Cavalli, A.; Manna, L. $Cu_{3-x}P$ Nanocrystals as a Material Platform for Near-Infrared Plasmonics and Cation Exchange Reactions. *Chem. Mater.* **2015,** *27*, 1120.

25. Manna, G.; Bose, R.; Pradhan, N. Semiconducting and Plasmonic Copper Phosphide Platelets. *Angew. Chem. Int. Ed.* **2013,** *52*, 6762.

26. Liu, Z.; Mu, H.; Xiao, S.; Wang, R.; Wang, W.; Wang, Y.; Zhu, X.; Lu, K.; Zhang, H.; Lee, S.-T.; Bao, Q.; Ma, W. Pulsed Lasers Employing Solution-Processed Plasmonic $Cu_{3-x}P$ Colloidal Nanocrystals. *Adv. Mater.* **2016,** *28*, 3535.

27. Voorhees, P. W. The Theory of Ostwald Ripening. *J. Stat. Phys.* **1985,** *38*, 231.

28. Pangborn, A. B.; Giardello, M. A.; Grubbs, R. H.; Rosen, R. K.; Timmers, F. J. Safe and Convenient Procedure for Solvent Purification. *Organometallics* **1996,** *15*, 1518.

29. Härtwig, J.; G., H.; E., F.; K., G.; K., W.; J., W. Remeasurement of Characteristic X-Ray Emission Lines and Their Application to Line Profile Analysis and Lattice Parameter Determination. *Phys. Stat. Sol. (a)* **1994,** *143*, 23.

30. Momma, K.; Izumi, F. VESTA 3 for Three-Dimensional Visualization of Crystal, Volumetric and Morphology Data. *J. Appl. Cryst.* **2011,** *44*, 1272.

31. Sheldrick, G. SHELXT - Integrated Space-Group and Crystal-Structure Determination. *Acta Crystallogr. A* **2015,** *71*, 3.